

EXPANDING THE REACH OF QUANTUM ENHANCED
GRAVITATIONAL-WAVE DETECTORS

by

DHRUVA GANAPATHY

B.Tech., Indian Institute of Technology, Delhi (2018)

Submitted to the Department of Physics
in partial fulfillment of the requirements for the degree of
Doctor of Philosophy in Physics

at the

MASSACHUSETTS INSTITUTE OF TECHNOLOGY

May 2024

© Dhruva Ganapathy 2024. All rights reserved.

The author hereby grants to MIT a nonexclusive, worldwide, irrevocable, royalty-free license to exercise any and all rights under copyright, including to reproduce, preserve, distribute and publicly display copies of the thesis, or release the thesis under an open-access license.

Authored by : Dhruva Ganapathy
Department of Physics
May 16, 2024

Certified by : Matthew Evans
Professor of Physics
Thesis Supervisor

Accepted by : Lindley Winslow
Associate Department Head of Physics

EXPANDING THE REACH OF QUANTUM ENHANCED GRAVITATIONAL-WAVE DETECTORS

by

DHRUVA GANAPATHY

Submitted to the Department of Physics

*on May 16, 2024 in partial fulfillment of the requirements for the degree of
Doctor of Philosophy in Physics*

ABSTRACT

The Advanced LIGO detectors are the most precise displacement sensors ever made, operating at the cutting edge of quantum noise limited sensitivity. The introduction of non-classical squeezed states to reduce quantum shot noise during the third gravitational wave observing run O3 ushered in the era of quantum-enhanced gravitational wave interferometry. This was, however, accompanied by an increase in measurement back-action, in the form of quantum radiation pressure noise which degraded detector sensitivity at low frequencies below 100 Hz. In the early 2000s, Kimble et. al. [1] proposed the use of optical filter cavities to prepare frequency dependent squeezed states which circumvent measurement back-action by suppressing radiation pressure noise at low frequencies while continuing to reduce shot noise across the rest of the gravitational wave signal band.

In this thesis, we explore frequency dependent squeezing for gravitational wave detectors, with an emphasis on optimal filter cavity design, and characterization of squeezing in optical systems. We then describe the commissioning of a 300 m filter cavity for the first realization of frequency dependent squeezing in gravitational wave interferometer for the fourth gravitational wave observing run O4. Along with significantly enhancing the astrophysical sensitivity of the LIGO detectors, this is also the latest milestone in several decades of research in quantum noise reduction.

We conclude the thesis by extending frequency dependent squeezing to alternate interferometer configurations by studying the feasibility of detuning the signal cavity of the interferometer to enhance sensitivity to kilohertz signals from neutron star post-mergers.

Thesis Supervisor: Matthew Evans

Title: Professor of Physics

To my family and the lives they have led. Those, whose sacrifices I will always strive to be worthy of.

Our minds are firewood. And now we spark the match, we set ourselves alight.

ENTER SHIKARI - MARIONETTES (II. THE ASCENT)

ACKNOWLEDGEMENTS

Being a part of LIGO has given me the privilege of working with and making connections with many amazing people, each of whom has played a vital role in the creation of this thesis. More importantly, however, it has also led to me realize that it is exactly these connections that make the shared pursuit of scientific knowledge a fulfilling endeavour. For that, I will be ever grateful. While mentioning everyone who has enriched my journey is an admittedly insurmountable task, I have done my best to put my gratitude down into words in the paragraphs that follow.

Making it through graduate school would have been impossible without the guidance of the several mentors I have been fortunate to have had over the last six years. I must extend my foremost thanks to Lee, whose seemingly infinite patience helped me navigate a completely new and unknown world to come into my own as an experimental physicist. Lisa has always looked out for my career, and if I can go as far as to claim that my graduate studies have been successful, this is in no small part thanks to her. Evan and Vivishek have provided me with much needed career guidance and helped me see the bigger picture by motivating me to think about the world that exists outside the confines of my own project. I thank Matt for giving me the freedom to find myself professionally while also making sure that the quality of work that I have put out has been up to a standard that I can be proud of.

I'd like to thank Chris and Vicky for making sure that I never felt alone while working on anything, be it in MIT, or at LIGO Hanford, and teaching me the joy (and sometimes, frustration) of finding my way through a project that was much larger than me, while fostering great friendships. Kentaro's presence during the initial period of our work in MIT was invaluable.

At LIGO MIT, I have had the good fortune of being surrounded by a phenomenal set of people, whom I have come to see as family. I must especially thank Marie, whose tireless effort made the very messy back and forth travel and paperwork that my (and everyone else's) work entailed possible, while also ensuring that everything in the office and labs ran smoothly. Peter, Kevin, Slawek, Rich, and Fabrice have always been ready to spend very valuable time to help me, often with very mundane problems. I should mention here that absolutely none of the filter cavity work in LASTI would have possible without Myron's expertise. I'm very thankful to the other graduate students and postdocs - Aaron, Alvaro, Ben, Sylvia, Nick, Wen, Hudson, Swadha, Regina, Dorotea, Sidd, Deep and Xinghui, whose company have made my time in NW22 one to remember and cherish for a long time to come.

My time at LIGO Hanford was equally invaluable and I must thank Sheila for her guidance and for trusting me with the squeezer and interferometer, an experience I cannot describe in words. Daniel and Jenne also added to the ever growing list of mentors I am fortunate to have learned from. Having Camilla, Nutsinee and Naoki around while working on the squeezer was a delight, and only enriched this experience further. At Hanford, I was also able to forge some of the deepest friendships I have come to know. Saying that Francisco, Varun, Ellie, Tony, Elenna, Louis and Mayra kept me going through what was arguably a period of great personal turmoil, would be an understatement.

My friends in Cambridge have been an important lifeline. From the moment I started here, Eugene, Calvin, Mikail and Somu have been constants in my life and it has been a privilege to share this journey with them. Arkya and Madhav have become an essential source of support and my closest friends here over the last few years. I must mention Aadi, who was one of the best flatmates and friends I could have possibly asked for. I'm extremely glad that I got to overlap with Avaneep, albeit for a short duration, and forge what I'm hoping is a lifelong friendship. I also thank Amogh, Ishir, Misha and Pratyusha for the incredible memories that they have gifted me with.

I would like to finally thank those who have been there for me for as long as I can remember. Sirish, I'm not sure the 10 year old versions of us would believe that we'd be stuck with each other as best friends 18 years down the line. My extended family in Seattle and Canada have given me something that is as close to a home as I can get so far away from India. My brother, Deb, and my parents, whom I was extremely fortunate to be around during the pandemic, have been a source of unwavering support, understanding and caring for me like no one else, all whilst reinforcing the idea that I must, first and foremost, be a good human being. I owe everything to them and their sacrifices.

LIST OF PUBLICATIONS

1. L. McCuller, C. Whittle, **D. Ganapathy**, K. Komori, M. Tse, A. Fernandez-Galiana, L. Barsotti, P. Fritschel, M. MacInnis, F. Matichard, K. Mason, N. Mavalvala, R. Mittleman, Haocun Yu, M.E. Zucker, and M. Evans “*Frequency-Dependent Squeezing for Advanced LIGO*” : **Phys. Rev. Lett.** **124**, 171102 [Chapter 3]
2. Kentaro Komori, **Dhruva Ganapathy**, Chris Whittle, Lee McCuller, Lisa Barsotti, Nergis Mavalvala, Matthew Evans “*Demonstration of an amplitude filter cavity at gravitational-wave frequencies*” : **Phys. Rev. D** **102**, 102003 [Chapter 4]
3. Chris Whittle, Kentaro Komori, **Dhruva Ganapathy**, Lee McCuller, Lisa Barsotti, Nergis Mavalvala, Matthew Evans “*Optimal detuning for quantum filter cavities*” : **Phys. Rev. D** **102**, 102002 [Chapter 4]
4. **Dhruva Ganapathy**, Victoria Xu, Wenxuan Jia, Chris Whittle, Lisa Barsotti, Matthew Evans, Lee McCuller “*Probing squeezing for gravitational-wave detectors with an audio-band field*” : **Phys. Rev. D** **105**, 122005 [Chapter 5]
5. **D. Ganapathy**, W. Jia, M. Nakano et al. “*Broadband quantum enhancement of the LIGO detectors with frequency-dependent squeezing*” : **Phys. Rev. X.** **13**, 041021 [Chapter 6]
6. **Dhruva Ganapathy**, Lee McCuller, Jameson Graef Rollins, Evan D. Hall, Lisa Barsotti, Matthew Evans “*Tuning Advanced LIGO to kilohertz signals from neutron-star collisions*” : **Phys. Rev. D** **103**, 022002 [Chapter 7]

CONTENTS

Abstract	iii
Acknowledgments	ix
List of Publications	xii
List of Figures	xvii
List of Tables	xxi
1 Introduction	23
1.1 Gravitational Wave Detectors	24
1.2 Quantum Noise	28
1.2.1 Shot Noise	30
1.2.2 Quantum Radiation Pressure Noise	31
1.2.3 The Standard Quantum Limit	32
1.3 Overview	34
2 Squeezed States of Light	35
2.1 Sidebands and Quadratures	35
2.2 Introduction to Squeezed States	38
2.3 Generation of Squeezed States	45
2.3.1 Phase Matching	47
2.4 Cavity Enhancement of Squeezing	48

2.4.1	Auxiliary Field Transfer Matrix	50
2.5	Homodyne Detection	54
2.6	Coherent Control of Squeezed States	56
2.7	Degradation of Squeezing	60
2.7.1	Loss	60
2.7.2	Phase Noise	60
2.8	Squeezing in Optical Systems	63
2.8.1	Squeezing in LIGO	65
3	Frequency Dependent Squeezing	67
3.1	Filter Cavity Model	68
3.2	Filter Cavity Control	71
3.3	16 m Prototype Filter Cavity	79
3.3.1	Experimental Setup	79
3.3.2	Squeezing Control	81
3.3.3	Results	82
4	Optimal Filter Cavity Design	85
4.1	Model	86
4.2	Application to the LIGO A+ filter cavity	91
4.2.1	Choice of signal extraction mirror	96
4.3	Amplitude Filter Cavity	96
4.3.1	Experimental setup	99
4.3.2	Results	99
4.3.3	Improvement in detector range	103
4.3.4	Technical advantages of an amplitude filter cavity	104
5	Characterizing Squeezing with an Audio-Band Field	107
5.1	Experimental Setup	108
5.2	Mathematical Description	110
5.3	Characterising the Squeezed Vacuum Source	112
5.3.1	Squeezing Angle	114

CONTENTS

5.3.2	Generated squeezing level	115
5.3.3	Loss	116
5.3.4	Phase Noise	117
5.4	Characterizing Optical Systems	118
5.4.1	Filter Cavity	122
5.4.2	Interferometer	124
6	Frequency Dependent Squeezing in LIGO	130
6.1	Experimental setup	130
6.2	Frequency Dependent Squeezing at H1	133
6.3	Squeezing and Filter Cavity Control	136
6.4	Characterizing Frequency Dependent Squeezing	144
6.4.1	Filter Cavity	144
6.4.2	Squeezing injection	151
6.4.3	Interferometer parameters	153
7	Tuning LIGO to Binary Neutron Star Postmergers	157
7.1	Interferometer Configurations	158
7.2	Binary Neutron-Star Post-merger Templates	163
7.2.1	Astrophysical Distributions of Model Parameters	164
7.3	Results	169
7.4	Additional Considerations	170
7.4.1	Loss in the signal extraction cavity	170
7.4.2	Operational Challenges	172
8	Outlook	175
A	List of Acronyms and Symbols	177
B	Optical Cavities	181
B.1	Fabry-Perot Cavity	181
B.2	Interferometer Optical Gain	182
B.3	Interferometer Shot Noise	184

C	Filter Cavity Initial Alignment	186
D	Filter Cavity Backscatter in LIGO	188
E	OPO Crystal Degradation	193
E.1	Crystal loss at 532 nm	193
E.1.1	Gray Tracking in KTP	193
E.1.2	Green OPO losses in LIGO	193
E.2	Crystal loss at 1064 nm	194
E.2.1	GRIIRA	194
E.2.2	LIGO squeezing losses from OPO red cavity losses	196
E.2.3	Crystal spot movement at H1	196
	Bibliography	198

LIST OF FIGURES

1.1	Advanced LIGO Interferometer Layout during Observing run O4	25
1.2	LIGO A+ Design Noise Budget.	27
1.3	Shot noise and radiation pressure noise.	29
1.4	The standard quantum limit	33
2.1	Squeezed states of light.	42
2.2	Photon number distributions for bright squeezed states	44
2.3	Cavity enhancement of squeezing	49
2.4	Auxiliary field transfer	51
2.5	Characterizing an OPO using non-linear gain measurements	53
2.6	Homodyne Detection Scheme.	55
2.7	Coherent control of squeezed states	56
2.8	CLF-LO error signal model	59
2.9	Best possible squeezing for given loss and phase noise	61
2.10	Non-linear gain sweep in an OPO to constrain loss and phase noise	62
3.1	Squeezing rotation for various filter cavity detunings	70
3.2	Block diagram of the resonant sideband locking scheme.	72
3.3	Numerical simulation of RLF-CLF signal	74
3.4	Numerical simulation of RLF-LO signal	75
3.5	Numerical simulation of online tuning of the RLF-CLF signal	77
3.6	Numerical simulation of online tuning of the RLF-LO signal	78

3.7	Schematic overview of the optical and electronic layout for the 16 m filter cavity experiment.	80
3.8	Frequency-dependent squeezing at gravitational-wave detector frequencies in a 16 m prototype filter cavity	84
4.1	Sensitivity enhancement for the detection of binary inspirals relative to using frequency-independent squeezing for various cavity detunings and input transmissivities.	89
4.2	Sensitivity enhancement factor for binary inspirals using filter cavities with various detunings and losses at a given input transmissivity . . .	90
4.3	The relative percentage range improvement obtained with the installation of a filter cavity in A+ for various filter cavity input transmissivities and SQL frequencies.	92
4.4	Relative percentage binary neutron star (BNS) inspiral range improvement gained by installing a filter cavity with A+ parameters	94
4.5	The effect of detuning fluctuations on filter cavity optimal detuning .	95
4.6	Binary neutron star range improvement as a function of arm power and filter cavity input transmissivity, for an SEM transmissivity of 20 %	97
4.7	Demonstration of an amplitude filter cavity at gravitational-wave frequencies.	100
4.8	Characterization measurement of the 16 m amplitude filter cavity . . .	102
4.9	Enhancement in $1.4-1.4M_{\odot}$ binary neutron star and $75-75M_{\odot}$ binary black hole inspiral detection range for filter cavities with detuning $\Delta\omega_{fc}$ set to 0 Hz.	105
5.1	Experimental layout of a squeezer system with an audio diagnostic field	109
5.2	Demodulation space spanned by the ADF-LO signal e^{\uparrow} for various squeezing levels.	113
5.3	Characterization of a 16-m filter cavity using a sweep of the audio diagnostic field.	122
5.4	16 m filter cavity loss, rotation, and dephasing calculated from ADF measurements	125

LIST OF FIGURES

5.5	Simulation of quadrature observables and squeezing degradation metrics for an ideal interferometer with (blue) and without (red) a filter cavity	126
6.1	Detailed optical and controls layout of frequency-dependent squeezing instrumentation in the LIGO detectors.	131
6.2	Observation of frequency-dependent squeezing in LIGO.	134
6.3	SHG open loop transfer function.	137
6.4	OPO open loop transfer function.	138
6.5	CLF open loop transfer function.	140
6.6	LO open loop transfer function.	141
6.7	In-loop measurement of CLF and LO phase noise, calibrated into units of mrad.	142
6.8	Filter cavity green open loop transfer function.	143
6.9	Filter cavity RLF lock open loop transfer function.	145
6.10	In-loop measurement of filter cavity length noise, calibrated into units of picometers.	146
6.11	Cavity ringdown measurement	147
6.12	Ringdown measurements	148
6.13	Audio field measurements of the 300 m filter cavity at LIGO Hanford (H1). The model curves are plotted along with the data.	149
6.14	Frequency-dependent squeezing on a diagnostic balanced homodyne detector at H1.	150
6.15	Squeezing trends for the first 5 months of O4	155
6.16	Measured squeezing data compared with a quantum noise model . . .	156
7.1	Interferometer configurations under comparison. Representative strain noise curves of the “A+”, detuned, and wideband configurations plotted for reference.	159
7.2	Astrophysical distribution of Lorentzian parameters	167
7.3	Performance comparison between detuned and wideband configurations.	171

7.4 The effect of SEC loss on BNS post-merger sensitivity in detuned interferometers. 173

B.1 Fabry-Perot cavity. 181

B.2 Fabry-Perot Michelson Interferometer. 183

C.1 Filter cavity initial alignment procedure 187

D.1 Conversion between filter cavity length noise and excess noise in the interferometer. 189

D.2 Filter cavity open loop length noise. The flat shot noise at high frequencies is the sensor’s noise floor. 190

D.3 Filter cavity true length noise. 191

D.4 Filter cavity length noise projected to the interferometer. 192

E.1 OPO 532 nm transmission at H1 during O4 after crystal movement in Oct. 2023. 195

E.2 Normalized distribution of measured squeezing at H1. As discussed in Section 6.4.3, the amount of measured squeezing increased after reducing the interferometer’s input laser power. Moving the beam spot on the crystal further increased the measured squeezing by a significant amount. 197

LIST OF TABLES

3.1	Experimentally determined parameters of the frequency-dependent squeezed vacuum source at MIT.	82
4.1	Parameters for our amplitude filter cavity experiment. Entries marked by an asterisk were determined by fitting to recorded data. In all cases fitting produced values consistent with independent measurements and their uncertainties.	101
4.2	Assumed parameters of an interferometric GW detector.	103
5.1	Experimentally determined parameters of the OPO and 16 m filter cavity used for frequency-dependent squeezing.	123
6.1	Detailed summary of LIGO interferometer and squeezer parameters. .	135
7.1	Parameters of detuned and wideband LIGO configurations.	161
7.2	Assumed astrophysical distributions for lorentzian binary neutron star postmergers	168
7.3	Optimal interferometer configurations and postmerger sensitivity improvement factors	169

Since their initial detection by the Advanced Laser Interferometer Gravitational Wave Observatory (LIGO) in 2015 [2], gravitational waves have provided a new window into the cosmos. These ripples in the fabric of space-time have significantly advanced our comprehension of the most extreme phenomena in the universe and have also provided strong confirmation of Einstein’s theory of general relativity [3].

Described by Einstein’s field equations, gravitational waves emanate radially outwards from a source with a spherically asymmetric mass-quadrupole moment. However, the oscillating strain $\Delta L/L$ associated with a gravitational wave reaching Earth from a distant astrophysical source is exceedingly minute. Only the most exceptional astrophysical events can generate gravitational waves detectable by terrestrial instruments. Until now, we’ve observed signals from colliding black holes and neutron stars. In its first three observing runs, the gravitational wave detector network identified 90 compact binary mergers [4], enabling us to explore key questions in astrophysics.

The observation of the binary neutron star merger GW170817 [5], with an electromagnetic counterpart [6], marked the beginning of a new era in multi-messenger astronomy [7]. It provided insights into the origin of heavy elements [8] and deepened our understanding of the extreme matter constituting neutron stars [9, 10]. Other noteworthy detections include a $\sim 150M_{\odot}$ binary black hole merger [11] offering evidence for intermediate mass black hole formation [12], neutron star-black hole mergers [13], and a high mass ratio compact binary merger [14]. These detections have

also shed light on the population properties of compact objects [15] and contributed to our understanding of cosmic expansion history [16].

Looking forward, gravitational wave astronomy holds vast untapped potential. Numerous sources remain undetected, such as rotating pulsars [17] and core-collapse supernovae [18]. Gravitational waves can also provide insights into profound mysteries like dark matter [19] and quantum gravity [20]. Thus, it is crucial to advance technologies and push the limits of our ability to detect gravitational waves, ensuring continued exploration of the abundant knowledge they have to offer.

1.1 GRAVITATIONAL WAVE DETECTORS

The Advanced LIGO detectors are dual-recycled Fabry-Perot Michelson interferometers with 4 km arms [21]. They are located in Hanford, Washington, USA (H1), and Livingston Louisiana, USA (L1). In addition to the LIGO detectors, the international gravitational wave detector network also consists of the 3 km Advanced Virgo detector in Cascina, Italy [22], a cryogenic detector, KAGRA, located in the Kamioka Observatory, Japan [23], and a 600 m prototype detector, GEO600, located in Hannover, Germany [24]. The current observing run, O4, started in May 2023, with the two LIGO detectors. The Virgo detector joined the observing run in 2024. GEO600 has been instrumental to prototyping many new technologies that have been implemented in gravitational wave detectors. LIGO India, which is under construction, aims to join the detector network within the next decade [25].

Fig. 1.1 shows a top-level layout of the O4 configuration of the Advanced LIGO detectors. A pre-stabilized laser source supplies up to 110 W of power at 1064 nm¹. Before injection into the interferometer, the laser passes through pre-mode cleaner and input mode cleaner cavities to strip off higher-order modes which can contaminate the signal and stabilize the laser's frequency. 40 kg input and end mirrors of the interferometer arms, also known as test masses, form the 4 km Fabry-Perot cavities which amplify the gravitational wave signal by a factor of ~ 300 . The power in the arms is further amplified by a factor of ~ 40 by a power-recycling cavity on the input

¹The nominal input power for the detectors during O4 is 60 W

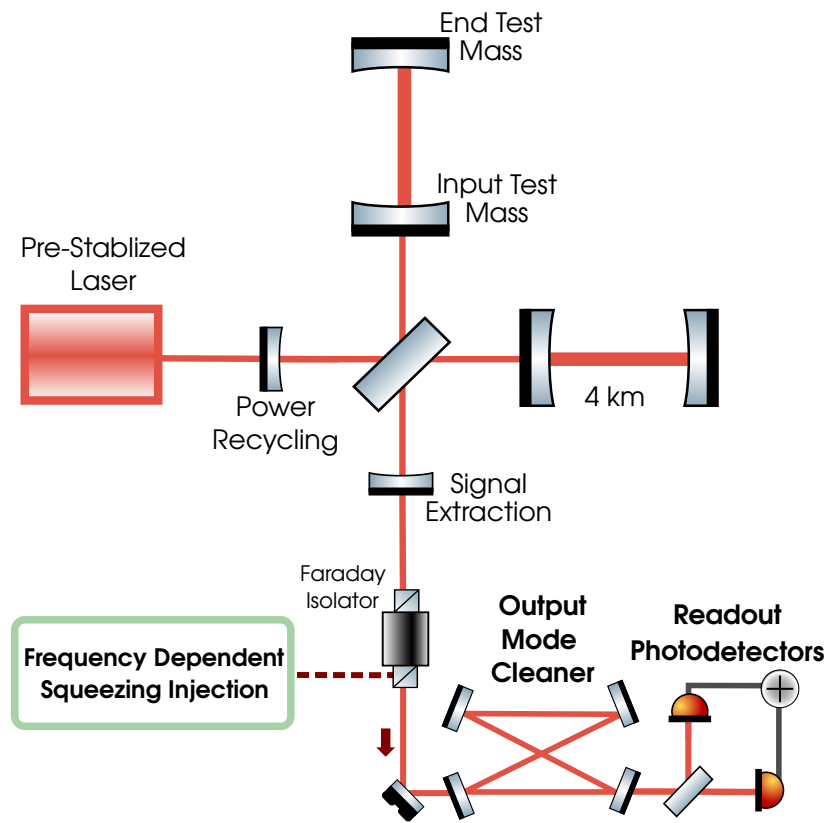


Figure 1.1: Advanced LIGO Interferometer layout during observing run O4.

port of the interferometer. A signal extraction cavity² on the output port of the interferometer, operated on carrier anti-resonance, increases the interferometer's signal bandwidth through resonant sideband extraction [26]. The beam from the interferometer then passes through the output Faraday Isolator. This is also the point, where non-classical light known as frequency dependent squeezed vacuum, the subject of this thesis, is injected to reduce noise from quantum fluctuations. A bow-tie output mode cleaner cavity then, removes all higher order modes and RF sidebands from the output, which is then split in two and read out as a sum of two photodetector signals.

A gravitational wave modulates the path length difference between the two arms, also known as the differential arm (DARM) degree of freedom. This modulates the power at the output port of the detector. Feedback is used to maintain DARM at a fixed operating point (~ 10 pm), and the signal associated with this feedback loop is calibrated into units of strain to measure a gravitational wave signal [27, 28]

In order to measure gravitational wave strains of the order of 10^{-23} , we need to have a comprehensive understanding of the noise in the detector. Fig. 1.2 shows a noise budget of LIGO A+³ which contains the modelled⁴ spectral densities of various sources of noise in the detectors. We see that the detector is designed to be maximally sensitive around 100 Hz which is the region in which most stellar mass compact binary merger signals are emitted. The LIGO mirrors are mounted on four stage pendulums [29], which ensure that seismic noise falls off rapidly over 10 Hz. However, this is dominant at low frequencies, along with Newtonian noise which is due to fluctuations in local gravity (for e.g. from Rayleigh waves). At high frequencies, the dominant sources of noise are due to the thermal motion of the mirror coatings and the quantum fluctuations of the laser light at the interferometer readout. Understanding and improving on these various sources of noise is key to achieving

²In literature, this is also commonly referred to as a signal recycling cavity. However, the term 'signal recycling' specifically refers to a resonant cavity which amplifies the gravitational wave signal which reducing the interferometer bandwidth.

³A+ is an upgraded version of Advanced LIGO with frequency dependent squeezing and reduced coating Brownian noise

⁴In addition to the modelled noises in the design curve, there are several sources of technical noise such as sensor noise, laser frequency and intensity noise, etc.

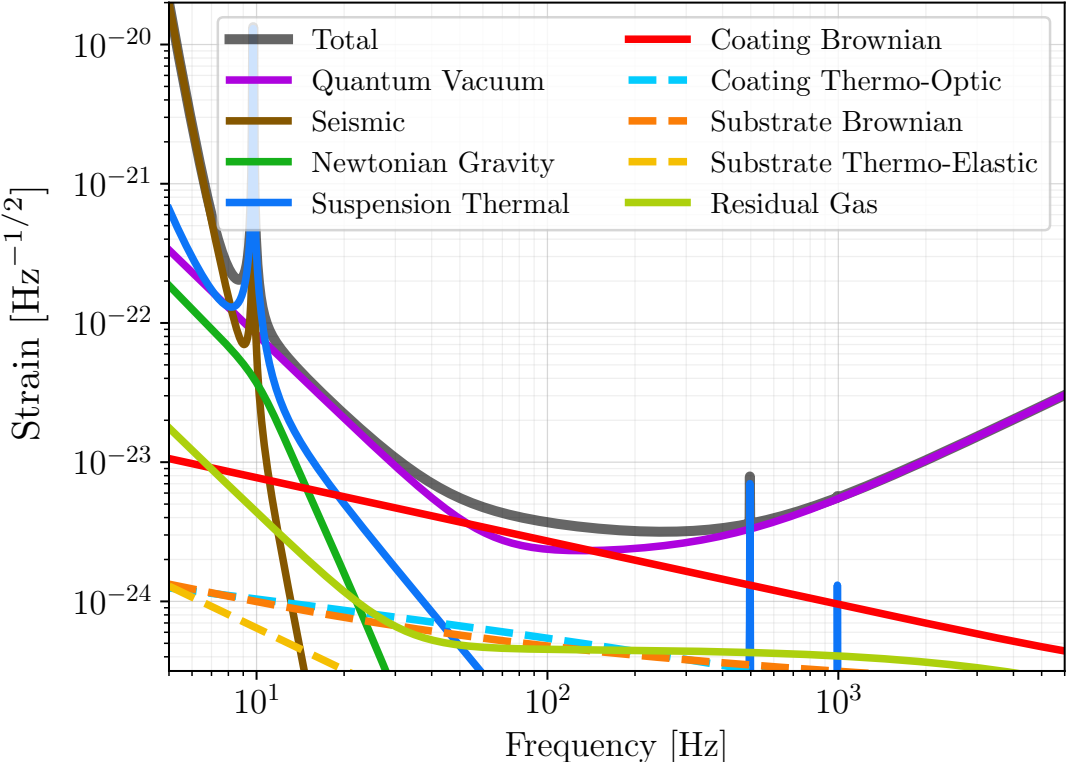


Figure 1.2: LIGO A+ Design Noise Budget.

LIGO's design sensitivity and is also essential for the development of 3rd generation detectors such as Cosmic Explorer [30, 31] and Einstein Telescope [32], which aim to out-perform current detectors by an order of magnitude in sensitivity. In this thesis, we specifically study quantum noise and the use of frequency dependent squeezed states of light to break existing limits in its reduction.

1.2 QUANTUM NOISE

The purple trace in Fig. 1.2 is the contribution from quantum noise to LIGO's total strain noise. This noise is linked to quantum fluctuations in the electromagnetic vacuum field entering the interferometer through its readout port. These fluctuations interact with the interferometer and subsequently manifest as noise on the readout photodetectors when they return to the readout port. This noise is linked to uncertainty in the phase and amplitude quadratures of the field (see Section 2.1), giving rise to two conceptually distinct components:

- Shot noise, caused by phase quadrature fluctuations, or equivalently, photon counting statistics at the interferometer readout. This dominates at high frequencies.
- Radiation pressure noise, caused by amplitude quadrature fluctuations, or equivalently, fluctuations in the photon flux impinging on the interferometer mirrors. This is dominant at low frequencies.

Fig. 1.3 depicts the contributions from shot noise and radiation pressure noise to the total quantum noise, which is usually described by a power spectral density. This can be normalized to get a spectrum calibrated in units of interferometer strain, S_h^{QN} , which is the sum of shot noise and quantum radiation pressure noise:

$$S_h^{\text{QN}} = S_h^{\text{SN}} + S_h^{\text{RPN}}. \quad (1.1)$$

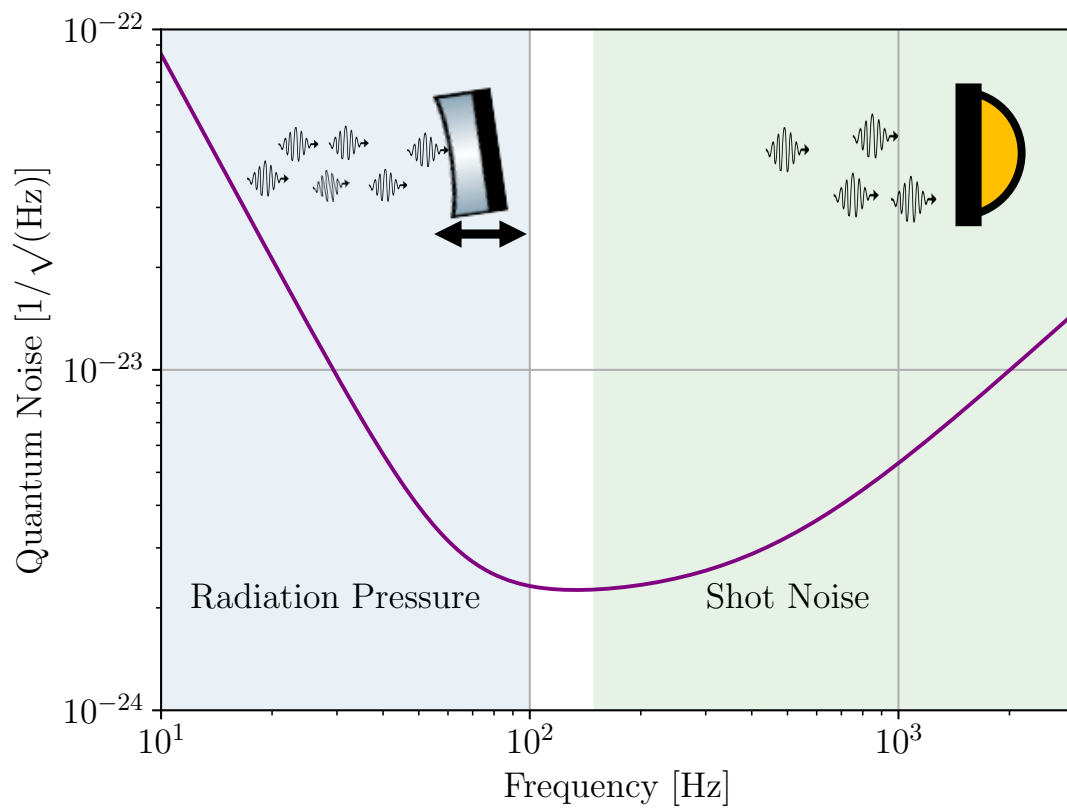


Figure 1.3: Shot noise and radiation pressure noise.

1.2.1 *Shot Noise*

The laser in a gravitational wave interferometer can be best described by a coherent state of light. A coherent state is defined as an eigenfunction of the annihilation operator

$$\hat{a}|\alpha\rangle = \alpha|\alpha\rangle. \quad (1.2)$$

In the photon number state basis, a coherent state can be written as

$$|\alpha\rangle = e^{-|\alpha|^2/2} \sum_0^{\infty} \frac{\alpha^n}{\sqrt{n!}} |n\rangle. \quad (1.3)$$

We introduce a ‘displacement operator’, $\hat{D}(\alpha)$ which transforms an electromagnetic vacuum state into a coherent state,

$$\hat{D}(\alpha)|0\rangle = |\alpha\rangle, \quad \hat{D}(\alpha) = \exp(\alpha\hat{a}^\dagger - \alpha^*\hat{a}). \quad (1.4)$$

In the Heisenberg picture, the displacement operator transforms the ladder operators as,

$$\hat{D}(\alpha)\hat{a}\hat{D}^\dagger(\alpha) = \hat{a} + \alpha, \quad \hat{D}(\alpha)\hat{a}^\dagger\hat{D}^\dagger(\alpha^*) = \hat{a}^\dagger + \alpha^*. \quad (1.5)$$

For a coherent state, the expected photon number and standard deviation are given by

$$\langle n \rangle = \langle \alpha | n | \alpha \rangle = |\alpha|^2, \quad \Delta n = \alpha, \quad (1.6)$$

and the probability of detecting n photons follows a Poisson distribution

$$P(n) = e^{-|\alpha|^2} \frac{|\alpha|^{2n}}{n!} = e^{-\langle n \rangle} \frac{\langle n \rangle^n}{n!}. \quad (1.7)$$

From Eq. (1.6), we can see that the shot noise limited signal to noise ratio, which is equivalent to the relative error in photon number, is given by $\Delta n / \langle n \rangle = 1 / \sqrt{\langle n \rangle}$, i.e. it scales with the inverse square root of the expected photon number. Calibrated into units of gravitational wave strain, shot noise S_h^{SN} decreases inversely with optical

power P and is given by [33]⁵,

$$S_h^{\text{SN}}(\Omega) = \frac{\hbar\gamma}{4kLP} \left(1 + \frac{\Omega^2}{\gamma^2}\right), \quad (1.8)$$

where Ω is the angular measurement frequency, k is the wavenumber of 1064 nm interferometer light, L is the arm cavity length.

1.2.2 Quantum Radiation Pressure Noise

In order to calculate the quantum radiation pressure noise, we can start with Heisenberg's uncertainty principle written in terms of spectral densities [34, 35],

$$S_x^{\text{SN}} S_F^{\text{RPN}} = \hbar^2. \quad (1.9)$$

Where S_x^{SN} and S_F^{RPN} are the displacement power spectrum of the shot noise and the force power spectrum of radiation pressure noise respectively. Here, the uncertainty principle is saturated for a coherent state. We can convert displacement to strain noise using,

$$S_h^{\text{SN}} = 1/L^2 S_x^{\text{SN}}. \quad (1.10)$$

Additionally, we can assume that the pendulum resonance of the test mass is much lower than the signal band which lets us approximate the force-strain transfer function of the reduced mass of the four test masses to $-4/(Lm\Omega^2)$, where $m = 40$ kg is the mass of the suspended mirrors. This gives us,

$$S_h^{\text{RPN}} = \frac{16S_F^{\text{RPN}}}{(mL\Omega^2)^2}. \quad (1.11)$$

Combining Eqs. (1.9) to (1.11) gives us the following expression for the power spectral density of quantum radiation pressure noise, which scales linearly with optical power P :

$$S_h^{\text{RPN}}(\Omega) = \frac{64\hbar k P}{m^2 L^3 \gamma \Omega^4} \left(1 + \frac{\Omega^2}{\gamma^2}\right)^{-1}. \quad (1.12)$$

⁵See Appendix B.3 for a derivation of the following expression

1.2.3 *The Standard Quantum Limit*

Eqs. (1.8) and (1.12) show that increasing or decreasing the optical power in a gravitational wave detector leads to a trade-off between shot noise and radiation pressure noise. Fundamentally, in terms of a continuous quantum measurement, this is due to the fact that increasing the strength of a measurement also increases the amount of measurement back-action [35–37]. When the measurement noise is uncorrelated with the back-action, this produces a lower bound in the total measured noise known as the standard quantum limit (SQL). The free mass SQL (plotted in Fig. 1.4) for a Fabry-Perot Michelson Interferometer, in units of strain, is given by [38],

$$S_{\text{SQL}}(\Omega) = \frac{8\hbar}{m\Omega^2 L^2}. \quad (1.13)$$

Eq. (1.1) can also be written as,

$$S_h^{\text{QN}} = S_h^{\text{SN}}(1 + \mathcal{K}(\Omega)^2), \quad (1.14)$$

where the optomechanical coupling, \mathcal{K} , is defined as,

$$\mathcal{K} = \frac{16\hbar k P}{mL^2 \gamma \Omega^2} \left(1 + \frac{\Omega^2}{\gamma^2}\right) = \frac{\Omega_{\text{SQL}}^2}{\Omega^2} \left(1 + \frac{\Omega^2}{\gamma^2}\right). \quad (1.15)$$

Ω_{SQL} is the frequency where the detector saturates the standard quantum limit. This frequency also sets a scale for the crossover between shot noise and radiation pressure noise.

The standard quantum limit can, however, be surpassed by correlating shot noise and radiation pressure noise [39]. The LIGO detectors have wielded the correlations arising from optomechanical interactions to show sub-standard quantum limit performance [40].

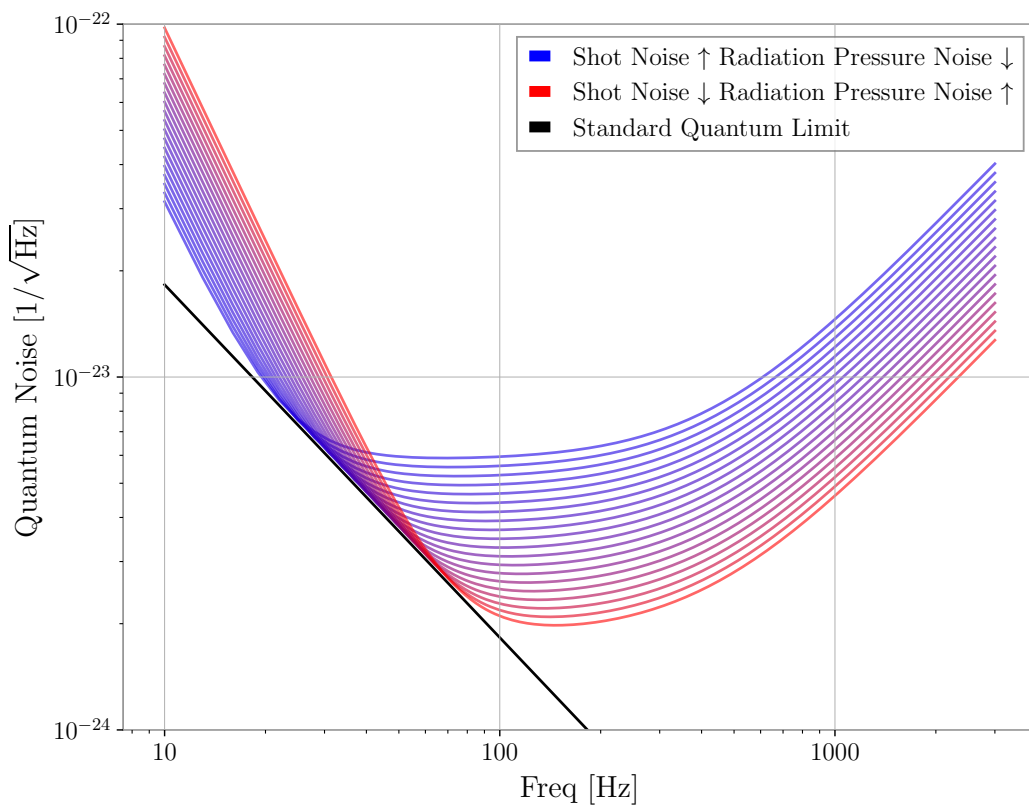


Figure 1.4: The standard quantum limit

1.3 OVERVIEW

Along with increasing the optical power in the interferometer, the injection of non-classical squeezed vacuum states has been pursued as a parallel means to reduce shot noise [41, 42]. These states are introduced in Chapter 2 of this work, along with the mathematical formalism that forms the foundation for the rest of the thesis. The improvement in detector sensitivity that can be achieved through squeezing, however, is limited by an increase in radiation pressure noise [40, 43]. Chapter 3 introduces the use of optical filter cavities to produce frequency dependent squeezed states which are capable of simultaneously reducing both shot noise and radiation pressure noise in the interferometer [44–46]. The design of these filter cavities is described in Chapter 4. Chapter 5 covers an experimental procedure to characterize squeezed vacuum sources and squeezing in optical systems using an auxiliary audio band field. The first realization of frequency dependent squeezing in a gravitational wave interferometer is detailed in Chapter 6. In Chapter 7, we shift our focus to detuned interferometers, with high frequency dips in quantum noise enhanced by frequency dependent squeezing, and the prospects of detecting neutron star post-mergers with them.

CHAPTER

2

SQUEEZED STATES OF LIGHT

Instead of introducing the coherent vacuum state into the interferometer, squeezed vacuum states, commonly referred to as ‘squeezing’, can be injected into the readout port. This approach reduces quantum noise and enhances the interferometer’s sensitivity [47]. The idea of using squeezed states in gravitational wave detectors was first proposed by Caves in the 1980s [48]. While GEO600 has employed squeezing since 2009 [41, 49, 50] and LIGO Hanford first demonstrated squeezing injection in 2011 [51], the first gravitational wave detections in squeezing enhanced interferometers were made during the observing run O3 [42, 52], nearly four decades after Caves’ initial proposal. In this chapter, we lay out the mathematical formalism required to describe squeezed states and how they interact with gravitational wave detectors.

2.1 SIDEBANDS AND QUADRATURES

In the frequency domain, gravitational waves signals can be thought of as (phase) modulations around a carrier frequency ω_0 . To understand quantum noise in an interferometer, it is necessary for us to introduce the quantum mechanical operators associated with the measurement of these modulations. After quantization, the electric field operator can be written in terms of the annihilation and creation operators,

\hat{a}_ω and \hat{a}_ω^\dagger , where ω refers to the mode frequency of the operator.

$$\hat{\mathcal{E}}(t) = \int_0^\infty \sqrt{\frac{2\pi\hbar\omega}{\mathcal{A}c}} (\hat{a}_\omega e^{-i\omega t} + \hat{a}_\omega^\dagger e^{i\omega t}) \frac{d\omega}{2\pi}, \quad (2.1)$$

where \mathcal{A} is the effective cross sectional area of the electromagnetic field and c is the speed of light. The ladder operators satisfy the usual commutation relations

$$[\hat{a}_\omega, \hat{a}_{\omega'}^\dagger] = 2\pi\delta(\omega - \omega'), \quad [\hat{a}_\omega, \hat{a}_{\omega'}] = [\hat{a}_\omega^\dagger, \hat{a}_{\omega'}^\dagger] = 0. \quad (2.2)$$

We define sideband operators around the carrier frequency by re-scaling the ladder operators

$$\hat{a}_\pm(\Omega) = \sqrt{\frac{\omega_0 \pm \Omega}{\omega_0}} \hat{a}_{\omega_0 \pm \Omega} \quad (2.3)$$

where Ω is the sideband frequency. For a gravitational wave detector, Ω ranges from 10 to 1000 Hz while the carrier frequency of the laser is around 3×10^{13} Hz. This allows us to make the approximation $\omega_0 \pm \Omega \approx \omega_0$ inside the square root. The sideband operators obey the following commutation relations

$$[\hat{a}_+(\Omega), \hat{a}_+(\Omega')] \approx [\hat{a}_+(\Omega), \hat{a}_+^\dagger(\Omega')] \approx 2\pi\delta(\Omega - \Omega'), \quad (2.4)$$

$$[\hat{a}_\pm(\Omega), \hat{a}_\pm(\Omega')] = [\hat{a}_\pm(\Omega), \hat{a}_\mp(\Omega')] = [\hat{a}_\pm(\Omega), \hat{a}_\mp^\dagger(\Omega')] = 0. \quad (2.5)$$

Writing the electric field in terms of sideband operators yields

$$\hat{\mathcal{E}}(t) = \sqrt{\frac{2\pi\hbar\omega_0}{\mathcal{A}c}} e^{-i\omega_0 t} \int_0^\infty (\hat{a}_+(\Omega) e^{-i\Omega t} + \hat{a}_-(\Omega) e^{i\Omega t}) \frac{d\Omega}{2\pi} + \text{h.c.} \quad (2.6)$$

To describe amplitude and phase modulations around a carrier frequency, which are combinations of positive and negative sidebands, we introduce the following

quadrature operators¹

$$\hat{a}_1(\Omega) = \frac{\hat{a}_+(\Omega) + \hat{a}_-^\dagger(\Omega)}{\sqrt{2}}, \quad \hat{a}_2 = \frac{\hat{a}_+(\Omega) - \hat{a}_-^\dagger(\Omega)}{i\sqrt{2}} \quad (2.7)$$

This can be written concisely as

$$\begin{bmatrix} \hat{a}_1 \\ \hat{a}_2 \end{bmatrix} = \mathbf{A} \begin{bmatrix} \hat{a}_+ \\ \hat{a}_-^\dagger \end{bmatrix}, \quad \text{or} \quad \vec{\mathbf{a}} = \mathbf{A}\mathbf{a} \quad (2.8)$$

where we use the matrix \mathbf{A} to change basis between sideband (\mathbf{a}) and quadrature ($\vec{\mathbf{a}}$) vectors.

$$\mathbf{A} = \frac{1}{\sqrt{2}} \begin{bmatrix} 1 & 1 \\ -i & i \end{bmatrix}, \quad \mathbf{A}^{-1} = \frac{1}{\sqrt{2}} \begin{bmatrix} 1 & i \\ 1 & -i \end{bmatrix}. \quad (2.9)$$

For brevity, we have made the frequency dependence of the quadrature operators implicit. In terms of these operators, the electric field can be written as

$$\hat{\mathcal{E}}(t) = \cos(\omega_0 t) \hat{\mathcal{E}}_1(t) + \sin(\omega_0 t) \hat{\mathcal{E}}_2(t) \quad (2.10)$$

where

$$\hat{\mathcal{E}}_j(t) = \sqrt{\frac{2\pi\hbar\omega_0}{\mathcal{A}c}} e^{-i\omega_0 t} \int_0^\infty (\hat{a}_j e^{-i\Omega t} + \hat{a}_j^\dagger e^{i\Omega t}) \frac{d\Omega}{2\pi} \quad j = 1, 2 \quad (2.11)$$

From Eq. (2.10), we can see that two quadratures, $\hat{\mathcal{E}}_{1,2}$ of the electric field can be associated with the amplitude and phase of the field. Consequently, the noise in the phase and amplitude of a field are directly related to the uncertainties in the quadrature operators $\hat{a}_{1,2}$ [1]. These operators are canonically conjugate and obey Heisenberg's uncertainty principle.

$$\sigma_{a_1}^2 \sigma_{a_2}^2 \geq \frac{1}{4} \quad (2.12)$$

¹The time domain quadrature operators are given by $\hat{a}_1(t) = (\hat{a}(t) + \hat{a}^\dagger(t))/\sqrt{2}$, $\hat{a}_2(t) = (\hat{a}(t) - \hat{a}^\dagger(t))/\sqrt{2}i$

For a coherent state, the variances of the quadrature operators are equal and their product is minimized.

$$\sigma_{a_1}^2 = \sigma_{a_2}^2 = \frac{1}{2} \quad (2.13)$$

Using the Wiener-Khinchin theorem [53], we can also calculate the (two-sided) power spectral densities of the quadrature operators,

$$S_{\hat{a}_1}(\Omega) = \int_{-\infty}^{\infty} dt e^{-i\Omega t} \langle \hat{a}_1(t) \hat{a}_1(0) \rangle, \quad S_{\hat{a}_2}(\Omega) = \int_{-\infty}^{\infty} dt e^{-i\Omega t} \langle \hat{a}_2(t) \hat{a}_2(0) \rangle \quad (2.14)$$

For a coherent vacuum state, it can be shown that $\langle \hat{a}_1(t) \hat{a}_1(0) \rangle = \langle \hat{a}_2(t) \hat{a}_2(0) \rangle = \delta(t)$, and it follows that the quadrature spectral densities are equal to 1,

$$S_{\hat{a}_1}(\Omega) = S_{\hat{a}_2}(\Omega) = 1 \quad (2.15)$$

The quantum response of any optical system can be encoded in a frequency dependent 2×2 matrix which acts on a sideband/quadrature vector. This is known as the **‘two-photon formalism’**[54].

2.2 INTRODUCTION TO SQUEEZED STATES

Just like coherent states, squeezed states are also minimum uncertainty states which saturate Heisenberg’s uncertainty principle, the main difference being that the uncertainty in one quadrature is reduced. As a result, the uncertainty in the other quadrature is increased. In order to mathematically describe squeezed states, we extend the scope of Eq. (1.2) to consider the eigenfunctions of a generalized operator \hat{b} , which is defined as follows,

$$\hat{b}|\beta\rangle = \beta|\beta\rangle, \quad \hat{b} = \nu_1 \hat{a} + \nu_2 \hat{a}^\dagger, \quad (2.16)$$

where

$$|\nu_1|^2 - |\nu_2|^2 = 1 \quad \nu_1, \nu_2 \in \mathbb{C}, \quad (2.17)$$

which is a Bogoliubov transformation of the ladder operators. Expanding $|\beta\rangle$ in terms of photon number states yields

$$|\beta\rangle = \sum_0^{\infty} c_n |n\rangle, \quad (2.18)$$

where the coefficients c_n are given by the following recursive relations,

$$c_1 = \beta\nu_1 c_0, \quad (2.19)$$

$$c_2 = \frac{\beta c_1 - \nu_2 c_0}{\sqrt{2}\nu_1}, \quad (2.20)$$

$$c_n = \frac{\beta c_{n-1} - \nu_2 \sqrt{n-1} c_{n-2}}{\sqrt{n}\nu_1}. \quad (2.21)$$

For $\beta = 0$, this state is known as a squeezed vacuum state, and can be written as

$$|0\rangle_b = \frac{1}{\sqrt{\cosh z}} \sum_0^{\infty} (-e^{2i\psi} \tanh z)^n \frac{\sqrt{2n!}}{2^n n!} |2n\rangle, \quad (2.22)$$

where $|z| = \tanh^{-1}(\nu_2/\nu_1)$ and $\arg z = 2\psi = \arg \nu_2/\nu_1$. Note that this is a state that only contains an even number of photons. Analogous to Eq. (1.4), we introduce a squeezing operator which transforms quantum vacuum to a squeezed vacuum state.

$$\hat{S}(z)|0\rangle = |0\rangle_b, \quad \hat{S}(z) = \exp\left(\frac{z^* \hat{a}^2 - z \hat{a}^{\dagger 2}}{2}\right), \quad (2.23)$$

Note that the quadratures described in Section 2.1 are composed of two distinct optical modes (sidebands). In order to understand squeezing in the sideband picture, we must extend the definition of \hat{S} to that of a two-mode squeezing operator,

$$\mathbf{S}(z, \psi) = \exp\left[z(\hat{a}_+ \hat{a}_- e^{2i\psi} - \hat{a}_+^\dagger \hat{a}_-^\dagger e^{-2i\psi})\right]. \quad (2.24)$$

The evolution of the sideband operators in the Heisenberg picture is given by the following Bogoliubov transformation (2.17),

$$\mathbf{S} \begin{bmatrix} \hat{a}_+ \\ \hat{a}_-^\dagger \end{bmatrix} \mathbf{S}^\dagger = \mathbf{H}_\mathbf{S} \begin{bmatrix} \hat{a}_+ \\ \hat{a}_-^\dagger \end{bmatrix}, \quad (2.25)$$

where

$$\mathbf{H}_\mathbf{S} = \begin{bmatrix} \cosh z & e^{-i2\psi} \sinh z \\ e^{i2\psi} \sinh z & \cosh z \end{bmatrix}. \quad (2.26)$$

Converting the above expression to the quadrature picture shows us that the squeezer matrix is diagonal and is given by

$$\mathbf{H}_\mathbf{S} = \mathbf{A}^\dagger \mathbf{R}_\psi \begin{bmatrix} e^z & 0 \\ 0 & e^{-z} \end{bmatrix} \mathbf{R}_\psi^\dagger \mathbf{A} = \mathbf{A}^\dagger \mathbf{R}_\psi \mathbb{H}_\mathbf{S} \mathbf{R}_\psi^\dagger \mathbf{A} \quad (2.27)$$

where the rotation matrix \mathbf{R}_ψ is defined conventionally as

$$\mathbf{R}_\psi = \begin{bmatrix} \cos \psi & -\sin \psi \\ \sin \psi & \cos \psi \end{bmatrix}. \quad (2.28)$$

We can see the effect of squeezing on quadrature variances by applying $\mathbb{H}_\mathbf{S}$ to the quadrature operators

$$\begin{bmatrix} \hat{b}_1 \\ \hat{b}_2 \end{bmatrix} = \mathbf{R}_\psi \mathbb{H}_\mathbf{S} \mathbf{R}_\psi^\dagger \begin{bmatrix} \hat{a}_1 \\ \hat{a}_2 \end{bmatrix} \quad (2.29)$$

$$\hat{b}_1 = e^z \hat{a}_1, \quad \hat{b}_2 = e^{-z} \hat{a}_2, \quad (\psi = 0) \quad (2.30)$$

$$\hat{b}_1 = e^{-z} \hat{a}_1, \quad \hat{b}_2 = e^z \hat{a}_2, \quad (\psi = \pi/2) \quad (2.31)$$

From Eq. (2.30) and Eq. (2.31), we see that after squeezing is applied to a state, one of the quadratures is scaled down (squeezed) by a factor of e^z , and the other is scaled up by the same factor (anti-squeezed). The quadrature being squeezed depends on the squeezing angle ψ and, in general, any linear combination of the two quadratures can be squeezed, with the orthogonal quadrature combination being anti-squeezed.

Consequently, the noise in the two quadratures is also squeezed/anti-squeezed,

$$\sigma_{\hat{a}_1}^2(\Omega) = \frac{e^{2z}}{2}, \quad \sigma_{\hat{a}_2}^2(\Omega) = \frac{e^{-2z}}{2}, \quad \psi = 0, \quad (2.32)$$

$$\sigma_{\hat{a}_1}^2(\Omega) = \frac{e^{-2z}}{2}, \quad \sigma_{\hat{a}_2}^2(\Omega) = \frac{e^{2z}}{2}, \quad \psi = \pi/2. \quad (2.33)$$

Similarly, the two-sided power spectral densities of the quadrature operators for a squeezed vacuum state are given by,

$$S_{\hat{a}_1}(\Omega) = e^{-2z}, \quad S_{\hat{a}_2}(\Omega) = e^{2z}, \quad \psi = 0, \quad (2.34)$$

$$S_{\hat{a}_1}(\Omega) = e^{2z}, \quad S_{\hat{a}_2}(\Omega) = e^{-2z}, \quad \psi = \pi/2. \quad (2.35)$$

To achieve sensitivity beyond quantum noise limits, squeezed vacuum states are injected into gravitational wave detectors, where the interferometer carrier laser is the local oscillator/mean field for the measurement. Mathematically, this can be represented as applying a displacement operator to the squeezed vacuum state,

$$|\alpha, z\rangle = \hat{D}(\alpha)\hat{S}(z)|0\rangle. \quad (2.36)$$

These are known as bright squeezed states. With respect to the phase reference of the local oscillator, it is now possible to introduce the concept of phase and amplitude squeezed states. Fig. 2.1 represents states with the uncertainty (ball) in the phase space defined by the two quadratures; we call these ball and stick figures. These are time-dependent and rotate around the origin at the optical frequency Ω (in the rotating frame of the carrier). A coherent state is represented by a circular distribution while squeezed states have elliptical distributions. The vector from the origin to center of the distribution (stick) corresponds to the displacement, $\hat{D}(\alpha)$, and can be interpreted as having the magnitude and phase of the α . From Fig. 2.1, we see that depending on the squeezing angle and local oscillator phase, the electric field obtain can have reduced uncertainty in amplitude or phase, at the expense of increased uncertainty in the other. We will henceforth refer to \hat{a}_1 and \hat{a}_2 as the amplitude and phase quadratures. For a bright squeezed state in the limit where the amplitude of the local oscillator

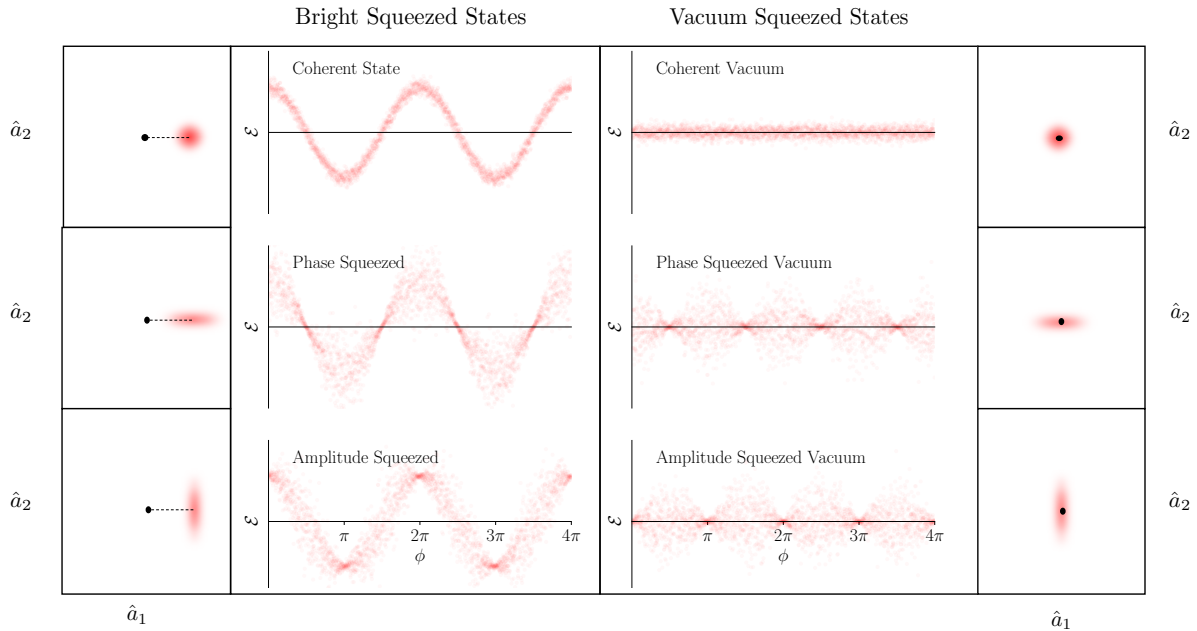


Figure 2.1: Squeezed states of light. The plots on the extreme left and right are ‘ball and stick’ figures which show the uncertainty in the phase space defined by the two quadratures. A darker shade corresponds to higher probability in phase space. The location of the center of the uncertainty blob corresponds to the phase and magnitude of the local oscillator (mean field). This is time-dependent and rotates around the origin at the optical frequency ω . The plots in the center are simulations of the electric field corresponding to these states. We can see that phase squeezed states have reduced uncertainty in phase and increased uncertainty in amplitude, while the opposite is true for amplitude squeezed states. The right half of the figure corresponds to vacuum states, which the left corresponds to bright states. It is important to note here that phase and amplitude squeezing can only be defined with respect to a local oscillator (phase reference). This is evident from the observation that the electric fields corresponding phase and amplitude squeezed vacuum are identical up to a phase shift.

is large ($\alpha \gg \sinh z$), we calculate the expectation value and the uncertainty of the measured photon number,

$$\langle \alpha, z | n | \alpha, z \rangle = |\alpha|^2, \quad \Delta n = |\alpha| \sqrt{\sinh^2 z + \cosh^2 z - 2 \sinh z \cosh z \cos 2\phi}. \quad (2.37)$$

Where the squeezing angle ϕ , is the relative phase between the squeezed vacuum and local oscillator. The relative error in the photon number is then given by,

$$\Delta n / \langle n \rangle = e^{-z} / |\alpha|, \quad (\phi = 0), \quad (2.38)$$

$$\Delta n / \langle n \rangle = e^z / |\alpha|, \quad (\phi = \pi/2). \quad (2.39)$$

This shows that bright squeezed states can have their relative photon number errors suppressed/amplified by a factor of e^z compared to a coherent state with the same amplitude. Henceforth, we shall also use the terms ‘squeezing’ and ‘anti-squeezing’ to specifically refer to the squeezing angles $\psi = 0$, and $\psi = \pi/2$ respectively. The probability of detecting n photons for a bright squeezed state given by [55],

$$P(n) = |\langle n | \alpha, z \rangle|^2 = \frac{(\frac{1}{2} \tanh z)^n}{n! \cosh z} \exp \left[-|\alpha|^2 - \frac{1}{2} (\alpha^{*2} e^{-2i\psi} + \alpha^2 e^{2i\psi}) \tanh z \right] \times |H_n [(\alpha \cosh z + \alpha^* e^{-2i\psi} \sinh z) (e^{-2i\psi} \sinh(2z))^{-1/2}]|^2, \quad (2.40)$$

where H_n is the n^{th} Hermite Polynomial. This distribution is plotted for squeezed, anti-squeezed and coherent states Fig. 2.2. In terms of photon counting, squeezing and anti-squeezing correspond to sub-Poissonian ($(\Delta n)^2 < \langle n \rangle$) and super-Poissonian ($(\Delta n)^2 > \langle n \rangle$) statistics respectively.

Since the quantum noise is suppressed or amplified by a certain factor, it is common to quote squeezing levels in units of decibels ($N_{\text{dB}} = 10 \log_{10}(P/P')$, where P/P' is a ratio of powers).

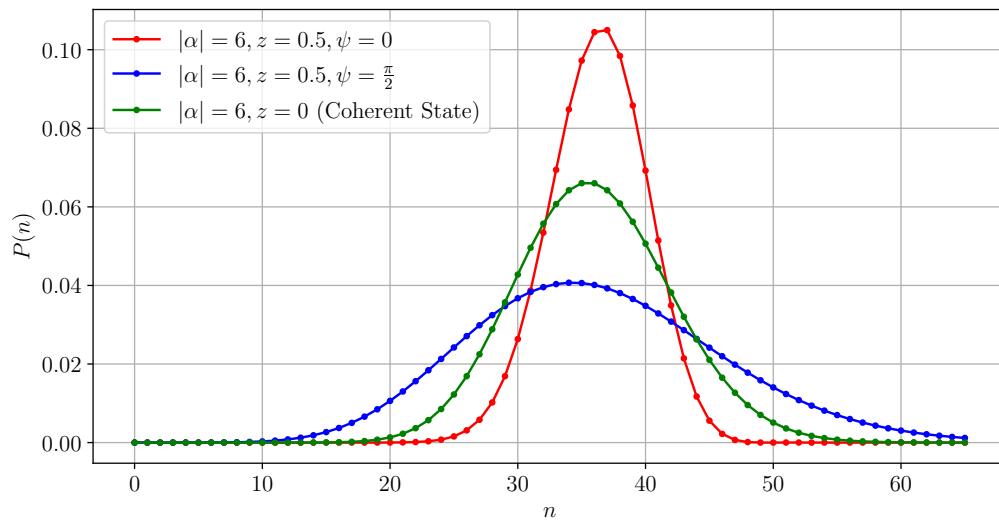


Figure 2.2: Photon number distributions for bright squeezed states with the same coherent amplitude $|\alpha| = 6$. The green distribution corresponds to a coherent state with a Poisson distribution, while the red and blue distributions correspond to squeezed and anti-squeezed states, with sub-Poissonian and super-Poissonian distributions respectively.

2.3 GENERATION OF SQUEEZED STATES

A variety of methods can be used to generate squeezed states of light [56–61]. However, the most common and reliable method of creating high levels of squeezing is by using nonlinear crystals with a second order non-linearity² [63]. The induced polarization \mathbf{P} in a non-linear material can be expressed as a power series in the electric field strength,

$$\mathbf{P} = \epsilon_0(\chi^{(1)} + \chi^{(2)}|\mathcal{E}| + \chi^{(3)}|\mathcal{E}|^2 + \dots)\hat{\mathcal{E}}. \quad (2.41)$$

$\chi^{(2)}$ is known as the second order susceptibility of the material, and the term associated with it creates oscillations at the sum and difference of the frequency components in the electric field. This effect is used to generate squeezing through a process known as spontaneous parametric down conversion (SPDC)³. In SPDC, a pump photon with higher energy breaks into a pair of entangled photons, known as the signal and idler, with energies (frequencies) that add up to that of the pump. SPDC can be classified into three types

- Type 0 : The signal and idler photons are same polarization, and are aligned with the pump polarization.
- Type 1 : The signal and idler photons are same polarization, but are orthogonal to the pump polarization.
- Type 2 : The signal and idler photons have orthogonal polarizations.

This process can also be classified into collinear and non-collinear based on whether the signal and idler beams are spatially aligned with each other; and into degenerate and non-degenerate based on whether the signal and idler photons have the same or different frequencies.

For the generation of squeezing, we consider collinear, non-degenerate Type 0 SPDC. We can represent the pump mode (at frequency $2\omega_0$) by the ladder operator \hat{a}

²This method also holds the current record for the maximum amount of measured optical squeezing[62]

³The third order susceptibility $\chi^{(3)}$ of a material can also be used to generate squeezed states of light through a different process known as the Kerr effect

and the pair of generated photons (at $\omega_0 \pm \Omega$) by the sideband ladder operators \hat{a}_\pm ⁴ (Eq. (2.3)).

To derive the time evolution of the sideband operators in the Heisenberg picture, we begin with the interaction Hamiltonian [64] of the second order non-linearity.

$$\hat{H}_{int} = \hbar \frac{\kappa}{2} (\hat{\alpha}^\dagger \hat{a}_+ \hat{a}_- - \hat{\alpha} a_+^\dagger a_-^\dagger), \quad (2.42)$$

where κ is the non-linear interaction strength. The first term corresponds to sum frequency generation where the two sideband photons are annihilated to produce a pump photon, while the second term corresponds to SPDC where a pump photon is annihilated to create the two sideband photons. Due to its high intensity, the pump field α can be treated classically ($\alpha^\dagger = \alpha^*$). The equations of motion for the sideband operators are then given by

$$\frac{d\hat{a}_+}{dt} = \frac{i}{\hbar} [\hat{H}_{int}, \hat{a}_+] = i\kappa\alpha\hat{a}_-^\dagger, \quad (2.43)$$

$$\frac{d\hat{a}_-^\dagger}{dt} = \frac{i}{\hbar} [\hat{H}_{int}, \hat{a}_-^\dagger] = -i\kappa\alpha^*\hat{a}_+. \quad (2.44)$$

This can be condensed into a matrix equation,

$$\frac{d}{dt} \begin{bmatrix} \hat{a}_+(t) \\ \hat{a}_-^\dagger(t) \end{bmatrix} = \begin{bmatrix} 0 & i\kappa\alpha \\ -i\kappa\alpha^* & 0 \end{bmatrix} \begin{bmatrix} \hat{a}_+(t) \\ \hat{a}_-^\dagger(t) \end{bmatrix}. \quad (2.45)$$

Assuming that the pump field $\alpha = |\alpha|e^{i\theta}$ is approximately constant (undepleted) across the material, the solution to this equation is given by.

$$\begin{bmatrix} \hat{a}_+(t) \\ \hat{a}_-^\dagger(t) \end{bmatrix} = \exp \left(\begin{bmatrix} 0 & i\kappa\alpha \\ -i\kappa\alpha^* & 0 \end{bmatrix} t \right) \begin{bmatrix} \hat{a}_+(0) \\ \hat{a}_-^\dagger(0) \end{bmatrix} \quad (2.46)$$

$$= \exp \begin{bmatrix} 0 & i\kappa \frac{L}{c} |\alpha| e^{i\theta} \\ -i\kappa \frac{L}{c} |\alpha| e^{-i\theta} & 0 \end{bmatrix} \begin{bmatrix} \hat{a}_+(0) \\ \hat{a}_-^\dagger(0) \end{bmatrix} \quad (2.47)$$

⁴The frequency dependence of these operators is implicit

Where we have set $\alpha = |\alpha|e^{i\theta}$ and have fixed $t = \frac{L}{c'}$ for a crystal of length L . c' is the speed of light in the crystal.

Setting $2\psi = -(\theta + \pi/2)$ and $\kappa|\alpha|L/c' = z$, we can write the evolution of the sideband operators after propagating through the entire length of the crystal as,

$$\begin{bmatrix} \hat{a}_+(L) \\ \hat{a}_-^\dagger(L) \end{bmatrix} = \begin{bmatrix} \cosh z & e^{-i2\psi} \sinh z \\ e^{i2\psi} \sinh z & \cosh z \end{bmatrix} \begin{bmatrix} \hat{a}_+(0) \\ \hat{a}_-^\dagger(0) \end{bmatrix} = \mathbf{H}_S \begin{bmatrix} \hat{a}_+(0) \\ \hat{a}_-^\dagger(0) \end{bmatrix} \quad (2.48)$$

where \mathbf{H}_S is the squeezer matrix (Eq. (2.26)). z is called the single pass squeeze factor of the squeezer's nonlinear crystal, and 2ψ is the squeezer pump phase. Note that the single pass squeeze factor of the crystal is proportional to the circulating pump intensity, or alternatively to the square root of pump power P_{pump} ,

$$z \propto |\alpha| \propto \sqrt{P_{\text{pump}}} \quad (2.49)$$

2.3.1 Phase Matching

In order to efficiently down-convert pump photons, the non-linear material must satisfy the phase-matching condition, i.e the wave-vector mismatch between the pump and the down-converted fields must be minimized to satisfy the conservation of momentum,

$$\Delta k = k_{\text{signal}} + k_{\text{idler}} - k_{\text{pump}} \quad (2.50)$$

This mismatch, however, is increased by dispersion as the fields propagate through the non-linear material. When this phase mismatch exceeds π , energy starts flowing back into the pump from the down-converted frequencies. Advanced LIGO uses periodically poled potassium titanyl phosphate (PPKTP) crystals as a squeezed vacuum source. Periodically poled materials are manufactured with domains that have alternating optic axis directions, and are used for a technique known as quasi-phase matching. This technique ensures a positive flow of energy from the pump to the converted frequencies in the presence of a wave-vector mismatch [65]. The optimal poling period is given by

$$L_p = 2\pi/\Delta k \quad (2.51)$$

The phase mismatch is sensitive to temperature and regular operation of a crystal squeezer requires active temperature stabilization in order to maximize non-linear interaction strength [66, 67].

2.4 CAVITY ENHANCEMENT OF SQUEEZING

The model described in this section corresponds to a sub-threshold optical parametric oscillator (OPO)⁵ shown in Fig. 2.3, consisting of a squeezer crystal resonantly enhanced in an optical cavity. The cavity round-trip phase shift, in matrix form, is given by

$$\Theta_{\text{cav}} = \begin{bmatrix} e^{-i\Delta} & 0 \\ 0 & e^{i\Delta} \end{bmatrix} \quad (2.52)$$

where the cavity detuning angle Δ is

$$\Delta = \frac{2\pi f}{f_{\text{FSR}}}, \quad (2.53)$$

f is the sideband frequency, and f_{FSR} is the free spectral range of the OPO cavity.

The OPO pump field and quantum vacuum, are injected via M_1 , and the squeezed vacuum is obtained on reflection at M_1 . For our specific OPO configuration, the effective OPO reflection matrix at M_1 is given by

$$\mathbf{H}_O = r_1 \mathbf{I} - t_1^2 \Theta_{\text{cav}} \mathbf{H}_S (\mathbf{I} - r_1 \Theta_{\text{cav}} \mathbf{H}_S)^{-1}. \quad (2.54)$$

The cavity is operated at resonance for the squeezed vacuum carrier frequency, i.e. $\Delta = 0$. Solving for \mathbf{H}_O (and comparing with Eq. 2.27) produces an modified squeezer matrix,

$$\mathbf{H}_O = \mathbf{A}^\dagger \mathbf{R}_\psi \begin{bmatrix} \frac{t_1^2 e^z}{1-r_1 e^z} - r_1 & 0 \\ 0 & \frac{t_1^2 e^{-z}}{1-r_1 e^{-z}} - r_1 \end{bmatrix} \mathbf{R}_\psi^\dagger \mathbf{A} \quad (2.55)$$

⁵The term optical parametric amplifier (OPA) is more appropriate, but we use the term OPO to be consistent with squeezing literature

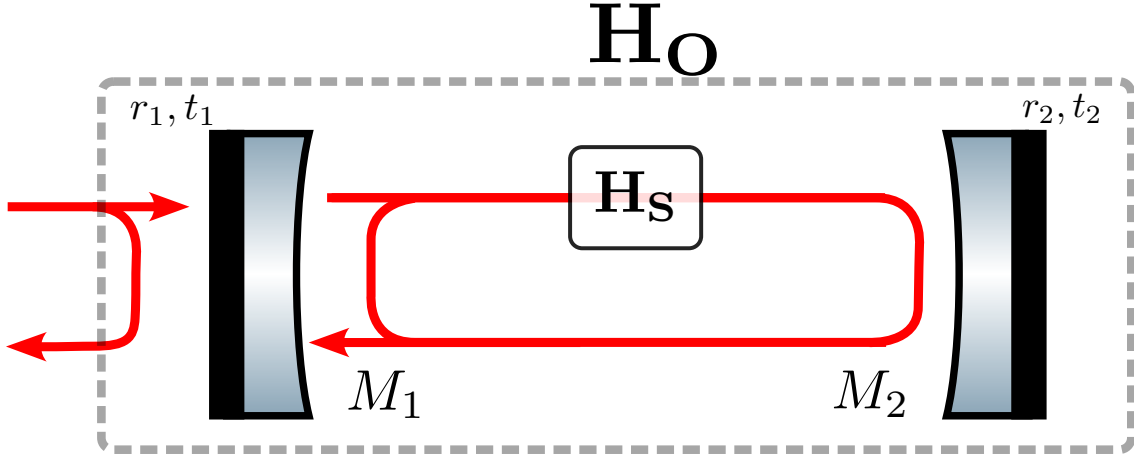


Figure 2.3: Cavity enhancement of squeezing. The transfer matrix of the cavity reflection from M_1 , corresponding to the block diagram depicted here, is given by Eq. (2.54).

$$= \mathbf{A}^\dagger \mathbf{R}_\psi \begin{bmatrix} e^Z & 0 \\ 0 & e^{-Z} \end{bmatrix} \mathbf{R}_\psi^\dagger \mathbf{A} \quad (2.56)$$

where Z is the effective squeeze factor. Assuming the cavity is lossless and $r_1^2 + t_1^2 = 1$, Eq. (2.55) and Eq. (2.56) then give

$$Z = \log \left(\frac{e^z - r_1}{1 - r_1 e^z} \right). \quad (2.57)$$

Z diverges as the internal squeeze factor z approaches $z = \log(1/r_1)$; this is known as threshold. Note that the above calculations do not depend on the specific configuration of the crystal in the squeezer cavity.

Dual Resonance : In order to maximize the squeeze factor Z , the OPO must be resonant for both the squeezed vacuum carrier frequency, ω_0 , and the pump frequency, $2\omega_0$. The cavity length can be adjusted by changing the crystal temperature but consequently, phase-matching might not be satisfied (Section 2.3.1). In order to overcome this constraint, the crystal is manufactured with a wedged side. As a result, translating the crystal in the transverse direction provides an additional degree of freedom to adjust cavity length [67].

2.4.1 Auxiliary Field Transfer Matrix

LIGO's squeezer uses various auxiliary sideband fields in order to control and characterize its squeezing system. These fields are injected into the OPO through an auxiliary port M_2 . Unlike the squeezing enhancement, the transfer matrix from M_2 to M_1 depends on the configuration of the crystal within the cavity. We consider three cases (shown in Fig. 2.4) :

- a) The auxiliary field exits the OPO via M_1 before passing through the squeezer crystal.
- b) The auxiliary field exits the OPO via M_1 after passing through the squeezer crystal.
- c) The auxiliary field passes through the crystal twice, before and after exiting the OPO via M_1 .

The first two cases represent two bowtie OPO configurations and the third corresponds to a linear OPO.

For the following calculations, it is assumed that the OPO is lossless, and the reflectivity of M_3 and M_4 is 1 in the bowtie cavities. It is also assumed that the reflectivity of auxiliary port M_2 is very close to 1 ($r_2 \approx 1$).

For the first case, a), the transfer matrix from the transmission from M_2 to M_1 is given by

$$\mathbf{H}'_O = t_1 t_2 (\mathbf{I} - r_1 \Theta_{\text{cav}} \mathbf{H}_S)^{-1} \quad (2.58)$$

$$\mathbf{H}'_O = t_1 t_2 \frac{\begin{bmatrix} 1 - e^{i\Delta} r_1 \cosh z & r_1 e^{-i(2\psi+\Delta)} \sinh z \\ r_1 e^{i(2\psi+\Delta)} \sinh z & 1 - e^{-i\Delta} r_1 \cosh z \end{bmatrix}}{r_1^2 - 2r_1 \cosh z \cos \Delta + 1}, \quad (2.59)$$

up to an overall phase, which has been omitted.

In the second case, b), the transfer matrix from the transmission from M_2 to M_1 is given by

$$\mathbf{H}'_O = t_1 t_2 \mathbf{H}_S (\mathbf{I} - r_1 \Theta_{\text{cav}} \mathbf{H}_S)^{-1} \quad (2.60)$$

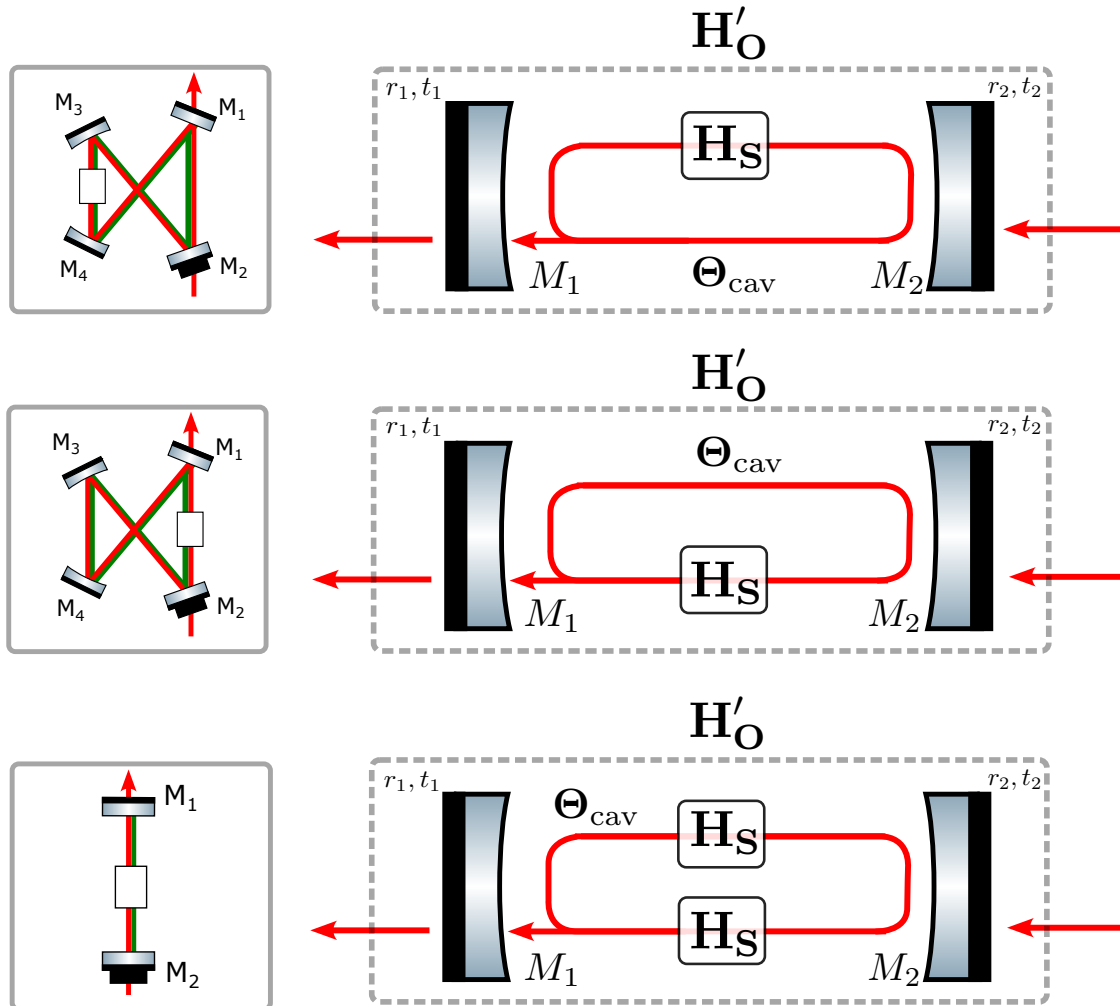


Figure 2.4: Auxiliary field transfer. The transmission matrix of the cavity squeezer from reflection from M_2 to M_1 depends on the configuration of the squeezer crystal in the OPO cavity. The optical layouts for the three cases are depicted on the left. The block diagrams on the right correspond to Eqs. (2.59), (2.61) and (2.63) respectively.

$$\mathbf{H}'_O = t_1 t_2 \frac{\begin{bmatrix} e^{i\Delta} \cosh z - r_1 & e^{-i(2\psi+\Delta)} \sinh z \\ e^{i(2\psi+\Delta)} \sinh z & e^{-i\Delta} \cosh z - r_1 \end{bmatrix}}{r_1^2 - 2r_1 \cosh z \cos \Delta + 1}. \quad (2.61)$$

In the third case, c), the transfer matrix from the transmission from M_2 to M_1 is given by

$$\mathbf{H}'_O = t_1 t_2 \mathbf{H}_S (\mathbf{I} - r_1 \mathbf{\Theta}_{\text{cav}} \mathbf{H}_S^2)^{-1}, \quad (2.62)$$

$$\mathbf{H}'_O = t_1 t_2 \frac{\begin{bmatrix} \cosh z(1 - e^{i\Delta} r_1) & e^{-i2\psi} \sinh z(1 + e^{-i\Delta} r_1) \\ e^{i2\psi} \sinh z(1 + e^{i\Delta} r_1) & \cosh z(1 - e^{-i\Delta} r_1) \end{bmatrix}}{r_1^2 - 2r_1 \cosh(2z) \cos \Delta + 1}. \quad (2.63)$$

Non-Linear Gain : A quantity known as non-linear gain \bar{g} , commonly used to characterize a squeezed vacuum source, refers to the gain in power of a transmitted seed field at the carrier frequency, with respect to no non-linearity.

In the sideband picture, a carrier field is represented as a sum of both upper and lower sidebands at $f = 0$.

$$\mathbf{a} = \mathbf{H}'_O \begin{bmatrix} e^{-i\Phi} \\ e^{i\Phi} \end{bmatrix}, \quad (2.64)$$

$$\bar{g} = \frac{\max(|\mathbf{a}|^2)}{\lim_{e^z \rightarrow 1} (|\mathbf{a}|^2)}. \quad (2.65)$$

For the two bowtie OPO configurations, a) and b), the non-linear gain \bar{g} is related to the single pass squeeze factor z as,

$$\bar{g}_a = \left(\frac{1 - r_1}{1 - r_1 e^z} \right)^2, \quad \bar{g}_b = \left(\frac{1 - r_1}{e^{-z} - r_1} \right)^2, \quad (2.66)$$

Typical usage of \bar{g} relates the transmission gain to the squeezing level using the Collett-Gardiner model [68] for the OPO. This model uses a Hamiltonian formulation that linearizes the internal squeezing operation within the cavity. The frequency-domain input-output model of Section 2.4 does not linearize the internal squeezing, which is why Eq. (2.66) is not exactly the same as in the references. For finite finesse

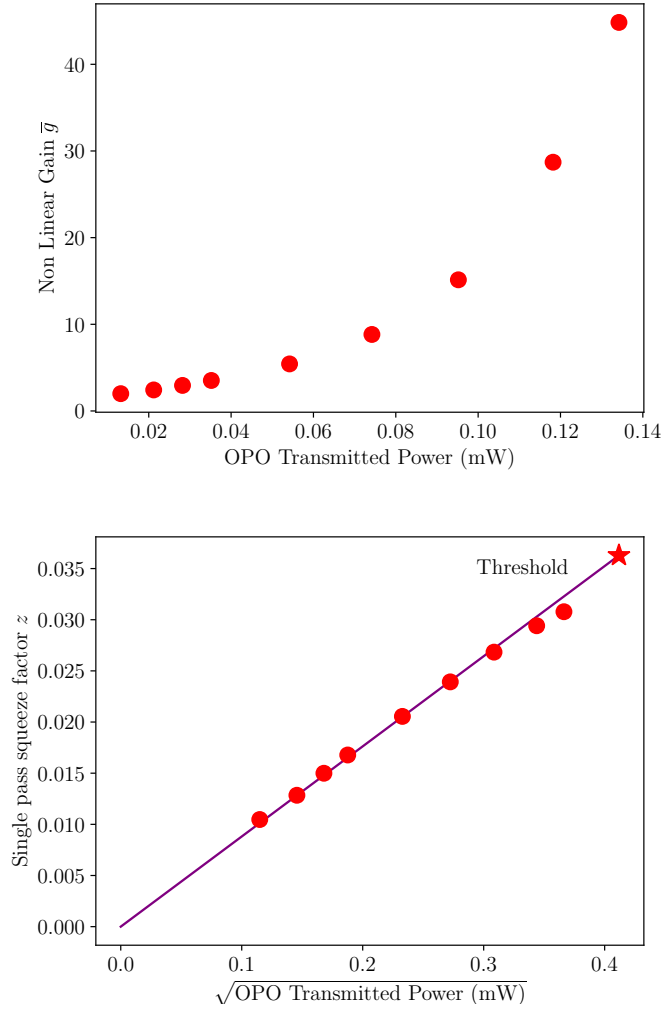


Figure 2.5: Characterizing an OPO using non-linear gain measurements at LIGO Hanford. In the top plot, the measured non-linear gain \bar{g} is plotted against the transmitted pump power from the OPO. Case b) of Eq. (2.66) is used to calculate the single pass squeeze factor from the measured data ($r_1 = \sqrt{0.93}$). This is plotted against the square root of the transmitted pump power in the bottom panel, with a linear fit according to Eq. (2.49). At high \bar{g} , the measured data deviates from the linear fit due to pump depletion caused by the high gain in seed power.

OPO's with the parameters used in this paper, the model used provides a few percent correction in its estimate of the squeezing level e^{-2Z} over the linearized model, but requires formulas that depend on the specific layout of the OPO. In the high finesse $r_1 \rightarrow 1$ limit, the two models are consistent.

Fig. 2.5 shows an OPO characterization measurement made at LIGO Hanford. The top plot shows the measured non-linear gain \bar{g} as a function of the pump power transmitted through the OPO. The bottom plot uses Eq. (2.66) to calculate the single pass squeeze factor z from the measured non-linear gain. We see that z is proportional to the square root of the OPO's pump power, thus being proportional to the squeezer pump intensity. This measurement, in addition to verifying the mathematical model described above (Eq. (2.49)), provides a direct calibration between transmitted pump power and the non-linear gain, which makes it possible to make in-situ measurements of the squeezing level, e^{-2Z} , without the use of a bright seed field, which disrupts regular operation of the squeezer.

2.5 HOMODYNE DETECTION

In order to measure and characterize squeezed vacuum, we interfere it with a bright local oscillator phase reference to create a bright squeezed state and measure the variance in power [69]. Fig. 2.6 shows the schematic for a balanced homodyne detector, a signal \hat{a} is measured by interfering it with a bright local oscillator α on a 50/50 beamsplitter and the difference between the powers (photo-currents) is measured at the output. The states on the output state of the detector \hat{b}_1, \hat{b}_2 are given by,

$$\begin{bmatrix} \hat{b}_1 \\ \hat{b}_2 \end{bmatrix} = \frac{1}{\sqrt{2}} \begin{bmatrix} 1 & 1 \\ 1 & -1 \end{bmatrix} \begin{bmatrix} \hat{a} \\ \alpha \end{bmatrix}, \quad (2.67)$$

where we can treat the local oscillator as a classical field. The measured photo-current I_{HD} is given by,

$$I_{\text{HD}} = \langle \hat{b}_1^\dagger \hat{b}_1 \rangle - \langle \hat{b}_2^\dagger \hat{b}_2 \rangle. \quad (2.68)$$

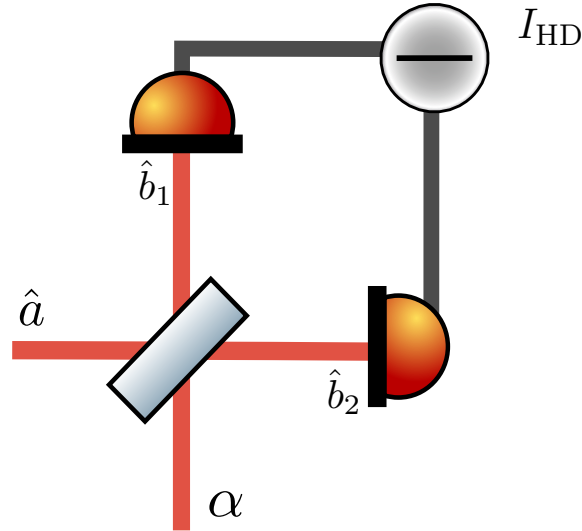


Figure 2.6: Homodyne Detection Scheme.

Combining Eq. (2.67) and Eq. (2.68) yields

$$I_{\text{HD}} = \langle \alpha^* \hat{a} + \alpha \hat{a}^\dagger \rangle = i|\alpha| \langle e^{i\zeta} \hat{a} - e^{-i\zeta} \hat{a}^\dagger \rangle, \quad (2.69)$$

where $\alpha = i|\alpha|e^{-i\zeta}$ is the local oscillator phase⁶. Using the two-photon formalism, we can replace \hat{a} and \hat{a}^\dagger with \hat{a}_+ and \hat{a}_-^\dagger respectively,

$$I_{\text{HD}} = |\alpha| \begin{bmatrix} ie^{i\zeta} & -ie^{i\zeta} \end{bmatrix} \begin{bmatrix} \hat{a}_+ \\ \hat{a}_-^\dagger \end{bmatrix} = \mathbf{v}^\dagger \mathbf{a}, \quad (2.70)$$

or equivalently, in the quadrature basis,

$$I_{\text{HD}} = 2|\alpha| \begin{bmatrix} \sin \zeta & \cos \zeta \end{bmatrix} \begin{bmatrix} \hat{a}_1 \\ \hat{a}_2 \end{bmatrix} = \vec{v}^\dagger \cdot \vec{a}. \quad (2.71)$$

The local oscillator field is represented by \mathbf{v} and \vec{v} in the sideband and quadrature pictures respectively. We have made the expectation value implicit for any scalar in

⁶We choose this phase convention so that $\zeta = 0$ corresponds to reading out the phase quadrature $\zeta = \pi/2$ corresponds to the amplitude quadrature

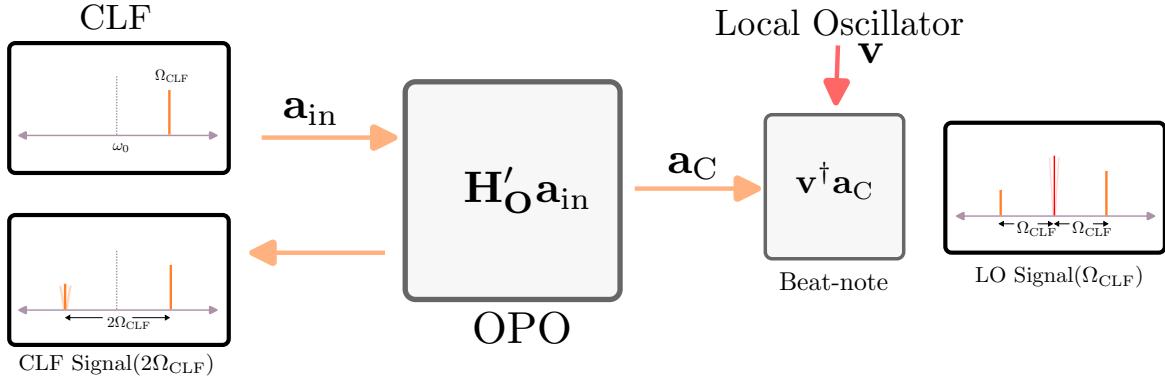


Figure 2.7: Block diagram of coherent control in the sideband picture. The CLF and LO signals are demodulated and used for feedback control of the squeezing angle.

the two-photon formalism. Eq. (2.71) shows that choosing a local oscillator phase allows us to choose a signal quadrature to probe. For squeezed vacuum, we can write the variance of the photo-current σ_{HD}^2 , normalized to no-squeezing as,

$$\sigma_{\text{HD}}^2 = \sin^2(\phi)\sigma_+^2 + \cos^2(\phi)\sigma_-^2, \quad (2.72)$$

where σ_{\pm} are the correspond to the variances of the two quadratures or, alternatively, the squeezing and anti-squeezing levels. Like Eq. (2.37), the squeezing angle ϕ is the relative phase between the squeezer pump and local oscillator.

2.6 COHERENT CONTROL OF SQUEEZED STATES

In the preceding sections, we have established that, for a measurement of squeezing, the squeezed quadrature or squeezing angle is dependent on the relative phase between the squeezed vacuum (squeezer pump) and local oscillator. In this section, we describe a widely used technique known as coherent control [70–72]. This control scheme uses an auxiliary field, which in our case is an RF-sideband of the carrier, to achieve this phase lock. This field is known as the ‘coherent locking field’ (CLF). In this method, the CLF is a single sideband injected into the OPO via an auxiliary port, as described in Section 2.4.1. The non-linearity in the OPO produces a copy

sideband on the other side of the carrier frequency. These sidebands beat with the squeezing measurement's local oscillator and produce a beat-note and the CLF detuning frequency Ω_{CLF} . They also beat with each other on reflection from the OPO to produce a beat-note at twice the CLF detuning frequency $2\Omega_{\text{CLF}}$. These beat-notes are demodulated to produce error signals for feedback control. Together the two control loops, which we will call the CLF and LO loops respectively, are used to stabilize the squeezing angle. A block diagram of the coherent control scheme is depicted in Fig. 2.7.

In the sideband picture, the incoming CLF field can be represent by a single sideband with amplitude a_0 and phase Φ ,

$$\mathbf{a}_{\text{in}} = a_0 \begin{bmatrix} e^{-i\Phi} \\ 0 \end{bmatrix}. \quad (2.73)$$

For the CLF loop error signal, while it is possible to calculate the entire expression for the $2\Omega_{\text{CLF}}$ beat-note, we only need to know the phase of the signal, which is proportional to the phase difference between the CLF and squeezer pump (Eq. (2.58) of [73]),

$$\arg(e_{\text{CLF}}) \propto 2\psi - 2\Phi. \quad (2.74)$$

Demoduating this signal provides an error signal of the form $\sin(2\psi - 2\Phi + C)$, which can be driven to 0 using feedback control. Here, C is the demodulation phase. This allows us to lock the CLF phase to the squeezer pump phase,

$$\Phi = \psi + C/2, \quad (2.75)$$

where C can be chosen to be 0. To model the LO loop error signal, we can apply the auxiliary field transfer matrix \mathbf{H}'_0 (Section 2.4.1) to \mathbf{a}_{in} to obtain the transmitted CLF field,

$$\mathbf{a}_{\text{C}} = \mathbf{H}'_0 \mathbf{a}_{\text{in}}. \quad (2.76)$$

Note that this will depend on the specific configuration of the OPO. While we only

calculate this for Case b)⁷ of Section 2.4.1, the same procedure can be used to model the error signals in the other cases. Using Eq. (2.61), we get,

$$\mathbf{a}_C = \frac{a_0 t_1 t_2 e^{-i\Phi}}{r_1^2 - 2r_1 \cosh z \cos \Delta + 1} \begin{bmatrix} e^{i\Delta} \cosh z - r_1 \\ e^{i(2\psi+\Delta)} \sinh z \end{bmatrix}. \quad (2.77)$$

Beating this with a local oscillator field (Eq. (2.69)) yields

$$e_{LO}(\phi) = \mathbf{v}^\dagger \cdot \mathbf{a}_C \propto -\frac{i}{\sqrt{2}} ((e^{i\Delta} \cosh z - r_1) e^{i\phi} - (e^{i\Delta} \sinh z) e^{-i\phi}), \quad (2.78)$$

where we have omitted a constant pre-factor and $\phi = \zeta - \psi$ is the squeezing angle and we have used the phase stability between the squeezer pump and CLF to set $\Phi = \psi$ (Eq. (2.75)). We can then use the demodulated signal for feedback control of the squeezing angle ϕ . The lock-point is given by the solution to the following equation,

$$\arg(e_{LO}(\phi)) - \theta_D = 0 \quad (2.79)$$

The squeezing angle can be set by choosing the demodulation phase θ_D according to the above equation. The CLF detuning relative to the OPO, Δ contributes an extra phase shift to the error signal, which scales with the squeezing level z . Consequently, in the left plot of Fig. 2.8, we see that the ellipse spanned by the error signal in polar coordinates becomes increasingly skewed as the level of generated squeezing increases. Note that the error signal magnitude also changes with squeezing angle. Operationally, this means that the bandwidth of the feedback also changes as a function of squeezing angle. The right plot of Fig. 2.8 shows the squeezing angle as a function of the chosen demodulation phase. The deviation from linearity increases with the level of generated squeezing. The experimental details of the coherent control scheme are described in Sections 3.3.2 and 6.3.

⁷This OPO configuration is identical to that used in Advanced LIGO

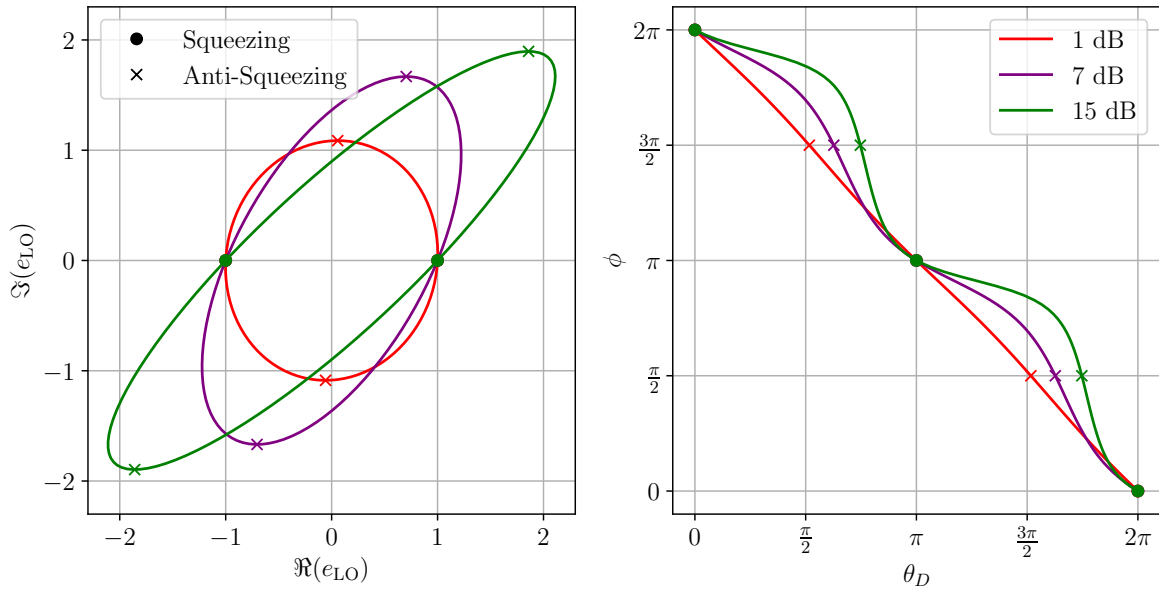


Figure 2.8: CLF-LO error signal model for various levels of generated squeezing. The left plot depicts the CLF-LO beat-note, e_{LO} (Eq. (2.78)) in polar coordinates. The axes represent the demodulated components of the beat-note. The signal is normalized to be equal to 1 for squeezing ($\phi = 0$). Different points on the ellipse correspond to different squeezing angles, which can be scanned through by changing the demodulation phase (Eq. (2.79)). The dots correspond to squeezing while the crosses correspond to anti-squeezing. The plot on the right shows the squeezing angle ϕ as a function of the demodulation phase θ_D . The OPO and CLF parameters used for this simulation are the same as those used at LIGO during O4 (see Table 6.1).

2.7 DEGRADATION OF SQUEEZING

The effective quantum noise reduction with squeezing, or the observed squeeze level, is affected by degradation mechanisms; optical loss, phase noise, and mode-mismatch. In this section, we discuss the first two effects. Mode-mismatch is discussed in more detail in Section 6.4.2.

2.7.1 Loss

Optical losses replace squeezed vacuum with coherent vacuum. The source with loss equal to Λ can be modelled as a beam-splitter with transmissivity $\sqrt{1 - \Lambda}$. The effective quantum noise of a squeezed/anti-squeezed state is then given by

$$\bar{\sigma}_{\mp}^2 = (1 - \Lambda)\sigma_{\mp}^2 + \Lambda. \quad (2.80)$$

Note that Λ can depend on frequency (which is generally the case for lossy optical systems that have a frequency response).

2.7.2 Phase Noise

Eq. (2.72) shows that the measured level of squeezing is dependent on the squeezing angle or the relative phase between the squeezer and local oscillator. Generally, a system would depend on feedback control, or passive isolation to stabilize this phase difference. The residual phase noise, however, mixes squeezing and anti-squeezing, thus reducing the level of measured (anti)squeezing [74, 75]. For a gaussian-distributed phase with a small standard deviation (rms) $\delta\phi$, the measured (anti)squeezing level is approximately given by

$$\bar{\sigma}_{\pm}^2 \approx \cos^2(\delta\phi)\sigma_{\pm}^2 + \sin^2(\delta\phi)\sigma_{\mp}^2, \quad (2.81)$$

For a system with phase noise, there is an optimum level of generated squeezing e^{-2Z} after which the degradation from anti-squeezing becomes larger than the improve-

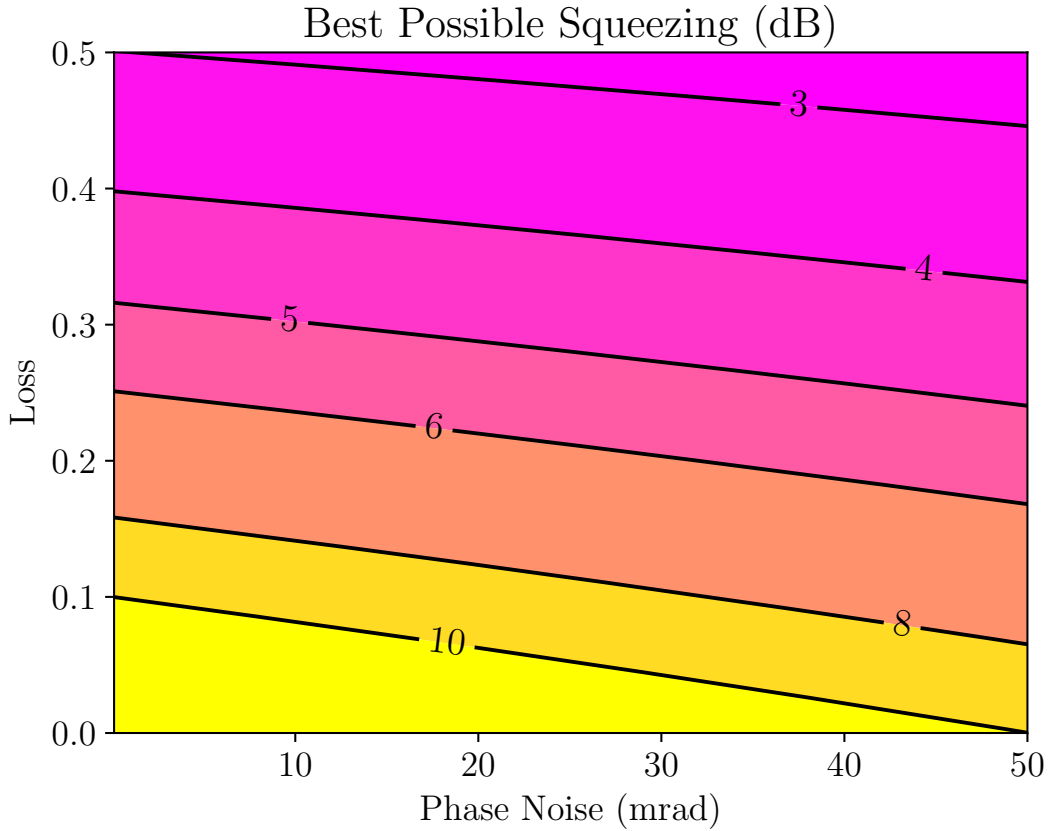


Figure 2.9: Best possible squeezing in dB as a function of loss and phase noise calculated using Eq. (2.84).

ment in squeezing. Since Eq. (2.80) and Eq. (2.81) can be applied to a state in any order without changing the final result, we can ignore the effect of loss and minimize the following expression to obtain the optimum squeezing level,

$$\min_Z (\cos^2(\delta\phi)e^{-2Z} + \sin^2(\delta\phi)e^{2Z}), \quad (2.82)$$

which yields,

$$e^{-2Z_{\text{opt}}} = \tan(\delta\phi). \quad (2.83)$$

Using the optimal value of Z for a given phase noise and loss yields the following

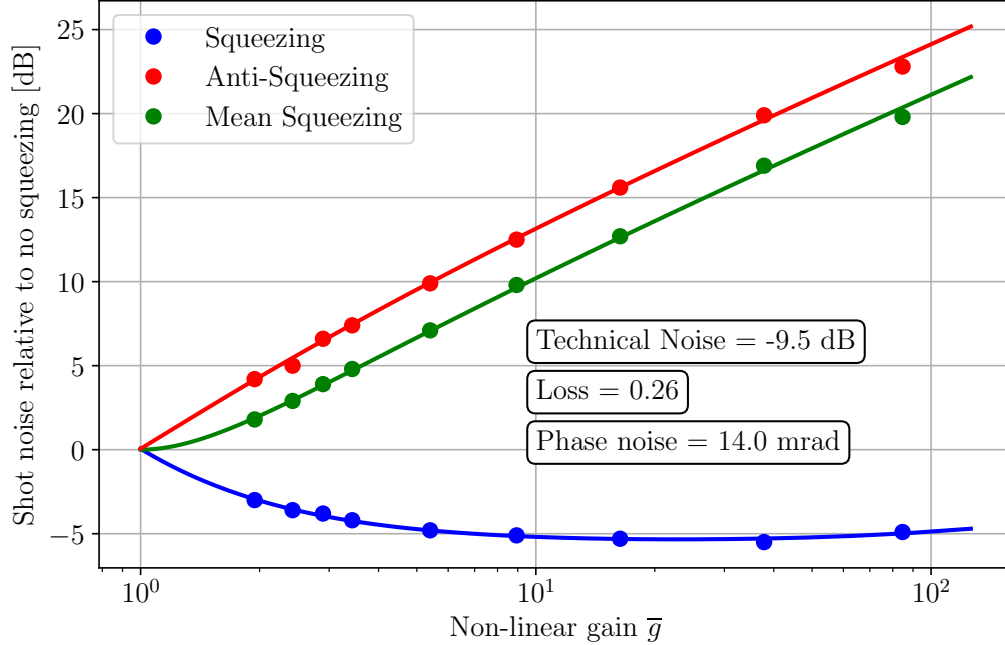


Figure 2.10: Non-linear gain sweep in an OPO to constrain loss and phase noise for the squeezed vacuum source at LIGO Hanford. Eqs. (2.57), (2.66), (2.80), (2.81) and (2.85) are used to model squeezing, anti-squeezing and mean squeezing levels as a function of non-linear gain \bar{g} . The noise model also assumes a flat technical noise floor which is inferred from fitting to data.

expression for the maximum possible squeezing achievable,

$$\min(\sigma) = (1 - \Lambda) \sin(2\delta\phi) + \Lambda. \quad (2.84)$$

Fig. 2.9 shows the maximum possible squeezing that can be measured for a given amount of loss and phase noise.

Phase noise is closely related to a more general frequency dependent quantity known as de-phasing which is observed in systems with frequency dependent loss[76]. Phase noise and dephasing are usually quoted in units of (m)rad.

Mean Squeezing - In the absence of any stabilization mechanism, the squeezing angle fluctuates randomly between 0 and π . The net effect of this is known as mean

squeezing and is given by the average of squeezing and anti-squeezing

$$\sigma_m^2 = \frac{1}{2}(\sigma_-^2 + \sigma_+^2). \quad (2.85)$$

A measurement of mean-squeezing is helpful for characterizing squeezing loss, because it is not sensitive to phase noise, the effect of which can be degenerate with loss. Fig. 2.10 shows a non-linear gain sweep measurement made on a homodyne detector in LIGO Hanford, where the measured squeezing, anti-squeezing and mean squeezing are plotted against various levels of non-linear gains. The generated squeezing is calculated from the non-linear gain \bar{g} using Eqs. (2.57) and (2.66). The data are then fit to Eqs. (2.80), (2.81) and (2.85), with the addition of a flat technical noise floor to constrain the loss and phase noise in the system.

2.8 SQUEEZING IN OPTICAL SYSTEMS

The quantum response of any optical system to the injection of squeezed states can be described by four frequency dependent parameters [76]: rotation, $\theta(\Omega)$; dephasing, $\Xi(\Omega)$; readout-quadrature parametric gain, $\Gamma(\Omega)$, and efficiency, $\eta(\Omega)$. These characteristics relate to the observed quantum noise spectrum N , normalized such that $N = 1$ for shot noise⁸,

$$N \approx \eta\Gamma (\sigma_-^2 \cos^2(\phi+\theta) + \sigma_+^2 \sin^2(\phi+\theta)) + 1-\eta, \quad (2.86)$$

$$\sigma_{\pm}^2 \equiv (1 - \Xi)e^{\pm 2Z} + \Xi e^{\mp 2Z}, \quad (2.87)$$

where σ_-^2 and σ_+^2 are expressions for the squeezed and anti-squeezed noise power, degraded by dephasing. The parameter Ξ includes all effects which create mixed states of the squeezed and anti-squeezed quadratures. This includes phase noise $\delta\phi$ (note that Eq. (2.81) and Eq. (2.87) have the same form). Ξ also has "intrinsic" contributions that occur as squeezed states are created or manipulated by off-resonance optical cavities or lossy optomechanics. The squeezing efficiency η is related to optical loss Λ

⁸The approximation indicates that the loss term $1 - \eta$ is not exact, as it depends on the location of the losses along the squeezing path. It is accurate when $\Gamma \sim 1$.

(Eq. (2.80)) as $\eta = 1 - \Lambda$.

Let us assume that the optical system can be described by a generic complex 2×2 matrix in the quadrature basis, \mathbb{H}_R , representing the linear frequency-dependent response of the system. Homodyne detection of the squeezed state injected into the optical system can be mathematically written as,

$$e = \vec{v}^\dagger \mathbb{H}_R \mathbf{R}_\phi \mathbb{H}_S(Z) \mathbf{R}_\phi^\dagger \vec{a}, \quad (2.88)$$

where $\mathbb{H}_S(Z)$ and \mathbf{R}_ϕ are defined in Eq. (2.27). The combined response of the optical system \mathbb{H}_R and local oscillator \vec{v}^\dagger gives us the homodyne observable with frequency-dependent quadratures, m_q and m_p ,

$$\begin{bmatrix} m_q & m_p \end{bmatrix} \equiv \vec{v}^\dagger \mathbb{H}_R, \text{ or } \begin{bmatrix} \sin \zeta & \cos \zeta \end{bmatrix} \mathbb{H}_R, \quad (2.89)$$

where ζ is the local oscillator angle (where 0 corresponds to phase quadrature readout and $\pi/2$ corresponds to amplitude quadrature readout), m_p and m_q can be used to calculate the frequency-dependent loss $\eta(\Omega)$, rotation $\theta(\Omega)$ and dephasing $\Xi(\Omega)$ experienced by the squeezed state as it interacts with an optical system \mathbb{H}_R . From Sec. IV and App. A of Ref. [76], the squeezing parameters relate to the quadrature observables as⁹

$$\eta\Gamma = |m_p|^2 + |m_q|^2, \quad (2.90)$$

$$\theta = \frac{1}{2} \arg \left(\frac{m_p + im_q}{m_p - im_q} \right), \quad (2.91)$$

$$\Xi = \frac{1}{2} - \sqrt{\frac{(|m_p|^2 - |m_q|^2)^2 + 4(\Re\{m_q m_p^*\})^2}{4(|m_p|^2 + |m_q|^2)^2}}. \quad (2.92)$$

⁹The expression for θ differs from the approximation of Eq. 37 in Ref. [76]. It is nearly numerically equivalent to the frequency-dependent rotation given by the singular value decomposition in App. A of Ref. [76]. Together, Eqs. 2.90-2.92 obviate the need for a decomposition.

2.8.1 Squeezing in LIGO

The total quantum noise in an interferometer contains contributions from uncertainties in both amplitude and phase quadratures. The displacement in the interferometer arms creates a signal that is measured as a phase shift. Uncertainty in the phase quadrature, thus, shows up as optical shot noise at the readout of the inteferometer, which can also be interpreted as photon number fluctuations at readout (Section 1.2). The mechanical pendulum response of the interferometer mirrors to the radiation pressure imparted by photons in the interferometer transforms amplitude fluctuations into phase fluctuations. As a result, fluctuations in the amplitude quadrature are also converted into phase errors at readout in form of quantum radiation pressure noise.

From Eqs. (2.34) and (2.35), we can see that, squeezing either phase or amplitude will suppress one of these noises by a factor of e^{2Z} while amplifying the other by the same amount. And, in general, when the shot noise sees squeezing with an angle ϕ , radiation pressure noise will be squeezed at the orthogonal angle $\pi/2 - \phi$. Adding the squeezed shot noise (Eq. (1.8)) and radiation pressure noise (Eq. (1.12)) for a simplified lossless interferometer model yields,

$$S_h^{\text{SQZ}} = S_h^{\text{QN}} \left[e^{-2Z} \cos^2(\phi - \theta(\Omega)) + e^{2Z} \sin^2(\phi - \theta(\Omega)) \right], \quad (2.93)$$

where S_h^{QN} is the quantum noise without squeezing (Eq. 1.1), ϕ is the squeezing angle relative to the readout quadrature, and $\theta(\Omega)$ is an effective rotation that arises from the opto-mechanical response of the interferometer:

$$\theta(\Omega) = \tan^{-1} \left[\frac{16kP}{mL\gamma} \frac{1}{\Omega^2} \left(1 + \frac{\Omega^2}{\gamma^2} \right)^{-1} \right]. \quad (2.94)$$

Note that Eq. (2.93) can also be written as Eq. (2.86), where the dephasing Ξ and squeezing efficiency η are both equal to zero for the idealized interferometer model. The optomechanical gain Γ is equivalent to $1 + \mathcal{K}(\Omega)^2$ (Eq. (1.14)). A more detailed description of the interferometer in the two photon formalism is discussed in Section 5.4.2. At low frequencies, where radiation pressure noise is dominant, Eq. (2.94)

can be rewritten as

$$\theta(\Omega) = \tan^{-1} \left[\frac{\Omega_{\text{SQL}}^2}{\Omega^2} \left(1 + \frac{\Omega^2}{\gamma^2} \right)^{-1} \right] \approx \tan^{-1} \left[\frac{\Omega_{\text{SQL}}^2}{\Omega^2} \right], \quad (2.95)$$

where Ω_{SQL} is defined in Eq. (1.15). When frequency-independent phase squeezing is injected, the above two equations simplify to

$$S_h^{\text{SQZ}}(\phi = 0) = e^{-2Z} S_h^{\text{SN}} + e^{2Z} S_h^{\text{RPN}}, \quad (2.96)$$

analogous to increasing the laser power by a factor of e^{2Z} . In this case, $S_h^{\text{SQZ}} > S_h^{\text{QN}}$ for frequencies below ~ 100 Hz due to interferometer back-action from the e^{2Z} enhanced radiation pressure term. When the injected squeezed states are instead prepared with frequency-dependent squeezing angles, $\phi(\Omega) = \theta(\Omega)$, the total quantum noise S_h^{SQZ} can be minimized to $e^{-2Z} S_h^{\text{QN}}$ across the detection band, analogous to increasing both laser power P and mirror mass m by a factor of e^{2Z} .

The appropriate frequency-dependent squeezing angles can be produced by reflecting the squeezed states off an optical filter cavity, detuned from the interferometer laser carrier frequency at $\Omega = 0$, before injection in the interferometer [1]. The next chapter introduces frequency dependent squeezing by providing a mathematical description of an optical filter cavity along with experimental results from a 16m filter cavity experiment in MIT.

The limitations of frequency independent squeezing in precision measurement can only be overcome by mitigating the increase in back-action (radiation pressure noise) accompanied by the injection of squeezing [37]. The term ‘quantum nondemolition’ was introduced to describe techniques that can circumvent back-action to surpass the standard quantum limit [77, 78]. During the 1980s, state preparation emerged as a nondemolition technique [79, 80] that can achieve a broadband reduction of quantum noise [81]. This involves preparation of squeezed vacuum state with a frequency dependent quadrature such that it has phase squeezing in the shot-noise-limited region and amplitude squeezing in the region where radiation pressure noise is dominant.

The seminal work by Kimble *et al.* [1] proposed using a low-loss optical filter cavity, detuned from carrier resonance, to provide the required quadrature rotation to produce a frequency dependent squeezed state. Since then, this technique has been developed and demonstrated experimentally by several groups [44–46, 82]. After several decades of research and development, frequency dependent squeezing was first deployed in the Advanced LIGO detectors during the fourth gravitational wave observing run, O4 (see Chapter 6). Apart from a single input filter cavity, there have been several studies of a variety of configurations of input and output filter cavities [83–86].

In addition to the use of filter cavities, several groups have also demonstrated

alternative methods of circumventing back-action in squeezing enhanced [87–89] and optomechanical systems [90].

In this chapter, we detail a mathematical model of filter cavities and frequency dependent squeezing. We also introduce a scheme for the control of filter cavities. We conclude by reporting the first experimental realization of a frequency dependent squeezed vacuum source at gravitational wave frequencies in a 16 m prototype filter cavity.

3.1 FILTER CAVITY MODEL

In the high finesse limit, the reflectivity of an optical cavity for a sideband at frequency Ω is given by [91]¹,

$$r_{\text{fc}}(\Omega) = 1 - \frac{2\gamma}{\gamma + \lambda + i(\Omega - \Delta\omega_{\text{fc}})}, \quad (3.1)$$

where,

$$\gamma = \frac{cT_{\text{in}}}{4L_{\text{fc}}}, \quad \lambda = \frac{c\Lambda}{4L_{\text{fc}}}, \quad (3.2)$$

are the *coupler-limited bandwidth* and *loss-limited bandwidth* respectively. T_{in} is the input mirror transmissivity, Λ is the filter cavity round trip loss, L_{fc} is the cavity length, $\Delta\omega_{\text{fc}}$ is the filter cavity detuning from the carrier frequency.

In the two-photon picture's sideband basis, an optical cavity can be represented by the following matrix In the quadrature basis, the filter cavity transfer matrix \mathbf{H}_{fc} is given by

$$\mathbf{H}_{\text{fc}} = \begin{bmatrix} r_+ & 0 \\ 0 & r_- \end{bmatrix}, \text{ using} \quad \begin{aligned} r_+ &= r_{\text{fc}}(\Omega) \\ r_- &= r_{\text{fc}}^*(-\Omega), \end{aligned} \quad (3.3)$$

where r_+ and r_- are the complex filter cavity reflectivity at frequencies corresponding

¹also see Appendix B.1

to the upper and lower sideband, respectively. In the quadrature basis, we have,

$$\mathbb{H}_{\text{fc}} = \mathbf{A}\mathbf{H}_{\text{fc}}\mathbf{A}^{-1} = \frac{1}{2} \begin{bmatrix} r_+ + r_- & i(r_+ - r_-) \\ -i(r_+ - r_-) & r_+ + r_- \end{bmatrix}. \quad (3.4)$$

For \mathbb{H}_{fc} , the quadrature observables can be calculated using Eq. (2.89), for phase quadrature readout, ($\zeta = 0$) are given by

$$m_p = \frac{1}{2}(r_+ + r_-) \quad m_q = -\frac{i}{2}(r_+ - r_-). \quad (3.5)$$

We can use Eq. (2.91) to calculate the rotation applied to the squeezed state by the filter cavity,

$$\theta = \frac{1}{2} \arg \left(\frac{r_+}{r_-} \right). \quad (3.6)$$

For a lossless filter cavity, $\lambda = 0$, this equates to,

$$\theta(\Omega) = \tan^{-1} \left(\frac{2\gamma\Delta\omega_{\text{fc}}}{\gamma^2 + \Omega^2 - \Delta\omega_{\text{fc}}^2} \right). \quad (3.7)$$

Physically, this corresponds to a squeezing rotation within the bandwidth of the filter cavity. Fig. 3.1 shows the frequency dependent squeezing rotation for various filter cavity detunings. For large detunings ($\Delta\omega_{\text{fc}} \gg \gamma$), this rotation is maximum at the resonant frequency of the filter cavity. The maximum rotation provided by a filter cavity is equal to $\pi/2$, which is a squeezing rotation into to the orthogonal quadrature. Far from resonance, the filter cavity has no effect and does not rotate squeezing.

To calculate the frequency dependent loss in a filter cavity, we use Eq. (2.90),

$$\eta\Gamma = |m_p|^2 + |m_q|^2. \quad (3.8)$$

Here, the noise gain Γ is 1 for a filter cavity. Substituting Eq. (3.5) in the above equation for a lossless cavity yields,

$$\eta = \frac{1}{2}(|r_+|^2 + |r_-|^2) = 1 \quad (3.9)$$

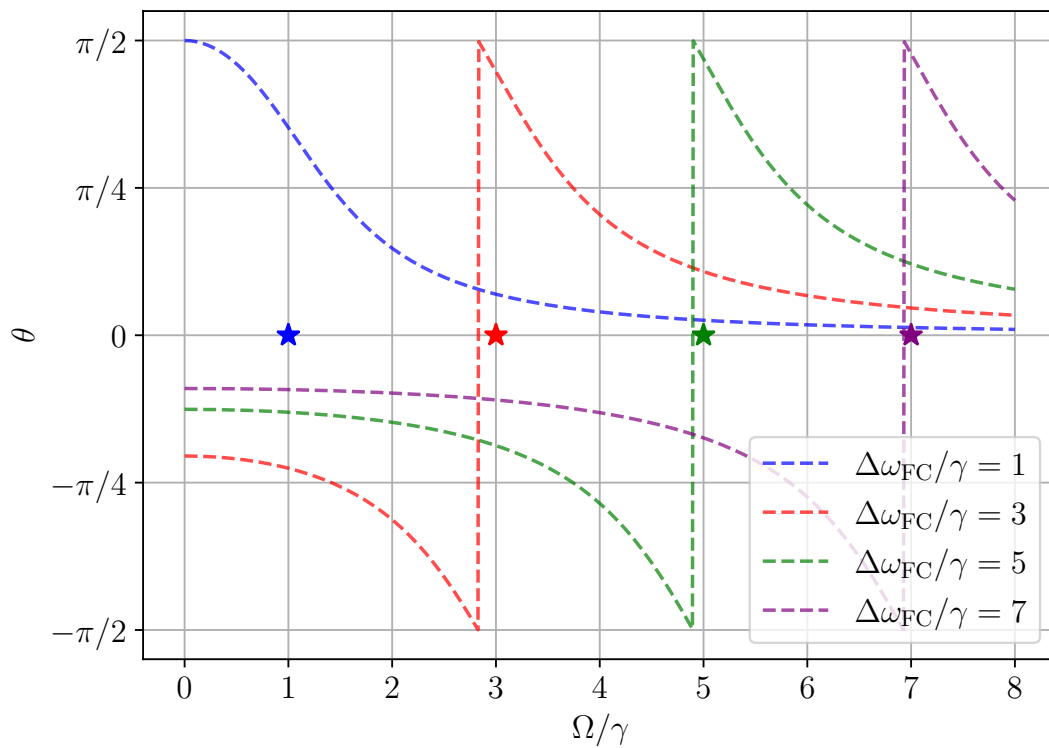


Figure 3.1: Squeezing rotation for various detunings in a lossless filter cavity. All frequencies are normalized to the filter cavity bandwidth. Cavity resonance is represented by a star.

This is expected as squeezing loss in the cavity is due to optical loss, which is assumed to be 0. For a lossy filter cavity, the squeezing loss increases as the cavity approaches resonance.

For frequency dependent squeezing in an interferometer, we can compare Eq. (3.7) with Eq. (2.95), which gives us,

$$\frac{2\gamma\Delta\omega_{fc}}{\gamma^2 + \Omega^2 - \Delta\omega_{fc}^2} = \frac{\Omega_{\text{SQL}}^2}{\Omega^2}. \quad (3.10)$$

This condition is satisfied when,

$$\Omega = \Delta\omega_{fc} = \frac{\Omega_{\text{SQL}}}{\sqrt{2}}. \quad (3.11)$$

Eq. (3.11) is, however, only valid for a lossless filter cavity. A detailed analysis for optimal filter cavity design with loss is provided in Chapter 4.

3.2 FILTER CAVITY CONTROL

Controlling filter cavity's length (detuning) is an essential part of producing frequency dependent squeezed states. Locking filter cavities for frequency dependent squeezing typically relies on the use of an auxiliary field propagating with the squeezed vacuum[45, 82, 92] that is resonant in the filter cavity. Since frequency dependent squeezing at gravitational wave frequencies requires filter cavities with a low bandwidth and high finesse, it is common to acquire lock using a frequency for which the cavity is lower finesse. In our case, we use the Pound-Drever-Hall locking method with a second harmonic (532 nm) field. Adjusting this green frequency allows the cavity to then be brought into resonance for the desired frequency for frequency dependent squeezing. However, for operation in a gravitational wave detector, there are strict constraints of residual length noise due to back-scatter isolation requirements (see Appendix D)[93]. In order to meet these requirements, the length noise in the filter cavity should be less than 10^{-16} m/ $\sqrt{\text{Hz}}$ above 10 Hz. However, any differential phase noise between the auxiliary field and squeezed field is re-injected into the

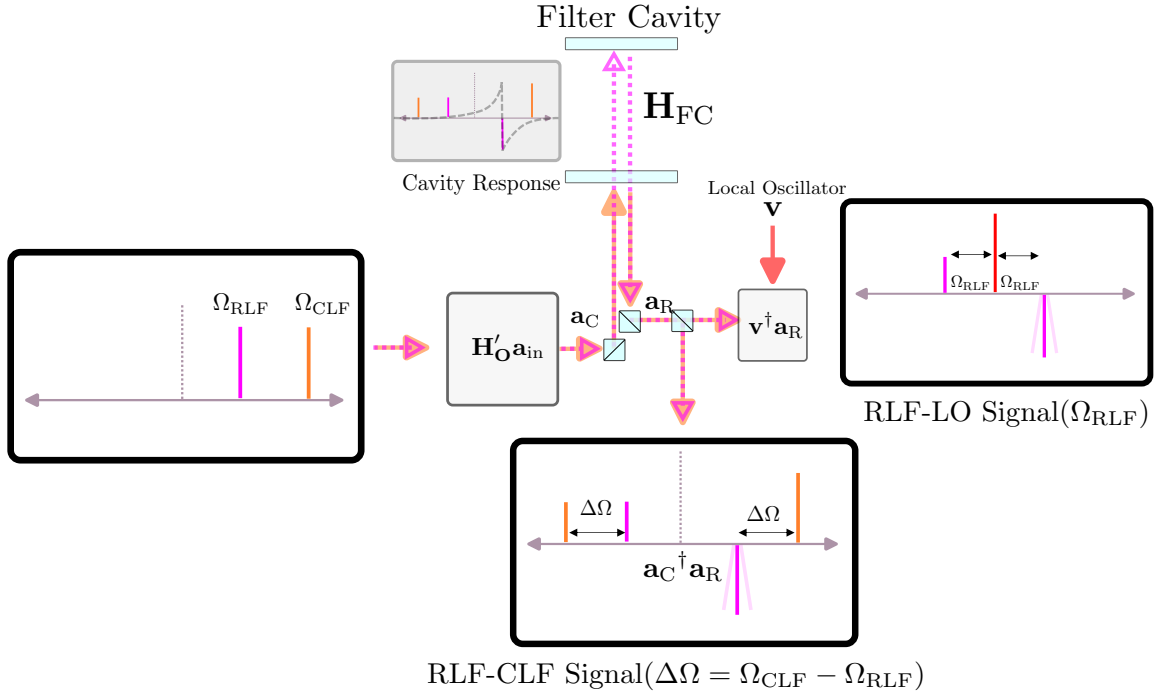


Figure 3.2: Block diagram of the resonant sideband locking scheme.

length feedback as controls noise. For a 532 nm field injected into the LIGO vacuum chamber via fiber, this noise is of the order of 10^{-2} rad/ $\sqrt{\text{Hz}}$ or 5×10^{-14} m/ $\sqrt{\text{Hz}}$ [94]. Therefore, locking the filter cavity only using a second harmonic field requires control loops that roll off aggressively at above 10 Hz, which is impractical for length control. In order to address limitation, we introduce a resonant sideband locking scheme. This method uses a sideband called the resonant locking field (RLF), which is generated and injected into the OPO's auxiliary port along with the CLF (Section 2.6). The frequency of this sideband is chosen to be resonant around the desired filter cavity detuning,

$$\Omega_{\text{RLF}} \approx \Delta\omega_{\text{fc}} + n\Omega_{\text{FSR}}, \quad n \in \mathbb{N}, \quad (3.12)$$

where Ω_{FSR} is the free spectral range of the cavity. The filter cavity imparts a phase shift to the RLF sideband(s), while reflecting the CLF sidebands with no phase shift. The beat-note between the CLF and RLF contains information about this phase shift and can be demodulated at their different frequency to generate a signal that can

be used for filter cavity length/detuning control. Additionally, beating the RLF with the squeezing measurement's local oscillator, produces a signal at the RLF detuning frequency which is alternative control signal for the filter cavity.

To mathematically model these signals in the sideband picture, we can use a procedure similar to that described in Fig. 2.7. Assuming that the RLF and CLF detuning frequencies are similar ($\Delta_{\text{RLF}} \approx \Delta_{\text{CLF}} = \Delta$) and making use of the fact that the RLF and CLF are generated and injected into the OPO together, we can assume that the RLF exiting the OPO is identical to the CLF, \mathbf{a}_C (Eq. (2.76)). On reflection from the filter cavity, the RLF vector is,

$$\mathbf{a}_R = \mathbf{H}_{\text{FC}} \mathbf{a}_C. \quad (3.13)$$

Combining Eq. (2.77) and Eq. (3.3) yields,

$$\mathbf{a}_R = \frac{a_0 t_1 t_2 e^{-i\Phi}}{r_1^2 - 2r_1 \cosh z \cos \Delta + 1} \begin{bmatrix} (e^{i\Delta} \cosh z - r_1) r_+ (\Omega_{\text{RLF}}) \\ (e^{i(2\psi+\Delta)} \sinh z) r_- (\Omega_{\text{RLF}}) \end{bmatrix}. \quad (3.14)$$

Beating the RLF with the CLF gives us the following signal,

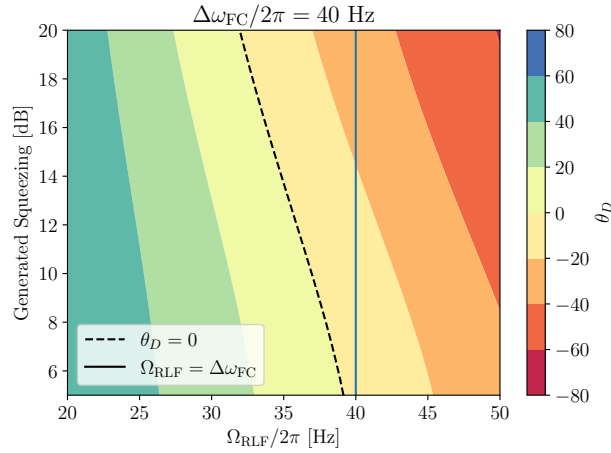
$$e_{\text{RLF-CLF}}(\Omega_{\text{RLF}}, \Delta\omega_{\text{fc}}) = \mathbf{a}_C^\dagger \mathbf{a}_R \propto (\cosh^2 z + r_1^2 - 2r_1 \cos \Delta \cosh z) r_+ + (\sinh^2 z) r_-, \quad (3.15)$$

while the RLF-LO beatnote is given by

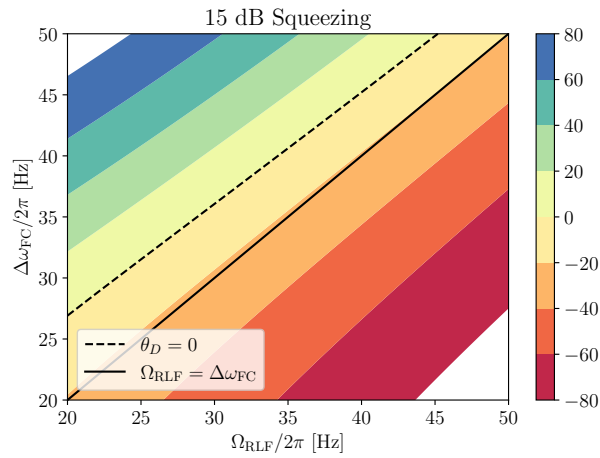
$$e_{\text{RLF-LO}}(\phi, \Omega_{\text{RLF}}, \Delta\omega_{\text{fc}}) = \mathbf{v}^\dagger \cdot \mathbf{a}_R \propto ((e^{i\Delta} \cosh z - r_1) r_+ e^{i\phi} - (e^{i\Delta} \sinh z) r_- e^{-i\phi}), \quad (3.16)$$

where we have modified the Eq. (2.78) to include the filter cavity response. Note that the RLF-CLF signal does not depend on the squeezing angle, while the RLF-LO signal does. Both these signals can be normalized to 1 for frequencies that are off-resonant for the filter cavity, where $r_+ = r_- = 1$. The beatnotes are demodulated and feedback is used to drive the imaginary part of the signal to 0. The lock-point of the filter cavity detuning is then given by the solution to the equation,

$$\arg(e_{\text{RLF}}(\Delta\omega_{\text{fc}})) - \theta_D = 0, \quad e_{\text{RLF}} = e_{\text{RLF-CLF}}, e_{\text{RLF-LO}}. \quad (3.17)$$



(a)



(b)

Figure 3.3: Numerical simulation of RLF-CLF signal (Eqs. (3.15) and (3.17)), normalized to 1 off-resonance. The colormap corresponds to the demodulation phase θ_D required to achieve the given given filter cavity detuning. (a) The detuning is constant at 40 Hz, and the demodulation phase is plotted as a function of RLF detuning frequency (with respect to carrier resonance, i.e. $n\Omega_{\text{FSR}}$), and the generated squeezing at the output of the OPO. (b) The squeezing level has been held constant at 15dB and the demodulation phase has been plotted as function of the RLF and filter cavity detuning frequencies. The OPO, CLF and RLF parameters used for this simulation are the same as those used at LIGO during O4 (see Table 6.1). Additionally, a filter cavity loss Λ_{fc} of 60 ppm has been assumed.

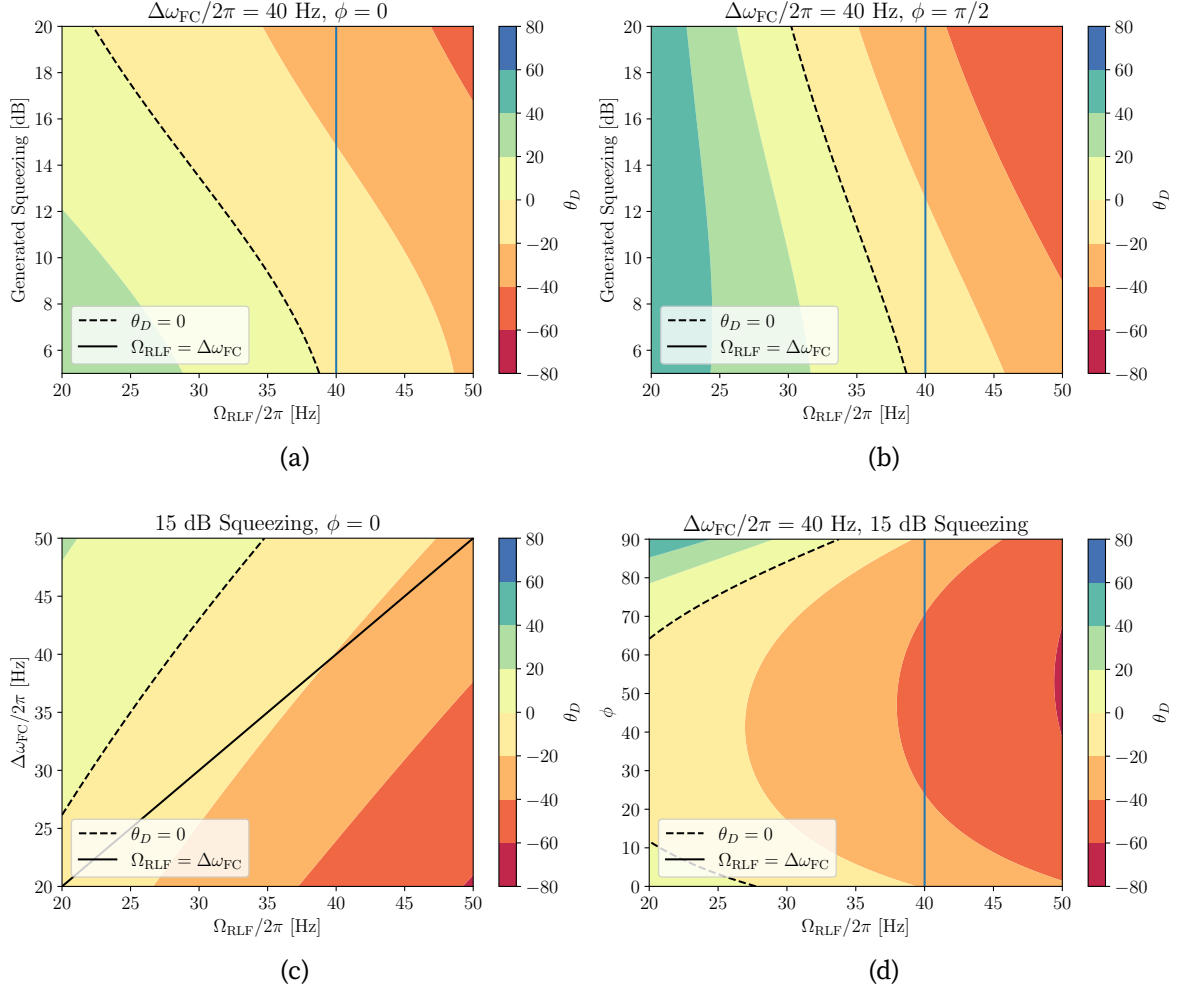


Figure 3.4: Numerical simulation of RLF-LO signal (Eqs. (3.16) and (3.17)), normalized to 1 off-resonance. The colormap corresponds to the demodulation phase θ_D required to achieve the given given filter cavity detuning. In the first two plots, the detuning is constant at 40 Hz, and the demodulation phase is plotted as a function of RLF detuning frequency (with respect to carrier resonance, i.e. $n\Omega_{\text{FSR}}$), and the generated squeezing at the output of the OPO. This is plotted for squeezing (a) and anti-squeezing (b). In (c), the squeezing level has been held constant at 15 dB ($\phi = 0$) and the demodulation phase has been plotted as function of the RLF and filter cavity detuning frequencies. In (d), the filter cavity detuning and generated squeezing have been held constant and θ_D has been plotted against the RLF frequency and the squeezing angle. The OPO, CLF and RLF parameters used for this simulation are the same as those used at LIGO during O4 (see Table 6.1). Additionally, a filter cavity loss Λ_{fc} of 60 ppm has been assumed.

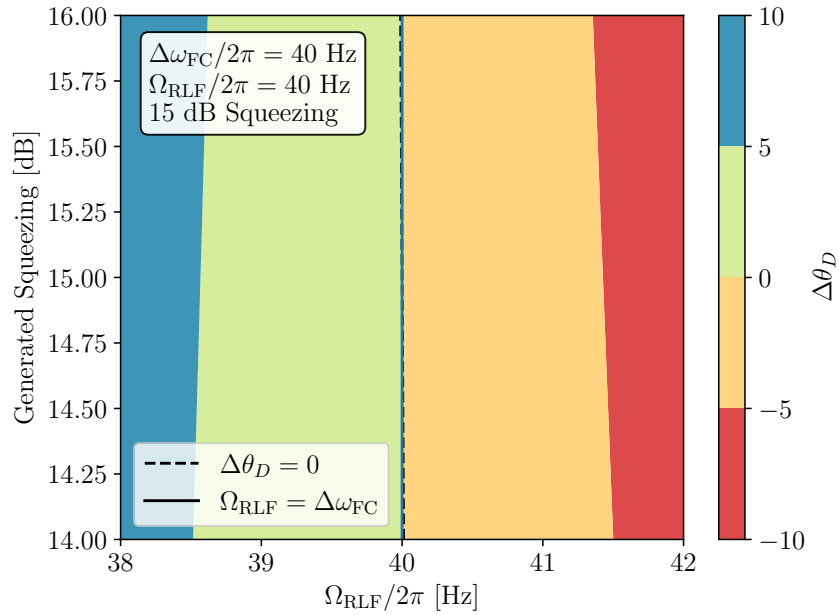
θ_D is the demodulation phase. This lock point depends on a various parameters including the level of generated squeezing, the RLF detuning frequency, the demodulation phase and the squeezing angle (for the RLF-LO signal). In order to achieved a filter cavity detuning, we can either choose a fixed Ω_{RLF} (for e.g. $= \Delta\omega_{\text{fc}}$), and set the demodulation phase θ_D according to Eq. (3.17) or, alternatively fix θ_D , (for e.g $= 0$) and set Ω_{RLF} .

Numerical simulations of the RLF-CLF and RLF-LO signals have been plotted in Figs. 3.3 and 3.4 respectively. Note that for a demodulation phase of 0 in both these signals, the RLF detuning frequency is close to but not equal to the filter cavity detuning frequency. This would be equal when the only phase shift being sensed is that which is imparted to the resonant RLF sideband. However, when the filter cavity resonance is close to the carrier frequency, the negative RLF sideband that is generated by the OPO also experiences a non-zero phase shift from the filter cavity. Additionally, the phase shift from the OPO detuning Δ also contributes to a shift in the lock point of the RLF-LO signal.

Given an operating point for a filter cavity, we can also calculate the change in demodulation phase or the RLF frequency required to account for changes in any other squeezing parameters. We plot these in Figs. 3.5 and 3.6. This ‘online tuning’ only normalizes the signal for the operating point, as opposed to the ‘setup tuning’ plotted in Figs. 3.3 and 3.4.

Briefly touching upon the relative merits and demerits of the two signals, note that, compared to the RLF-LO signal, the RLF-CLF signal is not sensitive to fluctuations in the level of generated squeezing, in addition to having no dependence on the squeezing angle. This makes it a good candidate for long term operation. However, measuring the RLF-CLF beat-note requires a pick-off in the squeezing path which contributes to squeezing loss. Additionally, the RLF and CLF are very weak fields and measuring their beat-note requires a high-gain transimpedance amplifier in order to be useful for feedback control.

The experimental details of the resonant sideband locking scheme are described in Sections 3.3.2 and 6.3



(a)

Figure 3.5: Numerical simulation of online tuning of the RLF-CLF signal, normalized to 1 off-resonance, only for the operating point which is described in the text box. The colormap corresponds to change in the demodulation phase $\Delta\theta_D$ required to achieve the given filter cavity detuning. $\Delta\theta_D$, along with the required adjustment to the RLF frequency Ω_{RLF} is plotted for a variable squeezing level. The OPO, CLF and RLF parameters used for this simulation are the same as those used at LIGO during O4 (see Table 6.1). Additionally, a filter cavity loss Λ_{fc} of 60 ppm has been assumed.

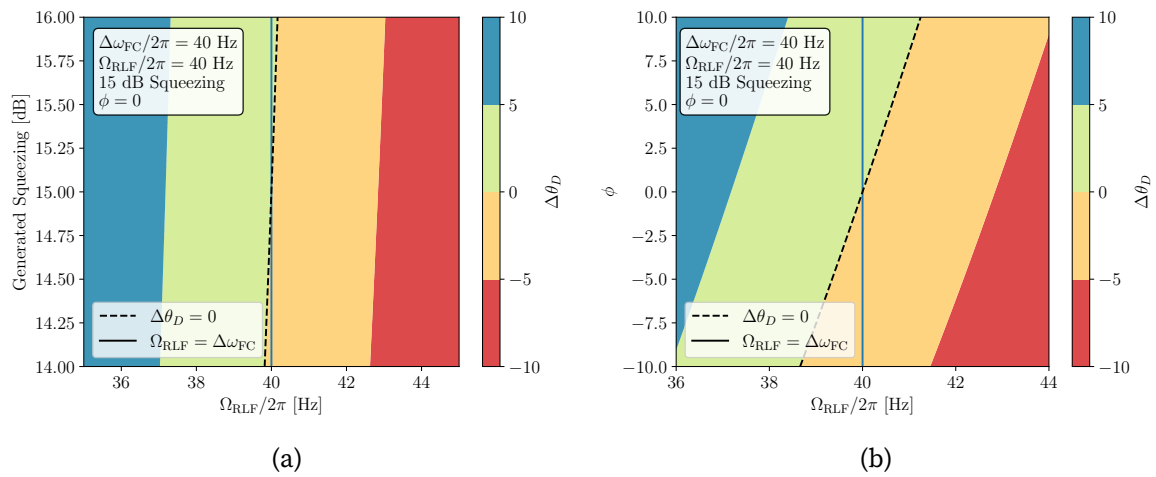


Figure 3.6: Numerical simulation of online tuning of the RLF-LO signal, normalized to 1 off-resonance, only for the operating point which is described in the text box. The colormap in both plots corresponds to change in the demodulation phase $\Delta\theta_D$ required to achieve the given filter cavity detuning. $\Delta\theta_D$, along with the required adjustment to the RLF frequency Ω_{RLF} is plotted for (a) variable squeezing level (b) variable squeezing angle. The OPO, CLF and RLF parameters used for this simulation are the same as those used at LIGO during O4 (see Table 6.1). Additionally, a filter cavity loss Λ_{fc} of 60 ppm has been assumed.

3.3 16 M PROTOTYPE FILTER CAVITY

This section describes the experimental realization of frequency dependent squeezing at gravitational wave frequencies using a 16 m filter cavity.

3.3.1 *Experimental Setup*

An overview of the experimental apparatus is shown in Fig. 3.7 and the key parameters of the system are listed in Table 3.1. The laser source for the experiment is a nonplanar ring oscillator (NPRO) at 1064 nm. A portion of the 1064 nm is frequency doubled to ~ 90 mW of 532 nm light via cavity enhanced second harmonic generation (SHG). A portion of the 532 nm light is used to pump the *frequency-independent* squeezed vacuum source, which is nearly identical to the one in used in Advanced LIGO during O3 [42]. The OPO is a bowtie cavity containing a wedged PPKTP crystal mounted on a translation stage [95, 96]. This beam is passed through an electro-optic modulator, driven at 78.9 MHz, to produce sidebands to lock the OPO cavity, using the Pound-Drever-Hall (PDH) scheme, to be dually resonant for the squeezer pump and the carrier frequencies. Around 15–20 mW of the 532 nm beam is injected into the OPO to produce squeezed vacuum. The squeezed vacuum source is located in a seismically-isolated, ultra-high vacuum chamber identical to those used in Advanced LIGO [97].

The squeezed beam is reflected off the 16 m detuned filter cavity. Two relay mirrors with remotely controllable picomotor mounts, and a translation stage mounted lens are used to optimize between the mode-matching and alignment between OPO and filter cavity. The filter cavity storage time is 2.8 ms and has a finesse of ~ 80000 for 1064 nm light. The inferred cavity round-trip loss, excluding input mirror transmissivity, is $\Lambda = 19$ ppm, corresponding to a decoherence time of 5.7 ms [98]. The input and end mirrors of the filter cavity are 2 inch super-polished fused-silica optics with radii of curvature of 18 m, mounted on tip-tilt suspensions [99]. These suspensions provide a single stage of seismic isolation and can be steered in pitch and yaw. The input mirror of the filter cavity is located in the same vacuum chamber as the squeezed vacuum source, while the end mirror is located in another vacuum chamber. The

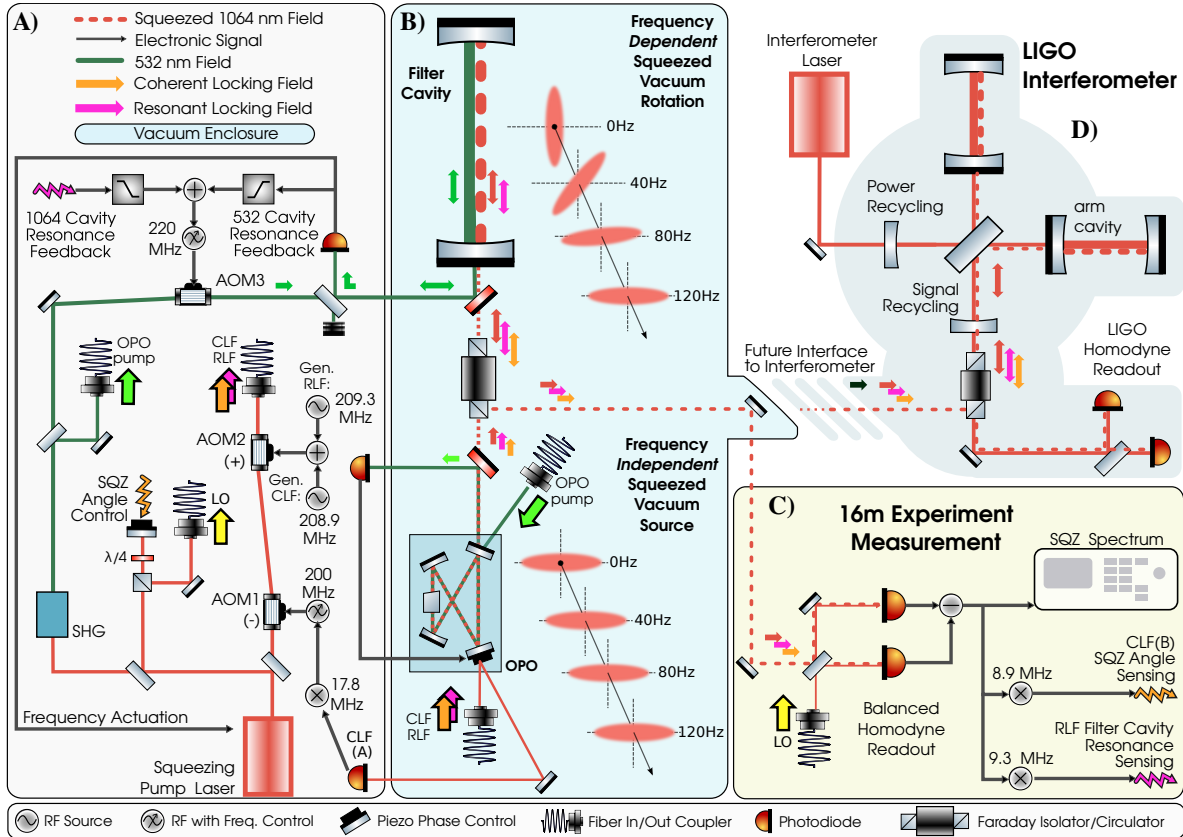


Figure 3.7: Schematic overview of the optical and electronic layout for the 16 m filter cavity experiment. Panel A): The output of a 1064 nm laser is used to produce a 532 nm field via a second harmonic generator (SHG), a local oscillator (LO) for homodyne detection, and two frequency-shifted fields (CLF and RLF) for generating error signals to control the squeeze angle and the filter cavity detuning. The squeezing angle is sensed using the coherent locking field (CLF), and the filter cavity detuning is sensed by the resonant locking field (RLF). The 532 nm field is split into two components, one for generating squeezing as well as controlling the length of the OPO, and the other for controlling the length of the filter cavity. Panel B): frequency-independent squeezed vacuum generated by the OPO is injected into the filter cavity, and experiences frequency-dependent rotation upon reflection. panel C): the frequency-dependent squeezing is measured on a balanced homodyne detector. Panel D): how the filter cavity will integrate optically with the LIGO interferometer.

two chambers are connected by a 16 m vacuum tube. A Faraday isolator then steers the returning squeezed beam from the filter cavity through a viewport towards an in-air balanced homodyne detector [69], where the frequency-dependent squeezed state is characterized. A portion of the laser source is used as the local oscillator of the homodyne measurement. A mirror mounted on a piezo-electric actuator is used to modulate the phase of the local oscillator.

3.3.2 *Squeezing Control*

The remaining 532 nm light from the output of the SHG is doubled passed through an acousto-optic modulator (AOM3 in Fig. 3.7) to shift it in frequency by 220 MHz. This beam is injected into the vacuum chamber via a viewport. This beam is co-aligned to the squeezed vacuum using a dichroic mirror, and is used for the initial PDH sensing of the filter cavity. The PDH signal is fed back to the 1064 laser frequency (slow) and AOM3 drive frequency (fast path). The frequency of AOM3 can be offset to scan the effective length of the cavity and bring it into resonance for the squeezed vacuum.

A part of the 1064 nm laser is also split off to produce auxiliary fields for coherent control (Section 2.6) and resonant sideband locking (Section 3.2). The beam is passed through two AOMs (AOM1 and AOM2 in Fig. 3.7) to produce sideband fields at 8.9 MHz for the coherent locking field (CLF) and 9.3 MHz for the resonant locking field (RLF). These fields are transmitted to the OPO via fiber and injected via an auxiliary port. The reflection from the OPO is directed to an in-air photodiode where the 17.8 MHz beatnote between the two CLF sidebands is sensed and demodulated. This is then fed back to the voltage controlled oscillator (VCO) driving AOM1 to lock the CLF phase to the squeezer pump. The CLF beats with the local oscillator at 8.9 MHz on the homodyne detector. The demodulated beat-note is fed back to the local oscillator phase to lock the squeezing angle. The RLF also beats with the local oscillator at 9.3 MHz, and the demodulated signal is fed back to the drive for AOM3. The resulting feedback loop locks the laser frequency to the filter cavity, stabilizing the effective filter cavity length (detuning).

Table 3.1: Experimentally determined parameters of the frequency-dependent squeezed vacuum source. Entries marked by an asterisk were determined most accurately through fitting to the data. In all cases fitting produced values in agreement with independent measurements and their uncertainties.

Parameter	Value
Filter cavity length	16.06 m
Filter cavity storage time	2.8(1) ms
OPO nonlinear gain	4.5(1)
OPO escape efficiency	98(1) %
Propagation loss*	17(1) %
Homodyne visibility	91.9(4) %
Photodiode quantum efficiency	99(1) %
Filter cavity round-trip loss	19(1) ppm
Freq. indep. phase noise (RMS)	10(5) mrad
Filter cavity length noise (RMS)*	0.7(1) pm
Filter cavity mode matching	92(1) %

3.3.3 Results

Fig. 3.8 shows squeezing measurements for various configurations of the filter cavity. First, a reference measurement without squeezing is taken to determine the shot noise. All subsequent measurements are normalized to this shot noise level. Next, a measurement of frequency-independent squeezing is taken by holding the filter cavity far from resonance (brown). The measured squeezing level of 4.4 dB establishes the parameters of the squeezed vacuum source, independent of the filter cavity.

All measurements of frequency-dependent squeezing shown are performed with a ~ 30 Hz filter cavity detuning. With this detuning, measurements are taken at five different homodyne angles: one for measuring the squeezed quadrature at frequencies outside the filter cavity bandwidth (purple), one for measuring the antisqueezed quadrature (blue) and intermediate homodyne angles (orange, green, red).

We use a detailed quantum noise model to verify our understanding of the system and the measured parameters [39]. Decoherence and degradation mechanisms arising from experimental imperfections are also included [91]. For each measurement, parameters that are difficult to measure directly (marked with asterisks in Table 3.1),

are determined from the model fits.

Under normal operating conditions in Advanced LIGO, the filter cavity will rotate the squeezed state to compensate the optomechanical interaction in the interferometer [40]. While this measurement does not include the LIGO interferometer, our model allows us to compute the maximum quantum noise reduction that could be measured if the interferometer's optomechanical interaction were present. This is shown in the black trace in Fig. 3.8. At frequencies near the rotation frequency (e.g., 30 Hz), the loss in the cavity causes this model projection to go above the shot-noise level. This is expected, given the finesse and optical losses of the 16 m cavity [100], and is part of the motivation for the 300 m long filter cavity for A+. Optics of similar quality in a 300 m filter cavity will result in little degradation of squeezing even at frequencies near the filter cavity resonance [93] (see Chapter 6).

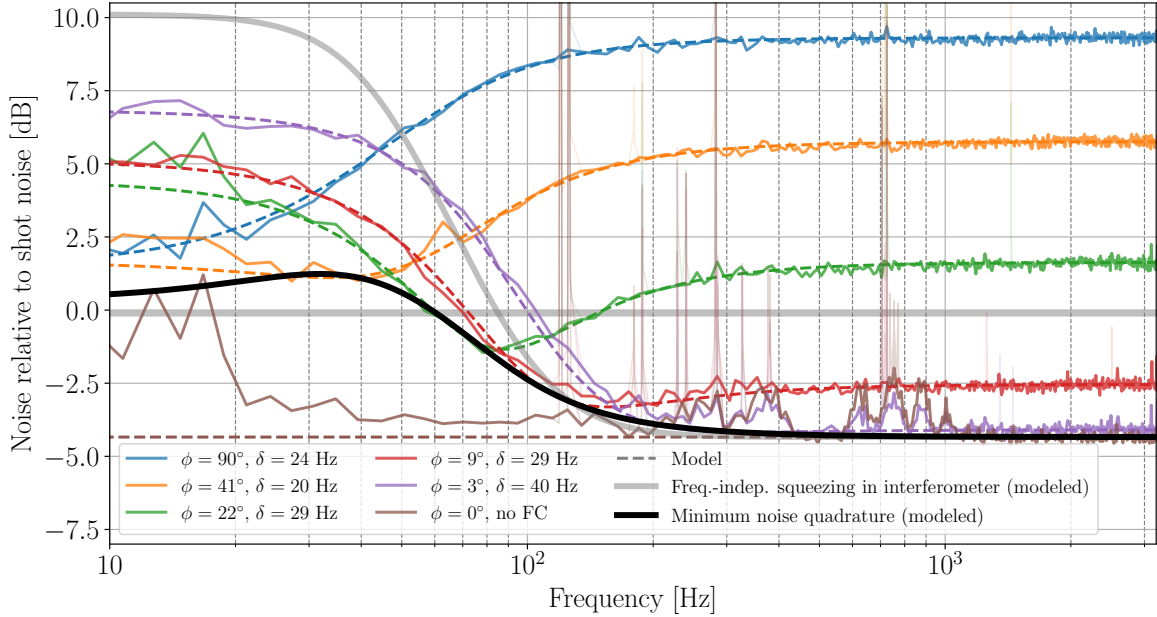


Figure 3.8: Frequency-dependent squeezing at gravitational-wave detector frequencies. Measured noise (solid) is plotted alongside models (dashed). Shot noise (gray) is shown to give a baseline of unsqueezed vacuum fluctuations. Frequency-independent squeezing (brown) shows the performance of our squeezer to low frequencies. The action of the cavity on the squeezed vacuum is demonstrated in both squeezed (purple) and anti-squeezed (blue) quadratures, as well as intermediate homodyne angles ϕ (orange, green, red). The cavity detunings δ were selected to be appropriate for gravitational-wave detectors (20-40 Hz). The detuning variations are from a nonlinear relationship between the squeezing angle and operating point of the RLF control scheme (Section 3.2). The black line shows the minimum relative quantum noise possible in an interferometer by squeezing after reflection by this cavity (detuned 30 Hz). For a relative comparison, the gray curve models the quantum noise change expected from injecting only the frequency independent source of this experiment into a matched interferometer [40]. Data coinciding with acoustic peaks have been excluded from the frequency-binned data, but are presented in the faded traces. The turn-up in each curve starting at 20 Hz is due to a mechanical resonance of the optical table.

CHAPTER

4

OPTIMAL FILTER CAVITY DESIGN

In order to maximize quantum noise reduction through frequency dependent squeezing, a filter cavity must be designed with a bandwidth and detuning corresponding to a squeezing rotation, which most effectively matches the optomechanics in the interferometer. In the previous chapter, we calculated the optimal bandwidth and detuning for ideal lossless filter cavity (Eq. (3.11)). We showed that the squeezing rotation from this cavity almost perfectly matches that of the interferometer. However, realistic filter cavities are affected by degradation mechanisms such as optical loss and detuning fluctuations. Computing optimal design parameters for filter cavities needs to account for the constraints set by these mechanisms [91, 100, 101].

In this chapter, we compute a concise form for quantum noise reduction in an interferometer, in the presence of realistic degradation mechanisms. We also run in-depth numerical optimization for the 300 m filter cavity in LIGO. We explore the choice of filter cavity detuning and input mirror transmissivity for varying round trip losses and interferometer arm powers in order to maximize the benefit from frequency-dependent squeezing. We conclude by considering a special case of an un-detuned, critically coupled cavity, known as an ‘amplitude filter cavity’ [86, 102].

4.1 MODEL

We start by calculating the optimal input mirror transmissivity and optimal detuning for a low-loss filter cavity. Here, low loss implies a round-trip loss Λ much smaller than the input mirror transmissivity T_{in} , i.e. $\Lambda \ll T_{\text{in}}$.

From Eq. (3.1), the phase of a reflected sideband at frequency Ω is given by,

$$\alpha_{\text{fc}}(\Omega) = \arctan \left(\frac{2\gamma(\Omega - \Delta\omega_{\text{fc}})}{-\gamma^2 + \lambda^2 + (\Omega - \Delta\omega_{\text{fc}})^2} \right). \quad (4.1)$$

The quadrature rotation angle (Eq. (3.6)) of the input light after reflection from the cavity is calculated as

$$\begin{aligned} \alpha_{\text{p}} &= \frac{\alpha_{\text{fc}}(+\Omega) + \alpha_{\text{fc}}(-\Omega)}{2} \\ &= \frac{1}{2} \arctan \left(\frac{A}{B + 2(\gamma^2 + \lambda^2)\Omega^2} \right), \end{aligned} \quad (4.2)$$

using

$$A = 4\gamma\Delta\omega_{\text{fc}}(\gamma^2 - \lambda^2 + \Omega^2 - \Delta\omega_{\text{fc}}^2), \quad (4.3)$$

$$B = (-\gamma^2 + \lambda^2)^2 + 2(-3\gamma^2 + \lambda^2)\Delta\omega_{\text{fc}}^2 + (\Omega^2 - \Delta\omega_{\text{fc}}^2)^2. \quad (4.4)$$

From our low-loss assumption, the coupler-limited bandwidth is much larger than the loss-limited one ($\gamma \gg \lambda$). This permits rewriting $\gamma^2 + \lambda^2 \simeq \gamma^2 - \lambda^2$ and subsequently simplifies the expression for the rotation significantly:

$$\begin{aligned} \alpha_{\text{p}} &\simeq \frac{1}{2} \arctan \left(\frac{A}{B + 2(\gamma^2 - \lambda^2)\Omega^2} \right) \\ &= \arctan \left(\frac{2\gamma\Delta\omega_{\text{fc}}}{\gamma^2 - \lambda^2 + \Omega^2 - \Delta\omega_{\text{fc}}^2} \right). \end{aligned} \quad (4.5)$$

The objective of the filter cavity is to apply an appropriate rotation to the squeezed state such that the optomechanical action of the interferometer results in reduced noise rather than enhanced radiation pressure noise [1]. Eq. (2.95) gives us the following

condition for optimal filter cavity design

$$\arctan\left(\frac{2\gamma\Delta\omega_{\text{fc}}}{\gamma^2 - \lambda^2 + \Omega^2 - \Delta\omega_{\text{fc}}^2}\right) = \arctan\left(\frac{\Omega_{\text{SQL}}^2}{\Omega^2}\right), \quad (4.6)$$

with the assumption that the interferometer bandwidth γ_{ifo} is much larger than Ω_{SQL} . Solving this equation yields the filter cavity parameters required for phase matching at all frequencies:

$$\begin{cases} 2\gamma\Delta\omega_{\text{fc}} = \Omega_{\text{SQL}}^2 \\ \gamma^2 - \lambda^2 - \Delta\omega_{\text{fc}}^2 = 0. \end{cases} \quad (4.7)$$

Thus, the optimal input transmissivity and detuning for matching a low-loss filter cavity to an interferometer with a known Ω_{SQL} can be written in terms of the filter cavity loss-limited bandwidth λ as

$$\begin{cases} \gamma = \sqrt{\frac{\lambda^2 + \sqrt{\lambda^4 + \Omega_{\text{SQL}}^4}}{2}} \\ \Delta\omega_{\text{fc}} = \sqrt{\frac{-\lambda^2 + \sqrt{\lambda^4 + \Omega_{\text{SQL}}^4}}{2}}. \end{cases} \quad (4.8)$$

While Eq. (4.8) explicitly states the optimal phase-matching conditions of a filter cavity in the low-loss limit, to examine the generality of Eq. (4.8), we need go beyond the low-loss limit and optimal phase-matching conditions and derive the sensitivity enhancement from squeezing by a factor e^{-z} in a more general parameter space. To do this, we break our calculation down into the contributions of the squeezing, anti-squeezing, and unsqueezed vacuum terms to the total quantum noise.

Defining two new parameters as

$$\mu = \frac{r_{\text{fc}}(+\Omega) + r_{\text{fc}}^*(-\Omega)}{2}, \quad (4.9)$$

$$\nu = -i\frac{r_{\text{fc}}(+\Omega) - r_{\text{fc}}^*(-\Omega)}{2}, \quad (4.10)$$

the quantum noise measured at the readout port of a gravitational-wave interferometer (normalized to shot noise) can be written as

$$N_{\text{tot}} = C_{\text{sqz}}e^{-2z} + C_{\text{anti}}e^{2z} + C_{\text{loss}}, \quad (4.11)$$

where

$$C_{\text{sqz}} = |\mathcal{K}\nu + \mu|^2, \quad (4.12)$$

$$C_{\text{anti}} = |-\mathcal{K}\mu + \nu|^2, \quad (4.13)$$

$$C_{\text{loss}} = (1 - |\mu|^2 - |\nu|^2) (\mathcal{K}^2 + 1). \quad (4.14)$$

These equations can be used to estimate the enhancement for any input transmissivity, loss, and detuning.

We now numerically compute the overall sensitivity enhancement resulting from frequency-dependent squeezing as a function of these three parameters: $\gamma/\Omega_{\text{SQL}}$, $\ell \equiv \lambda/\Omega_{\text{SQL}}$ and $\Delta\omega_{\text{fc}}/\Omega_{\text{SQL}}$. The enhancement factor is defined using a frequency-weighted integral of N_{tot} from Eq. (4.11), normalized by the same frequency-weighted integration of quantum noise with frequency-independent squeezing. It can be written as

$$I = \frac{\int_0^\infty d\Omega [\Omega^{-7/3} N_{\text{tot}}^{-1} \mathcal{K}\Omega^2]}{\int_0^\infty d\Omega [\Omega^{-7/3} (\mathcal{K}^2 e^{2z} + e^{-2z})^{-1} \mathcal{K}\Omega^2]}. \quad (4.15)$$

An integration weighted by $\Omega^{-7/3}$ can be used as a proxy for the enhancement of the signal-to-noise (SNR) ratio for gravitational waves detected from a binary inspiral. The $-7/3$ frequency exponent comes directly from the power spectrum of a binary inspiral [103]. Additionally, we now also incorporate detuning fluctuations as a squeezed state degradation mechanism. These fluctuations arise from residual cavity length noise and create a form of frequency-dependent phase noise. We give this noise in a dimensionless form $\xi = \delta\omega_{\text{fc}}/\Omega_{\text{SQL}}$ by normalizing the r.m.s. detuning fluctuation $\delta\omega_{\text{fc}}$ by the SQL frequency.

Fig. 4.1 shows the enhancement factor with varying $\Delta\omega_{\text{fc}}$ and γ , while fixing the loss ℓ and detuning fluctuation ξ . An optical loss as large as $\ell = 0.5$ limits the sensitivity enhancement to below 1 dB, and should remain smaller than 0.15 in order to

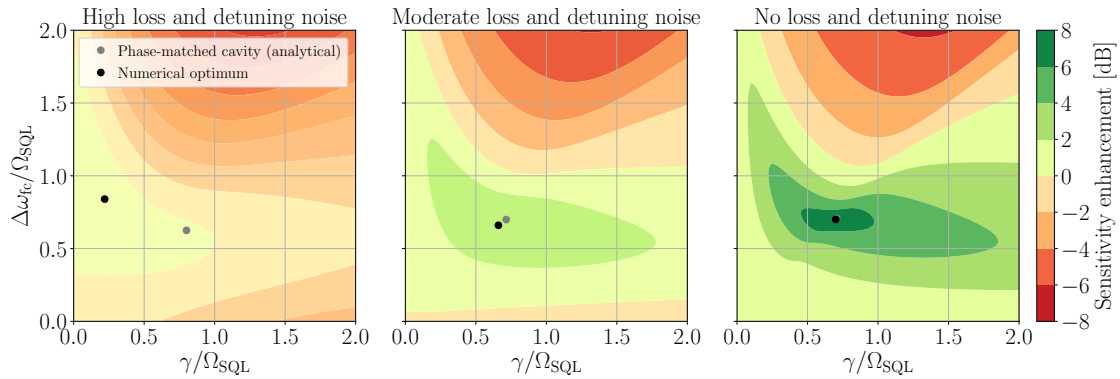


Figure 4.1: Sensitivity enhancement for the detection of binary inspirals relative to using frequency-independent squeezing for various cavity detunings and input transmissivities. From left to right, the three plots have round-trip losses and detuning fluctuations of $(\ell, \xi) = (0.5, 0.2)$, $(0.15, 0.1)$, and $(0, 0)$. The enhancement factors are calculated by integrating the quantum noise spectrum over frequency, weighted by the gravitational-wave spectrum (Eq. (4.15)). The injected squeezing level is 10 dB ($e^{-2z} = 0.1$). The gray point in each plot shows the input transmissivity and detuning calculated from the phase-matching condition (Eq. (4.8)), which assumes low loss, for the given parameters. The black points mark the numerical maxima.

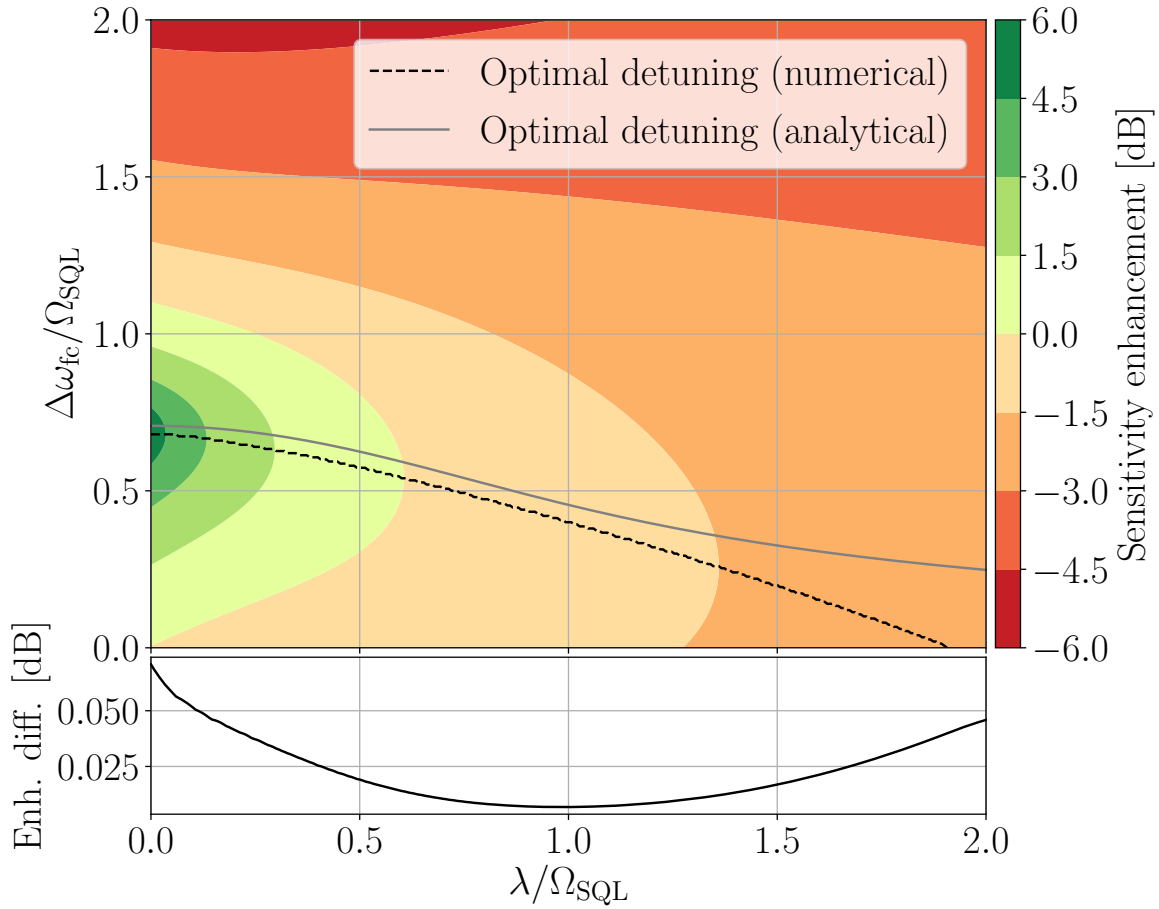


Figure 4.2: Sensitivity enhancement factor for binary inspirals (Eq. (4.15)) using filter cavities with various detunings and losses at a given input transmissivity $\gamma/\Omega_{\text{SQL}} = 1/\sqrt{2}$ and detuning fluctuation $\xi = 0.1$. The black and gray lines represent the best detuning at a given optical loss from numerical optimization and Eq. (4.8) respectively. The lower panel shows the ratio between the numerically-optimized and analytically-optimized sensitivity enhancements, calculated along each of the curves in the top panel. The optimal detuning decreases with larger losses. We also find that the detuning derived from the analytical equation gives almost the same factor of improvement as the numerical maximum.

achieve around 3 dB. When $\ell \lesssim 0.15$ is enforced, the optimal input transmissivity and detuning given by Eq. (4.8)—for which the low-loss and low-noise limit is assumed—is very close to the numerical maximum.

For operational purposes, it is important to investigate the flexibility of a filter cavity with a fixed input transmissivity, but varying round trip losses. We calculate the enhancement factor for a variable $\Delta\omega_{fc}$ and λ in Fig. 4.2. As expected, the loss-less filter cavity with $\Delta\omega_{fc}/\Omega_{\text{SQL}} = 1/\sqrt{2}$ gives the most squeezing. The black dashed line shows the optimal detuning of the cavity at each optical loss. The optimal detuning decreases with increasing optical losses. The gray line shows the analytical optimal detuning computed using Eq. (4.8). Despite deriving our analytical model assuming ideal conditions, it also appears valid in more general scenarios of filter cavity operation.

4.2 APPLICATION TO THE LIGO A+ FILTER CAVITY

Here we apply the above formalism to the A+ filter cavity design [93] parameters as a worked example ¹. This design has a length of 300 m with a budgeted 60 ppm round-trip loss. An input optic with 1000 ppm transmissivity was chosen to optimize detector performance up to the target A+ arm power of 750 kW. We now explore this choice of input coupler, as well as the optimal detuning of the filter cavity. We use the binary neutron star (BNS) inspiral range of the detector as our metric of performance, defined as the distance to a coalescence of two $1.4M_{\odot}$ neutron stars that is detected by the interferometer with an SNR of 8, averaged over the entire sky [104]. A+ is designed to reach a BNS range of 345 Mpc. Similar to Eq. (4.15) used in Figs. 4.1 and 4.2, this metric uses an $\Omega^{-7/3}$ -weighted integration, but now casts the result in an astrophysical context. We now also include the full array of A+ classical noise curves alongside the varying quantum noise. We present this as a percentage improvement over the range of an equivalent interferometer with only frequency-independent squeezing: a 100 % increase in range corresponds to a 6 dB enhancement of sensitivity.

We first explore the selection of a filter cavity input transmissivity. Fig. 4.3 shows

¹The actual experimental parameters of the LIGO filter cavity are described in Chapter 6

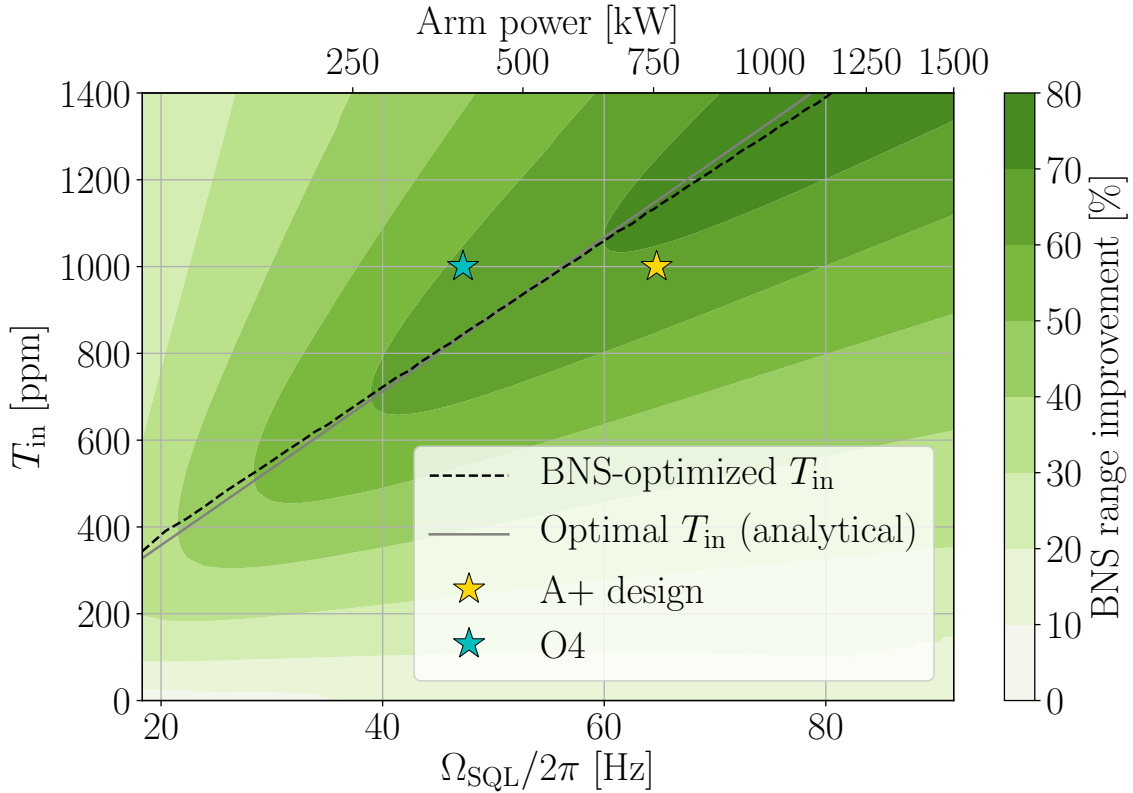


Figure 4.3: The relative percentage range improvement obtained with the installation of a filter cavity in A+ for various filter cavity input transmissivities and SQL frequencies. The arm power corresponding to each SQL frequency is shown in the twin axis. We assume the A+ budgeted round-trip loss $\Lambda = 60$ ppm. The dashed black line indicates the optimal transmissivity at each arm power, while the gray line shows that derived from Eq. (4.8). The yellow star indicates the A+ design, using a filter cavity with $T_{\text{in}} = 1000$ ppm and a 750 kW arm power. The cyan star marks the operating power that was planned for the fourth observing run (O4), 400 kW, at least twice that measured for O3. This plot shows that a 1000 ppm input coupler is close to optimal for a wide range of prospective arm powers.

the optimal choice for varying interferometer arm powers and, correspondingly, SQL frequencies. The range improvement for a given arm power and input coupler is calculated by optimizing the filter cavity detuning and squeezing level. This plot is particularly relevant for interferometers undergoing iterations of upgrades; the usage of highly-transmissive input couplers to target high-power operation penalizes operation at lower powers. For Advanced LIGO progressing into A+, we see that a choice of 1000 ppm is within 5 % of optimal BNS range for arm powers in the range 400–800 kW. We also consider this choice with a signal extraction cavity adjusted for higher power in Section 4.2.1. Upon realizing the A+ design, the filter cavity input optic can be optimized for long-term observation at the final interferometer configuration. Finally, we note that the analytical solution from Eq. (4.8) is valid in this regime.

Suppose we use Fig. 4.3 to design our filter cavity and arrive at the A+ design input transmissivity of 1000 ppm with a budgeted loss of 60 ppm and a 300 m filter cavity (0.2 ppm/m), we can now consider sensitivities achieved from the application of this fixed filter cavity to interferometers with varying SQL frequencies. Fig. 4.4 shows how the filter cavity detuning should be adjusted to compensate for interferometer powers for which the cavity was not designed. The detuning must change to approximately offset the varying interferometer rotation frequency. As expected, the greatest improvement in performance—nearly doubling the BNS inspiral range—is reserved for the designed interferometer power.

The second derivative of range with respect to detuning gives a scale for the loss of sensitivity due to detuning noise. We can use the narrow region of optimum performance in Fig. 4.4, centered on the dashed line, to infer a detuning noise requirement for the filter cavity. For instance, if we demand that the standard deviation of the detuning remains within 1 % of the maximum range, we derive an upper limit for the detuning noise RMS of 1.2 Hz (1.3 Hz) for A+ (O4), or equivalently an effective length noise RMS of 1.3 pm (1.4 pm). The A+ filter cavity design chooses a detuning noise constraint that limits the injected anti-squeezing noise to be no greater than the squeezed shot noise itself, leading to a slightly more restrictive length noise upper bound of 0.8 pm [93]. Ref. [91] discusses detuning noise requirements based on the

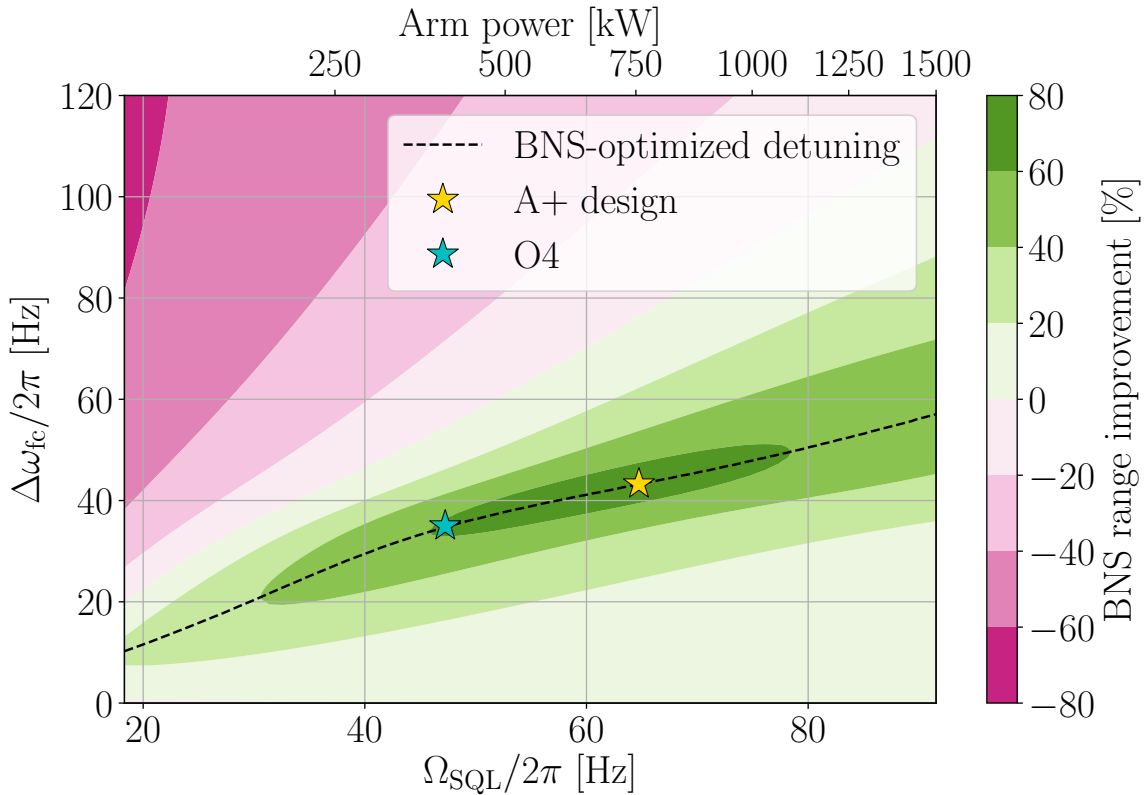


Figure 4.4: Relative percentage binary neutron star (BNS) inspiral range improvement gained by installing a filter cavity with A+ parameters ($T_{\text{in}} = 1000$ ppm, $\Lambda = 60$ ppm) at various interferometer SQL frequencies. The arm power corresponding to each SQL frequency is shown in the twin axis. The vertical axis explores possible filter cavity detunings, with the black dashed line highlighting the optimal such value for each Ω_{SQL} . The yellow star marks the designed A+ arm power. We see that small adjustments in operating point can be used to mostly compensate for deviations from the designed arm power from 50 Hz to 70 Hz SQL frequencies.

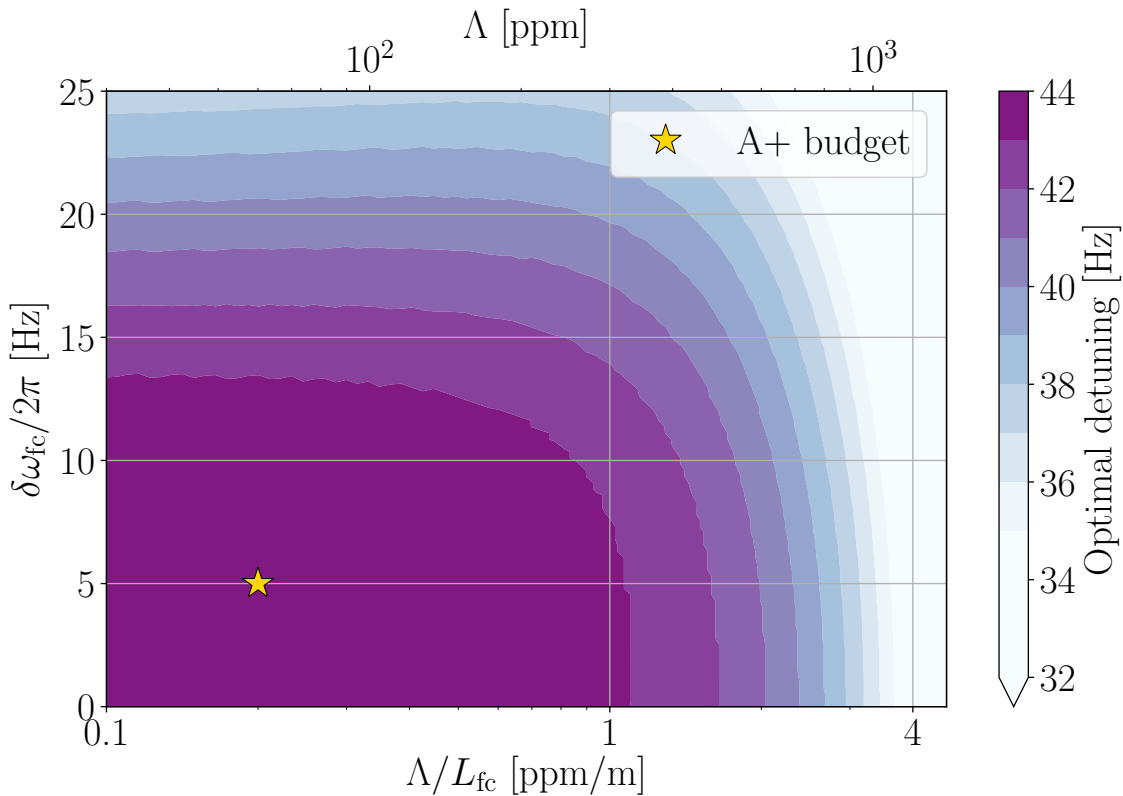


Figure 4.5: The required detuning to accommodate increasing losses or detuning fluctuations. The yellow star marks the budget for the A+ filter cavity design. For any realistic round-trip loss or detuning noise, only small changes in $\Delta\omega_{fc}$ are required.

resulting frequency-dependent phase noise in more detail.

We additionally explore the required detuning shifts to compensate for more severe squeezing degradation. In particular, Fig. 4.5 shows the required change in filter cavity detuning given varying round-trip loss and detuning fluctuations. In general, we find that worse filter cavities require operation closer to carrier resonance. This is consistent with the trend shown in Fig. 4.2. Further, we note that the A+ design filter cavity is highly tolerant of a range of degradations, requiring a detuning shift of only a few Hz for losses of up to a few hundred ppm and ~ 15 Hz of detuning noise. Compare these to the measured values of 19 ppm and 12 Hz measured using a 16 m filter cavity with a comparable bandwidth in Section 3.3.1.

4.2.1 Choice of signal extraction mirror

The existing signal extraction mirror (SEM) in Advanced LIGO was chosen to optimize for a low power operation. Moving from 400 kW to 750 kW, the detector becomes more limited by quantum noise than thermal noise in the ~ 100 Hz region. Insofar as it is quantum noise limited, the range hits a maximum as radiation pressure noise and shot noise trade off due to the Ω_{SQL} nearing merger frequencies.

Furthermore, while we can reduce the quantum noise with frequency-dependent squeezing, quantum radiation pressure noise also acts to enhance any optical scattering noises above the squeezed vacuum, scaling with Ω_{SQL} . This effect motivates lowering Ω_{SQL} to diminish the impact of technical noises. Such a change amounts to modifying the interferometer bandwidth, in turn changing Ω_{SQL} as

$$\Omega_{\text{SQL}} = 4\sqrt{\frac{P_{\text{arm}}\omega_0}{cmL_{\text{arm}}\gamma_{\text{ifo}}}}, \quad (4.16)$$

where P_{arm} is the intra-cavity arm power, ω_0 is the carrier frequency, m is the test mass and L_{arm} is the arm length. These factors additionally manifest in the overall differential displacement due to quantum noise as [40]

$$\Delta x^2(\Omega) = N_{\text{tot}} \frac{\gamma_{\text{ifo}}^2 + \Omega^2}{\gamma_{\text{ifo}}} \frac{\hbar c L_{\text{arm}}}{4\omega_0 P_{\text{arm}}}. \quad (4.17)$$

At design power, a decrease in SEM transmission from 35 % to 20 % is being considered [21]. This increases the interferometer bandwidth from 429 Hz to 751 Hz. As a result, Ω_{SQL} is shifted from 61.4 Hz down to 49 Hz. In Fig. 4.6, we show that the choice of $T_{\text{in}} = 1000$ ppm similarly achieves great range improvement for the A+ design in this configuration, as well as even higher arm powers.

4.3 AMPLITUDE FILTER CAVITY

Fig. 4.2 shows us that as the round trip loss in a filter cavity increases, its optimal detuning trends towards zero. This zero-detuning cavity is known as a amplitude

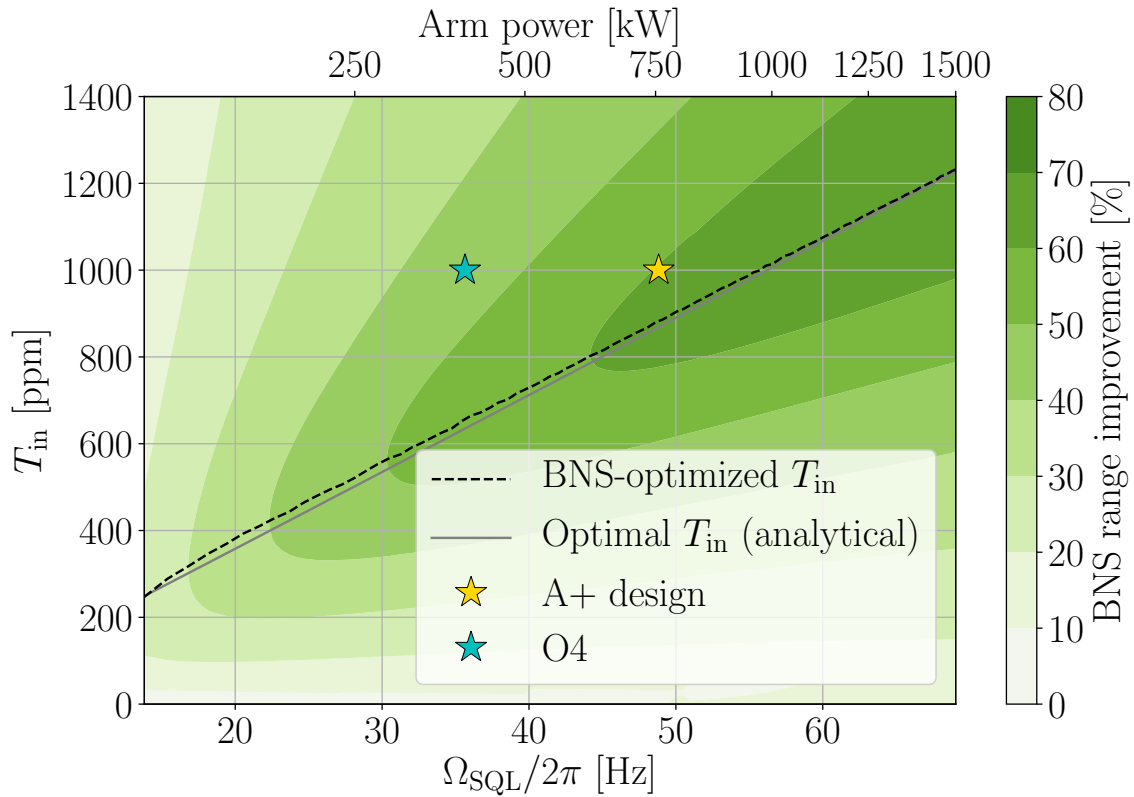


Figure 4.6: The range improvement as a function of arm power and filter cavity input transmissivity, now using an SEM transmissivity of 20%. We see that 1000 ppm is again a good choice for this configuration, giving near-optimal range improvement for powers at and extending beyond the A+ design goal.

filter cavity [86, 102]. While a detuned filter cavity counters the increase in radiation pressure by rotating the squeezing angle, an amplitude filter cavity (AFC) is conceptually distinct, effectively replacing squeezed vacuum with un-squeezed vacuum in radiation pressure dominated regions. This is maximally effective when the cavity is critically coupled, i.e. $\gamma = \lambda$. An AFC can be used as an alternative to a conventional detuned cavity in situations where it is not practically feasible to meet the very stringent cavity round trip loss requirements for frequency dependent squeezing. There are other technical advantages of using an AFC, which we are described in Section 4.3.4.

For a critically-coupled cavity on resonance, and $\Delta\omega_{fc} = 0$ Hz, so the reflectivity is given by

$$r_{\text{afc}}(\Omega) = \frac{i\Omega}{2\gamma + i\Omega} = \frac{i\Omega}{\gamma_{\text{afc}} + i\Omega}, \quad (4.18)$$

where $\gamma_{\text{afc}} = 2\gamma$ is the bandwidth of the filter cavity. On resonance, the $+\Omega$ and $-\Omega$ sidebands encounter a symmetric response [91] which prevents squeezed state rotation, and allows us to simplify the analysis by only considering the amplitude of the reflectivity $\eta_{\text{afc}}(\Omega)$. The phase of the reflectivity does not affect the quantum noise. This efficiency is given by

$$\eta_{\text{afc}}(\Omega) = |r_{\text{afc}}|^2 = \frac{(\Omega/\gamma_{\text{afc}})^2}{1 + (\Omega/\gamma_{\text{afc}})^2}. \quad (4.19)$$

To determine the merits of the amplitude filter cavity technique, we consider the change of the quantum noise in an interferometer with an AFC with and without squeezing. Assuming no losses other than those from the AFC, the reduction in noise is given by

$$\begin{aligned} I_{\text{GW}}(\Omega) &= \frac{N(\Omega, z)}{N(\Omega, z = 0)} \\ &= \frac{[1 + \eta_{\text{afc}}(e^{2z} - 1)] \mathcal{K}^2 + 1 + \eta_{\text{afc}}(e^{-2z} - 1)}{\mathcal{K}^2 + 1}. \end{aligned} \quad (4.20)$$

$I_{\text{GW}}(\Omega)$ demonstrates the following two limits: at high frequencies, where $\mathcal{K} \ll 1$, squeezing is achieved based on the squeezing level and residual efficiencies where,

ideally, $\eta_{\text{afc}} \simeq 1$ and $I_{\text{GW}} \simeq e^{-2z}$. At low frequencies, where $\mathcal{K} \gg 1$, only the radiation pressure term remains and this is where $\eta_{\text{afc}} \simeq 0$ and $I_{\text{GW}} \simeq 1$.

Without the interferometer, we measure the amplitude filter cavity using a balanced homodyne detector to record the noise spectrum of the squeezed field. The two limits of Eq. (4.20) are established by making separate measurements of the squeezing and of the anti-squeezing. The spectrum relative to the coherent-state vacuum is given by

$$N_{\text{HD}}(\Omega, \pm z) = \eta_{\text{afc}} e^{\pm 2z} + 1 - \eta_{\text{afc}}, \quad (4.21)$$

where squeezing and anti-squeezing quadrature observations correspond to $-z$ and $+z$, respectively. Together, the two measurements allow one to construct the interferometer relative quantum noise as the weighted average of the homodyne measurements:

$$I_{\text{GW}}(\Omega, z) = \frac{N_{\text{HD}}(\Omega, +z)\mathcal{K}^2 + N_{\text{HD}}(\Omega, -z)}{\mathcal{K}^2 + 1}. \quad (4.22)$$

Fig. 4.7 shows the modeled interferometer quantum noise and its subsequent improvement upon the introduction of an amplitude filter cavity.

4.3.1 *Experimental setup*

The 16 m filter cavity setup at MIT was used to demonstrate an amplitude filter cavity. The experimental layout is identical to the one described in Section 3.3.1. In order to change the cavity from the over-coupled cavity ($\gamma > \lambda$) required to rotate squeezing, to critically coupled, the alignment of the cavity was changed and the new beam spot on the cavity mirrors experienced higher optical loss. The experimental parameters of the amplitude filter cavity experiment are listed in Table 4.1

4.3.2 *Results*

Fig. 4.7 shows the measured squeezing spectra normalized to quantum shot noise. First, the noise spectrum is measured in the absence of squeezed vacuum with the local oscillator to determine the shot noise (0 dB) reference. Next, frequency-independent squeezing and anti-squeezing data are taken to estimate the squeezing

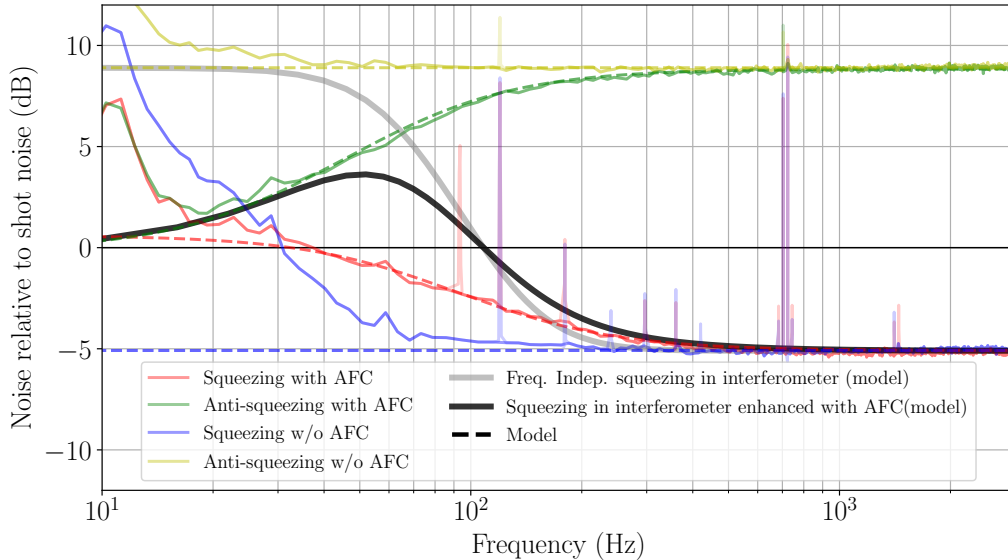


Figure 4.7: Demonstration of an amplitude filter cavity at gravitational-wave frequencies. The measured data (solid) are plotted alongside the quantum noise model (dashed). The noise is plotted relative to quantum shot noise (0 dB). We demonstrate the effect of a near critically-coupled filter cavity on both squeezed (red) and anti-squeezed (green) states. We see that the curves fall toward shot noise at low frequencies as expected from a critically-coupled cavity on resonance. The slight excess with respect to shot noise at low frequencies is due to detuning noise coupled with the fact that the cavity is slightly overcoupled. For reference, we have also plotted frequency-independent squeezed (blue) and anti-squeezed (yellow) data. The noise excess over the model at lower frequencies is due to modulated back-scattered light from the homodyne detector. We observe that the amplitude filter removes some of this back-scattered light at low frequencies through loss, an effect not observed for detuned filter cavities. The acoustic peaks in the data have been excluded from frequency-bin averaging but have been included in the plot as faded traces. The black and gray solid traces are modeled noise improvements when squeezing is applied to an interferometer with Ω_{SQL} and signal bandwidth equal to those of the test interferometer described in Table 4.2.

Table 4.1: Parameters for our amplitude filter cavity experiment. Entries marked by an asterisk were determined by fitting to recorded data. In all cases fitting produced values consistent with independent measurements and their uncertainties.

Parameter	Value
Filter cavity length	16.0611(2) m
Filter cavity storage time	2.1(1) ms
OPO nonlinear gain*	4.6(1)
OPO escape efficiency	98(1) %
Propagation loss*	15(1) %
Homodyne visibility	96.8(7) %
Photodiode quantum efficiency	99(1) %
Input mirror transmission	51.5 ppm
Filter cavity round-trip loss	46 ppm
Freq. indep. phase noise (RMS)*	10(5) mrad
Detuning fluctuation (RMS)*	12.5 Hz
Filter cavity mode matching	94(1) %

level generated ($e^{\pm 2z}$) and injection/readout optical loss. We measure 5 dB squeezing and 9 dB anti-squeezing respectively, which implies 11 dB generated squeezing and 21% total optical loss. For the above measurements, we hold the filter cavity far from resonance with respect to the carrier using the 532 nm light to avoid any resonant effects. Lastly, we repeat the squeezing and anti-squeezing measurements with the filter cavity resonant for the carrier. Our measured data (solid traces) fit our model (dotted traces) well. Except for the detuning and squeezer angle which are inferred from the fit, all other parameters of the setup are measured independently (see Table 4.1). Fig. 4.7 also shows the modeled interferometer quantum noise and its subsequent improvement upon the introduction of an AFC. The red trace, corresponding to the squeezing with the AFC, slightly exceeds shot noise at low frequencies due to a combination of detuning fluctuation and the fact that the cavity is slightly overcoupled.

Some technical noise artifacts are visible in our measured spectra. The peak around 10 Hz is due to a mechanical resonance in the optics table. Harmonics of the power supply and acoustic peaks appear above 100 Hz. There is a broad excess below several tens of Hz that is attributed to back-scattered local oscillator light reflecting

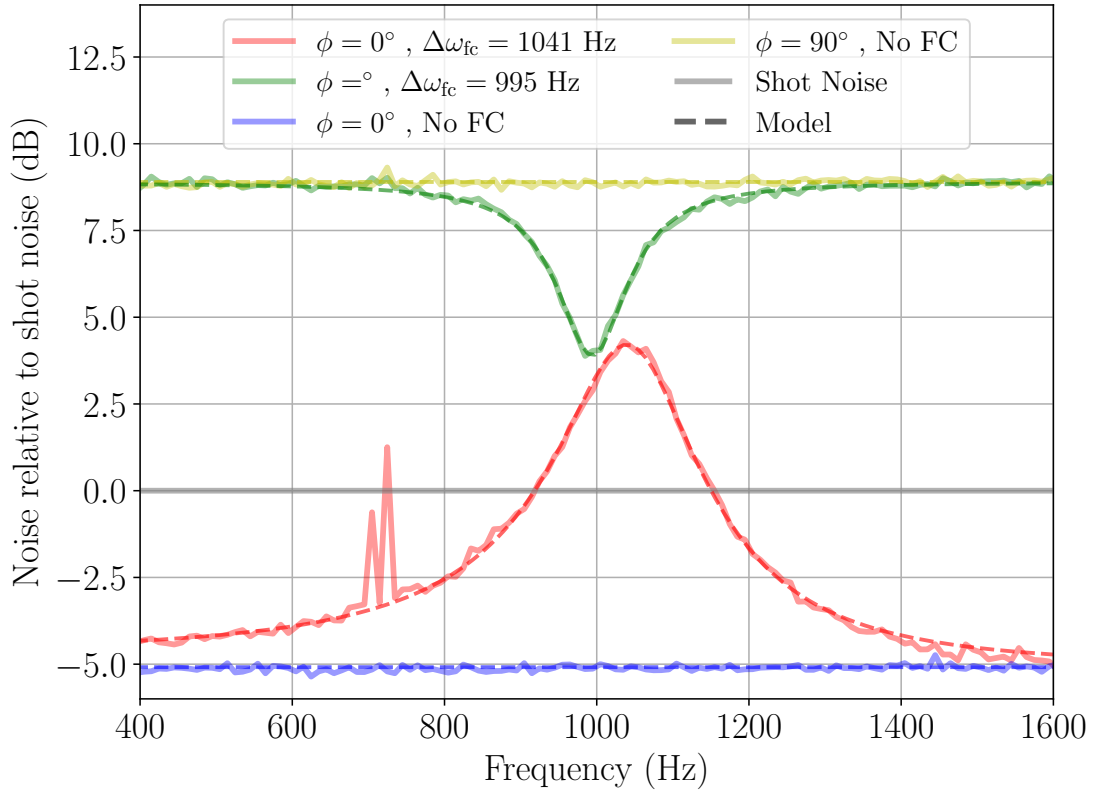


Figure 4.8: Squeezing spectra with the filter cavity detuned 1 kHz. The detuning fluctuation of the filter cavity and the propagation loss of the squeezed vacuum are inferred by fitting our model to the measured data. The other parameters used in the model were measured directly. Acoustic peaks have been omitted for fitting to the quantum noise.

Table 4.2: Assumed parameters of an interferometric GW detector.

Parameter	Value
Arm power	750 kW
Signal bandwidth	450 Hz
Scale Ω_{SQL}	63 Hz
Classical noises	Thermal noise [100]
Injected squeezing	12 dB
Injection loss	5 %
Readout loss	10 %

off the homodyne optics. This light propagates through the squeezed vacuum path, leaking through the Faraday isolator before being reflected from the filter cavity to return to the homodyne detector along with the squeezed vacuum field. We note that the back-scatter noise apparent in the spectra taken without the filter cavity (e.g., the blue curve Fig. 4.7) is diminished in the spectra measured with the AFC due to the attenuation of the cavity.

We additionally measured spectra with the filter cavity detuned at around 1 kHz (See Fig. Fig. 4.8) to characterise the detuning fluctuation, arising from residual cavity length noise and frequency noise on the laser, which is difficult to measure independently. The cavity linewidth and mode-matching into the cavity were determined from independent measurements. We infer the detuning fluctuation in our cavity to be 12 ± 4 Hz, implying a residual length noise of 0.7 ± 0.2 pm. This measurement is performed at high frequency to avoid bias from the back-scatter noise present at low frequencies.

4.3.3 *Improvement in detector range*

In this section, we discuss advantages of the amplitude filter cavity when integrated into a gravitational-wave detector. Fig. 4.9 shows the increase/decrease in the binary inspiral detection range when a filter cavity with $\Delta\omega_{\text{fc}} = 0$ Hz is applied to an interferometer with parameters listed in Table 4.2. We see that, for a resonant cavity with a given bandwidth, the improvement in range is maximum when it is critically coupled.

Additionally, the improvement in range also increases with bandwidth to a point. This is expected; anti-squeezing, which enhances radiation pressure noise caused by interferometer back-action, is destroyed by greater cavity losses. For binary neutron stars however, increasing the AFC bandwidth can become detrimental to the range by degrading squeezing at frequencies which are not affected by radiation pressure noise. Heavier binary inspirals, such as those of two $75M_{\odot}$ black holes, merge at lower frequencies and are completely dominated by radiation pressure noise, resulting in the detection range continuing to improve with increasing filter cavity bandwidth.

4.3.4 *Technical advantages of an amplitude filter cavity*

The AFC configuration has a number of technical advantages. Firstly, it relies on larger optical losses in the cavity for critical coupling and consequently, considerably shorter cavities are sufficient to achieve the desired bandwidth. For optomechanical detectors with limitations on the length or losses of a filter cavity, an amplitude filter can therefore offer low-frequency improvements with more forgiving requirements with respect to a detuned filter cavity.

Secondly, AFCs attenuate classical as well as quantum noise, relaxing scatter noise requirements on the optics relaying beams between the cavity, squeezed-state source, and interferometer. It is possible to mitigate scattered light noise by using optical isolation elements, but this comes at the cost of increasing broadband propagation loss on the squeezed vacuum path. As we have observed in our data, an amplitude filter cavity partially solves the back-scatter problem by destroying back-scattered light within its bandwidth through loss.

Finally, AFCs have relaxed detuning noise requirements relative to detuned filter cavities as they do not need to be precisely held on resonance to achieve attenuation. Detuning fluctuation causes some of the squeezed vacuum to rotate into the orthogonal anti-squeezed quadrature, thereby increasing noise. In order to compare the impact of the detuning fluctuation to the filter cavities, we compute the derivative of

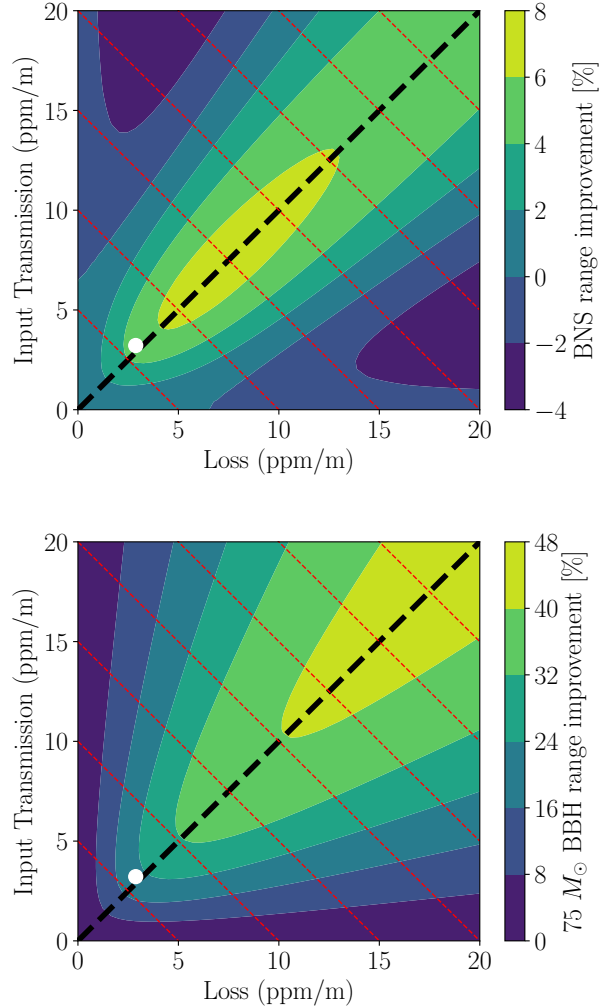


Figure 4.9: Enhancement in $1.4\text{-}1.4M_{\odot}$ binary neutron star (top) and $75\text{-}75M_{\odot}$ binary black hole (bottom) inspiral detection range for filter cavities with detuning $\Delta\omega_{fc}$ set to 0 Hz. The colorbar represents the relative increase/decrease in binary inspiral range when the AFC is applied versus a squeezing-enhanced interferometer (parameters listed in Table 4.2) without an AFC. The black dashed line corresponds to critically-coupled AFCs and the white marker corresponds to the setup that we have demonstrated in this paper, the parameters of which are listed in Table 7.1. Filter cavity bandwidths are constant along the red dashed lines. It is evident that, for a given bandwidth, the range enhancement is maximum when the detector is a critically coupled AFC.

the phase shift of a reflected beam (Eq. (4.1)) with respect to filter cavity detuning,

$$\frac{\partial \alpha_p}{\partial \Delta \omega_{fc}}(\Omega) = \frac{2\gamma(\gamma^2 + \Delta \omega_{fc}^2 - 2\Delta \omega_{fc}\Omega - \lambda^2 + \Omega^2)}{((\gamma - \lambda)^2 + (\Delta \omega_{fc} - \Omega)^2)((\gamma + \lambda)^2 + (\Delta \omega_{fc} - \Omega)^2)}. \quad (4.23)$$

At cavity resonance for a lossless detuned filter cavity, i.e. $\Omega = \Delta \omega_{fc} = \gamma$, this is given by,

$$\left. \frac{\partial \alpha_p}{\partial \Delta \omega_{fc}} \right|_{\Delta \omega_{fc}=\gamma, \lambda=0} = \frac{2}{\gamma}, \quad (4.24)$$

whereas, for an AFC, at $\Omega = \Delta \omega_{fc} = 0$, this evaluates to,

$$\left. \frac{\partial \alpha_p}{\partial \Delta \omega_{fc}} \right|_{\Delta \omega_{fc}=0, \lambda=\gamma} = \frac{1}{2\gamma}. \quad (4.25)$$

The factor-of-4 difference between the two quantities makes it clear that an AFC is significantly less sensitive to fluctuations in detuning than a detuned filter cavity. Numerical simulations of the quantum noise at 100 Hz show that detuning fluctuations degrade noise by 2 dB with the detuned filter cavity, but only 0.06 dB with the AFC, using the parameters from Table 4.2 and an RMS detuning of 10 Hz.

CHAPTER

5

CHARACTERIZING SQUEEZING WITH AN AUDIO-BAND FIELD

Probing and controlling interactions of the squeezed vacuum field with the optical systems it propagates is difficult, because excess light at the main carrier frequency readily contaminates and degrades the level of observed squeezing. Therefore, the control of the squeezed field relies on off-resonant auxiliary coherent fields that co-propagate with the squeezed states from their source and through subsequent optical systems. Injecting a single off-resonant sideband through the squeezer produces two phase-stable sidebands centered about the carrier frequency. Phase-sensitive detection of these two sidebands after the optical system is then sensitive to the path traversed by the squeezed vacuum light, as well as the amount and quality of squeezing.

The frequency-independent squeezed light source installed in the Advanced LIGO detectors [42] already utilizes one such off-resonant auxiliary field, the coherent locking field (CLF) [70], to actively stabilize path length fluctuations between the squeezed vacuum carrier, the squeezer pump, and an external local oscillator fields. However, to enable continuous squeezer operation without contaminating the astrophysical signal band, the CLF is typically detuned by a significant fraction of the linewidth of the optical parametric oscillator (OPO). As a result, the CLF is not representative of the squeezed carrier field itself, and does not directly sense the astrophysical signal band.

Here, we introduce a new auxiliary field which is generated at a small audio-

frequency offset, well within the linewidth of the OPO and signal band. The small offset allows the transmitted audio field to experience the same transformations and degradations as the generated squeezed state.

5.1 EXPERIMENTAL SETUP

For the first experimental demonstration of our diagnostic scheme, we utilized the prototype frequency dependent squeezed vacuum source at MIT, which is described in Section 3.3.1. Fig. 5.1 contains the experimental setup of a squeezed vacuum source along with an injected audio sideband. The audio diagnostic field (ADF) is a single-frequency field that is shifted at acoustic frequencies from the 1064 nm carrier field, and it is generated using two acousto-optic modulators (AOMs). This allows for the creation of sidebands at arbitrary audio band frequencies and suppresses contamination by carrier frequency light[71]. The ADF is generated along with the CLF field and other auxiliary control beams. The ADF and the CLF are injected into the OPO via mirror M_2 , and they co-propagate with the squeezed vacuum after exiting the OPO through mirror M_1 .

Using the reflection of the CLF from the OPO, the CLF phase is stabilized with respect to the phase of the squeezer pump field using the AOM2 drive frequency as an actuator. As the ADF and CLF are generated simultaneously, the coherent control scheme also stabilizes the ADF phase with respect to the squeezer pump phase. The ADF and the squeezed vacuum field then beat with a local oscillator at the readout, generally after passing through an optical system. The local oscillator can be provided explicitly, as for the balanced homodyne readout used for the experimental data in this chapter, or it can be supplied by the optical system, as done for Michelson-fringe readout used by gravitational-wave interferometers. While the local oscillator phase can be changed freely in the former case, it is generally fixed during the latter.

The beatnote between the ADF and the local oscillator is measured on a photodetector, where it is demodulated at the ADF sideband frequency into real (I) and imaginary (Q) quadratures. The nonlinear optical interaction of the OPO which generates squeezing also modifies the injected ADF. As a result, the I and Q signals carry

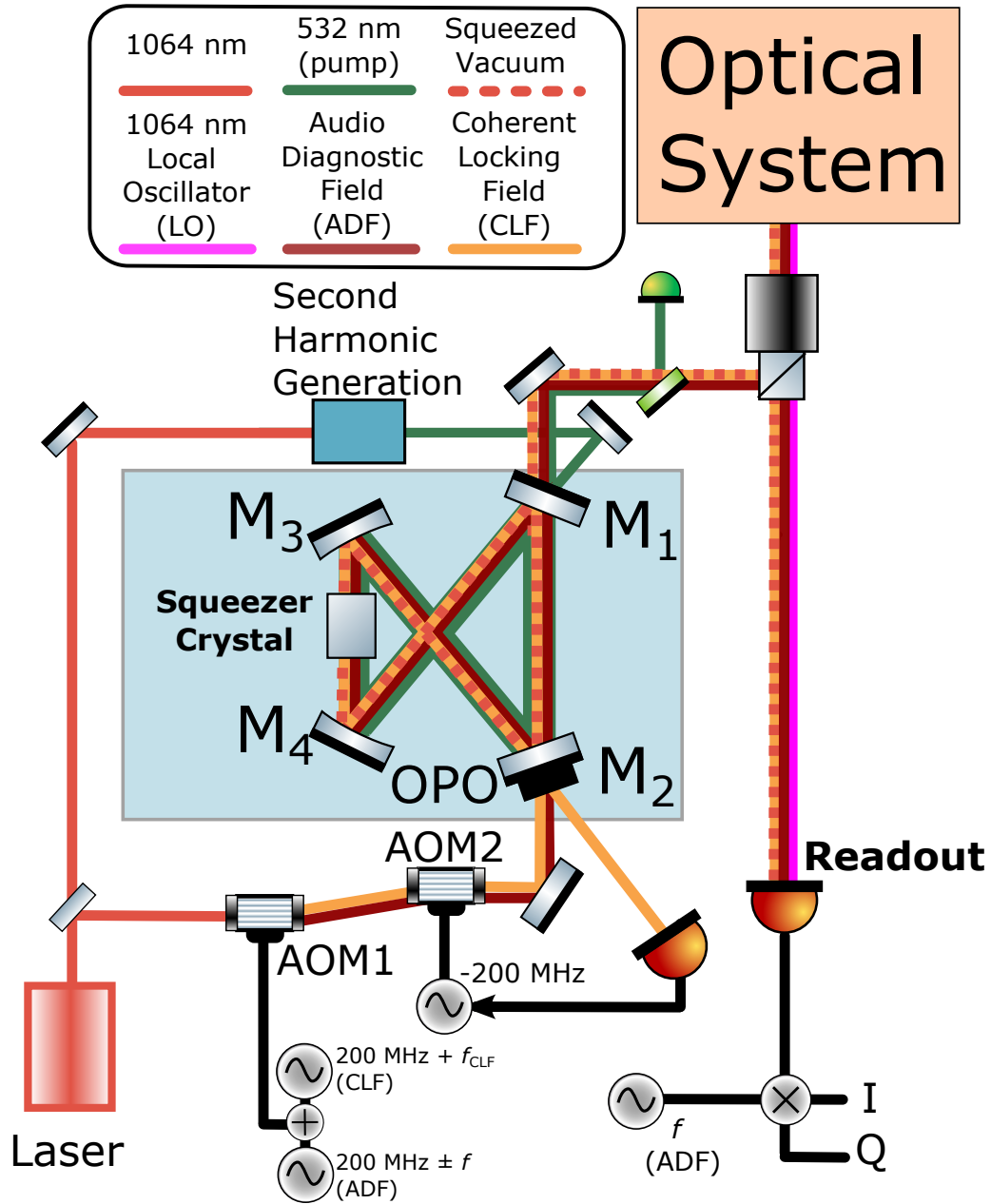


Figure 5.1: Experimental layout of a squeezer system with an audio diagnostic field.

information about the squeezing angle, squeezing level, local oscillator angle, and the optical system, all of which can be measured specifically at any chosen frequency.

5.2 MATHEMATICAL DESCRIPTION

The audio sideband field can be generated at a frequency offset $\pm f$ above or below the squeezed vacuum carrier field. In the sideband basis, the upper and lower audio fields incident on the OPO are

$$\mathbf{a}^\uparrow = a \begin{bmatrix} e^{-i\Phi} \\ 0 \end{bmatrix} \quad \mathbf{a}^\downarrow = a \begin{bmatrix} 0 \\ e^{i\Phi} \end{bmatrix}, \quad (5.1)$$

where a is the (real) sideband field amplitude, and Φ is a global phase of the audio field. Note that in these and future expressions, the ADF offset frequency f that the injected amplitude, phase, and responses may depend upon, is implicit.

After interacting with the OPO, the audio field emitted with the squeezing is

$$\mathbf{d}^\uparrow = \mathbf{H}'_0 \mathbf{a}^\uparrow, \quad (5.2)$$

where \mathbf{H}'_0 is the transfer matrix from the ADF injection port to the transmission port of the OPO, derived for our cavity configuration in Section 2.4.1. Because the audio sideband is generated at small detuning relative to the squeezer bandwidth, it can be treated as on-resonance in the OPO cavity.

Injecting a single audio sideband, \mathbf{a}^\uparrow , through the squeezer produces the output field, \mathbf{d}^\uparrow , occupying frequencies above and below the carrier

$$\mathbf{d}^\uparrow = \delta \begin{bmatrix} \alpha e^{-i\Phi} \\ \beta e^{i(2\psi-\Phi)} \end{bmatrix} \quad \mathbf{d}^\downarrow = \delta \begin{bmatrix} \beta e^{-i(2\psi-\Phi)} \\ \alpha e^{i\Phi} \end{bmatrix}, \quad (5.3)$$

with an overall scale factor

$$\delta = a \frac{t_1 t_2}{r_1^2 - 2r_1 \cosh z + 1} \quad (5.4)$$

and relative sideband amplitudes

$$\alpha = 1 - r_1 \cosh z \qquad \beta = r_1 \sinh z \qquad (5.5)$$

that depend on the level of generated squeezing. Here, z is the single-pass squeeze factor through the OPO's internal crystal, ψ is the phase of squeezer pump field, t_1 and t_2 are the transmissivities of mirrors M_1 and M_2 , respectively, and r_1 is the reflectivity of M_1 .

Note that the above expression specifically corresponds to case (a) described in Section 2.4.1 (Fig. 2.4). For case (b), the ADF exiting the OPO is modified to

$$\mathbf{d}^\dagger = a \frac{t_1 t_2 e^{-i\Phi}}{r_1^2 - 2r_1 \cosh z + 1} \begin{bmatrix} \cosh z - r_1 \\ e^{i2\psi} \sinh z \end{bmatrix}. \qquad (5.6)$$

This can also be written as Eq. (5.3) with the modified parameters

$$\alpha = \cosh z - r_1 \qquad \beta = \sinh z. \qquad (5.7)$$

For a linear OPO described in case (c), injecting upper an audio sideband into the OPO produces the transmitted audio field,

$$\mathbf{d}^\dagger = a \frac{t_1 t_2 e^{-i\Phi}}{r_1^2 - 2r_1 \cosh(2z) + 1} \begin{bmatrix} \cosh z(1 - r_1) \\ e^{i2\psi} \sinh z(1 + r_1) \end{bmatrix}. \qquad (5.8)$$

Here, a cavity round-trip involves passing the squeezer crystal twice. We can replace this with an effective single pass through a crystal with double the original squeeze factor and scale z down to $z/2$. In this case,

$$\alpha = (1 - r_1) \cosh\left(\frac{z}{2}\right) \qquad \beta = (1 + r_1) \sinh\left(\frac{z}{2}\right), \qquad (5.9)$$

Beating the transmitted audio field against a local oscillator field \mathbf{v}^\dagger with phase ζ

$$\mathbf{v}^\dagger = \begin{bmatrix} -ie^{i\zeta} & ie^{-i\zeta} \end{bmatrix} / \sqrt{2} \quad (5.10)$$

produces the audio beatnote e^\ddagger in the photodetector readout of

$$e^\ddagger = \mathbf{v}^\dagger \mathbf{d}^\ddagger. \quad (5.11)$$

Consider homodyne detection of the upper audio sideband after injection through the squeezer. This ADF-LO beatnote is given by

$$e^\ddagger = -\frac{i}{\sqrt{2}} \delta (\alpha e^{i\phi} - \beta e^{-i\phi}), \quad (5.12)$$

here expressed as a function of the squeezing angle ϕ . Reducing this equation to a function of ϕ is possible because we use the coherent control scheme (Section 2.6), which stabilizes the relative phase between the audio diagnostic, local oscillator, and squeezer pump fields. As a result, the audio field is phase-stable with the pump field, setting $\psi = \Phi$. Coherent control also maintains the squeeze angle with respect to the pump field as $\phi = \zeta - \psi$. By our conventions, $\phi = 0$ corresponds to squeezing (suppression of quantum shot noise) while $\phi = \pi/2$ corresponds to anti-squeezing (amplification of quantum shot noise).

The ADF-LO beatnote expression contains the factors δ , α , and β which vary by the squeezing amplitude. Calibrating these factors and the overall magnitude of δ enables in-situ measurements of the squeezing parameters and intervening losses using the ADF beatnote.

5.3 CHARACTERISING THE SQUEEZED VACUUM SOURCE

Before probing mechanisms which degrade the observable levels of squeezing, one can first characterise the squeezed vacuum state generated by the source. The audio field can provide an accurate and in-situ probe of the squeezed vacuum source due to its co-propagation and close detuning with the squeezed vacuum field. The level of squeezing generated at the output of the squeezer, and the angle of the squeezed

5.3. CHARACTERISING THE SQUEEZED VACUUM SOURCE

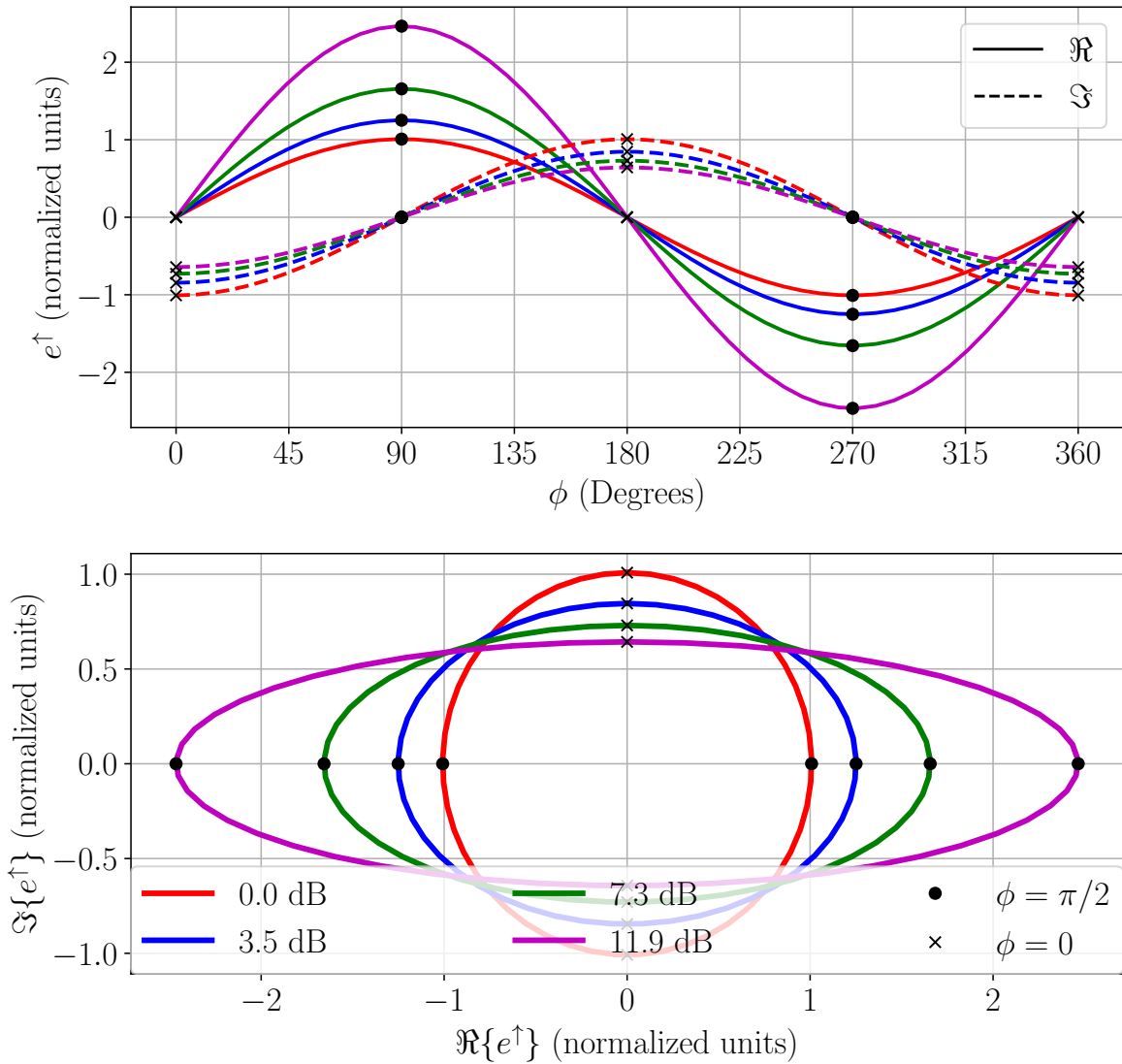


Figure 5.2: Demodulation space spanned by the ADF-LO signal e^\dagger for various squeezing levels. In both plots, the different colors correspond to different levels of generated external squeezing (expressed in dB of noise reduction; see Eq. (5.20)) by an OPO with a reflectivity r_1 of 0.935. The upper plot shows the real (\Re) and imaginary parts (\Im) of the signal as a function of squeezing angle ϕ in degrees. The crosses correspond to squeezing ($\phi = 0$) while the dots correspond to anti-squeezing ($\phi = \pi/2$). The lower shows a parametric plot of the real and imaginary quadratures of demodulated ADF-LO beatnote signal. Here, the dot and cross markers also correspond to the respective major and minor axes of the ellipse. Their ratio can be used to compute the external squeezing level generated by the OPO (Eq. (5.19)). The units of e^\dagger have been chosen to normalize the case of no squeezing, $z = 0$, to a unit circle.

state are key in calculating the maximum possible reduction in quantum noise that the squeezer can offer.

To begin, the ADF-LO beatnote from Eq. (5.12) can be expressed in terms of squeezer parameters as

$$e^\dagger = \frac{\delta}{\sqrt{2}} \left((1 - e^{-z} r_1) \sin \phi - i(1 - e^z r_1) \cos \phi \right), \quad (5.13)$$

Demodulating the beatnote signal into real (I) and imaginary (Q) quadratures, one can parametrically plot the two quadrature signals as a function of squeezing angle ϕ to produce the ellipse shown in Fig. 5.2.

5.3.1 Squeezing Angle

The location of the signal on the ADF-LO ellipse corresponds to the squeezing angle ϕ

$$\phi = -\arctan \left(\frac{1 \Re(e^\dagger)}{G \Im(e^\dagger)} \right), \quad (5.14)$$

where G is the ratio between the largest (anti-squeezing) and smallest (squeezing) magnitude signals on the ellipse

$$G = \frac{\alpha + \beta}{\alpha - \beta} = \frac{1 - r_1 e^{-z}}{1 - r_1 e^z}. \quad (5.15)$$

This quantity can be easily measured experimentally by rotating the squeezing angle ϕ using the control system, while recording the minimum and maximum of the I and Q demodulation magnitude given by $|e^\dagger|$.

For the alternate bowtie OPO (Eq. (5.7)), this modifies to,

$$G = \frac{e^z - r_1}{e^{-z} - r_1}, \quad (5.16)$$

and for a linear OPO (Eq. (5.8)), this is,

$$G = \frac{e^z - r_1}{1 - e^z r_1}. \quad (5.17)$$

5.3.2 *Generated squeezing level*

The level of squeezing generated by the OPO at its output is related to the shape of the ADF-LO beatnote ellipse from the ratio G . Inverting Eq. (5.15) allows one to calculate z from a measurement of G

$$z = \log \left(\frac{G - 1 + \sqrt{(G - 1)^2 + 4Gr_1^2}}{2Gr_1} \right). \quad (5.18)$$

This internal squeezing level z is then used to calculate parameters of fields transmitted through the squeezer, such as δ , α , and β for the propagated audio field.

In terms of the ADF-LO beatnote ratio G , the effective squeeze factor Z , derived in Eq. (2.57) is

$$Z = \log \left(\frac{G - 1 + \sqrt{(G - 1)^2 + 4Gr_1^2}}{2r_1} \right), \quad (5.19)$$

which corresponds to a quantum noise reduction in decibels of

$$N_{\text{dB}} = 10 \log_{10}(e^{-2Z}) = -8.6Z. \quad (5.20)$$

Similar expressions can be derived for the alternate OPO configurations. The transmission ratio G (Eq. (5.15)) of an injected near-carrier field is similar to the “nonlinear gain,” \bar{g} described in Section 2.4.1. The main difference between the two is that G is a ratio of the maximum to minimum quadrature gain in field units while \bar{g} is a ratio of the maximum quadrature power to the “gain-free” $z = 0$ transmission power.

A practical advantage of using the ADF transmission ratio G as opposed to the non-linear gain \bar{g} is that measurements of the latter usually require a significant amount of carrier power. This can lead to pump-depletion and deviation from the

squeezer model. On the other hand, accurate measurements of G do not require a high ADF power, as the ADF-LO beatnote can be made arbitrarily large by increasing the LO power.

The ADF is transmitted from M2 to M1 of the OPO, while the squeezed field is obtained in reflection from M1. As a result, the OPO transforms the coherent ADF and squeezing ellipses differently. This distinction is notable when calculating external squeezing levels based on normalization of the ADF-LO beatnote ellipse. In brief, the ellipses differ because a field transmitting through the OPO can only be maximally squeezed by 6 dB in power (corresponding to a minimum normalized minor axis of $1/2$) unlike the vacuum field reflected from the OPO, which ideally reaches arbitrary squeezing levels (sending the minor axis to 0).

Mathematically, this can be seen by calculating the minor axis magnitude (i.e., with $\phi = 0$) of the ADF-LO beatnote e_s^\uparrow in the limit of high and negligible squeezing, respectively:

$$\lim_{e^z \rightarrow r_1^{-1}} |e_s^\uparrow| = \frac{a}{\sqrt{2}} \frac{t_2}{t_1}, \quad \lim_{e^z \rightarrow 1} |e_s^\uparrow| = \frac{a}{\sqrt{2}} \frac{t_1 t_2}{1 - r_1}. \quad (5.21)$$

The ratio of the two gives the high squeezing limit of the normalized minor axis of Fig. 5.2. As the OPO's nonlinear gain nears the threshold of oscillation ($e^{-Z} \rightarrow 0$, or $e^z \rightarrow r_1^{-1}$), the maximal external squeezing level is reached; here, the normalized ADF minor axis reduces to a minimum value of $1/2$ when $1 - r_1 \approx t_1^2/2$, while the major axis increases continuously as δ diverges.

This indicates that ADF measurements of G are primarily determined by the major axis at high squeezing levels, and are not limited by the ability to resolve the minor axis above noise.

5.3.3 Loss

Optical loss, described in Section 2.7.1, is a dominant source of squeezing degradation. Losses reduce the ADF-LO beatnote magnitude e^\dagger by a factor of $\sqrt{1 - \Lambda}$, where Λ is the total fraction of squeezed vacuum that is replaced with coherent vacuum due to

loss. With Λ , the ADF-LO beatnote from Eq. (5.12) (setting $\phi = 0$) is modified to

$$e^\dagger = -i\delta(\alpha - \beta)\sqrt{1 - \Lambda}. \quad (5.22)$$

Making independent estimates of propagation and readout loss is usually done ex-situ by budgeting optical loss via power measurements throughout the system. Calibrating the ADF signal to a known or estimated level of frequency independent loss Λ and a known level of squeezing, corresponding to fixed α and β , allows us to monitor losses as they drift over time. Using α' , β' and δ' to account for drifts in the generated squeezing level over time, the loss at a later time Λ' is

$$\sqrt{1 - \Lambda'} = \sqrt{1 - \Lambda} \frac{\delta}{\delta'} \frac{\alpha - \beta}{\alpha' - \beta'}. \quad (5.23)$$

5.3.4 Phase Noise

In addition to loss, phase noise (Section 2.7.2) is another important mechanism of squeezing degradation.

The ADF provides a convenient way to experimentally measure squeezer phase noise, by way of measuring small angle fluctuations in the squeezing ellipse described by Eq. (5.13). Measuring angle fluctuations provides an estimate of the phase noise along the squeezing path. By setting the quadrature angle to squeezing ($\phi = 0$), Eq. (5.14) can be expanded in the limit of small angle fluctuations $\Delta\phi \ll 1$ to obtain an expression for the RMS squeezer phase noise,

$$\Delta\phi = \frac{1}{G} \sqrt{\left\langle \left(\frac{\Re(e^\dagger)}{\Im(e^\dagger)} \right)^2 \right\rangle}. \quad (5.24)$$

Experimentally, this would involve rotating the ADF-LO beatnote signal completely into one demodulation quadrature, and measuring the RMS fluctuations in the orthogonal quadrature.

In the above section, we have shown that ADF provides a rapid and convenient way of making accurate in-situ measurements of the squeezer and time-varying system

losses. Traditional methods of characterizing the squeezed vacuum source are based on injecting a strong field at the carrier frequency through the squeezer, which cannot be used during regular squeezing operation, or using photodetector quantum noise spectra, which requires long averaging times [42]. Additionally, as loss and phase noise both effectively lower the levels of measured squeezing and anti-squeezing, it is hard to separate those effects using quantum noise spectra alone.

5.4 CHARACTERIZING OPTICAL SYSTEMS

After characterizing the squeezed state source parameters, the audio diagnostic field can probe how squeezed states rotate, dephase, and mix with vacuum via losses as they propagate through an optical system. In Section 2.8, we introduced the idea of describing an optical system by a transfer matrix, \mathbb{H}_R , in the two photon picture. Gravitational-wave interferometers are the key target of study using the ADF technique, and they have several properties that our study of squeezing must accommodate. First, interferometers typically read with a fixed local oscillator angle, $\zeta \approx 0$ ¹, to measure phase shifts of the light in their arms. Second, because of their high arm power, they affect optical states through quantum radiation pressure noise, which applies a frequency-dependent parametric gain to the squeezed state or fields incident on the interferometer.

With a model of the optical system being probed, ADF measurements can be used to estimate model parameters. However, fully characterizing an arbitrary optical system in a model independent way requires both readout quadratures ($\zeta = 0, \pi/2$) and both the upper and lower ADF signal injections to measure all of the terms of \mathbb{H}_R . Thus, one cannot fully characterize the optical response of interferometers due to the fixed readout quadrature; however, for a known local oscillator angle, ADF measurements at squeezing and anti-squeezing can be used to compute the quadrature observables of the optical system, m_q, m_p , defined in Eq. (2.89). Using Eqs. (2.90) to (2.92), these observables can be used to measure all the quantities that

¹The local oscillator angle of an interferometer using DC homodyne readout is determined by the amount of excess light at the dark fringe of the interferometer. This is discussed further in Section 6.4.3

are relevant to squeezing. To calculate the ADF-LO beatnote, the previously defined fields must first be expressed in the quadrature basis.

$$\vec{v}^\dagger = \mathbf{v}^\dagger \mathbf{A}^{-1} = \begin{bmatrix} \sin(\zeta) & \cos(\zeta) \end{bmatrix}, \quad (5.25)$$

The ADF is driven and demodulated at a specific frequency f , and can measure m_p and m_q at $\Omega = 2\pi f$. Propagating the ADF through an optical system \mathbb{H}_R modifies the ADF-LO beatnote from Eq. (5.12) to

$$e'^{\uparrow\downarrow} = \vec{v}^\dagger \mathbb{H}_R \mathbf{A} \mathbf{d}^{\uparrow\downarrow} \quad (5.26)$$

in the quadrature basis. The following calculations assume a constant local oscillator angle $\zeta = 0$.

The audio beatnote can be then calculated at squeezing ($\phi = 0$),

$$e_s'^{\uparrow} = \frac{\delta}{\sqrt{2}}(m_q(\alpha + \beta) - im_p(\alpha - \beta)) \quad (5.27)$$

$$e_s'^{\downarrow} = \frac{\delta}{\sqrt{2}}(m_q(\alpha + \beta) + im_p(\alpha - \beta)) \quad (5.28)$$

and anti-squeezing ($\phi = \pi/2$),

$$e_a'^{\uparrow} = \frac{\delta}{\sqrt{2}}(m_p(\alpha + \beta) + im_q(\alpha - \beta)) \quad (5.29)$$

$$e_a'^{\downarrow} = \frac{\delta}{\sqrt{2}}(m_p(\alpha + \beta) - im_q(\alpha - \beta)). \quad (5.30)$$

Rearranging the above equations, the squeezing parameters m_p and m_q can be obtained in terms of the measured ADF-LO beatnote,

$$m_p = \frac{e_a'^{\downarrow} + e_a'^{\uparrow}}{\sqrt{2}\delta(\alpha + \beta)} = -\frac{e_s'^{\uparrow} - e_s'^{\downarrow}}{\sqrt{2}\delta i(\alpha - \beta)}. \quad (5.31)$$

$$m_q = \frac{e_s'^{\uparrow} + e_s'^{\downarrow}}{\sqrt{2}\delta(\alpha + \beta)} = \frac{e_a'^{\uparrow} - e_a'^{\downarrow}}{\sqrt{2}\delta i(\alpha - \beta)}. \quad (5.32)$$

After passing the ADF through an unknown optical system, the ADF is modified and

the ADF-LO beatnote ellipse (Sec. Section 5.3) measurement of the level of generated squeezing becomes biased. Instead, these modified ADF-LO beatnote signals e'^{\updownarrow} can be combined to make an unbiased measurement of G that is applicable to any system using

$$G = \frac{\alpha + \beta}{\alpha - \beta} = -i \frac{e_a'^{\uparrow} + e_a'^{\downarrow}}{e_s'^{\uparrow} - e_s'^{\downarrow}} = i \frac{e_s'^{\uparrow} + e_s'^{\downarrow}}{e_a'^{\uparrow} - e_a'^{\downarrow}}, \quad (5.33)$$

which can then be put into Eq. (5.19) to calculate the generated squeezing level. This generalizes Eq. (5.15) for systems that may affect sideband balancing from nonlinear interactions, like radiation pressure.

It is worthwhile here to point out the significance of the “symmetrization” implied by the sums and differences of Eq. (5.31) and Eq. (5.32). The ADF, as proposed, is created by injecting a single upper or lower sideband into the OPO. At cost of increased complexity, one could alternatively inject balanced sidebands with relative phases chosen to create pure amplitude or phase quadrature modulations in the coherent field. Such injections would more directly measure m_p, m_q in two separate measurements. The sums and differences above achieve the same goal, but avoid the experimental complexity of stably creating and phasing two audio field frequencies into a signal AOM.

Normalized beatnote measurements. The audio field can serve as an intermediary diagnostic for a single optical system embedded in a larger composite system. The response of an individual system can be isolated by normalizing the ADF-LO beatnote measurements between experimental configurations where the ADF does, or does not, pass through the optical system \mathbb{H}_R using

$$\bar{e}^{\updownarrow} = \frac{\vec{v}^{\dagger} \mathbb{H}_R \mathbf{A} \mathbf{d}^{\updownarrow}}{\vec{v}^{\dagger} \mathbf{A} \mathbf{d}^{\updownarrow} \sqrt{\eta_{\text{rel}}}}. \quad (5.34)$$

Realistically, when the ADF is not passing through the optical system, it is redirected to a diagnostic readout that has a simple response including only the relative detection efficiency η_{rel} . That simple response is indicated in the denominator of Eq. (5.34). The normalized ADF-LO beatnote is calibrated to be unity on the diagnostic reference. The quadrature observables can then be calculated from the normalized ADF

measurements as

$$\frac{m_p}{\sqrt{\eta_{\text{rel}}}} = \frac{\bar{e}_s^\uparrow + \bar{e}_s^\downarrow}{2} = \frac{\bar{e}_a^\uparrow + \bar{e}_a^\downarrow}{2} \quad (5.35)$$

$$\frac{m_q}{\sqrt{\eta_{\text{rel}}}} = \frac{(\bar{e}_s^\uparrow - \bar{e}_s^\downarrow)}{2i} \left(\frac{\alpha - \beta}{\alpha + \beta} \right) = \frac{(\bar{e}_a^\uparrow - \bar{e}_a^\downarrow)}{2i} \left(\frac{\alpha + \beta}{\alpha - \beta} \right). \quad (5.36)$$

Eq. (5.33) can also be re-written in terms of the normalized signals and used similarly to measure generated squeezing levels

$$G = \sqrt{\frac{(\bar{e}_s^\uparrow - \bar{e}_s^\downarrow)}{(\bar{e}_a^\uparrow - \bar{e}_a^\downarrow)}}. \quad (5.37)$$

However, when using a reference readout, the squeezer characterization of Section 5.3 is convenient and sufficient. The above expressions are useful to check if the squeezing levels are changing between reference measurements and optical system measurements.

Using the normalized ADF-LO signal is advantageous because it simplifies calibrations. For instance, this normalization cancels scale factors from the beatnote signal, such as the transmitted audio field amplitude δ , or the propagation and readout losses that constitute Λ . While cancelling these factors also allows minute duration drifts (i.e. drifts over the ADF scan) in generated squeezing levels δ and system losses Λ to influence the beatnote measurement, these drifts are expected to be small. More importantly, the normalized beatnote signal is practical because it factors out frequency-dependent phase delays that the ADF picks up for technical reasons, from e.g. propagation delay and electronics. For our audio field measurements, we measure the normalized beatnote signal to remove such phase delays from our measurements of the system response.

Note that the above method is only valid for measurements taken at squeezing and anti-squeezing. Operationally, however, sometimes it is difficult to exactly know the squeezing angle, e.g. due to squeezing rotation from detuned cavities in an interferometer. In such a situation, rather than estimating m_q and m_p , it is usually more practical to treat the squeezing angle as an independent parameter in models

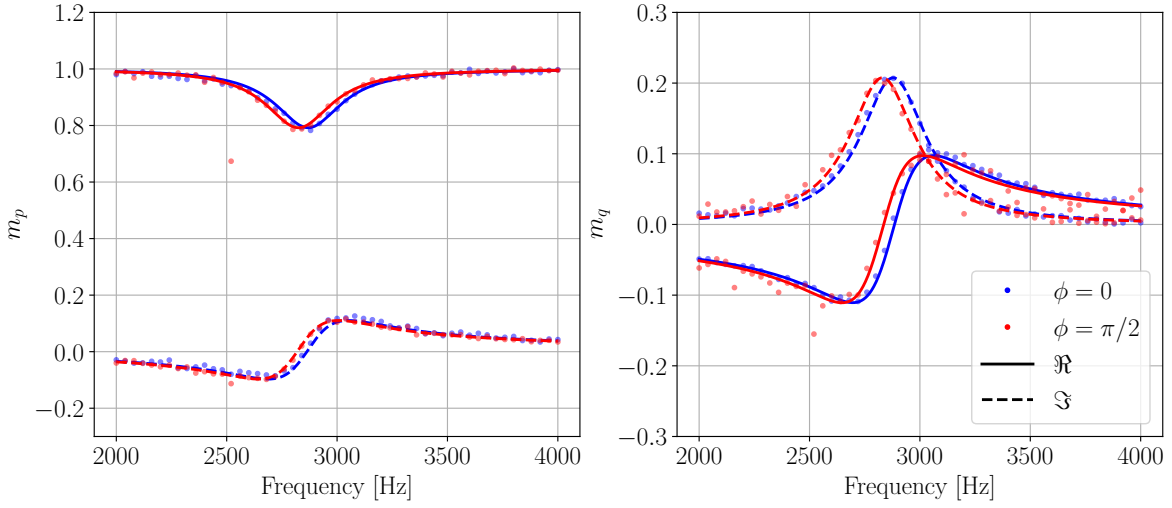


Figure 5.3: Characterization of a 16-m filter cavity using a sweep of the audio diagnostic field. Quadrature observables m_p and m_q are calculated from measurements of the normalized ADF-LO beatnote \bar{e}^{\ddagger} at two different squeezing angles, squeezing ($\phi = 0$, blue) and anti-squeezing ($\phi = \pi/2$, red), using Eqs. (5.35) and (5.36). The normalized beatnote data is compared to the filter cavity model from Eq. (3.5). The plot presents the experimental data, demodulated into real (solid) and imaginary (dashed) parts, along with the model curves fit to the data. The generated squeezing level measured by demodulating the ADF after the filter cavity (Eq. (5.37)) was verified against the squeezing level measured by demodulating the ADF directly after the squeezer (Eq. (5.19)). The fit parameters are given in Table 5.1.

of the ADF-LO beatnote (Eq. (5.26)).

The following analysis focuses on two specific examples; experimental measurements of a 16 m filter cavity, and a simplified theoretical model of a gravitational-wave interferometer with frequency-dependent squeezing.

5.4.1 Filter Cavity

We use the filter cavity model described in Section 3.1, modifying the sideband reflectivity to include a simplified expression for mode matching efficiency Υ_{fc} ,

$$r'_{fc} = \Upsilon_{fc} r_{fc} + (1 - \Upsilon_{fc}) r_{fc} \quad (5.38)$$

<i>Parameter</i>	Value
	<i>Independently Measured</i>
OPO M_1 Reflectivity (r_1^2)	0.875
OPO M_2 Reflectivity (r_2^2)	0.9985
Filter cavity length (L_{fc})	16 m
Filter cavity input mirror transmissivity (T_{in})	63.7 ppm
	<i>Estimated using the ADF</i>
Generated Squeezing in OPO	5.5 dB
Filter cavity round-trip loss (Λ)	181 ppm
Filter cavity mode matching (Υ_{fc})	0.80
Filter cavity detuning ($\Delta\omega_{fc}/2\pi$)	2879 Hz ($\phi = 0$) 2830 Hz ($\phi = \pi/2$)

Table 5.1: Experimentally determined parameters of the OPO and 16 m filter cavity used for frequency-dependent squeezing.

In the experimental results that follow, these quantities are evaluated at $\Omega = 2\pi f$, where the ADF is generated at frequency f . Combined with Eqs. (5.35) and (5.36), our analysis connects measurements of the normalized ADF-LO beatnote $\bar{e}^{\dagger\ddagger}$ to both the optical response of the filter cavity \mathbb{H}_{fc} , and squeezed state propagation through the cavity.

Fig. 5.3 shows the use of audio field diagnostics of our 16-m filter cavity, and its preparation of a frequency-dependent squeezed state. To characterize the filter cavity at 3 kHz detuning, the ADF frequency f was swept from 2 kHz to 4 kHz. m_p and m_q are calculated from the normalized ADF-LO beatnote signals $\bar{e}^{\dagger\ddagger}$ (Eq. (5.34)), obtained by balanced homodyne detection of the audio field after passage through the 16-m filter cavity. To normalize the ADF sweep and isolate the filter cavity response, the audio sweep was performed with the filter cavity locked near-resonance with the squeezed field, and then again with the cavity off-resonance; the on- and off-resonance responses were divided to yield the normalized beatnote signals $\bar{e}^{\dagger\ddagger}$. m_p and m_q were then calculated from measurements of $\bar{e}^{\dagger\ddagger}$ using Eqs. (5.35) and (5.36).

Table 5.1 summarizes the filter cavity parameters extracted from fits to these

audio sweep measurements. Data obtained from the normalized LO beatnote were converted to m_p and m_q using Eqs. (5.35) and (5.36) and fit to the filter cavity model described in Eq. (3.5) in order to estimate the cavity detuning $\Delta\omega_{fc}$, round trip loss Λ , and mode-matching Υ_{fc} with the squeezed vacuum field. The squeezing level was also measured using the normalized ADF-LO beatnote \bar{e}^\dagger (Eq. (5.37)). The precise filter cavity detuning has percent-level variations between squeezing and anti-squeezing, due to technical challenges in stabilizing the filter cavity length at kilohertz detunings (cite RLF). Relevant parameters measured independently without the audio field include the filter cavity's input mirror transmissivity T_{in} , and the reflectivity of mirror M_1 in the OPO r_1 .

In Fig. 5.4, the squeezing degradation is calculated from the m_p and m_q data using Eqs. (2.90) to (2.92) to determine the frequency-dependent squeezing efficiency $\eta\Gamma$, rotation θ , and dephasing Ξ introduced by the filter cavity. From this plot it is easy to see that the high round trip loss in the filter cavity limits the squeezing rotation to less than 10° while adding considerable dephasing and squeezing loss. As these specific degradation mechanisms affect the frequency-dependent squeezing spectra in degenerate ways, it is difficult to distinguish between them using photodetector noise spectrum measurements.

5.4.2 Interferometer

We now consider the response of an ideal, Fabry-Perot interferometer, with a filter cavity for frequency dependent squeezing. The following calculations assume on-resonance operation in a lossless interferometer, which has no mode mismatch with the injected squeezed beam. Such an interferometer can be represented by the following two-photon matrix,

$$\mathbb{H}_{\text{IFO}} \simeq \begin{bmatrix} \tau & 0 \\ -\mathcal{K} & \tau \end{bmatrix} \quad (5.39)$$

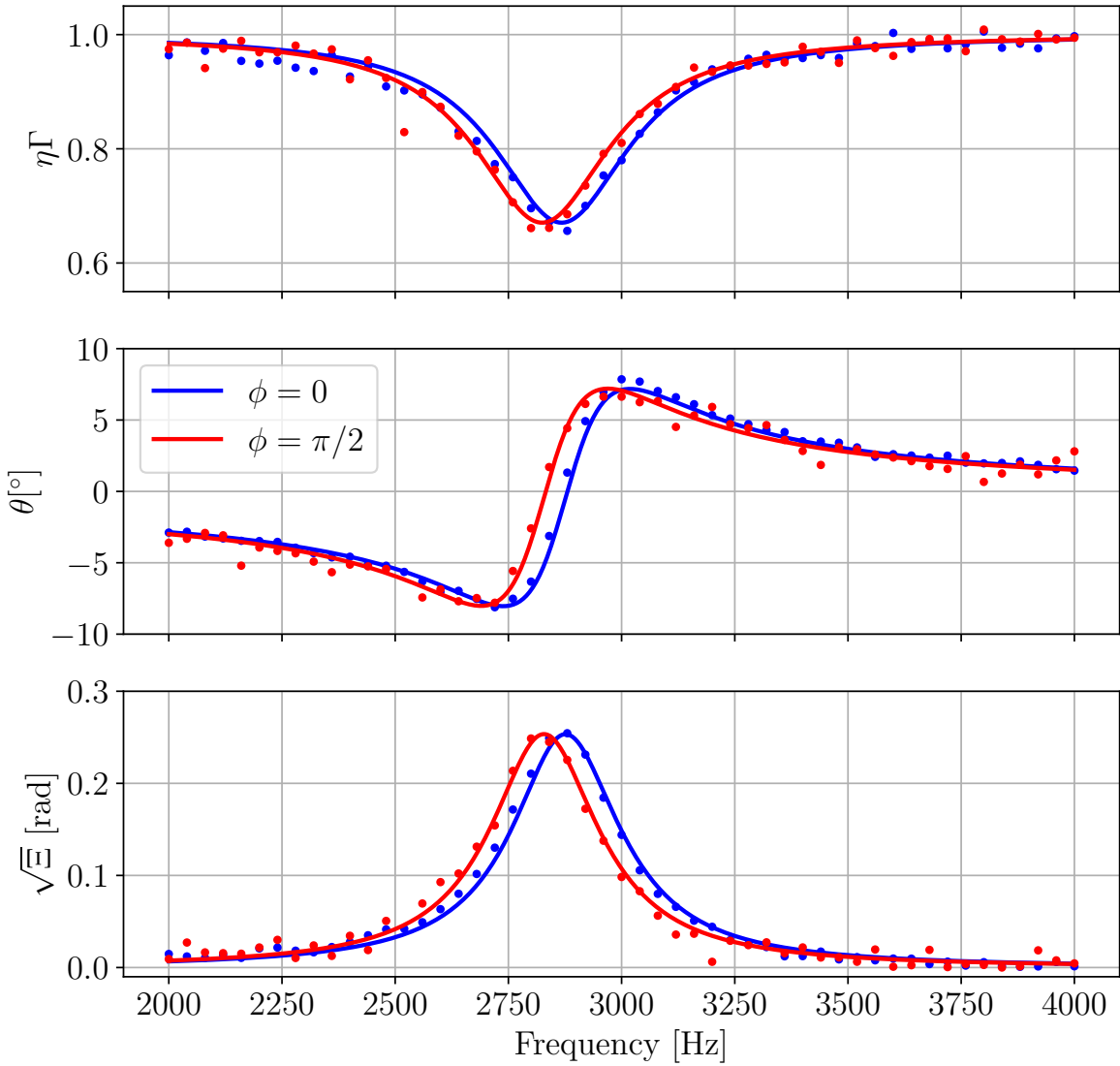


Figure 5.4: Filter cavity loss, rotation, and dephasing calculated from m_p and m_q (from Fig. 5.3) using Eqs. (2.90) and (2.91) and Eq. (2.92) plotted along with model curves (solid). The top plot corresponds to the squeezing efficiency η multiplied by the noise gain Γ which is 1 for the filter cavity. The middle plot shows the squeezing rotation θ in degrees. The bottom plot contains the square root of the frequency-dependent dephasing Ξ . $\sqrt{\Xi}$ has a similar effect on squeezing as phase noise $\Delta\phi$ with the same RMS value, and therefore it has been represented in units of radians. Blue corresponds to squeezing while red corresponds to anti-squeezing.

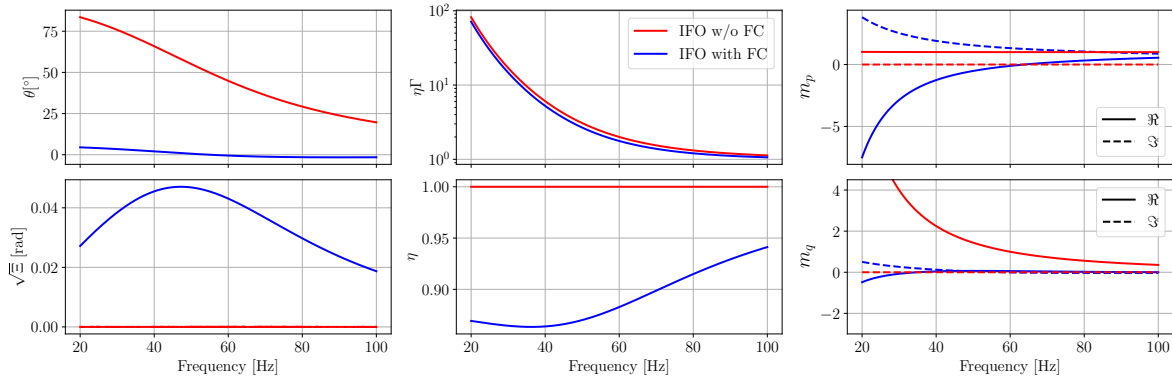


Figure 5.5: Simulation of quadrature observables and squeezing degradation metrics for an ideal interferometer with (blue) and without (red) a filter cavity. The left curves correspond to the rotation θ and dephasing Ξ ($\sqrt{\Xi}$ has been represented as equivalent RMS phase noise in radians) of the two configurations. The center plots contain the squeezing efficiency η along with the optomechanical gain from the interferometer Γ . For an interferometer with losses, the efficiency and gain cannot be measured independently. However, models of the frequency dependence of these effects would allow us to discriminate between and make independent estimates of the two quantities. Following this, we can also back out the loss of the inteferometer-filter cavity combination by normalizing to the gain, Γ , fit from the measured interferometer. The right plots show the quadrature observables m_p , m_q which have been generated using Eq. (5.43). Eqs. (2.90) and (2.92) are used to convert the quadrature observables into squeezing metrics. It is assumed that the interferometer reaches the standard quantum limit at a frequency of $\Omega_{\text{SQL}} = 2\pi \cdot 60$ Hz. Simulation parameters, representing design specifications for frequency-dependent squeezing in LIGO [93], assume round trip filter cavity losses of 60 ppm, input mirror transmissivity of 1200 ppm, cavity detuning of 43 Hz, and mode matching efficiency of 0.99.

where τ is related to the signal bandwidth γ_A of the interferometer

$$\tau \simeq \frac{\gamma_A - i\Omega}{\gamma_A + i\Omega}, \quad (5.40)$$

and \mathcal{K} is the interaction strength of the interferometer, defined in Eq. (1.15). The transfer matrix for propagation through a filter cavity followed by an ideal interferometer is

$$\mathbb{H}_R = \mathbb{H}_{\text{IFO}} \mathbb{H}_{\text{fc}}, \quad (5.41)$$

from which Eq. (2.89) yields the quadrature observables

$$m_p = \frac{\tau}{2}(r_+ + r_-) - \frac{i\mathcal{K}}{2}(r_+ - r_-) \quad (5.42)$$

$$m_q = -\frac{i\tau}{2}(r_+ - r_-) - \frac{\mathcal{K}}{2}(r_+ + r_-). \quad (5.43)$$

Fig. 5.5 contains simulation results of quadrature observables and squeezing metrics for an inteferometer with and without a filter cavity. We observe that the interferometer (red curve), through its optomechanics, produces a squeezing rotation of around 90° at low frequencies, which is equivalent to rotating squeezing into anti-squeezing. The addition of an optimally detuned filter cavity (blue curve) seeks to reverse this rotation (Chapter 4). However, the filter cavity also introduces loss and dephasing, which can degrade the squeezing measured at the readout. The parameters of the simulation have been chosen to be representative of the frequency-dependent squeezing upgrade to LIGO [93]. The filter cavity has been designed to optimize squeezing rotation while keeping squeezing degradation to a minimum. The ADF can help diagnose these effects, which would be difficult to measure otherwise, and consequently inform operational choices for filter cavities in interferometers.

ADF measurements of the interferometer alone, without the filter cavity, also provide valuable insight into how squeezing degrades in the interferometer's various coupled cavities, which itself is not precisely understood due to lack of intermediary diagnostics in the system. For eg. we can better constrain degradation arising from losses and mode-mismatch of the signal extraction and arm cavities. With and without a filter cavity, the ADF directly measures the interferometer noise gain and

efficiency $\eta\Gamma$. This parameter can be used to determine the true local oscillator angle of the readout by its effect on the noise gain, as was done using an involved squeezing measurement [76]. We anticipate the ADF can provide additional diagnostics while commissioning a balanced homodyne detection upgrade in gravitational-wave interferometers. Such an upgrade enables freely changing the local oscillator angle, but only implicitly knowing the angle from a control system error point and the calibrated signal sensitivity. The noise gain is useful to know precisely, as it scales the magnitude of certain classical noises in the interferometer, such as backscatter.

Time-resolved fluctuations. In addition to jointly characterizing the interferometer and filter cavity, the ADF also enables a time-resolved view of how large-RMS interferometer motions will degrade squeezing. In particular, insufficiently controlled motions of the interferometer and filter cavities will cause drifting squeezing rotations inside the resonance of the drifting cavities, leading to frequency-dependent phase noise. This form of degradation is difficult to resolve using squeezing alone, because squeezing spectrum measurements require integrating for longer than drift time-scales and at multiple squeezing levels. The ADF can probe for changing squeezed state rotation at specific frequencies.

The first such example is using the ADF above the interferometer arm bandwidth $\gamma_A \approx 2\pi \cdot 430$ Hz (for LIGO) but within the signal cavity bandwidth $\gamma_S \approx 2\pi \cdot 80$ kHz. At these frequencies, the signal extraction cavity may have residual motion as its length L_s drifts, which causes the squeezed state to rotate. The frequency dependence of that rotation, given length fluctuations, is given by Eq. (69) of [76], which can be expressed

$$\frac{d\theta_{\text{IFO}}(\Omega)}{dL_s} \approx \frac{-8k}{T_s} \left(\frac{\gamma_S^2}{\gamma_S^2 + \Omega^2} - \frac{\gamma_A^2}{\gamma_A^2 + \Omega^2} \right), \quad (5.44)$$

where k is the wavenumber of the carrier light. Similarly, length changes of the filter cavity will cause its rotation to change. For a lossless filter cavity at its optimal detuning, the sensitivity of the squeezed state rotation to length changes is given by

the derivative of Eq. (18) in [91], which can be written

$$\frac{d\theta_{\text{FC}}(\Omega)}{dL_{\text{fc}}} \approx \frac{-8k}{T_{\text{fc}}} \left(\frac{\gamma_{\text{fc}}^2 \Omega^2}{\Omega^4 + 4\gamma_{\text{fc}}^4} \right) \leq \frac{-4k}{T_{\text{fc}}}. \quad (5.45)$$

Here γ_{fc} is the HWHM bandwidth of the filter cavity, optimal at $\gamma_{\text{fc}} \approx \Omega_{\text{SQL}}/\sqrt{2}$, and the cavity is detuned by its bandwidth γ_{fc} to cause a 90° rotation. This expression indicates the high sensitivity of the detuned filter cavity to length noise, due to its small input transmissivity required to create its small bandwidth.

For the interferometer phase drift measurement, where $\gamma_{\text{A}} < \Omega < \gamma_{\text{S}}$, the normalized beatnote measurement can be used. There, the interferometer should not be changing the sideband balancing, so $\bar{e}^\uparrow = \bar{e}^\downarrow$. Under that condition, it is possible to measure the fluctuations in the effective squeezing angle caused by these changes using the methods described in Sec. Section 5.3.

For a lossy, detuned filter cavity with or without the interferometer in series, $\bar{e}^\uparrow \neq \bar{e}^\downarrow$, so the methods of Section 5.4 are required to calculate θ . This poses a problem for time resolved measurements, as both the upper and lower ADF cannot be simultaneously driven. In this case, the effects of length fluctuations of a specific system model on the ADF is required to relate independent upper and lower ADF measurements along with measurements during squeezing and anti-squeezing.

CHAPTER

6

FREQUENCY DEPENDENT SQUEEZING IN LIGO

As part of the A+ upgrade to Advanced LIGO, frequency dependent squeezing was deployed for the first time in a working gravitational wave interferometer during the observing run O4. This chapter describes the implementation of frequency dependent squeezing at the LIGO Hanford (H1) detector.

6.1 EXPERIMENTAL SETUP

Fig. 6.1 shows the experimental implementation of frequency-dependent squeezing via a filter cavity in LIGO, with an overview of the full interferometer. The entire squeezing setup consists of in-air optics on two tables; SQZT0 and SQZT7, and in-vacuum optics in two seismically isolated vacuum chambers; HAM7 and HAM8¹. The control scheme for frequency dependent squeezing is described in Section 6.3. Measured and inferred values of experimental parameters are listed in Table 6.1

The squeezer pump light and auxiliary control fields are generated on SQZT0, which houses the 1064 nm squeezer pump laser. Similar to the setup described in Section 3.3.1, the pump beam is generated using second harmonic generation, which is also used to produce a 532 nm beam for filter cavity control. All the beams from SQZT0 are carried to the in-vacuum optics in HAM7 via optical fiber. The squeezed

¹HAM = Horizontal Access Module

6.1. EXPERIMENTAL SETUP

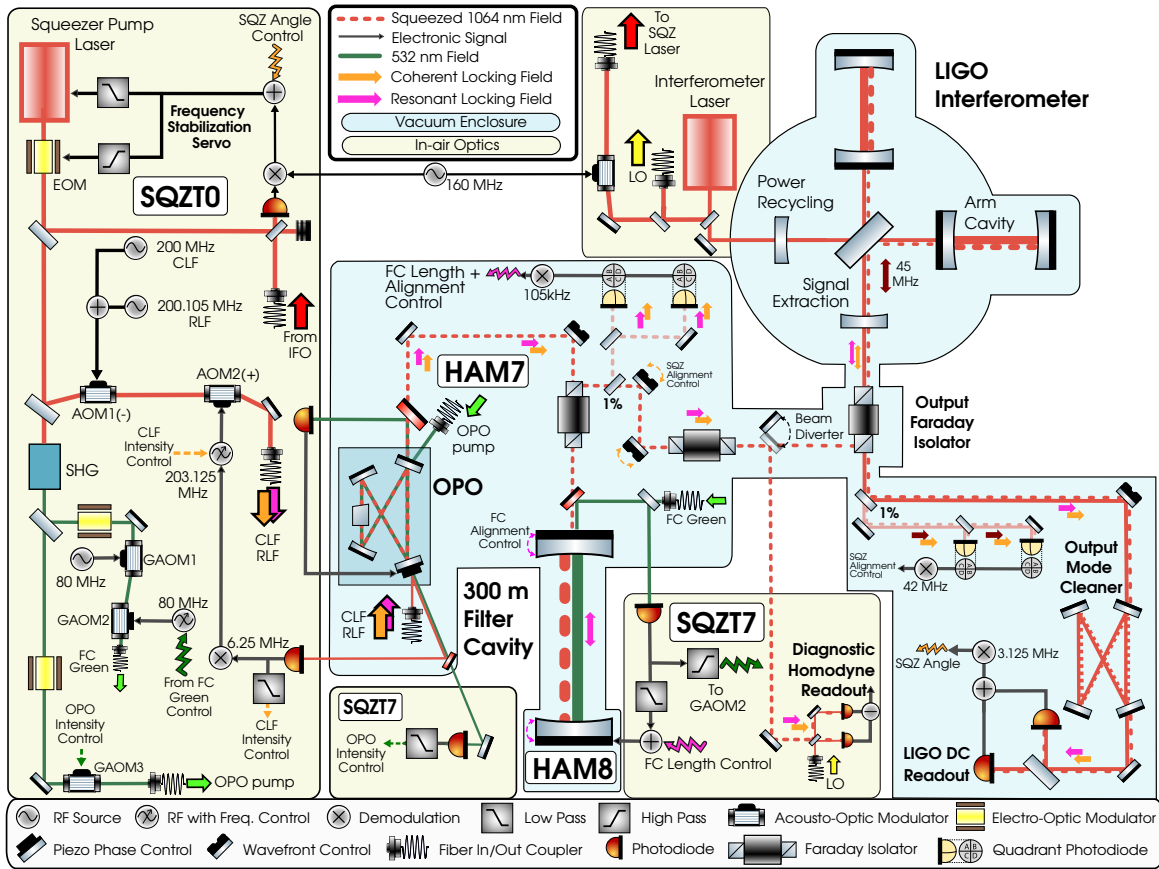


Figure 6.1: Detailed optical and controls layout of frequency-dependent squeezing instrumentation in the LIGO detectors.

vacuum source is a sub-threshold bowtie OPO which is nearly identical to the one used in O3 [42]. However, with the expectation that backaction could be mitigated by frequency-dependent squeezing injection, the OPO cavity finesse and green pump optics were upgraded to generate higher squeezing levels in preparation for O4.

Squeezed vacuum then undergoes a frequency-dependent phase shift upon reflection from a 300 m, in-vacuum, optical filter cavity, producing a frequency-dependent rotation of the squeezed state for frequencies within the cavity resonance. The filter cavity has a full-width-half-maximum linewidth of ~ 74 Hz and a detuning from carrier of ~ 35 Hz to impart a squeezing rotation that counters the opto-mechanical response of the interferometer, while minimizing squeezing loss [93] (Chapter 4). Both cavity mirrors use triple pendulum suspensions [105] mounted on isolated in-vacuum optical tables [97] for vibration isolation, while relay optics use either single or double suspensions [106]. Measured filter cavity parameters are presented and discussed in Section 6.4.1. The input mirror is located in HAM7 while the end mirror is located in HAM8, with a 300 m vacuum tube connecting the two. The system is engineered [93] to suppress noise from stray interferometer light that is misdirected along the squeezing injection path, and subsequently scattered back to the interferometer readout, modulated by vibrations of the filter cavity and squeezer optics (see Appendix D). Along with extremely high levels of isolation, three custom high-efficiency Faraday isolators were installed in preparation for O4 [107], decreasing total loss, which limited squeezing during O3 [42, 76], and improving stray light isolation.

After reflection from the filter cavity, the frequency dependent squeezed vacuum is sent through a relay tube into the main interferometer's vacuum enclosure where it is injected via the interferometer's output Faraday isolator. Before the relay tube, there is a switchable beam diverter that can be used to direct the squeezed vacuum onto a diagnostic balanced homodyne detector on SQZT7 via a periscope. The reflected 532 nm beams from the OPO and the filter cavity are also sent to SQZT7 via periscopes for sensing and control.

In addition to optical losses, mode mismatch between the squeezer and interferometer beams also limited squeezing efficiency in O3 [76]. Piezo-deformable mirrors [108] were installed as relay optics on the squeezing propagation path to

improve mode matching between the squeezer, interferometer, and filter cavity. A thermally deformable mirror [109] was installed on the interferometer’s output path to optimize the mode-matching between the interferometer and output mode cleaner (OMC).

6.2 FREQUENCY DEPENDENT SQUEEZING AT H1

We present data from the H1 LIGO detector during the commissioning period preceding O4 (February 2023). For this data, the detector operated with approximately 360–380 kW of circulating power in its interferometer arm cavities. The strain noise amplitude spectral density of the detector is shown in Fig. 6.2.

With frequency-dependent squeezing, we achieved a quantum enhancement of the detectors that simultaneously reduced both shot noise and quantum radiation pressure noise. Compared to the measured detector noise without squeezing (Fig. 6.2, black), and the detector noise with frequency-independent squeezing (Fig. 6.2, green), frequency-dependent squeezing provided broadband improvement (Fig. 6.2, purple), with measurable reductions in the total detector noise from several kHz down to frequencies as low as 60 Hz.

In the shot-noise-limited region around 1 kHz, both detectors measured higher squeeze levels than O3, due to the higher generated squeezing levels and reduced cumulative optical losses along the squeezing path. In the H1 detector, squeezing reduced the shot noise amplitude by a factor of 1.6 (4.0 dB) near 1 kHz. Since shot noise is the largest noise source in the kHz frequency band, the total interferometer noise was similarly reduced.

While these kHz noise improvements are essential to study the post-merger physics of binary neutron stars [110, 111], the injection of frequency-independent squeezing significantly degraded detector performance around 100 Hz, which is detrimental to standard metrics of astrophysical sensitivity. For gravitational-wave detectors, a standard figure-of-merit is the distance to which a binary neutron star (BNS) or binary black hole (BBH) merger can be detected [112]²; such metrics heavily

²Calculation of the BNS range uses a standard $1.4M_{\odot}$ template for the coalescence of two $1.4M_{\odot}$

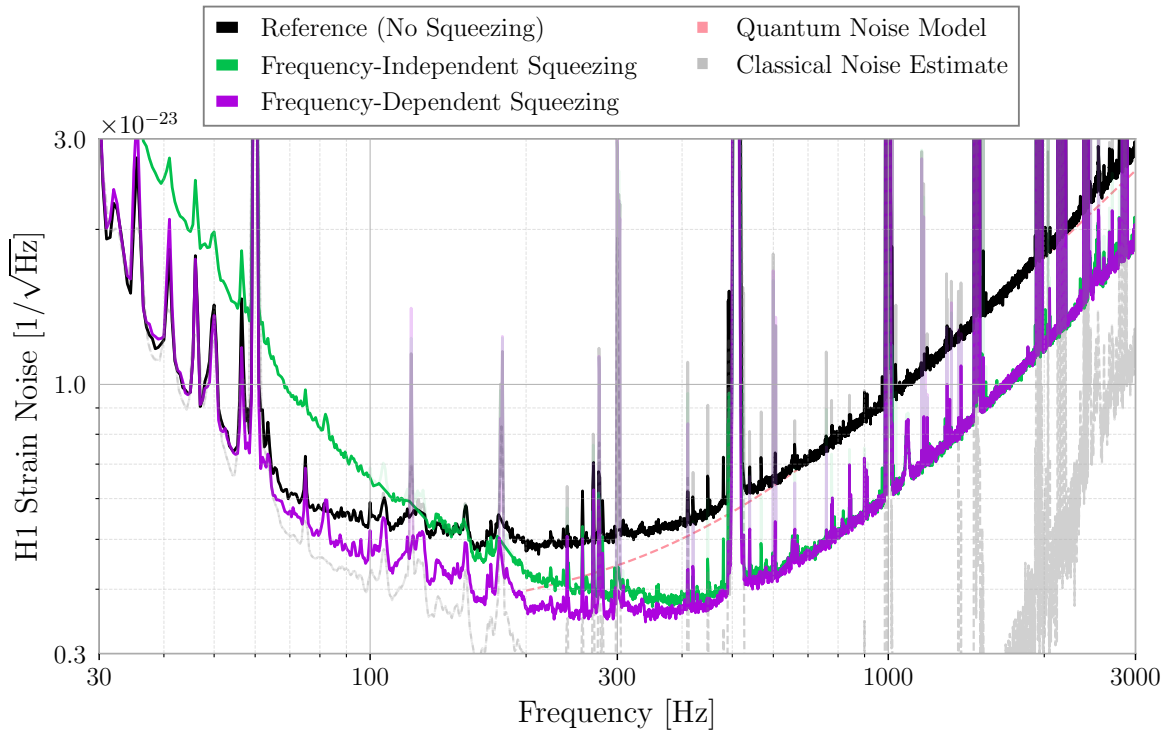


Figure 6.2: Observation of frequency-dependent squeezing in LIGO. The top and bottom plots show strain noise spectra of the LIGO Hanford (H1) detector in amplitude spectral density units, measured in the commissioning period leading up the fourth observing run, O4. Reference measurements of detector noise spectra without squeezing are shown in black, and measured with the squeezed beam diverted away from the detector. Without squeezing, the classical noise estimate (gray), i.e., the sum of non-quantum noises, is obtained by subtracting the calculated quantum noise (red) from the measured detector noise (black). Frequency-independent squeezing spectra (green) are measured with the squeezed beam injected and the filter cavity end mirror misaligned, to have the input mirror act as a high-reflector. With frequency-independent squeezing, shot noise reduction of 4.0 dB is observed around 1 kHz, alongside the corresponding increase in quantum radiation pressure noise below a few hundred Hz. Frequency-dependent squeezing spectra (purple) are obtained by locking the filter cavity near-resonance, demonstrating the broadband reduction of detector quantum noise. In addition to the squeezed shot noise reduction, the filter cavity reduces total detector noise by 1-2 dB from 60-100 Hz, with quantum enhancement visible from kHz down to tens of Hz.

6.2. FREQUENCY DEPENDENT SQUEEZING AT H1

Table 6.1: Detailed summary of interferometer and squeezer parameters at LIGO Hanford (H1). The observed squeezed shot noise reduction at 1 kHz is used to infer a lower bound on the total squeezing throughput. Entries marked by an asterisk were determined by comparing measured squeezing data to a quantum noise model.

Interferometer parameters	
Arm power	360–380 kW*
SEC detuning (round-trip phase)	0.54°
Readout angle	-27°
Readout efficiency	
Optical throughput (SEC to OMC)	97.5%
OMC transmission	95.7%
Photodiode quantum efficiency	98 %
Total readout efficiency	91%
Squeezing parameters	
Generated squeezing	16.9 dB
Measured squeezing	-4.0 dB
Measured anti-squeezing	14.4 dB
OPO input mirror (M_1) reflectivity r_1^2	0.935
OPO throughput	98.5%
Injection efficiency (OPO to SEC)	91.6%
CLF Frequency	3.125 MHz
RLF Frequency	3.020 MHz
Phase noise (RMS)	< 20 mrad
Total expected throughput	84%
Inferred throughput	> 63%
Filter cavity parameters	
Filter cavity length	297.77 m
Filter cavity detuning	-36 Hz*
Filter cavity full-linewidth	74 Hz
Filter cavity finesse	6700
Filter cavity round-trip loss	< 50 ppm
Filter cavity mode-matching	98%
Filter cavity length noise (RMS)	< 0.5 Hz

weigh the detector noise around 100 Hz. As a result, the frequency-independent squeezing spectra corresponded to a 10 – 15% reduction in BNS range, compared to no squeezing.

In contrast, frequency-dependent squeezing recovered low frequency sensitivity, improving the BNS inspiral range by 15% and the BBH inspiral range by 12%, with respect to no squeezing. Since event rates scale with the volume of the observed Universe, this corresponds to an increase of up to 65% in BNS detection rates and 40% in BBH detection rates.

6.3 SQUEEZING AND FILTER CAVITY CONTROL

Figure 6.1 shows the in-air preparation (yellow) of squeezer control signals before their delivery to the vacuum system (blue) via optical fibers. Arrows indicate how various alignment and length control signals are sensed and actuated across the squeezer system.

Squeezer controls are largely the same as in O3 [42]. The squeezer pump laser is a 1064 nm laser that is frequency-stabilized to the main interferometer laser with 100 kHz bandwidth using a table-top frequency stabilization servo (TTFSS). A pick-off from the main interferometer laser is frequency shifted by 160 MHz and fed to an in-air squeezer optics tables via an optical fiber. Here, the beat-note between the squeezer laser and the frequency-shifted interferometer laser is sensed and demodulated to provide the error signal for the TTFSS loop. This signal is fed back to the frequency of the squeezer pump laser.

Both OPO and SHG cavities are locked to the squeezer laser using Pound-Drever-Hall (PDH) sensing. The open loop transfer functions of the OPO and SHG locks are plotted in Figs. 6.3 and 6.4 respectively. The output from the SHG is split off into two beams which serve as the OPO pump and the filter cavity locking fields respectively. Before injecting into the squeezer, the OPO pump is passed through an acousto-optic modulator (GAOM3) for intensity control. The reflected 532 nm power from the OPO

neutron stars. Calculation of the BBH range uses a $30M_{\odot}$ template, which is representative of a typical BBH merger [113].

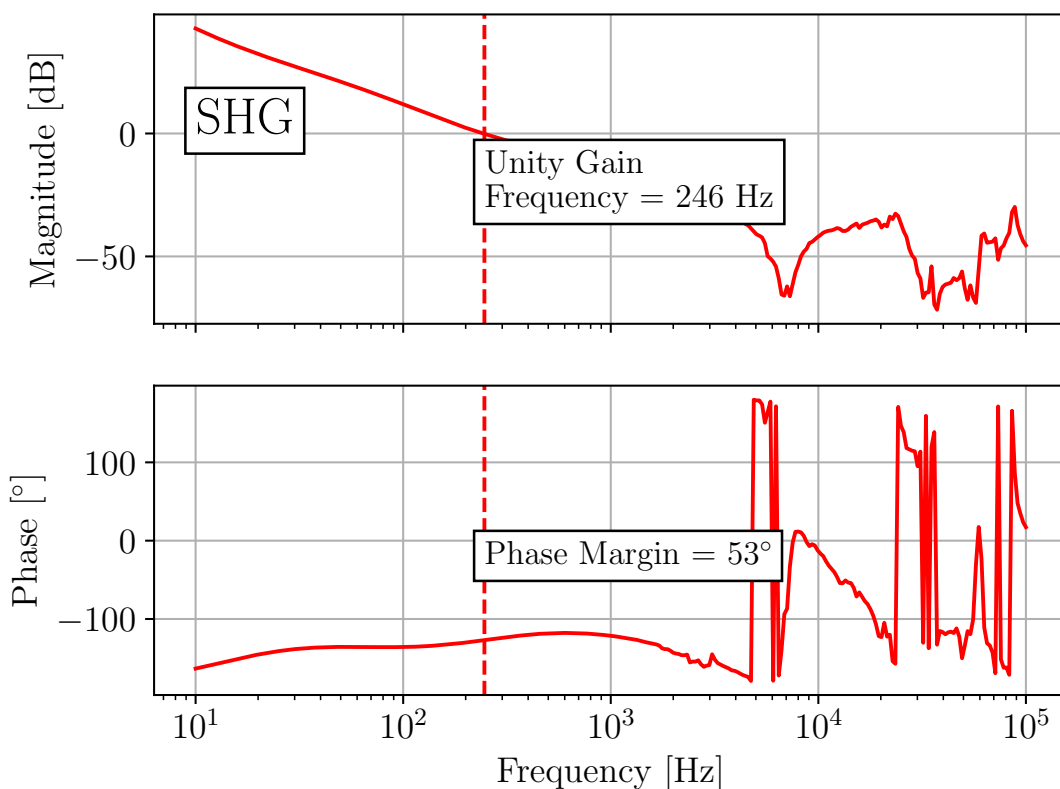


Figure 6.3: SHG open loop transfer function.

is used as an error signal to feed back to the amplitude of GAOM3's drive voltage for the OPO's intensity stabilization loop.

Two acousto-optic modulators (AOM1 and AOM2), in series, generate two RF sidebands, the coherent locking field (CLF) and resonant locking field (RLF) at detunings of 3.125 MHz and 3.020 MHz, for coherent control of the squeezing angle (Section 2.6) and filter cavity length (Section 3.2). To sense the relative phase between the squeezed field and the interferometer's local oscillator field, the CLF sideband is injected through the OPO's auxiliary port and co-propagates alongside squeezed vacuum through to the detector readout. The reflected CLF sidebands from the OPO beat with each other at 6.25 MHz. This beat-note is sensed in-air on SQZT7 and de-

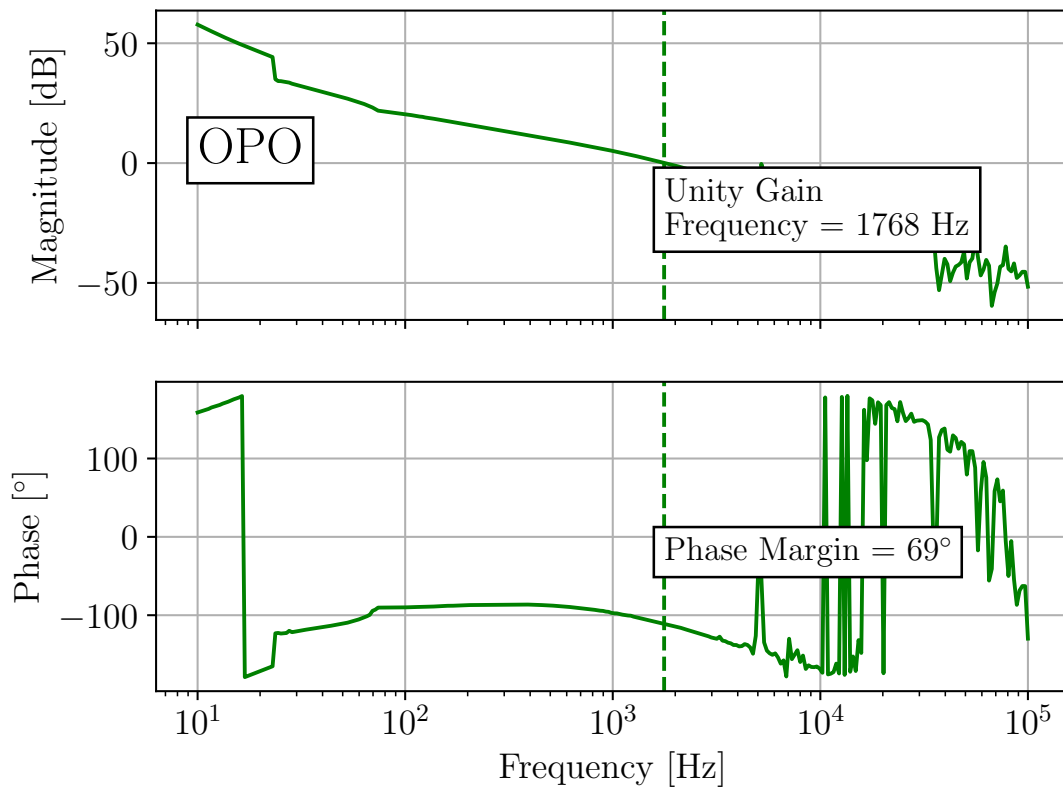


Figure 6.4: OPO open loop transfer function.

modulated to produce the error signal for the CLF loop, which then actuates on the frequency of the electronic input to AOM2 to lock the CLF phase to that of the squeezer pump. The open loop transfer function of this loop is plotted in Fig. 6.5. The beat-note between the interferometer laser and the CLF is sensed at the detector's output photodetectors in order to generate the LO error signal. This signal is then fed back as an offset to the TTFSS signal in order to lock the squeezer pump to the interferometer laser's phase at output, thus controlling the squeezer angle. Fig. 6.6 shows the open loop transfer function of the LO loop. The residual in-loop phase noise in the coherent control loops is plotted in Fig. 6.7. The DC power level of the reflected CLF is fed back to AOM2's drive voltage to stabilize the CLF's intensity.

After exiting the output Faraday isolator, 1 % of the squeezed output is picked off and redirected to a pair of quadrant photodetectors (QPDs). These are used to sense the relative alignment between the injected squeezed vacuum and interferometer laser by measuring the 42 MHz beat-note between the CLF and a 45 MHz sideband field used for interferometer control. These signal are fed back to two relay mirrors (ZM4, ZM5) between the filter cavity and interferometer for alignment control.

The filter cavity length is controlled using the resonant sideband locking scheme described in Section 3.2. Length control of the 298 m high-finesse filter cavity is initially acquired using a part of the 532 nm output from the SHG, for which the cavity is lower finesse. The control is subsequently transferred to 1064 nm during nominal operation. Before injecting into the filter cavity, the 532 nm is passed through two acousto-optic modulators (GAOM1, GAOM2) in order to provide a tunable frequency offset. With green PDH sensing, this light is first frequency-locked to stabilize the cavity-laser detuning with high bandwidth. This enables the low-bandwidth feedback to the filter cavity mirror suspensions to then bring the physical cavity length under control with length actuation via electro-magnetic coils along the mirrors' triple suspensions [105]. Fig. 6.8 shows the open loop transfer function of the green PDH lock.

After locking the cavity length in green, the cavity is made to be resonant for the RLF by changing the green frequency offset. The RLF frequency is chosen to be near the CLF frequency such that it largely inherits the phase stability of the CLF with

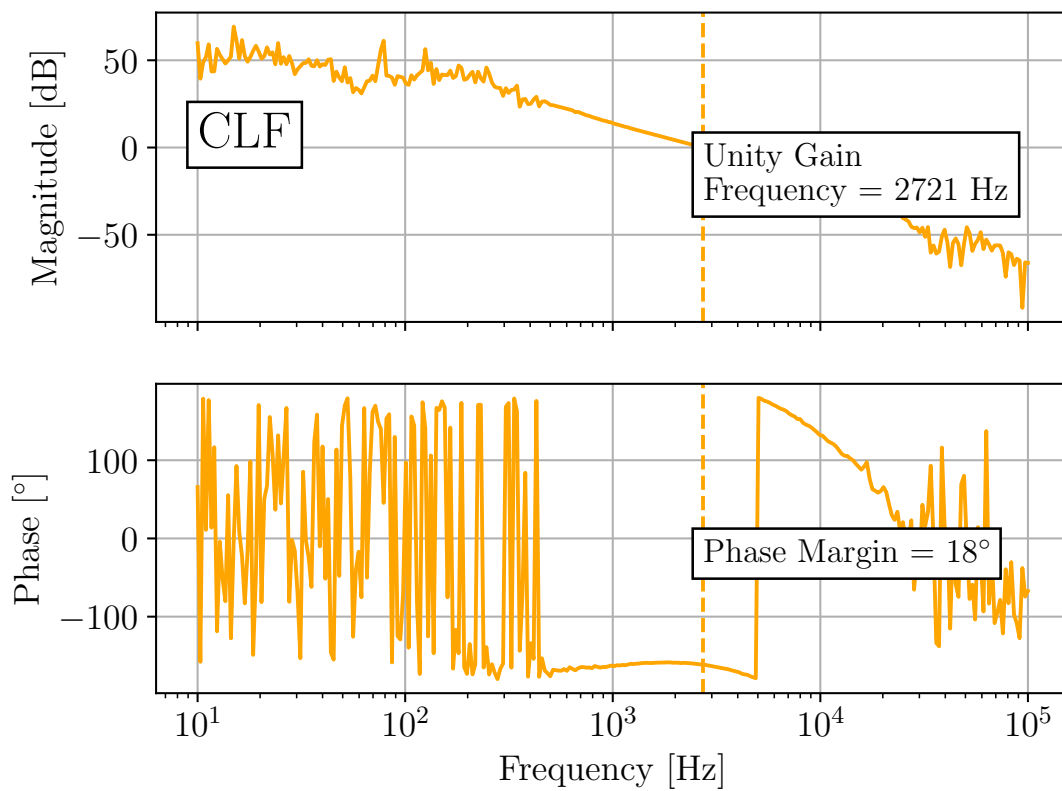


Figure 6.5: CLF open loop transfer function.

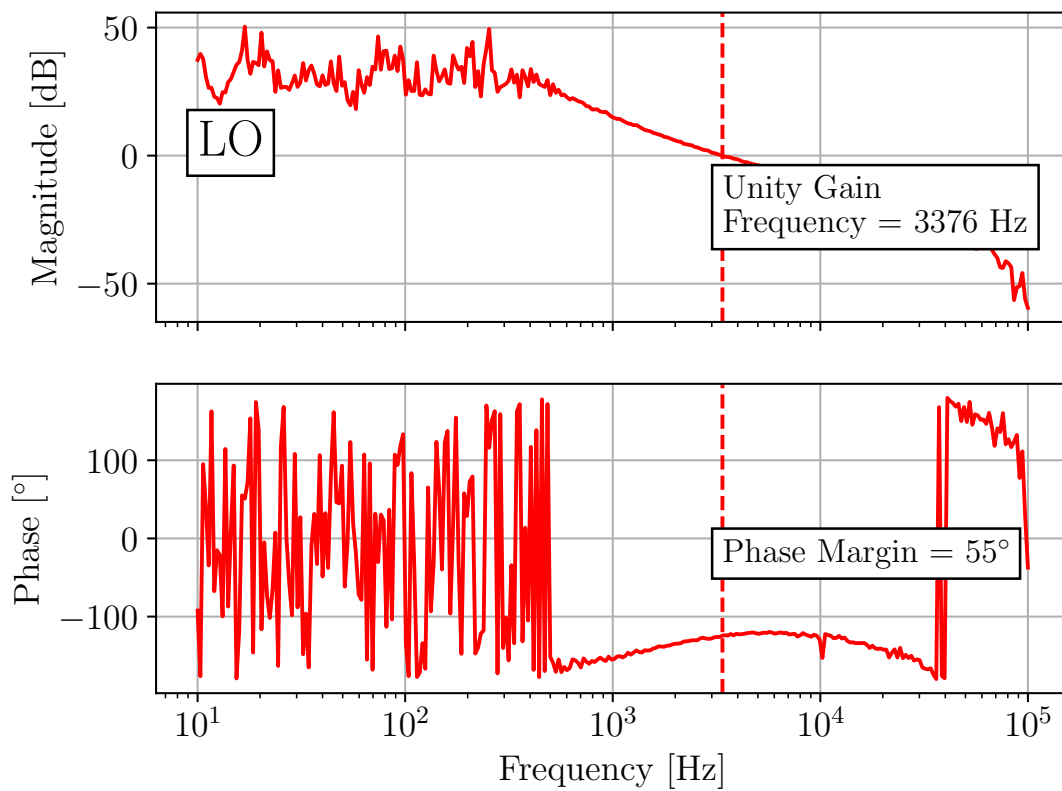


Figure 6.6: LO open loop transfer function.

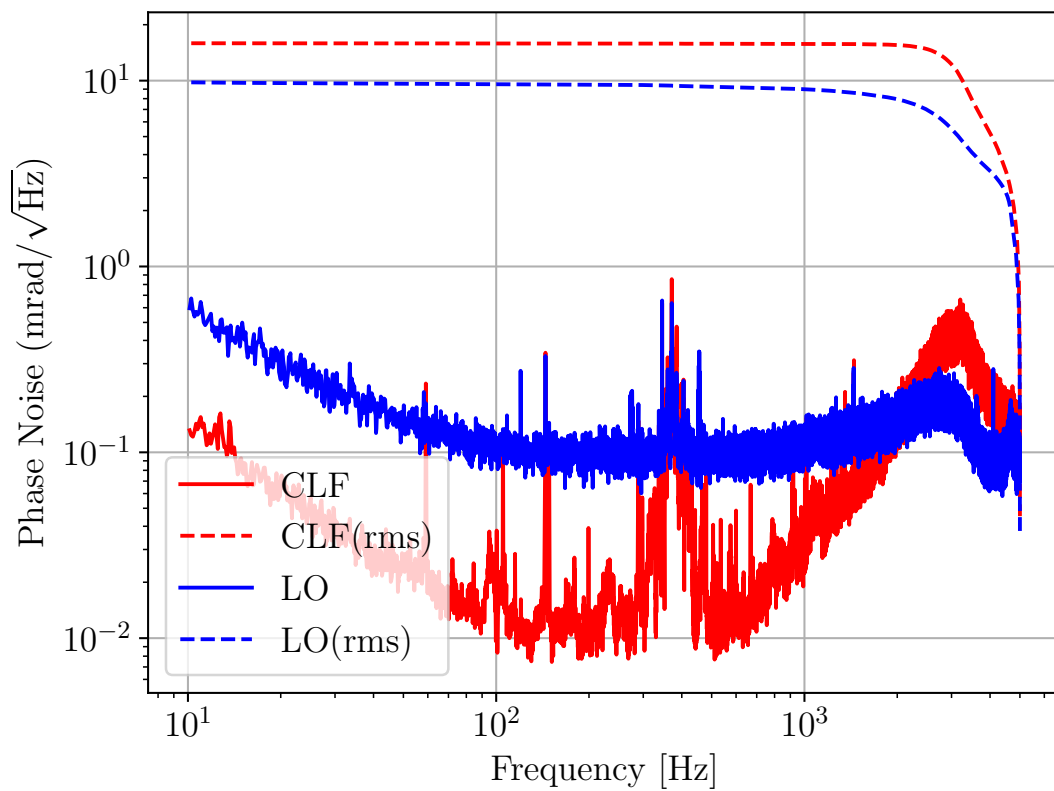


Figure 6.7: In-loop measurement of CLF and LO phase noise, calibrated into units of mrad.

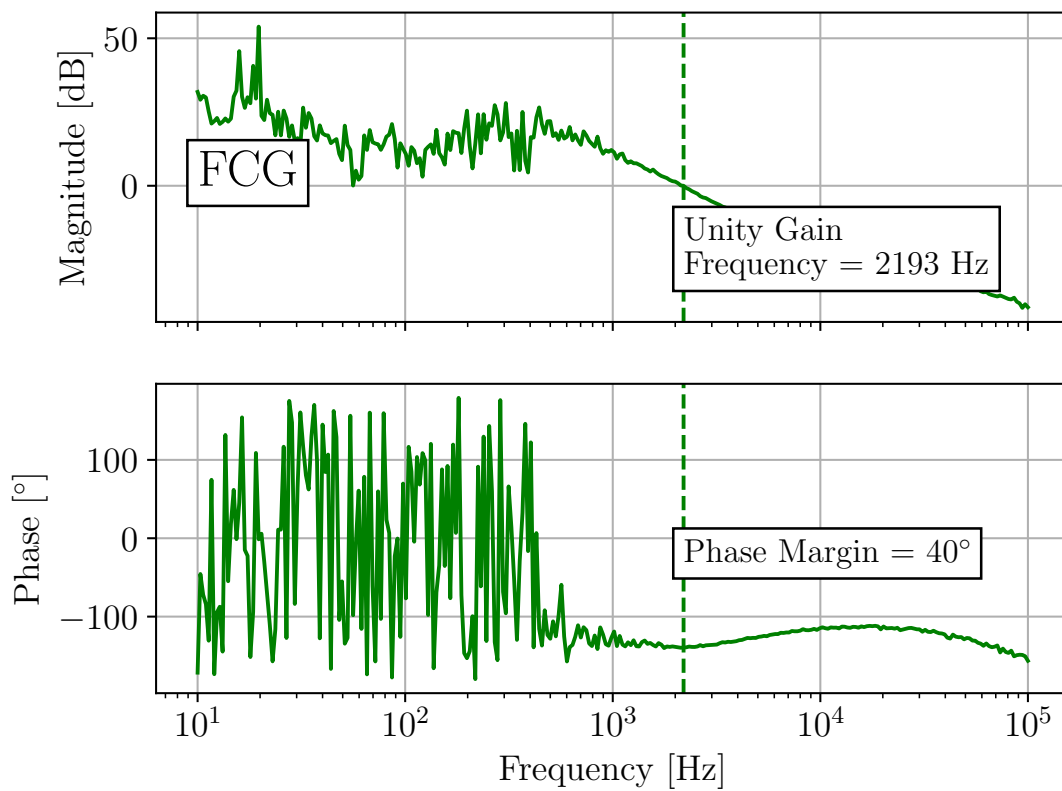


Figure 6.8: Filter cavity green open loop transfer function.

respect to interferometer light while still resonating in the filter cavity. This puts the RLF at a 105 kHz offset from the CLF, which is about six free spectral ranges (FSR) above carrier resonance in the filter cavity ($6 \times \text{FSR} + \delta$). The RLF and CLF co-propagate through the OPO to reach the filter cavity. The filter cavity length is then locked onto the RLF resonance such that the CLF is off-resonant; past the filter cavity, the resonant RLF beats against the off-resonant CLF, producing an error signal at the beat-note frequency of 105 kHz. A 1% optical pick-off for fast, high-gain QPDs is installed in the squeezer path on reflection from the filter cavity; these QPDs have a >120 kHz response and are shot-noise-limited with only 10 nW per quadrant. These QPDs are demodulated to provide error signals for both length (i.e., detuning) and alignment control of the filter cavity. Length control actuates on the filter cavity end mirror suspension. Alignment control actuates on pitch and yaw of the filter cavity mirrors, aligning the cavity axis to the incident beam from the OPO. The open loop transfer function and in-loop length noise (calibrated into picometers) are plotted in Figs. 6.9 and 6.10. The filter cavity length is stabilized by the RLF locking scheme to within 1 Hz RMS (equivalently, ~ 1 pm RMS). The servo bandwidth to the filter cavity length control servo is cut-off at as low frequency as possible (<50 Hz) such that the sensing noise of the RLF error signal, injected through the servo, does not compromise the vibration isolation of the triply-suspended filter cavity mirrors.

6.4 CHARACTERIZING FREQUENCY DEPENDENT SQUEEZING

6.4.1 *Filter Cavity*

There are standard methods to characterize a high-finesse optical cavity [98], and subsequently its application to frequency-dependent squeezing in gravitational-wave interferometers [76, 91].

Tables 6.1 lists key optical properties of the high-finesse filter cavity at H1. The filter cavity length is precisely measured by sweeping an optical sideband to measure the free spectral range [114, 115]. The optical storage time in the cavity, which determines the full-width-half-maximum linewidth, is measured using a ringdown technique

6.4. CHARACTERIZING FREQUENCY DEPENDENT SQUEEZING

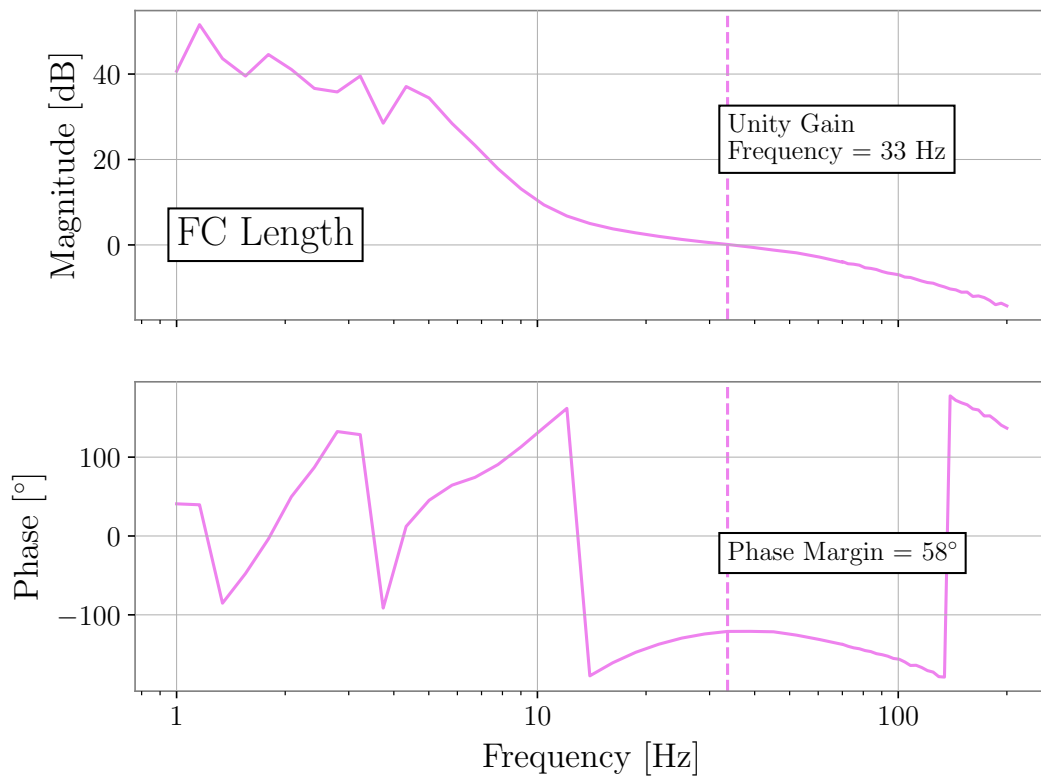


Figure 6.9: Filter cavity RLF lock open loop transfer function.

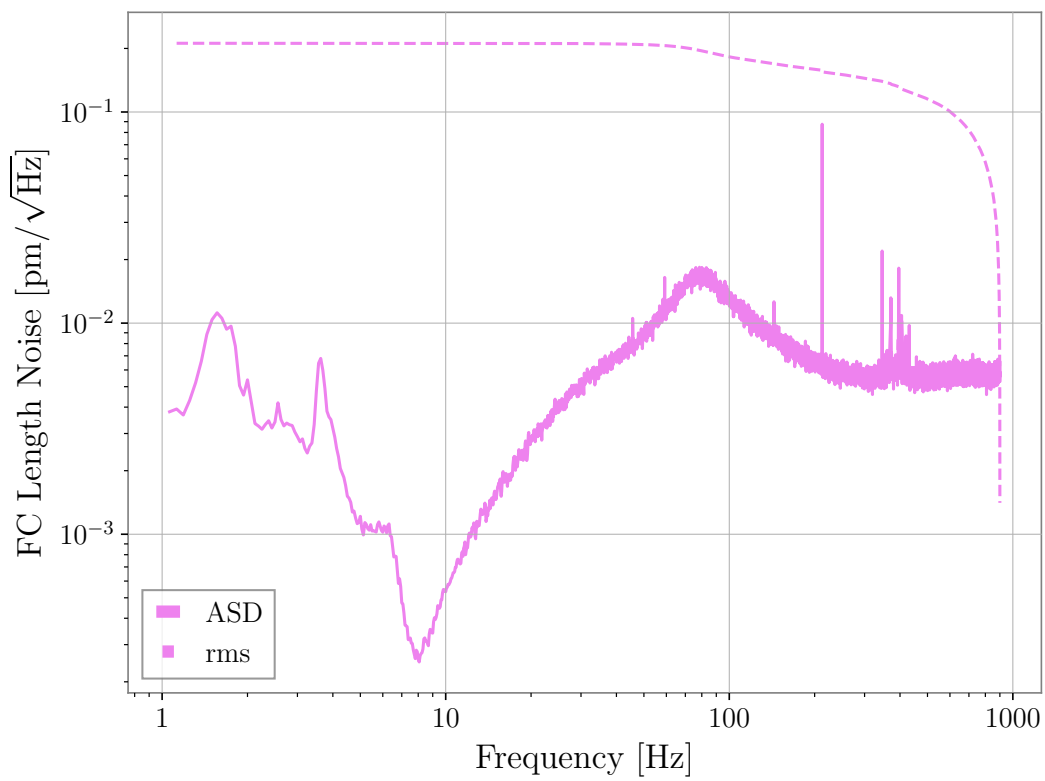


Figure 6.10: In-loop measurement of filter cavity length noise, calibrated into units of picometers.

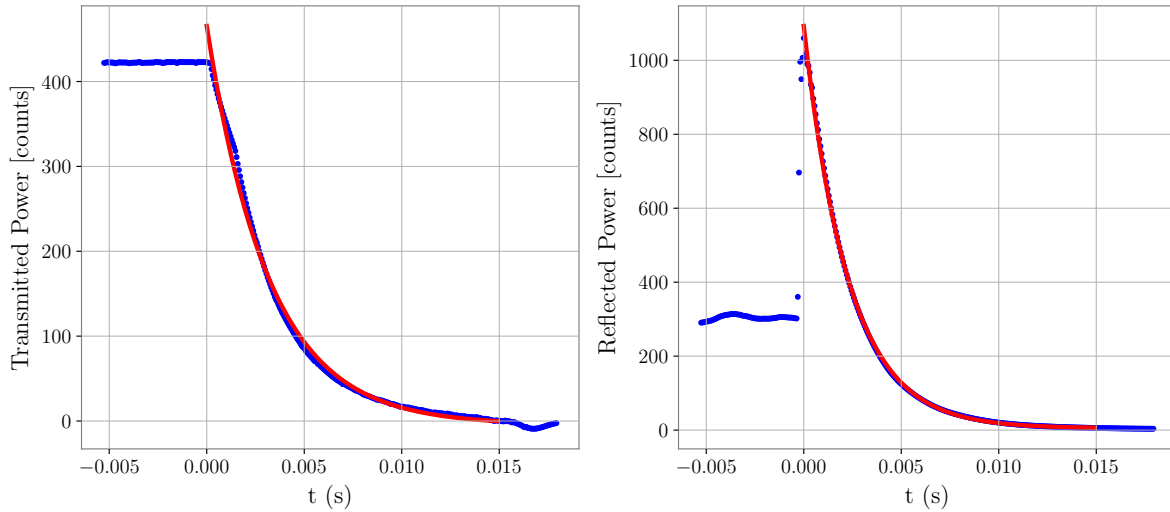


Figure 6.11: Ringdown measurement of the 300 m filter cavity. The left and right plots show the transmitted and reflected power (in units of ADC counts) respectively of a bright carrier field resonant in the cavity until it is shuttered at $t = 0$. The red traces correspond to exponential fits to the data. The time constant of the exponential decay of the power gives the storage time of the cavity.

in both cavity transmission and reflection [98]. For the ringdown measurement, we make the filter cavity resonant for a bright carrier field. The beam is then shuttered, and the transient decay of power is measured on transmission and reflection from the filter cavity. An example of a ringdown measurement is given in Fig. 6.11. The results from a collection of ringdown measurements are presented in Fig. 6.12. There is significant variance between measurements but the average value of the inferred storage time and linewidth are close to expected design parameters [93], and those measured by audio field sweeps, which are discussed later in this section.

Mode-mismatch between the squeezed beam from the OPO and the filter cavity is measured by scanning the filter cavity length and measuring the optical modes in transmission using a camera and photodiode power sensor [116]. For this, a bright carrier beam is resonantly transmitted through the OPO in place of the squeezed vacuum beam. Using this method, the mode-mismatch is constrained to be less than 2%.

An auxiliary audio field, ADF (Section 5.1), is used to further constrain mode-

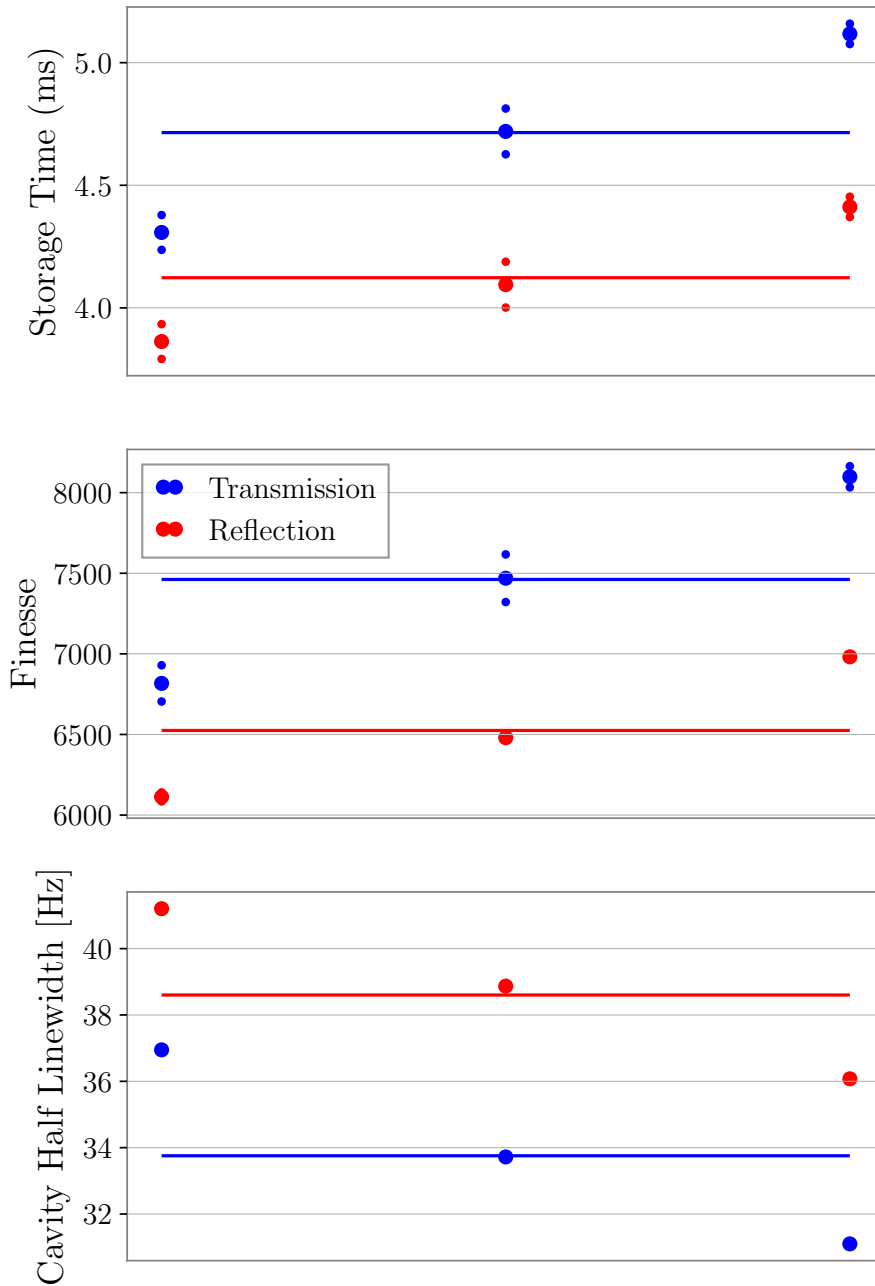


Figure 6.12: Results from a collection of cavity ringdown measurements. The horizontal lines correspond to the average of the measurements. There is variance of the order of 10 % between parameters inferred from various measurements. Additionally, there is a 20 % discrepancy between transmission and reflection based estimations.

6.4. CHARACTERIZING FREQUENCY DEPENDENT SQUEEZING

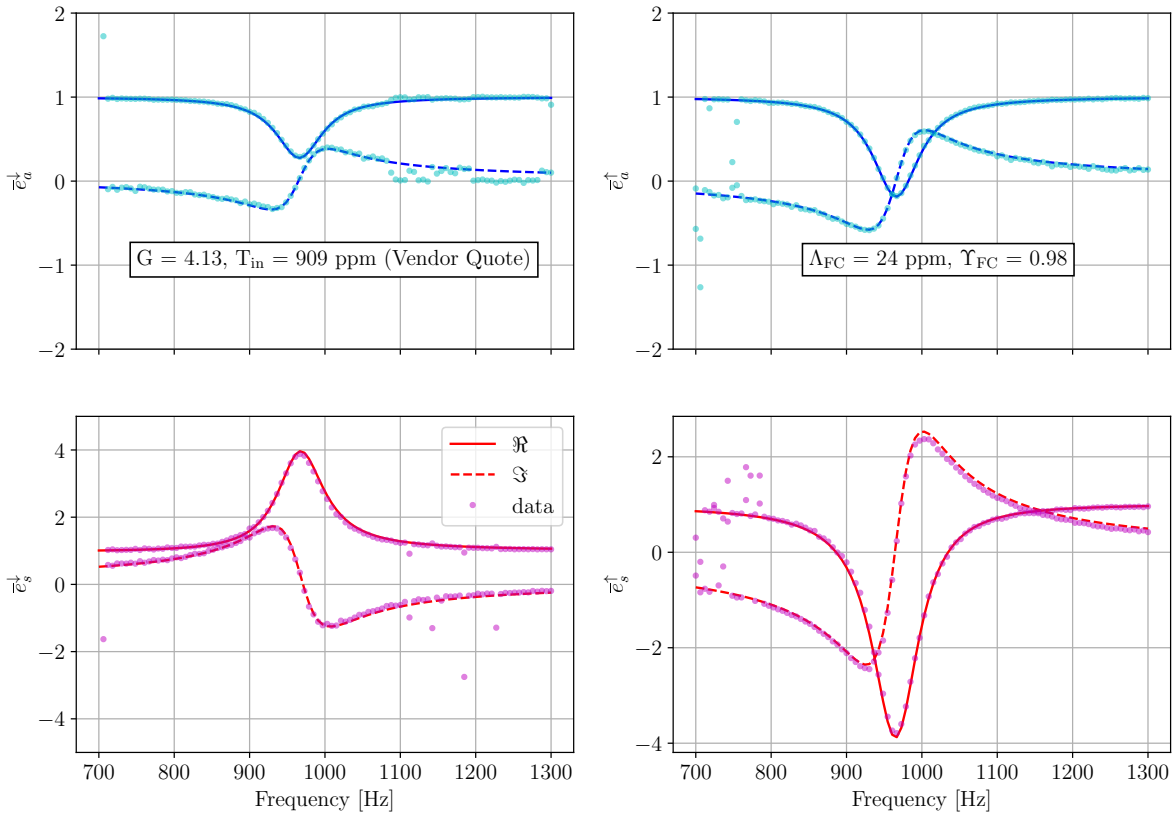


Figure 6.13: Audio field measurements of the 300 m filter cavity at LIGO Hanford (H1). The model curves are plotted along with the data.

matching and round-trip loss in the filter cavity. From the measured cavity linewidths and the vendor-specified input coupler power transmissivities of 910 ppm, we estimate filter cavity round-trip power losses of 25–50 ppm. Normalized ADF measurements (Eq. (5.34)) along with model inferred parameters are shown in Fig. 6.13.

In order to verify the measured parameters by the ADF, frequency-dependent squeezing is measured on the diagnostic homodyne detector (Fig. 6.14) described in Section 6.1, and compared to a model [91]. From the figure, we observe measured data is highly consistent with the the independently measured filter cavity parameters.

During normal operation, the filter cavity detuning in-situ is inferred by comparing detector noise spectra to a quantum noise model.

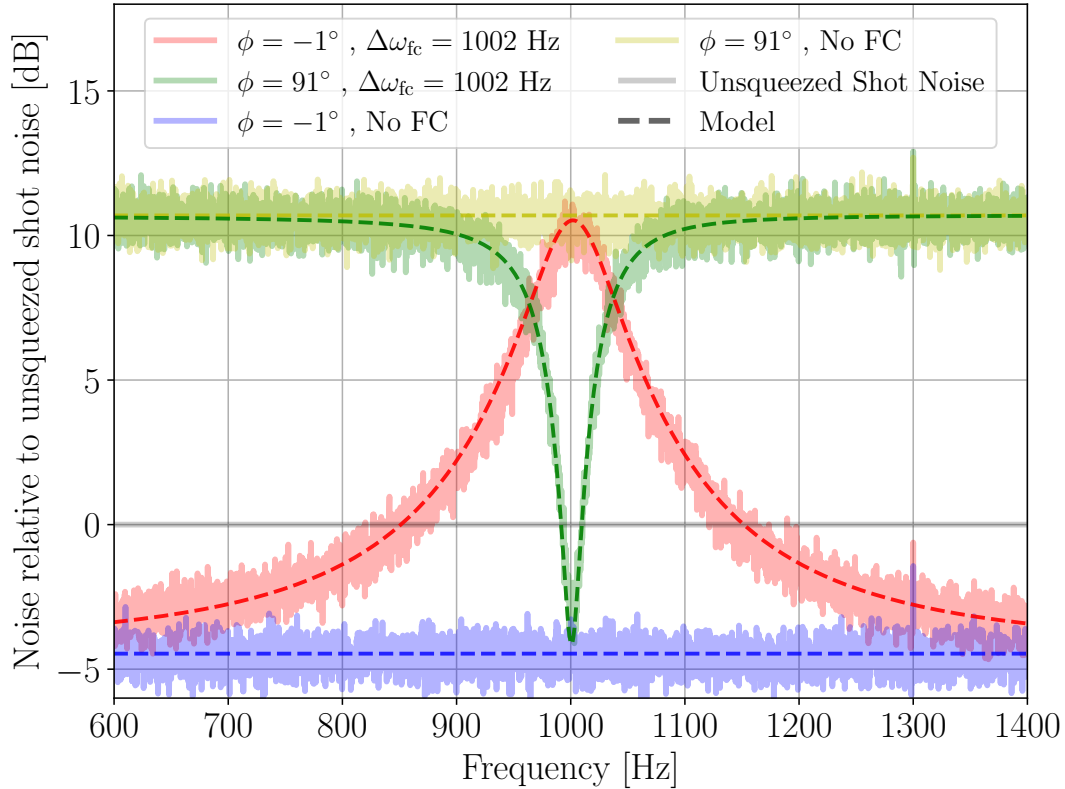


Figure 6.14: Frequency-dependent squeezing on a diagnostic balanced homodyne detector at H1. The blue and yellow traces show frequency-independent squeezing spectra measured with the filter cavity end mirror misaligned. The red and green traces show frequency-dependent squeezing spectra, measured with the filter cavity locked at a detuning of $\delta \sim 1 \text{ kHz}$ from the local oscillator. The quantum noise model with independently measured parameters is shown by the dotted lines. The plot legend gives the corresponding squeeze angle, ϕ , and filter cavity detuning, δ , for each trace.

6.4.2 *Squeezing injection*

As discussed in Section 2.7, the effective quantum noise reduction with squeezing, or the observed squeeze level, is determined by the amount of generated squeezing and by degradation mechanisms such as phase noise, optical loss, and mode-mismatch.

Phase noise - In H1, the phase noise is controlled to less than 20 mrad in both detectors, as inferred from in-loop error signals (Fig. 6.7) and from sweeps of the generated squeezing levels using diagnostic homodyne measurements (Fig. 2.10). Additionally, filter cavity detuning fluctuations contribute an additional frequency-dependent phase noise within the cavity bandwidth. This detuning is stabilized to within 1 Hz or equivalently 1 pm (Fig. 6.10), adding ~ 5 mrad of excess phase noise around the detuning frequency. Overall, at the measured levels of generated squeezing, 20 mrad of RMS phase noise reduces measured squeezing by less than 0.2 dB.

Optical losses - Losses can be separated into two categories: the injection losses that affects the squeezed beam before entering the interferometer, and the readout losses in the optical path from the signal extraction mirror to the readout photodetectors.

Optical losses in the injection path start from the squeezing generation in the non-linear crystal. These injection losses include OPO cavity losses, filter cavity losses, and four passes through Faraday isolators before reaching the interferometer, i.e., arriving at the signal extraction mirror. The in-chamber squeezer injection losses are externally measured by injecting a bright carrier field through the OPO in place of the control sidebands; we measure the OPO cavity's optical throughput to be 98.5–98.7%, in addition to the in-chamber throughput of 93%. Custom low-loss Faraday isolators were implemented in preparation for O4, with measured single-pass throughput on the order of 99–99.5% [107]. With four isolator passes, through two isolators on the squeezer injection platform (one more than O3) and the interferometer's output Faraday isolator, the O4 isolators provide a significant reduction in losses over those used in O3, which each had 96–97% single-pass efficiency. In total, known optical losses limit the maximum squeezing injection efficiency to about 91%.

Filter cavities at both sites are measured to have < 50 ppm of round-trip loss which, near resonance (~ 40 Hz), contributes an additional 10% of squeezing loss (see Eq. 53

and 57 of [76]). At the interferometer output, readout losses limit throughput of both the interferometer signal and the measured squeeze level. These losses are largely common to the interferometer and squeezer, and inform our estimate of classical noise. Based on independently measured optical losses at the output port, readout efficiencies of up to 91% at H1.

Given known optical losses, the total expected throughput is around 84%. However, a minimum squeezing throughput of 63% is inferred from measured squeezing levels, i.e., the measured shot noise power reduction with squeezing at 1 kHz of 4.0 dB³.

Mode-mismatch - Unlike optical loss, which incoherently mixes squeezed vacuum with unsqueezed vacuum, mode-mismatch is a coherent mechanism. Due to mismatch between cavities, a part of the squeezed vacuum is scattered into higher order spatial modes, which accumulate extra Gouy phase shifts during propagation (see Eq. 72 of [76]). When these modes are scattered back into the fundamental mode with a different squeezing angle, the resulting loss has a frequency dependent signature. Along with the magnitude of mode-mismatch, the squeezing degradation also depends on the phase of the mismatch which quantifies the relative amount of mismatch in beam waist size and waist location.

The remaining unknown losses are likely dominated by residual mode-mismatch and misalignment between the squeezed field, the interferometer cavities, and the output mode cleaner cavity. In H1, this hypothesis is supported by estimations of the squeeze level after classical noise subtraction, where the quantum noise reduction from 100–200 Hz is higher, at 4.8 dB, suggesting that unknown losses are frequency-dependent and thus likely due to mode-mismatch of the squeezer and interferometer.

To optimize mode-matching on the squeezing injection path, three doubly-suspended active optics elements, realized by piezo-deformable mirrors [108], were installed. The first deformable mirror optimizes mode-matching between the OPO and the filter cavity, while the other two mirrors optimize the mode-matching of the frequency-dependent squeezed vacuum beam to the interferometer.

³Part of this discrepancy has since been resolved after discovering extra loss in the OPO crystal [117]. See Appendix E for more details.

6.4.3 *Interferometer parameters*

Readout losses - Readout losses impact both the shot-noise-limited interferometer sensitivity without squeezing, and the total quantum noise reduction achievable with injected squeezing. From the detailed schematic in Fig. 6.1, readout losses from the output of the signal extraction mirror to the readout photodetectors include one outgoing pass through the output Faraday isolator, several optical pick-offs required to stabilize alignments between the interferometer and the output mode cleaner (OMC), optical round-trip losses in the OMC cavity, and the quantum efficiency of the readout photodetectors. Separately, the squeezer and interferometer beams may have different mode-matching through the OMC, leading to possible differences in readout loss between the interferometer and squeezer beams. Excluding mode-mismatch, the expected readout efficiency is 91% in H1.

Readout losses without squeezing - Many readout losses are common to the squeezer and interferometer, and thus estimating the shot noise level requires knowledge of the interferometer's output losses independent of squeezing. Without squeezing, detector noise around 1 kHz is dominated by shot noise; this level can be compared to a shot noise model (e.g. Eq. (1.8)) to estimate the in-situ readout losses, beyond the known optical losses in the path. The shot noise model is primarily determined by the interferometer laser power and optical response, both of which can be independently measured.

Key parameters that characterize the interferometer optical response are the interferometer readout angle and the detuning of the signal extraction cavity (SEC). Differential losses in the interferometer's arms lead to an imperfect dark fringe with excess field at the output, known as the contrast defect. Since this excess field does not contain information about the differential arm length signal, it results in a non-zero angle between the signal and readout quadratures, which increases the shot noise levels at high frequency [39]. Measuring the residual optical power at the dark fringe of the interferometer provides an upper limit on the readout angle, given in Table 6.1 [118].

Next, the SEC detuning, often quoted as the round-trip phase shift through the

cavity in degrees, can be estimated by measuring the interferometer response to an external drive of the end mirrors [28, 119]. Given this optical response, the shot noise model without squeezing [39, 76] (Fig. 6.2, red) can be compared to the measured noise spectra without squeezing (Fig. 6.2, black) to estimate the interferometer readout losses.

For H1, an analysis of readout losses is complicated by uncertainty in the arm power, a larger SEC detuning, and a larger readout angle as constrained by the contrast defect. For the reported parameters in Table 6.1, we estimate less than 20% additional interferometer readout losses compared to known losses.

For both detectors, the additional interferometer readout losses can be related to mode-mismatch. For instance, mode-matching of the interferometer output beam through the OMC is imperfect, and highly dependent on the thermal state of the interferometer [76]. Another source of mode-mismatch is intra-cavity mismatch between the signal extraction cavity and the two arm cavities, which varies with the thermal state of the interferometer and optical defects across the LIGO's core optics [120]. The strong dependence of measured squeezing that results from this can be seen in the long term squeezing trend in O4 (Fig. 6.15), where we note that reducing the laser power injected into the interferometer led to a significant increase in measured squeezing.

Quantum noise spectra can also be compared to a model to estimate interferometer parameters, especially those which are difficult to measure independently, for e.g. mode-mismatch. Removing non-quantum noise from interferometer noise spectra is important to get an accurate picture of quantum noise. Classical noise can be estimated by assuming basic interferometer parameters and subtracting modelled shot noise from the interferometer spectrum without squeezing. This classical noise, can then be subtracted from the interferometer noise spectra with varying squeezing angles to provide several quantum noise curves. An example is shown in Fig. 6.16, where interferometer parameters are roughly estimated from noise spectra [121] using an interactive script [122]. More accurate estimations would require rigorous methods such as Markov-Chain Monte Carlo (MCMC), which are beyond the scope of this work.

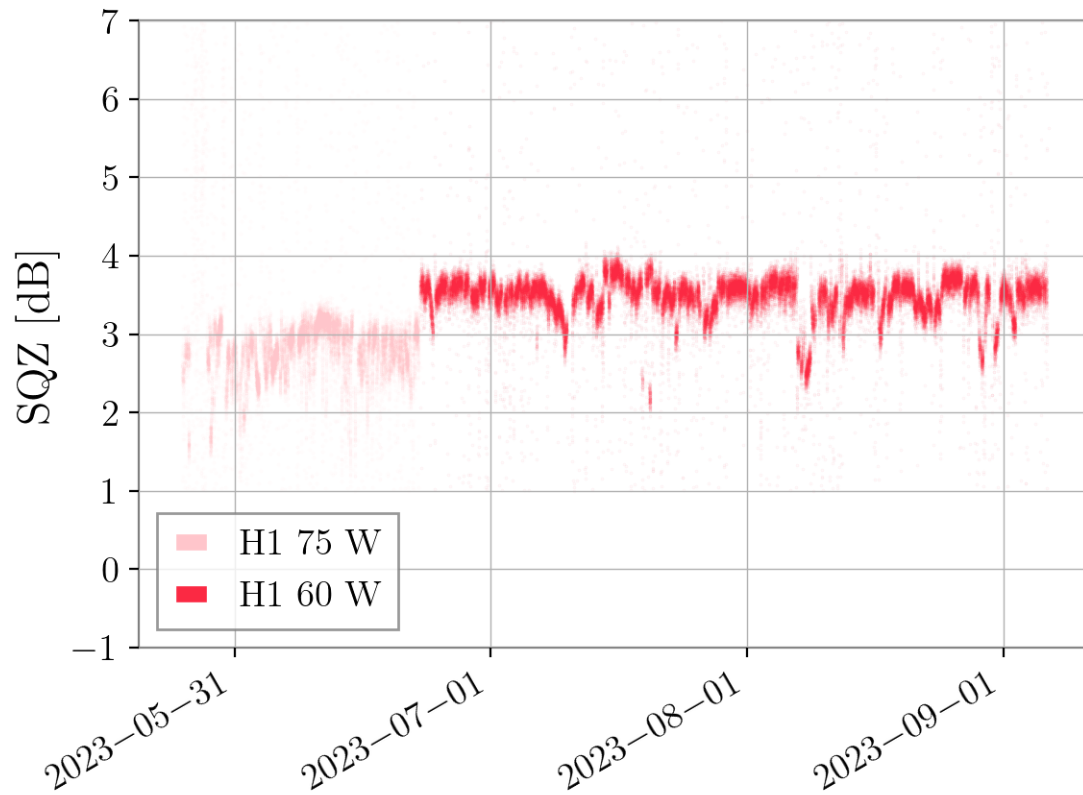


Figure 6.15: Squeezing trends for the first 5 months of O4. The legend corresponds to the laser power injected into the interferometer.

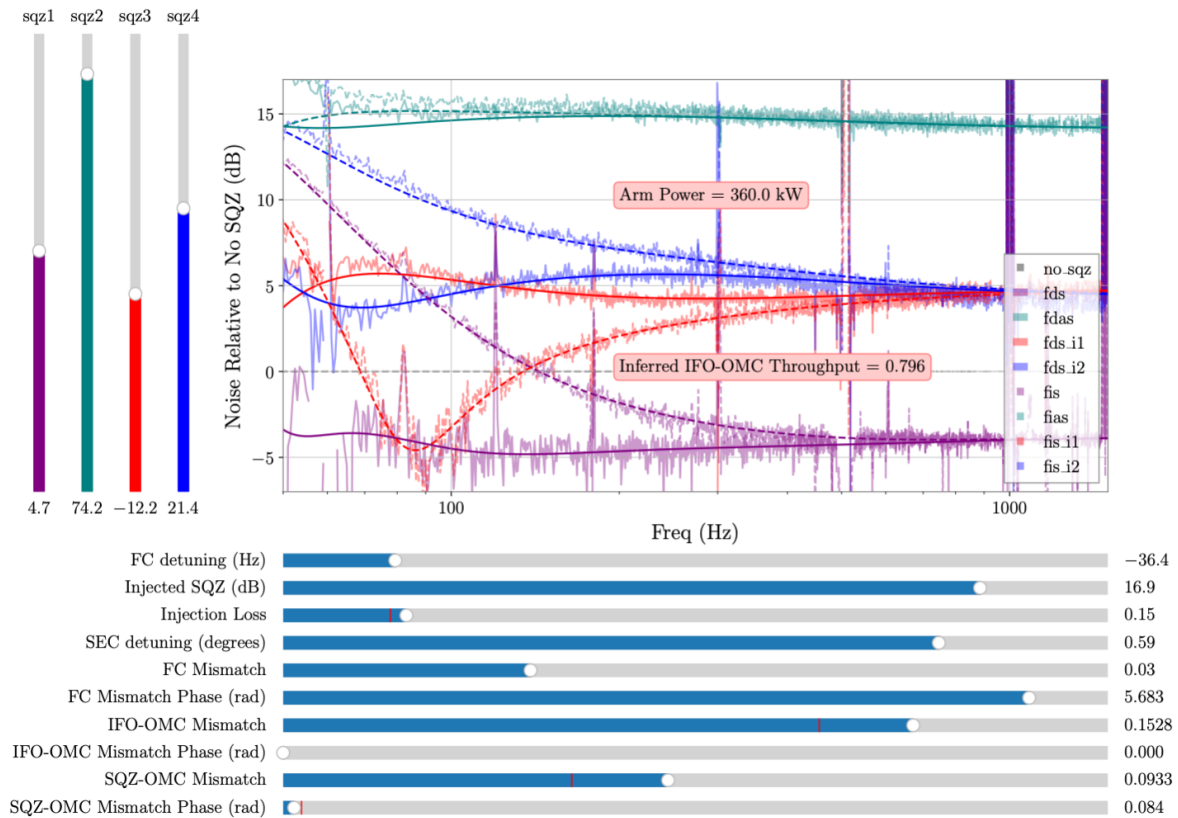


Figure 6.16: Measured squeezing data [121] compared with a quantum noise model. Model parameters are not obtained from fitting but instead are manually adjusted using sliders in an interactive squeezing code [122].

CHAPTER

7

TUNING LIGO TO BINARY NEUTRON STAR POSTMERGERS

The discovery of a binary neutron star (BNS) merger by LIGO and Virgo in 2017 (GW170817) [5], and the electromagnetic followup observations of a kilonova [7], have heralded a new era of observational neutron star physics. Information about the tidal deformability of the constituent objects [123] is encoded in the gravitational waveforms of binary mergers, both in the inspiral phase before coalescence [124], and in the post-merger phase promptly thereafter [125].

While the inspiral effects occur primarily below 1 kHz, the post-merger signal is expected at kilohertz frequencies [110, 111]. Understanding the post-merger physics therefore requires improving or targeting detector sensitivity at these higher frequencies. In particular, post-merger waveforms have been simulated for various models of the neutron star equation of state (EoS) and their Fourier spectra typically show a narrow band of signal energy concentrated around 2 kHz [125].

In a scenario where multiple gravitational-wave detectors are operational, it may be beneficial to maximize one or more detectors for sensitivity to these BNS post-merger signals, while relying on other detectors in the network for inspiral detection and source localization. Optimizing detectors at high frequencies has been investigated in the context of future major upgrades in current and new facilities [126, 127], and in a proposal for a new dedicated high-frequency gravitational-wave interferometer [128]. Here we quantify the sensitivity to high-frequency, narrowband post-merger signals for modified “tunings” of the LIGO interferometers and their upcoming “A+”

upgrade [129, 130].

Two modifications are considered, with their strain spectra densities shown in Fig. 7.1. The first is the “wideband” configuration, where the interferometer bandwidth is increased to encompass the expected post-merger resonances, and the second is the “detuned” configuration, where the A+ interferometer is operated with a high-frequency, narrow-band dip. The only physical changes to the optical system associated with these new configurations are the transmissivity of the LIGO signal extraction mirror and filter cavity input mirror. Neither of these new configurations requires modifying the facility, vacuum envelope or suspension design, so either could be readily adopted as a near-term modification to an A+ LIGO interferometer.

7.1 INTERFEROMETER CONFIGURATIONS

The sensitivity of existing gravitational-wave interferometers at frequencies above a few hundred hertz is limited almost exclusively by quantum shot noise [33, 131]. Quantum shot noise can be reduced by increasing power in the arms of the interferometer [1], injecting squeezed vacuum states into the output port [42], and by trading sensitivity at some frequencies for others by changing the optical parameters of the interferometer [132].

The LIGO detectors [33] use arm cavities to both increase the arm power and shape the interferometer frequency response, with the addition of a signal extraction mirror (SEM) to implement the “resonant sideband extraction” scheme [26]. The SEM forms a signal extraction cavity (SEC) that determines the detector bandwidth. In the baseline A+ configuration the SEC is operated to resonantly couple the signal out of the arm cavities, broadening the bandwidth of the detector from 40 Hz to 450 Hz.

The parameters of the A+ design, shown in Table 7.1, are optimized for detecting inspiral signals, with quantum noise and classical thermal noise similarly affecting the detection range. The detector bandwidth, adjusted by the SEM transmissivity, is chosen to balance the peak sensitivity determined by shot noise and the degradation at low frequencies caused by radiation pressure noise. Frequency-dependent squeezing is employed to enhance the interferometer sensitivity at all frequencies. For the

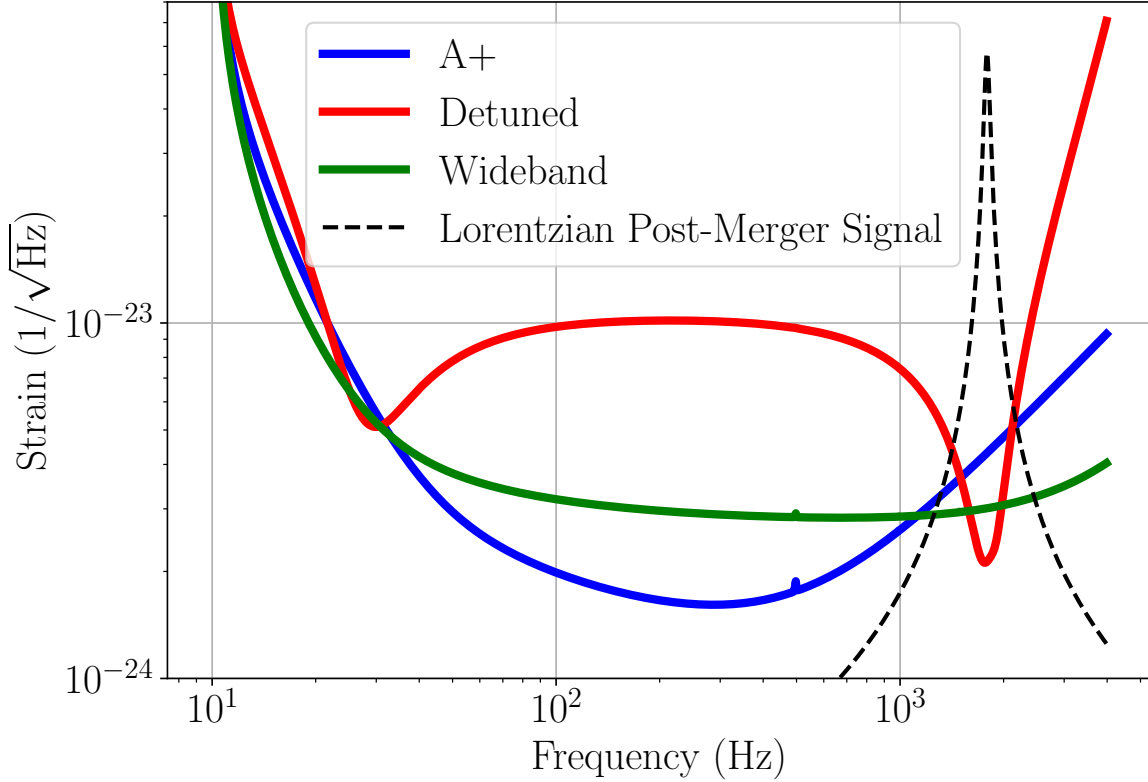


Figure 7.1: Interferometer configurations under comparison. Representative strain noise curves of the “A+”, detuned, and wideband configurations are plotted for reference. Both altered configurations sacrifice sensitivity at low frequencies in order to increase high-frequency sensitivity. The sensitivity improvement for the detuned configuration is across a relatively narrow band, and is achieved by detuning the signal extraction cavity in order to obtain a high-frequency resonant enhancement. In the wideband configuration, the input transmission of the signal extraction cavity is reduced in order to increase the interferometer bandwidth. The dashed black curve corresponds to the strain $\tilde{h}_{\text{DS}}(f)$ of a lorentzian post-merger signal (Eq. (7.1)) with $f_0 = 1798$ Hz and $Q = 28.32$, observed at 100 Mpc with $0.1M_{\odot}$ converted to gravitational wave energy during post merger (see Eq. (7.8)). It is plotted in spectral density units using the form $2\sqrt{f}|\tilde{h}_{\text{DS}}(f)|$. Using Eq. (7.10), the signal-to-noise ratio is calculated to be around 3 for the baseline A+ configuration.

various configurations described, an injected squeezing of 12 dB is assumed. Taking into account the injection and readout losses, which are assumed to be 5% and 10% respectively, the effective broadband quantum noise suppression in A+ is estimated to be around 7 dB. As radiation pressure noise is not an observable effect at the frequencies of interest for a post-merger, the relative phase between the squeezed field and the main interferometer field has been chosen to minimize shot noise.

Representative strain noise curves for the wideband and detuned configurations described below are shown along with the A+ curve in Fig. 7.1. Notably, squeezing enhancement plays a crucial role when comparing these alternative configurations. At post-merger signal frequencies of ~ 2 kHz, squeezed vacuum states are temporarily stored in the signal extraction cavity, experiencing its roundtrip loss, Λ_{SEC} , repeatedly over multiple traversals. For A+, this amounts to a loss of $\sim 10\Lambda_{\text{SEC}}$. The wideband and detuned configurations change the storage time of the signal extraction cavity, which can result in strongly degraded squeezing as the SEC loss becomes comparable to other loss in the system.

Wideband - The wideband configuration increases the bandwidth of a LIGO interferometer by further reducing the SEM transmissivity. We consider $T_{\text{SEM}} = 0.05$, reducing the peak strain sensitivity, but extending the bandwidth beyond 3 kHz. This value is chosen so that the interferometer is sensitive to a wide range of frequencies where BNS post-merger signals are expected to lie. This configuration is not optimized for any particular post-merger model, so it is effective for detecting a variety of signals.

The decrease in peak sensitivity additionally reduces quantum radiation-pressure noise, requiring the filter cavity bandwidth to be decreased. This only affects sensitivity below 100 Hz and is not important for the analysis of post-merger signals. Similarly to A+, squeezing provides a broadband enhancement to the wideband configuration. Because the arms and SEC stay on resonance, the wideband configuration adds no additional frequency dependence to squeezing; however, decreasing T_{SEM} modifies how the loss Λ_{SEC} limits the squeezing enhancement.

In the wideband configuration, the loss added by the interferometer becomes $\sim 20\Lambda_{\text{SEC}}$ to $\sim 40\Lambda_{\text{SEC}}$, increasing for signals approaching the detector bandwidth. The

7.1. INTERFEROMETER CONFIGURATIONS

Table 7.1: Parameters of LIGO configurations. T_{SEM} and T_{FC} are the signal extraction mirror and filter cavity input mirror transmissions respectively, while ϕ_{SEC} and $\Delta\omega_{\text{FC}}$ are the SEC and filter cavity detuning in units of phase and frequency respectively.

Parameter	Value		
Arm power	750 kW		
Power on beam-splitter	5.4 kW		
Classical noises	Thermal noise [100]		
SEC length	55 m		
SEC loss (Λ_{SEC})	0.1 %		
Injected squeezing	12 dB		
Injection loss	5 %		
Readout loss	10 %		
Filter cavity length	300 m		
Filter cavity loss	60 ppm		
	A+	Wideband	Detuned
SEM transmission (T_{SEM})	0.325	0.05	Table 7.3
SEC detuning (ϕ_{SEC})	0°	0°	Table 7.3
Signal 3dB bandwidth	450 Hz	4.8 kHz	Fig. 7.3
Filter cavity transmission (T_{FC})	0.0012	0.0004	Table 7.3
Filter cavity detuning ($\Delta\omega_{\text{FC}}$)	46 Hz	16 Hz	Table 7.3

loss changes with frequency as the squeezing field transitions from being stored in the arms to being stored in the SEC, and the increased loss is due to the lower SEM transmissivity and correspondingly longer storage time. Even so, this increased loss is still subdominant to the input and output path losses, so squeezing performance is similar between the A+ and wideband configurations.

Detuned- The SEC can alternatively be operated in a “detuned” state, where it is held slightly off of resonance by maintaining an optical phase shift ϕ_{SEC} using feedback control. In this state, the interferometer optical response forms a resonant peak, resulting in a dip in the quantum noise spectrum in units of strain. This increases sensitivity at high frequencies at the expense of sensitivity at lower frequencies [33, 39, 133]. When the detuning is optimized for resonances in the kilohertz region, an additional narrowband optomechanical spring resonance is formed at low frequencies (10–30 Hz), but overall, this configuration is substantially less sensitive for inspiral detection and source localization.

The choice of detuning phase ϕ_{SEC} affects the frequency of the quantum noise dip; additionally, the transmissivity of the SEM narrows the resonance of the signal response and correspondingly deepens the dip in the noise spectrum. In the detuned configuration, T_{SEM} and ϕ_{SEC} must be optimized to achieve maximum signal-to-noise ratio (SNR) given a distribution of center frequencies and signal bandwidths for post-merger signals. The configuration will depend on the particular post-merger model and the performance is computed for several parameter distributions which are described in Section 7.2.1.

Balanced homodyne readout of the gravitational-wave signal is proposed for A+ as an improvement over LIGO’s current fringe-offset readout [134, 135]. For the detuned case, the interferometer signal sidebands are strongly imbalanced above and below the laser frequency at the resonant dip, so there is not a preferred readout angle for the post-merger signal detection. Varying the readout angle does not significantly improve the results or impact the discussion for post-merger signals, and does not improve low frequency sensitivity, for the detuned case, beyond what is shown in Fig. 7.1.

The detuned configuration considerably affects squeezing in two ways. First, the

unbalanced optical response of the interferometer results in a frequency-dependent rotation of the phase of the squeezed field relative to the main interferometer field, which must be compensated using a similarly unbalanced filter cavity. Along with the SEC parameters, this analysis optimizes the filter cavity input mirror transmission and resonance frequency $\Delta\omega_{\text{FC}}$ to maximize average SNR (see Eq. (7.11)) for each parameter model. The filter cavity roundtrip loss is kept constant at the A+ design level of 60 ppm.

Second, for the parameters of Table 7.1, the lower SEM transmissivity required for detuning causes the interferometer to inflict a squeezing loss of $\sim 200\Lambda_{\text{SEC}}$ within the narrow frequency band of the optical resonance. This loss is equal or greater than the expected total input and output losses, which prevents squeezing from providing as large a benefit to the peak strain sensitivity in the detuned case as for the wideband or A+ cases, even with optimized filter cavity parameters. Instead, the frequency dependence of the effective loss outside the interferometer bandwidth causes the squeezing to increase the effective band of the dip in strain spectral noise density. This effect is shown in the noise curves in Fig. 7.3, where optimized configurations with and without squeezing have been plotted together.

7.2 BINARY NEUTRON-STAR POST-MERGER TEMPLATES

Binary neutron star post-merger waveform models consistently show that much of their gravitational strain signal energy is contained within a limited frequency band [125]. For the purpose of comparing the SNR of detections, we approximate each post-merger narrowband signal as a damped sinusoid (DS) [136], which has a frequency-domain representation that is the symmetric composition of positive and negative frequency complex lorentzian damped envelopes (DE):

$$\tilde{h}_{\text{DS}}(f) = \tilde{h}_{\text{DE}}(f) + \tilde{h}_{\text{DE}}^*(-f), \quad (7.1)$$

$$\tilde{h}_{\text{DE}}(f) = \sqrt{\frac{H}{4\pi}} \cdot \frac{e^{i\theta(f)} \sqrt{f_0/Q}}{f_0/2Q + i(f - f_0)}. \quad (7.2)$$

Here f_0 is the signal's central frequency, and its bandwidth is set by its Q factor. H is the total energy of the strain signal. $e^{i\theta(f)}$ indicates additional parameters in the phase response [136], but these do not affect the SNR calculations, which rely only on the magnitude of the frequency-domain signal. For the detuned configuration, the interferometer's optical resonance bandwidth and dip frequency produces the greatest SNR when it is well matched to the waveform bandwidth and center frequency, but due to loss, the interferometer dip is generally of lower Q than the templates.

The ability to match the detector to the signals is limited by the natural variability in the center frequency of post merger waveforms. Simulations of neutron star inspiral models have informed phenomenological relations between astrophysical system parameters and parameters of the resulting post-merger signal [136, 137]. These relations lead to a varying waveforms with distribution function $p(f_0)$, resulting from the distribution of binary neutron star systems. Table 7.2 shows seven such distributions and their associated optimized interferometer parameters. These distributions, derived in the following section, are not tied to specific neutron star models, but instead span the uncertainty of the phenomenological waveform parametrizations.

7.2.1 *Astrophysical Distributions of Model Parameters*

This section establishes the phenomenological parameterizations used for the waveform template distributions. The form for the templates and their underlying phenomenological fits is derived from a set of numerical binary neutron star inspiral simulations [136]. The simulations and fits provide the general form for relating BNS system mass M to the post-merger waveform central frequency, f_0 . The cited work does not provide relations for the waveform Q , and this is discussed below.

In Section 7.2 the BNS post-merger signal was modeled as a lorentzian with central frequency f_0 and quality factor Q . From Eq. (7.2), the peak frequency-domain strain amplitude for the lorentzian is

$$h_{\text{peak-f}} = |\tilde{h}_{\text{DS}}(f_0)| \approx \sqrt{\frac{QH}{\pi f_0}}, \quad (7.3)$$

which may be related to the peak strain in the time-domain waveform as

$$h_{\text{peak-t}} \approx \frac{2\pi f_0}{Q} h_{\text{peak-f}}. \quad (7.4)$$

These peak strain formulas in time and frequency domains can be applied to Table 1. of [136] to derive the waveform Q value for each numerical simulation.

Using the peak strain values and the Q , one can then determine the waveform signal energy, normalized by total mass and distance. The strain signal energy for a general template is

$$H = \int_{-\infty}^{\infty} |h(t)|^2 dt = \int_{-\infty}^{\infty} |\tilde{h}(f)|^2 df. \quad (7.5)$$

For signals with a bandwidth small enough that the interferometer noise spectrum can be considered approximately constant in frequency, this expression leads to $\text{SNR}^2 \approx 4H/\text{PSD}(f_0)$. This approximation is why strain signal energy provides a particularly morphology independent SNR metric to be computed from numerical simulations. Additionally, H can be related to the total energy emitted in the form of gravitational waves into the ringing post-merger signal. The energy in a strain signal is [111]

$$E_{\text{GW}} = \frac{c^3}{G} \frac{4}{5} \pi^2 D^2 \int_{-\infty}^{+\infty} f^2 |\tilde{h}(f)|^2 df, \quad (7.6)$$

where D is the distance to the source. This expression has an unphysical divergence if integrated to frequencies above $2f_0$ for the damped-sine model. When the integral is confined to frequencies where h_{DS} is a good approximation, then in the limit $Q \gg 1$, the energy of a damped sine can be approximated as

$$E_{\text{GW}} = \frac{c^3}{G} \frac{4}{5} \pi^2 D^2 f_0^2 H. \quad (7.7)$$

M_{PM} is the amount of mass that is converted to gravitational wave energy during the

post-merger

$$H = (2\pi f_0 D)^{-2} \frac{5G}{c} M_{\text{PM}}. \quad (7.8)$$

These waveform properties are used to formulate the dependence of the model templates on astrophysical parameters. The center frequency f_0 of the lorentzian template model depends only on the total mass M of the binary [137]:

$$f_0(M, q) = \frac{C_1}{M}. \quad (7.9)$$

The constant C_1 parameterizes this dependence, and it is related to the tidal deformability constant $\tilde{\Lambda}$ of the binary. The distribution of f_0 then depends on the astrophysical distribution of masses of neutron stars in merging binary systems. For this, we assume a gaussian distribution of neutron star masses [138] centered around $1.35M_\odot$ with a width of $0.05M_\odot$.

In principle, the Q is expected to depend on the binary's parameters, such as the mass ratio, the tidal deformability, and the equation of state. For a given post merger model, it could be assumed that the EoS and tidal deformability are constant, with the only important parameter varying astrophysically being the mass ratio q . Using Eq. (7.4), I of [136] is used to calculate Q and plot it against these parameters. Fig. 7.2 shows that the dependence of Q on the mass ratio q does not appear to follow any particular functional form, but Q lies between 15 and 60 for mass ratios $q < 1.6$. In order to remain within this range, Q is unlikely to be a strong function of q . Because the expected mass ratio makes typical values of $q < 1.2$, the astrophysical variability of Q is sufficiently small that it does not affect this analysis, so it is fixed in each distribution. As a result, each distribution has only an astrophysical variation of f_0 . The choice of constants, C_1 and Q for each distribution is listed in Table 7.2.

The SNR of each signal is calculated from each configuration's power spectral

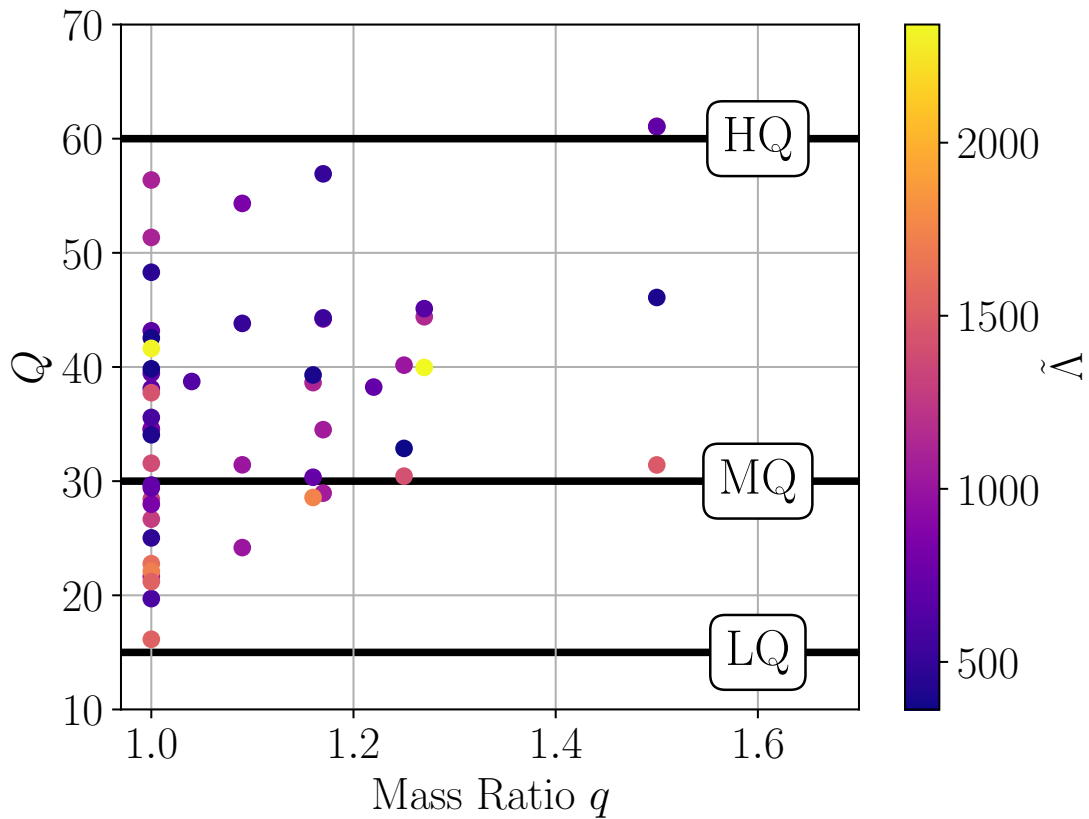


Figure 7.2: Lorentzian Q factors inferred from simulation data contained in I of [136] plotted against the mass ratio q of the binary. The colorbar shows the mass weighted tidal deformability $\tilde{\lambda}$. The solid lines correspond to the values of Q that have been chosen for the astrophysical distributions (see Table 7.2) of lorentzian signals in the analysis. These value are chosen in order to cover the range that is seen in simulation results.

Table 7.2: Different astrophysical distributions for various choices of constants C_1 in Eq. (7.9). The second last $M(f_0)$ represents the most likely f_0 for the distribution. Values of C_1 have been chosen in accordance with Table 1 of [137] to cover a range of frequencies (and tidal deformations). The distributions use fixed Q s which have been chosen to cover the range of values that are obtained from simulation results (See Fig. 7.2)

Distribution	C_1 (kHz M_\odot)	$M(f_0)$ (Hz)	Q
LQLF	4.86	1800	15
MQLF	4.86	1800	30
HQLF	4.86	1800	60
LQMF	7.02	2600	15
MQMF	7.02	2600	30
HQMF	7.02	2600	60
HQHF	9.10	3333	60

density (PSD) and the signal's waveform, $\tilde{h}_{\text{DS}}(f)$, using

$$\text{SNR}_{\text{config}}^2 = 4 \int_0^\infty \frac{|\tilde{h}_{\text{DS}}(f)|^2}{\text{PSD}_{\text{config}}(f)} df, \quad (7.10)$$

where \tilde{h}_{DS} depends on the waveform's central frequency f_0 and its Q factor. The average ratio of the detuned SNR to the wideband SNR, weighted over the distribution $p(f_0, Q)$, provides a figure of merit, η , to compare configurations:

$$\eta^2 \equiv \int p(f_0, Q) \frac{\text{SNR}_{\text{detuned}}^2}{\text{SNR}_{\text{wideband}}^2} df_0 dQ. \quad (7.11)$$

Similarly, the efficacy of the wideband configuration compared to the baseline of A+ is expressed as

$$\eta_{\text{WB/A+}}^2 \equiv \int p(f_0, Q) \frac{\text{SNR}_{\text{wideband}}^2}{\text{SNR}_{\text{A+}}^2} df_0 dQ. \quad (7.12)$$

Table 7.3: Optimal interferometer configurations and improvement factors, η (see Eq. (7.11)) for various astrophysical distributions, which are described in Table 7.2. The SEC is 55 m long with a roundtrip loss Λ_{SEC} of 0.1 %. The filter cavity is 300 m long with a roundtrip loss of 60 ppm. $\eta_{\text{WB/A+}}$ (see Eq. (7.12)) shows the average SNR improvement provided by the wideband configuration with respect to A+. The last column f_{peak} is the frequency (in Hz) that corresponds to the peak sensitivity in the detuning dip.

Dist.	T_{SEM}	ϕ_{SEC}	T_{FC}	$\Delta\omega_{\text{FC}}(\text{Hz})$	η	$\eta_{\text{WB/A+}}$	f_{peak}
LQLF	0.72%	2.38°	0.30%	1843	1.29	1.38	1741
MQLF	0.70%	2.36°	0.29%	1846	1.34	1.41	1748
HQLF	0.69%	2.36°	0.28%	1850	1.37	1.42	1753
LQMF	0.83%	1.37°	0.62%	2766	1.04	1.76	2505
MQMF	0.78%	1.37°	0.59%	2765	1.07	1.81	2519
HQMF	0.76%	1.36°	0.56%	2764	1.09	1.83	2527
HQHF	1.13%	0.76°	1.04%	3783	1.00	2.10	3227

7.3 RESULTS

Table 7.3 shows the optimal interferometer parameters and relative improvement that is achieved by detuning the SEC for various astrophysical distributions of BNS post-merger signals. The wideband configuration provides an average SNR improvement $\eta_{\text{WB/A+}}$ of 1.38 – 2.10 over A+. The average SNR improvement from detuning, η , lies between 1.00 and 1.37 relative to the wideband for the optical parameters of Table 7.1.

The improvement provided by detuning the interferometer is generally lower for distributions that center around higher frequencies and lower Q factors. The case in which detuning is most favorable, corresponding to the distribution labelled HQLF (high- Q low-frequency), is presented in Fig. 7.3, which shows strain noises and the SNR improvement over a range of lorentzian signals. This configuration has an $\eta = 1.37$.

From the shaded magenta region in Fig. 7.3, which encloses 90% of the signals under the HQLF model, the detector dip is sufficiently wide to provide a benefit over the entire range of expected parameters. This is noas the astrophysical distribution of the center frequencies has a spread of approximately 200 Hz, which makes the

distribution cover a wider band than the templates themselves for $Q > 10$. Because of this spread, even if the interferometer were lower loss and could obtain higher peak strain sensitivity in the detuned configuration, it cannot be configured to optimally match the interferometer resonance to the template resonance due to the distribution of center frequencies. Instead, loss widens the sensitive band to cover the distribution of templates, but reduces the peak sensitivity and relative SNR improvement.

The relative benefit for the detuned interferometer, reported independently for each model distribution, provides a best-case analysis where the astrophysical model of BNS post-mergers is assumed to be sufficiently constrained to allow interferometer optimization. The relative SNR can be cubed to represent the relative improvement to the detection volume or, relatedly, the relative rate of detections. The largest $\eta = 1.37$ corresponds to a factor of 2.57 increase in post-merger signal detection rate over the wideband configuration. If the post-merger model is not known, the detuning center frequency must be scanned by tuning the SEC roundtrip phase, distributing time amongst potential detection frequencies. Scanning can thus significantly reduce the rate benefit of detuning. The wideband optimization has improved sensitivity at all of the potential models and avoids the need for scanning.

7.4 ADDITIONAL CONSIDERATIONS

7.4.1 *Loss in the signal extraction cavity*

Fig. 7.4 shows the effect of SEC loss on the relative performance improvement of the detuned configuration over the wideband configuration. This figure indicates how severely the SEC detuning method is limited by optical loss within the SEC. The decreased SEM transmissivity required for a narrowband response creates an optical cavity where signal field crosses several optic surfaces and substrates such as the beamsplitter many more times than in the A+ or wideband configurations. Because of its use of optical resonance, the detuned configuration can nearly saturate the sensitivity available given the loss [139], and squeezing tends to simply increase the bandwidth at peak sensitivity, as shown in the strain curve in Fig. 7.3. On the

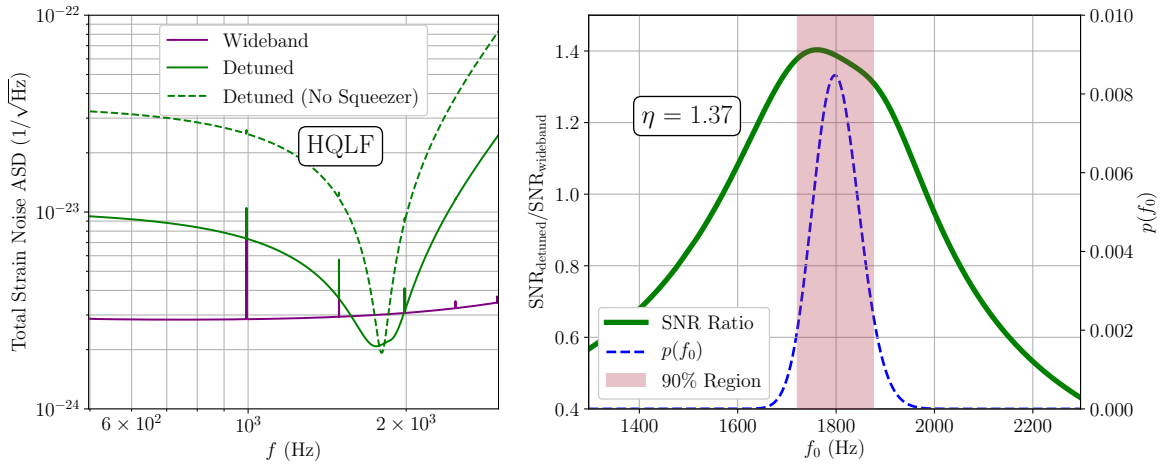


Figure 7.3: Performance comparison between the detuned and wideband configurations for the high-Q-low-frequency (HQLF) distribution of BNS post-merger signals (Table 7.2) which peaks at $f_0 = 1.8$ kHz, and has $Q = 60$. The left plot shows the strain noise curves for wideband, detuned and purely detuned (without squeezing) configurations. For the detuned configurations, the enhancement provided by squeezing in the resonant dip is degraded due to the roundtrip loss of the SEC. However, the width of the dip is broadened significantly. The plot on the right shows the signal-to-noise ratio (green trace) of the detuned configuration with respect to the wideband configuration over a range of lorentzian central frequencies. The dashed blue trace corresponds to the probability distribution of signals as a function of central frequency. The detuned interferometer has been optimized to maximize η for the distribution HQLF. The parameters of the detuned configuration are given in the third row of Table 7.3. The shaded magenta region corresponds to the region containing 90% of the signal probability. The overall SNR improvement η is calculated to be 1.37 for this configuration.

other hand, because of squeezing, the wideband configuration also approaches the maximum possible sensitivity, given loss, without sacrificing signal bandwidth.

A roundtrip power loss of 0.1 % in the SEC is used for the interferometer models in this analysis. This value is optimistic and results from adding assumed losses from all anti-reflection (AR) coating transmissions (500 ppm), reflections (200 ppm), clipping on the beam splitter and other optics (100 ppm), and imperfect interference at the beam splitter (200 ppm). Measurements from the LIGO interferometers in the third observing run (O3) establish an upper bound of 0.3% loss.

The A+ upgrade intends to address issues that impact loss, but is unlikely to drive the SEC loss below the optimistic value used herein, reiterating that the relative improvements quoted for detuning represent best-case scenarios. Further improvements, or future detectors, may achieve lower loss in the SEC by reducing the number of AR-coating transmissions (e.g., by flipping the beam splitter to favor the SEC and removing compensation plates), reducing the number of reflections (e.g., by avoiding telescope optics in the SEC), and by reducing wavefront phase distortion (e.g. better compensating substrate index variations during polishing).

7.4.2 *Operational Challenges*

Both the wideband and detuned configurations require lowering the SEM transmissivity from $T_{\text{SEM}} \approx 30\%$, which will alter the operating parameters of the interferometer and require time to implement. In addition to the signal fields, the interferometers also employ radio-frequency sideband fields to sense internal degrees of freedom related to the the power and signal extraction cavities, as well as the alignment of optics. The wideband configuration maintains the same operating modes for these fields and cavities, adjusted only by SEM transmission becoming $T_{\text{SEM}} \rightarrow 5\%$.

The detuned configuration requires a more extreme adjustment with $T_{\text{SEM}} \rightarrow 0.8\%$. In addition, detuned operation results in imbalanced sidebands that not only impact the signal, but also the RF control fields used for alignment control and stabilizing internal degrees of freedom. Maintaining detuning using the current configuration of auxiliary fields requires adding control-point offsets, which can impact the reliability of continuous operation [140, 141]. In total, detuning requires a considerable alteration

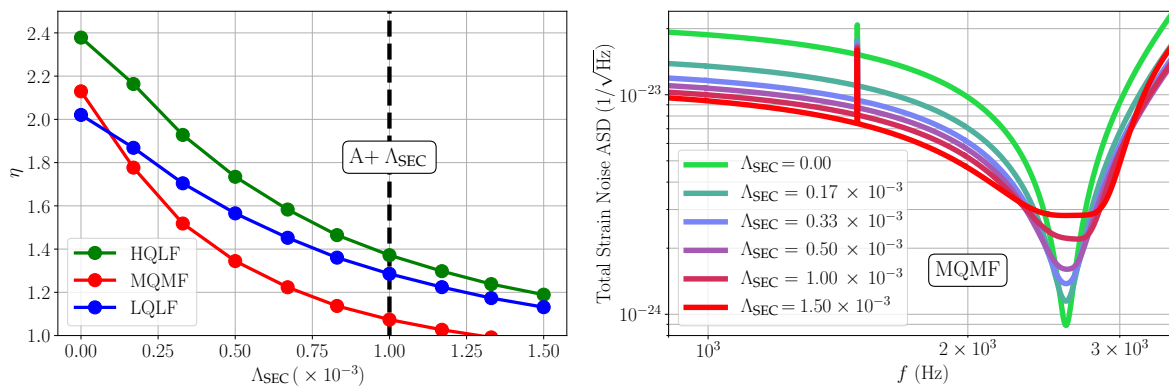


Figure 7.4: The effect of SEC loss on BNS post-merger sensitivity. The plot on the left demonstrates how the relative improvement factor for optimized interferometers (Eq. (7.11)) is limited by the roundtrip SEC loss Λ_{SEC} for various distribution models used for interferometer optimization. The $A + \Lambda_{\text{SEC}}$ loss limits sensitivity improvement to around 50% of the zero loss case. The right plot shows optimum strain curves for distribution model MQMF as SEC loss Λ_{SEC} is varied. Loss lowers the Q of the resonant band and squeezing widens the band to create a flat response. To maintain optimal performance, the resonance and squeezing effects of loss on dip bandwidth are balanced using the SEM transmission.

of the operating controls and electronics, which would require significant time to implement.

In this thesis, we have described the latest improvement to quantum noise limited sensitivity in inteferometric gravitational wave detectors. After four decades of research in quantum noise reduction in gravitational wave detectors, frequency dependent squeezing was deployed in the LIGO detectors deployed for the first time during the fourth gravitational wave observing run. This technique, which is routinely used in both LIGO detectors at the time of writing, has been instrumental in significantly increasing the detection rate of gravitational wave events. In addition to astrophysical impact, this has also ushered in the era of quantum non-demolition gravitational wave detectors that operate at sensitivities which surpass the standard quantum limit [142].

Optical loss and transverse mode-mismatch, however, severely limit the total noise reduction provided by squeezing. In order to achieve high levels of measured squeezing, it is imperative to understand and mitigate these sources of degradation. Future observing runs and third generation detectors aim to reach 10 dB of squeezing. Achieving this would require the total effective loss to be limited to less than 10%. The sum of the known losses is currently a factor of 2 above this and it is necessary to develop high quality optics in order to minimize propagation and intracavity losses. Of particular interest is a careful study of the effect of squeezer crystal losses and degradation which becomes dominant as other losses are reduced. Additionally, minimizing effective loss requires achieving near perfect mode-matching between the

various cavities of the interferometer. This is especially challenging in the presence of thermal effects that are exacerbated by the increasing power circulating in the arm cavities. Addressing this requires significant advances in our mode sensing and actuation capabilities; this is a highly active area of research in gravitational wave detection [120, 143, 144].

Beyond improvements to frequency dependent squeezing, there are also several proposals to explore novel techniques in quantum noise reduction [145–149]. In order to apply these techniques to working gravitational wave interferometers would, however, require significant progress in overcoming technical and operational challenges that currently limit the feasibility of these methods.

Finally, we also note that the technologies developed in the pursuit of improving quantum noise reduction in LIGO can have a far reaching impact in the field of optical precision measurement in general, where reducing imprecision and subsequent back action to overcome the standard quantum limit plays a pivotal role in the future of such experiments [150–154].

APPENDIX



LIST OF ACRONYMS AND SYMBOLS

Acronym	Description
ADF	Audio Diagnostic Field
AFC	Amplitude Filter Cavity
AOM	Acousto-Optic Modulator
ASD	Amplitude Spectral Density
BBH	Binary Black Hole
BNS	Binary Neutron Star
CLF	Coherent Locking Field
DARM	Differential Arm Length
DE	Damped Envelope
EOM	Electro-Optic Modulator
FC	Filter Cavity
FCG	Filter Cavity Green
HAM	Horizontal Access Module
HD	Homodyne
H1	LIGO Hanford Detector
HWHM	Half-width half-maximum
IFO	Interferometer
L1	LIGO Livingston Detector
LIGO	Laser Interferometer Gravitational Wave Observatory

APPENDIX A. LIST OF ACRONYMS AND SYMBOLS

Acronym	Description
LO	Local Oscillator
OPO	Optical Parametric Oscillator
OMC	Output Mode Cleaner
PDH	Pound Drever Hall
PPKTP	Periodically Poled Potassium Titanyl Phosphate
PSD	Power Spectral Density
QPD	Quadrant Photodiode
RMS	Root Mean Square
RLF	Resonant Locking Field
SEC	Signal Extraction Cavity
SEM	Signal Extraction Mirror
SHG	Second Harmonic Generation
SNR	Signal to Noise Ratio
SPDC	Spontaneous Parameter Downconversion
SQL	Standard Quantum Limit
SQZ	Squeezing
TTFSS	Table Top Frequency Stabilization Servo
VCO	Voltage Controlled Oscillator
WB	Wideband

Symbol	Description
\hat{a}, \hat{a}^\dagger	Optical mode ladder operators
$\hat{a}_+, \hat{a}_-^\dagger$	Sideband ladder operators
\hat{a}_1, \hat{a}_2	Quadrature ladder operators
$\mathbf{a}/\bar{\sigma}$	Sideband/Quadrature vector
\hat{b}	Generalized ladder operator
c	Speed of light, $c = 299\,792\,458$ m/s
e	Scalar quantity/Error signal
E	Energy
\mathcal{E}	Electric Field
f	Frequency
\bar{g}	Nonlinear gain
G	Gravitational Constant, $G = 6.674 \times 10^{-11} \text{m}^3 \text{kg}^{-1} \text{s}^{-2}$
G	ADF transmission gain (Chapters 5 and 6)
h	Strain
\hbar	Reduced Planck constant, $\hbar = 1.055 \times 10^{-34}$ Js
\hat{H}	Hamiltonian
H	Strain signal energy
\mathbf{H}/\mathbb{H}	Optical system transfer matrix (sideband/quadrature basis)
I	Photocurrent
k	Wavenumber
\mathcal{K}	Optomechanical coupling
L	Length
m	Mass
m_p, m_q	Quadrature observable
N	Noise
P	Power
\mathbf{P}	Induced polarization
Q	Quality Factor
r	Optical field reflectivity
R	Optical power reflectivity
S_x	Power spectral density of quantity x

APPENDIX A. LIST OF ACRONYMS AND SYMBOLS

Symbol	Description
t	Optical field transmissivity
T	Optical power transmissivity
z	Squeeze factor
Z	Cavity enhanced squeeze factor
α	Coherent field amplitude
γ	Bandwidth
Δ	Detuning angle
η	Squeezing efficiency
Λ	Optical loss
θ	Squeezing rotation
θ_D	Demodulation angle
ω	Angular frequency $\omega = 2\pi f$
Ω	Angular sideband frequency
ϕ	Squeezing angle
ψ	Squeezer pump phase
σ_X^2	Variance of operator X
Υ	Mode matching efficiency
χ	Susceptibility
Ξ	Dephasing
ζ	Local oscillator phase

APPENDIX

B

OPTICAL CAVITIES

B.1 FABRY-PEROT CAVITY

An optical Fabry-Perot cavity, shown in Fig. B.1, consists of an input and an output mirror. We denote the field reflectivities of the input and output mirrors by r_1 and r_2 respectively. Similarly, the field transmissivities are denoted by t_1 and t_2 . The roundtrip phase of the cavity is given by 2ϕ , where $\phi = kL$ for a cavity length L and wavenumber k . The relation between the incoming and reflected fields is given by [155],

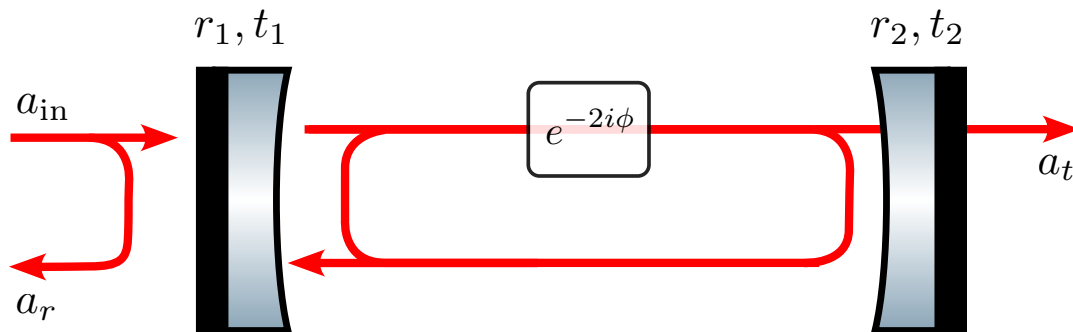


Figure B.1: Fabry-Perot cavity.

$$r = \frac{a_r}{a_{\text{in}}} = r_1 - \frac{t_1^2 r_2 e^{-2i\phi}}{1 - r_1^2 r_2 e^{-2i\phi}}. \quad (\text{B.1})$$

For a resonant cavity, the round trip phase is a multiple of 2π , i.e., $e^{2i\phi} = 1$. Using this, ϕ can also be written in terms of the frequency detuning from resonance, Ω ,

$$\phi = \Omega L/c. \quad (\text{B.2})$$

In the following calculations, we assume that the output mirror is completely reflective ($r_2 = 1, t_2 = 0$) and the cavity mirrors do not have loss, i.e. $r_1^2 + t_1^2 = 1$. For a small detuning, we can expand the exponential in Eq. (B.1) to write,

$$r_c = \frac{r_1 - (1 - 2i\phi)}{1 - r_1(1 - 2i\phi)}. \quad (\text{B.3})$$

Using the high finesse approximation where $t_1 \ll 1$, we can write,

$$r_c = \sqrt{1 - t_1^2} \approx 1 - T_1/2, \quad (\text{B.4})$$

where $T_1 = t_1^2$, is the power transmissivity of the input mirror. This gives us the following expression for the cavity reflectivity:

$$r_c = \frac{-T_1/2 + 2i\phi}{T_1/2 + 2i\phi - iT_1\phi} \approx -\frac{1 - 4i\phi/T_1}{1 + 4i\phi/T_1} = -\frac{1 - i\Omega/\gamma}{1 + i\Omega/\gamma}, \quad (\text{B.5})$$

where $\gamma = cT_1/4L$ is known as the cavity half bandwidth or cavity pole. The transfer function between the circulating and output fields of a cavity is given by,

$$t_c = \frac{t_1}{1 - r_1 e^{-2i\phi}} \approx \frac{\sqrt{T_1}}{T_1/2 + 2i\phi} = \sqrt{\frac{c\gamma}{L}} \frac{1}{\gamma + i\Omega}. \quad (\text{B.6})$$

B.2 INTERFEROMETER OPTICAL GAIN

In this section, we calculate the transfer from a displacement signal in a Fabry-Perot Michelson interferometer (Fig. B.2) to the output power at the interferometer's

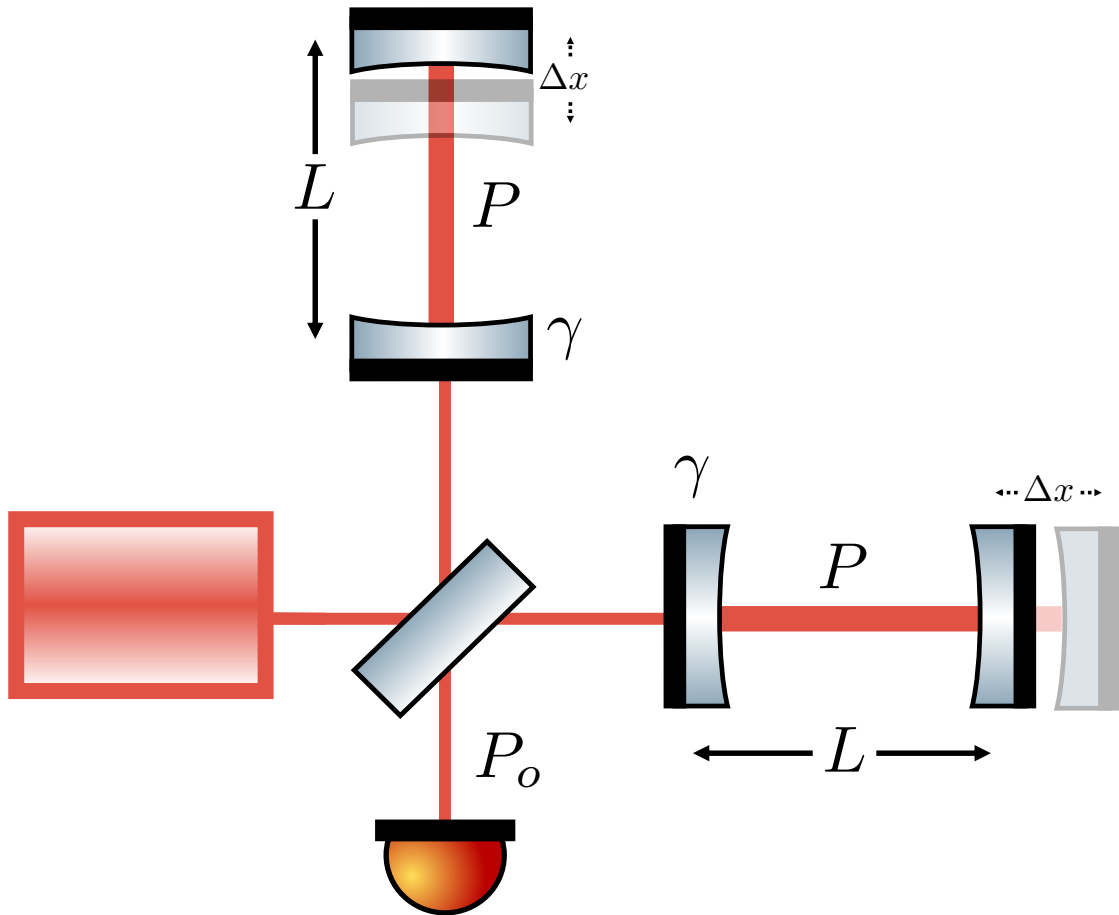


Figure B.2: Fabry-Perot Michelson Interferometer.

antisymmetric port. The arm cavity power, bandwidth and length are given by P , γ and L respectively. At a sideband frequency Ω , a displacement modulation $\Delta x(\Omega)$ provides a phase shift of $e^{-2ik\Delta x}$ to the circulating field in the cavity. The field exiting one of the arm cavities is given by

$$\mathcal{E}_1(\Omega) \approx t_c(\Omega)\sqrt{P}(1 - 2ik\Delta x(\Omega)), \quad (\text{B.7})$$

where t_c is the cavity field output given in Eq. (B.6). Similarly, the field exiting the other arm cavity sees the same phase shift but with an opposite sign, and is given by,

$$\mathcal{E}_2(\Omega) \approx t_c(\Omega)\sqrt{P}(1 + 2ik\Delta x(\Omega)). \quad (\text{B.8})$$

The field at the anti-symmetric port of the interferometer is then given by,

$$\mathcal{E}_{\text{as}}(\Omega) = \frac{\mathcal{E}_2 - \mathcal{E}_1}{\sqrt{2}} = 4ik \frac{t_c(\Omega)}{\sqrt{2}} \sqrt{P} \Delta x(\Omega). \quad (\text{B.9})$$

The output field in the interferometer beats with a bright field with power P_o at the carrier frequency known as a local oscillator. In LIGO's DC homodyne readout, this local oscillator is generated by operating the interferometer slightly offset from the dark fringe. The beatnote between the signal and local oscillator at the output photodetector is given by

$$P_{\text{sig}}(\Omega) = \sqrt{P_o} \mathcal{E}_{\text{AS}}(\Omega) \quad (\text{B.10})$$

The optical gain at frequency Ω is thus, given by,

$$g(\Omega) = P_{\text{sig}}(\Omega)/\Delta x(\Omega) = 4k \sqrt{PP_o} \sqrt{\frac{c\gamma}{2L}} \frac{1}{\gamma + i\Omega} \quad (\text{B.11})$$

B.3 INTERFEROMETER SHOT NOISE

The optical power measured by photo-detector is related to the photon flux,

$$P_{\text{pd}} = \hbar\omega_0 \hat{N} = \hbar\omega_0 \hat{a}^\dagger \hat{a} \quad (\text{B.12})$$

For a homodyne measurement of a signal with a local oscillator, this can be written as

$$P_{\text{pd}} = \hbar\omega_0 \hat{N} = \hbar\omega_0(\alpha^* + \delta\hat{a}^\dagger)(\alpha + \delta\hat{a}), \quad (\text{B.13})$$

where $\delta\hat{a}$ corresponds to the signal/noise field. Writing the local oscillator $\alpha = |\alpha|e^{i\phi}$. We can then write the above expression as

$$P_{\text{PD}} = P_o + \sqrt{2}\hbar\omega_0|\alpha|(\hat{a}_1 \cos \phi + \hat{a}_2 \sin \phi) + O(\hat{a}_1^2) + O(\hat{a}_2^2), \quad (\text{B.14})$$

where $P_o = \hbar\omega_0|\alpha|^2$ is the local oscillator's DC power on the photodiode, and \hat{a}_1, \hat{a}_2 are the quadrature operators of the signal field. For a bright local oscillator, we can ignore the higher order terms in \hat{a}_1 . The power spectral density of the measured power can be calculated using the Wiener-Khinchin theorem [53],

$$S_P(\Omega) = \int_{-\infty}^{\infty} dt e^{-i\Omega t} \langle P_{\text{PD}}(t) P_{\text{PD}}(0) \rangle. \quad (\text{B.15})$$

Without loss of generality, we can set $\phi = \pi/2$ ¹. The spectral density of the measured power is, then, given by,

$$S_P(\Omega) = 2\hbar^2\omega_0^2|\alpha|^2 \int_{-\infty}^{\infty} dt e^{-i\Omega t} \langle \hat{a}_2(t) \hat{a}_2(0) \rangle = 2\hbar\omega_0 P_o S_{\hat{a}_2}(\Omega) \quad (\text{B.16})$$

From Eq. (2.15), we know that the spectral density of a quadrature for a coherent vacuum state is equal to 1. Thus, we can write Eq. (B.16) as,

$$S_P^{\text{SN}} = 2\hbar c K P_o. \quad (\text{B.17})$$

We can then use the optical gain calculated in Eq. (B.11) to convert this expression into units of strain

$$S_h^{\text{SN}} = S_P^{\text{SN}} / |Lg(\Omega)|^2 = \frac{\hbar\gamma}{4kLP} \left(1 + \frac{\Omega^2}{\gamma^2} \right) \quad (\text{B.18})$$

¹We choose this value so that the measurement probes the phase quadrature. Choosing $\phi \neq 0$ will yield a combination of the spectral densities of the two quadratures, which are equal for a coherent vacuum state

APPENDIX



FILTER CAVITY INITIAL ALIGNMENT

This appendix describes the initial alignment of 300 m filter cavities at the LIGO detectors. The cavity mirror alignments are initially estimated from the survey results obtained during the construction of the cavity infrastructure [156, 157]. After this, the following procedure (Fig. C.1) is followed to align the cavity to the 532 nm locking field,

- a) The steering mirrors before the filter cavity are adjusted to make sure that the cavity single pass beam exits the vacuum chamber's view port. Both filter cavity mirrors' transmissivity in 532 nm is 1 %, and a 1 mW input beam would result in a single pass transmission power of $10 \mu\text{W}$, which is bright enough to be used for alignment.
- b) The filter cavity input mirror is adjusted such that the incoming beam and the retro-reflection are co-aligned with each other.
- c) A retro-reflector is installed on the single path transmission from the filter cavity. This beam undergoes another reflection from the filter cavity end mirror. The filter cavity end mirror is then adjusted so that all the reflections line up with each other. At this point, cavity flashes should be visible on transmission and can be used for precise alignment of the filter cavity.

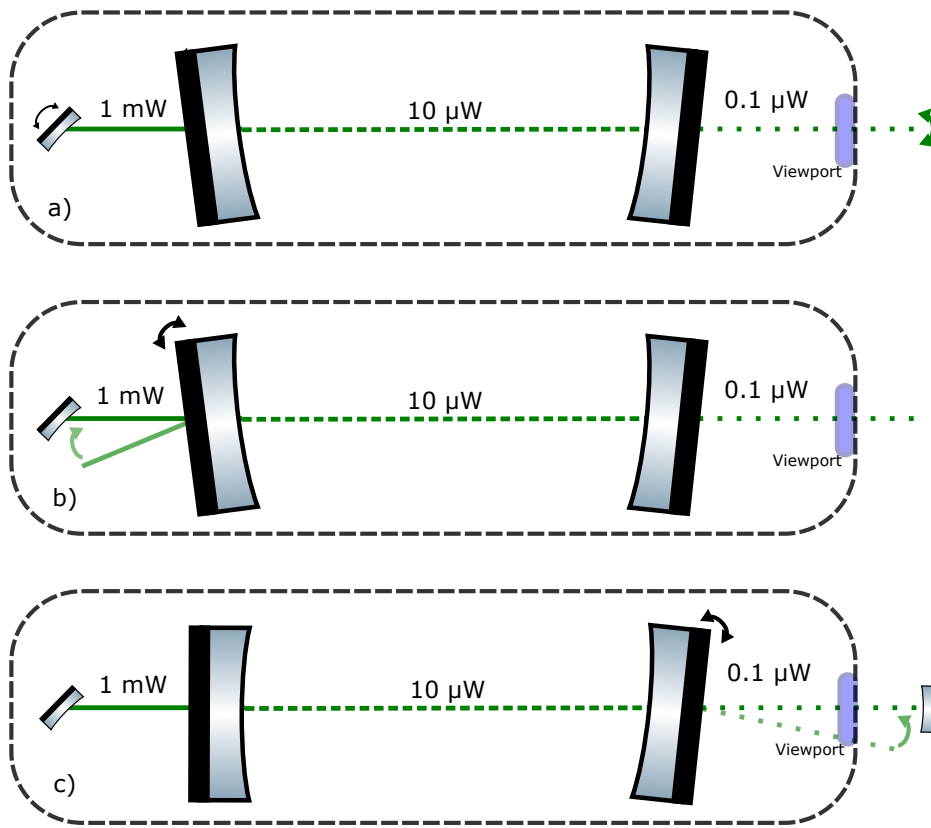


Figure C.1: Filter cavity initial alignment procedure

Light leaking from the LIGO interferometer’s output Faraday isolator into the squeezing injection path is modulated by residual length noise in the filter cavity to produce parasitic signals that contaminate the measured gravitational wave signal with noise. In this appendix, we roughly compute the contribution of the this backscattered light to the noise curve of the interferometer.

In other to measure the conversion between filter cavity length modulations and the displacement signal observed on the interferometer, the filter cavity end mirror position was driven with a large 40 Hz excitation [158] with an rms of 9 pm. This in turn, produced a excess in noise in a 2.5 Hz band around 40 Hz with an r.m.s. noise of 6.8×10^{-20} m. From this measurement we can roughly calculate that the conversion between filter cavity length and excess noise in DARM is around 7.5×10^{-19} m/pm. After accounting for the radiation pressure gain in the interferometer arms which can be approximated as a $1/f^2$ response below 35 Hz, we can make an model a rough conversion between filter cavity length noise and excess noise in DARM (Fig. D.1).

The filter cavity length noise shown in Fig. 6.10 is measured in-loop. In order to compute the true length noise of the filter cavity, we need to account for the sensing noise that is re-injected by the control loop. After removing the loop suppression of the RLF length control (Fig. 6.9), we observe in Fig. D.2 that the most of the environmental noise in the filter cavity length is at low frequencies below 10 Hz¹. Since the sensor is

¹For these computations, the gain of the measured transfer function has been adjusted in order to

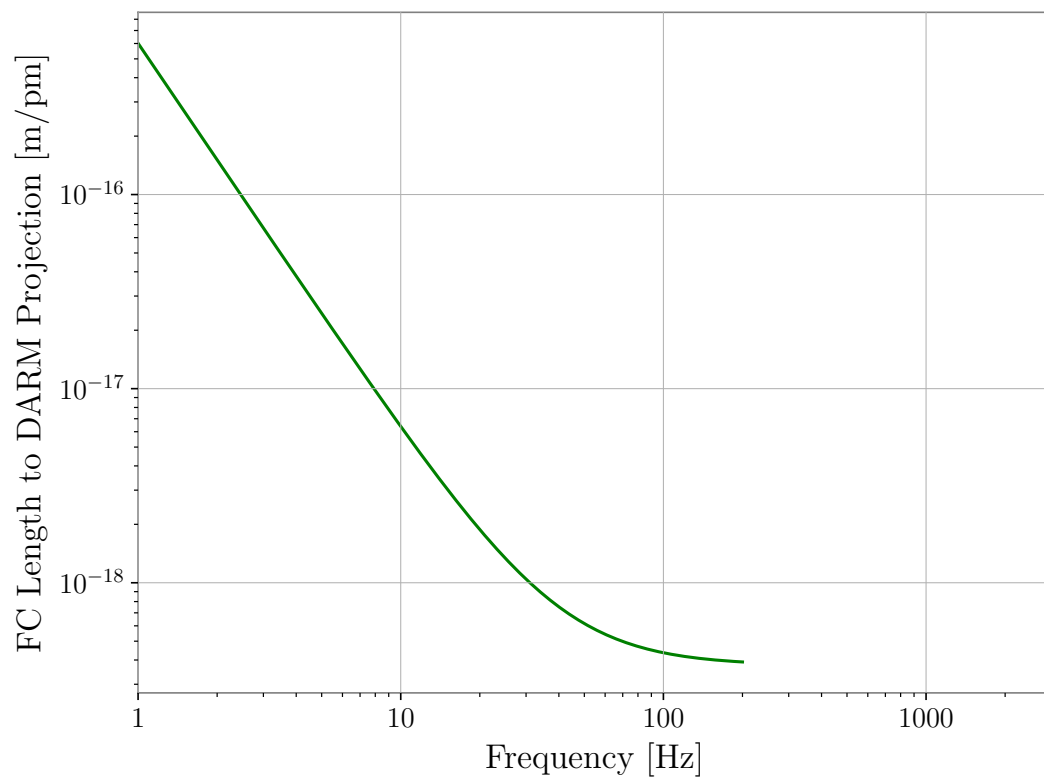


Figure D.1: Conversion between filter cavity length noise and excess noise in the interferometer.

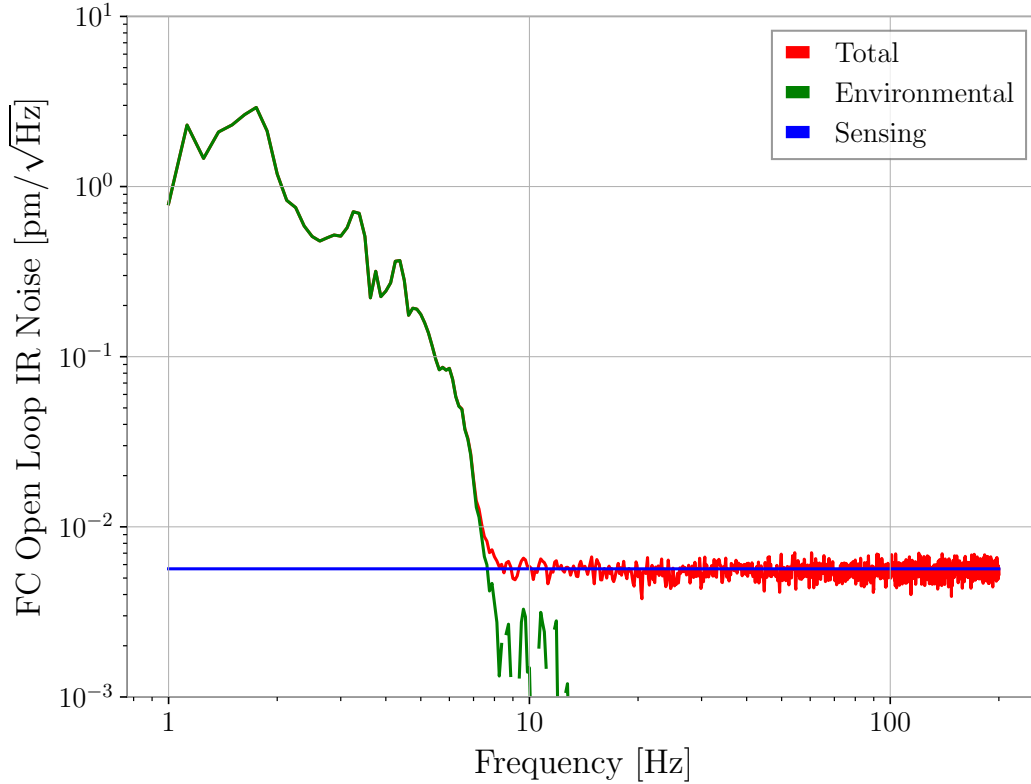


Figure D.2: Filter cavity open loop length noise. The flat shot noise at high frequencies is the sensor’s noise floor.

shot-noise limited, it follows that the sensing noise is flat.

After applying the loop suppression to the environmental noise and the closed loop gain to the sensing noise, we can estimate the true length noise of the filter cavity (Fig. D.3). Projecting this length noise to the interferometer (Fig. D.1) gives us an estimate of the contribution of the backscatter from the filter cavity to the interferometer’s noise spectrum. This is shown in Fig. D.4. We see that while this noise is below the interferometer’s noise floor, this difference is less than two orders of magnitude below. For future upgrades to the LIGO detectors which include higher

account for changes in the plant

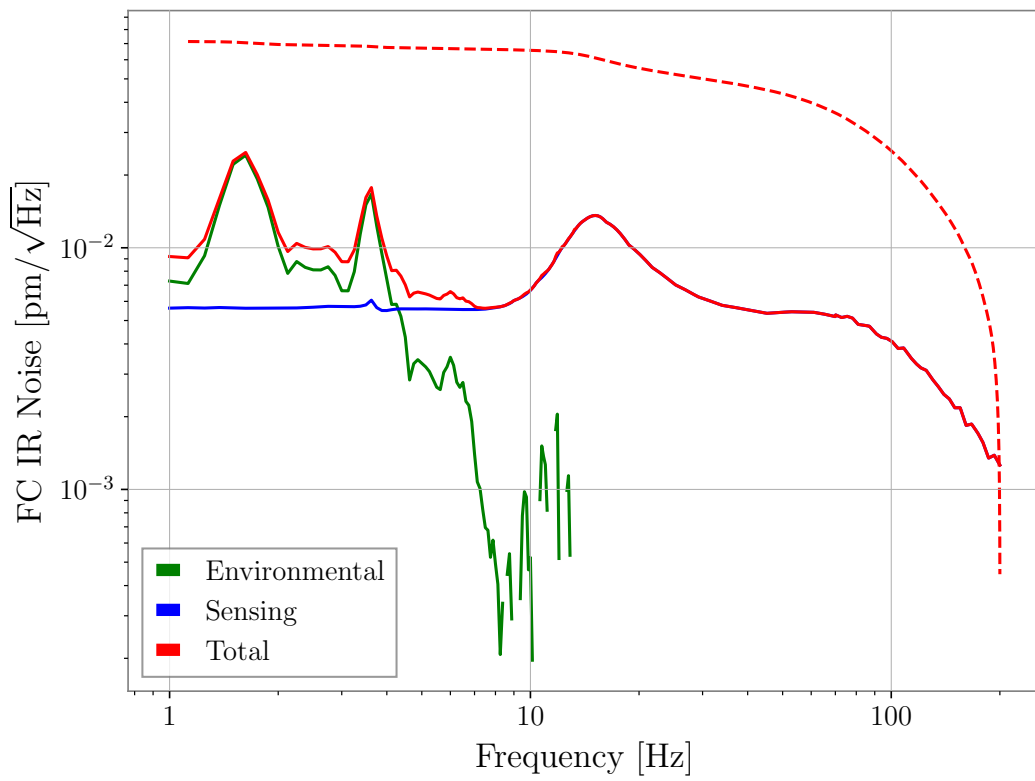


Figure D.3: Filter cavity true length noise.

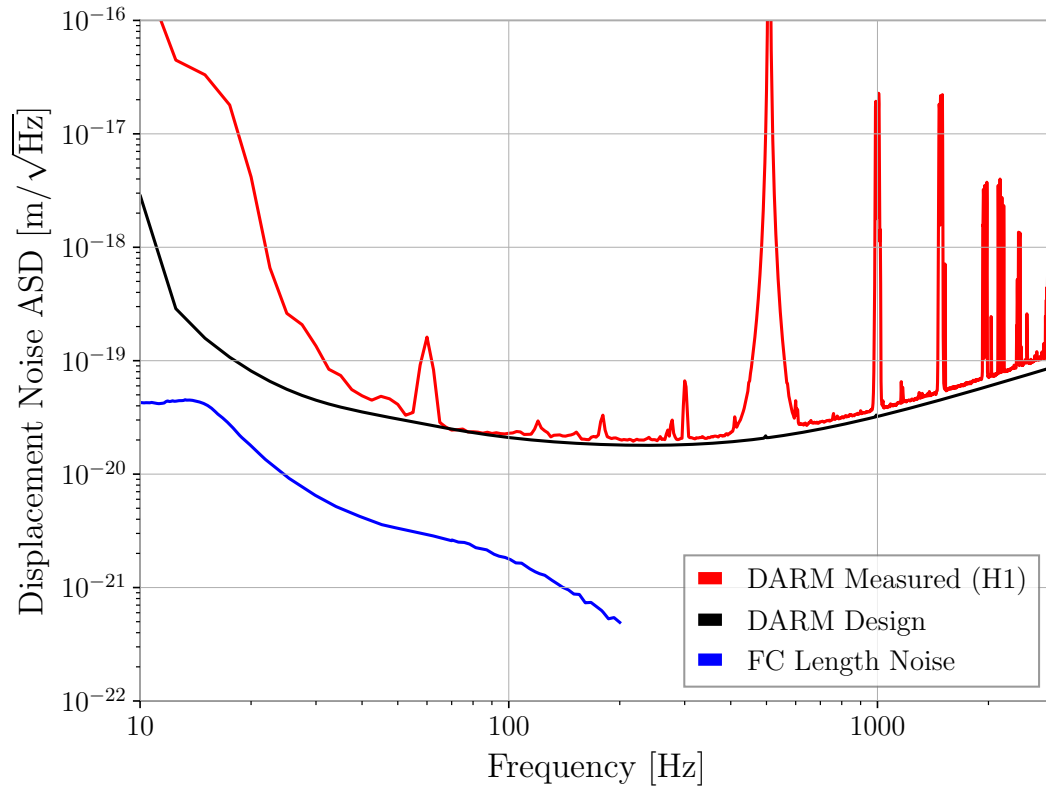


Figure D.4: Filter cavity length noise projected to the interferometer.

levels of power and squeezing, it is imperative to mitigate the effect of backscatter and further minimize residual filter cavity length noise.

APPENDIX



OPO CRYSTAL DEGRADATION

E.1 CRYSTAL LOSS AT 532 NM

Green losses present an operational issue as LIGO moves towards higher generated squeezing levels.

E.1.1 *Gray Tracking in KTP*

Gray tracking refers to laser induced photochromic and electrochromic damage in KTP that lead to the formation of visible ‘gray tracks’ [159]. Irradiation by laser power (which contains energy that is mostly above the crystal bandgap) leads to the formation of electron/hole pairs in the crystal. In most case, these pairs rapidly recombine without altering the material. However, some of these electrons and holes are captured by Fe^{3+} and Ti^{4+} impurities, which leads to the creation of absorption centers in the crystal.

E.1.2 *Green OPO losses in LIGO*

Green loss studies at LIGO Livingston (L1) [160] and LIGO Hanford (H1) [161] suggest the presence of gray tracking effects. Both sites show a rapid degradation in 532 nm transmission through the OPO in the first 1-2 weeks following a crystal position

movement (Fig. E.1), which asymptotically flattens out soon after. The intensity of pump light in the crystal is of the order of 10-100 kW/cm². This short timescale is consistent with gray tracking related green loss reported in literature. Higher intensities result in degradation with timescales as short as 15 minutes being recorded for 100 MW/cm² intensities [162–164]. Apart from pump intensity, damage from gray tracking depends on other factors too. Higher crystal temperatures correspond to lower damage related loss, with gray tracking vanishing for crystals that are operated above 150°C [162]. Additionally, the method of crystal growth also affects gray tracking, with hydro-thermally grown KTP being more resistant to gray tracking than flux grown KTP [165]. Annealing KTP in air has also been shown to make it more resistant to gray tracking [166]

Because of the cavity enhancement for generating 1064 nm squeezed light, the amount of green pump power required to produce high levels of squeezing is significantly lower than what is required for single pass crystals. As a result, LIGO's 532 nm pump intensity is 3-4 orders of magnitude below those studied in literature and a direct comparison between the different timescales is not very informative.

E.2 CRYSTAL LOSS AT 1064 NM

Red crystal losses directly limit usable squeezing levels. Such losses can be observed as OPO intracavity loss, and are often referred to as the OPO escape efficiency.

E.2.1 GRIIRA

Studies of GRIIRA (Green Induced InfraRed Absorption) show that while green light does induce infrared loss in KTP, this too happens on fast timescales that are similar to those of the green degradation. Additionally, once the crystal ceases to be illuminated by green light, the infrared losses reduce over relatively short timescales, with the absorption reducing to unmeasurable levels after relaxation for a few days [163]. The cited study used 320 MW/cm² of green light.

GRIIRA thus suggests that green light can indeed introduce red absorption losses,

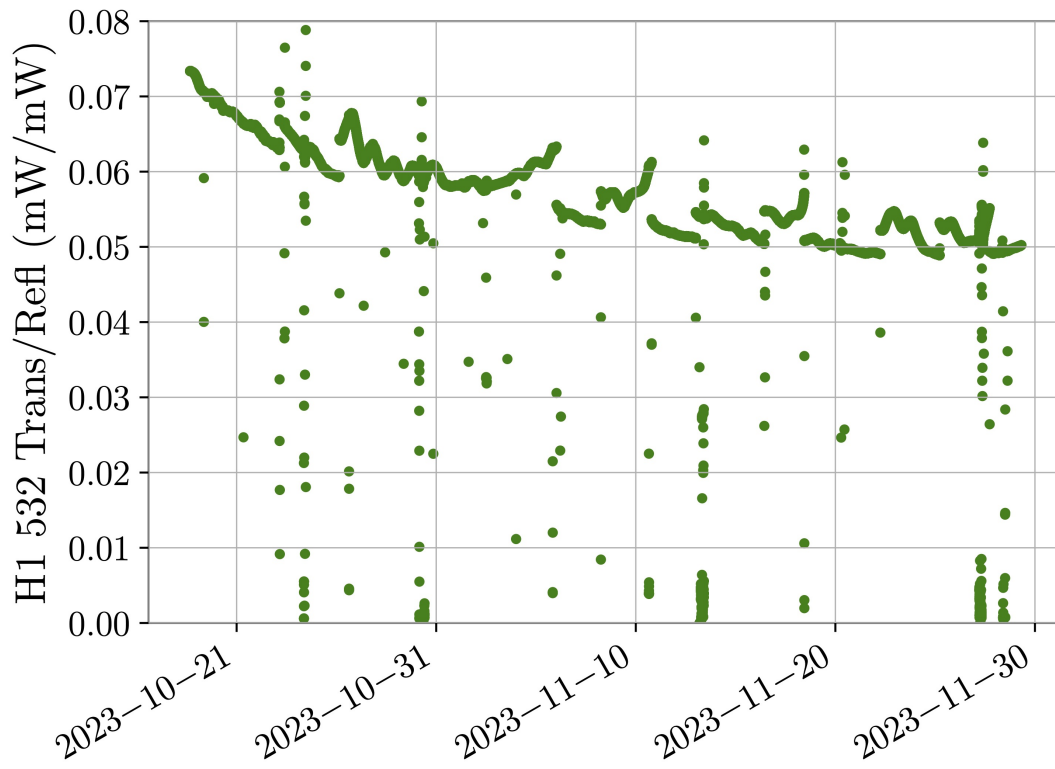


Figure E.1: OPO 532 nm transmission at H1 during O4 after crystal movement in Oct. 2023.

but that these red losses quickly return to almost unmeasurable levels after turning off green pump light for a few days. It is unknown whether this effect is a limitation for squeezing at the low pump intensities used in LIGO.

E.2.2 *LIGO squeezing losses from OPO red cavity losses*

No evidence of a slow degradation of IR loss in the OPO is clear from looking at long term squeezing trends in O4 (Fig. 6.15). For the LIGO OPO, there are limited measurements of red crystal losses after installation, as no 1064 nm light is coupled in through M1 port (the squeezed light out-coupler). Making this path available would allow *in-situ* red cavity scans sensitive to intracavity squeezing losses. Due to the high reflectivity of the 1064 nm in-coupler (M2), measurements of the ratio of transmitted OPO seed power to reflected OPO seed power are not very sensitive to small changes in 1064 nm intracavity losses [167].

E.2.3 *Crystal spot movement at H1*

In an attempt to track down unknown squeezing loss, the OPO pump beam spot on the squeezer crystal at H1 was moved in October 2023 [117]. The crystal movement resulted in an increase in the amount of measured squeezing in both the diagnostic homodyne detector and interferometer (Fig. E.2). However, there is no evidence to suggest that the excess loss before the crystal move was related to the green light induced absorption loss in the crystal. It is more likely that the previous beam position on to lie in a region of the crystal with excess optical loss. Further study to understand squeezing loss after long term squeezer operation in LIGO is ongoing.

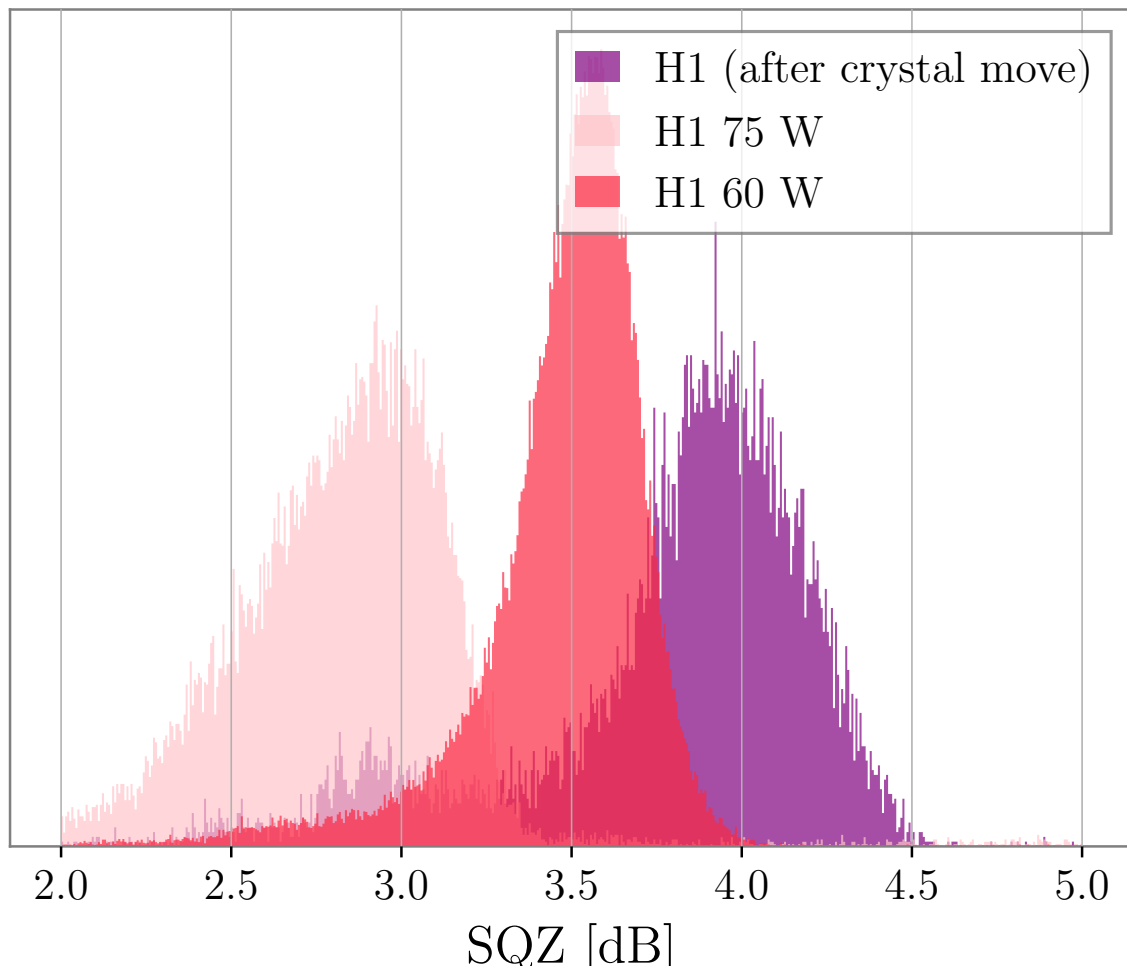


Figure E.2: Normalized distribution of measured squeezing at H1. As discussed in Section 6.4.3, the amount of measured squeezing increased after reducing the interferometer’s input laser power. Moving the beam spot on the crystal further increased the measured squeezing by a significant amount.

BIBLIOGRAPHY

- [1] H. J. Kimble et al. “Conversion of conventional gravitational-wave interferometers into quantum nondemolition interferometers by modifying their input and/or output optics”. In: *Phys. Rev. D* 65.2 (2 Dec. 2001), p. 022002.
- [2] B. P. Abbott et al. “Observation of Gravitational Waves from a Binary Black Hole Merger”. In: *Phys. Rev. Lett.* 116.6 (6 Feb. 2016), p. 061102.
- [3] R. Abbott et al. “Tests of general relativity with binary black holes from the second LIGO-Virgo gravitational-wave transient catalog”. In: *Phys. Rev. D* 103 (12 June 2021), p. 122002.
- [4] R. Abbott et al. “GWTC-3: Compact Binary Coalescences Observed by LIGO and Virgo during the Second Part of the Third Observing Run”. In: *Phys. Rev. X* 13 (4 Dec. 2023), p. 041039.
- [5] B. P. Abbott et al. “GW170817: Observation of Gravitational Waves from a Binary Neutron Star Inspiral”. In: *Physical Review Letters* 119.16 (16 Oct. 2017), p. 161101.
- [6] B. P. Abbott et al. “Gravitational Waves and Gamma-Rays from a Binary Neutron Star Merger: GW170817 and GRB 170817A”. In: *The Astrophysical Journal Letters* 848.2 (Oct. 2017), p. L13.
- [7] B. P. Abbott et al. “Multi-messenger Observations of a Binary Neutron Star Merger”. In: *The Astrophysical Journal* 848.2 (Oct. 2017), p. L12.
- [8] Daniel Kasen et al. “Origin of the heavy elements in binary neutron-star mergers from a gravitational-wave event”. In: *Nature* 551.7678 (2017), pp. 80–84.

-
- [9] B. P. Abbott et al. “GW170817: Measurements of Neutron Star Radii and Equation of State”. In: *Physical Review Letters* 121.16 (Oct. 2018).
- [10] B. P. Abbott et al. “Constraining the p -Mode- g -Mode Tidal Instability with GW170817”. In: *Phys. Rev. Lett.* 122 (6 Feb. 2019), p. 061104.
- [11] B. P. Abbott et al. “GW190425: Observation of a Compact Binary Coalescence with Total Mass $\sim 3.4 M_{\odot}$ ”. In: *The Astrophysical Journal* 892.1 (Mar. 2020), p. L3.
- [12] Abbott, R. et al. “Search for intermediate-mass black hole binaries in the third observing run of Advanced LIGO and Advanced Virgo”. In: *A&A* 659 (2022), A84.
- [13] R. Abbott et al. “Observation of Gravitational Waves from Two Neutron Star-Black Hole Coalescences”. In: *The Astrophysical Journal Letters* 915.1 (June 2021), p. L5.
- [14] R. Abbott et al. “GW190814: Gravitational Waves from the Coalescence of a 23 Solar Mass Black Hole with a 2.6 Solar Mass Compact Object”. In: *The Astrophysical Journal* 896.2 (June 2020), p. L44.
- [15] R. Abbott et al. “Population Properties of Compact Objects from the Second LIGO-Virgo Gravitational-Wave Transient Catalog”. In: *The Astrophysical Journal Letters* 913.1 (May 2021), p. L7.
- [16] R. Abbott et al. “Constraints on the Cosmic Expansion History from GWTC-3”. In: *The Astrophysical Journal* 949.2 (June 2023), p. 76.
- [17] R. Abbott et al. “All-sky search for continuous gravitational waves from isolated neutron stars using Advanced LIGO and Advanced Virgo O3 data”. In: *Phys. Rev. D* 106 (10 Nov. 2022), p. 102008.
- [18] R. Abbott et al. “All-sky search for short gravitational-wave bursts in the third Advanced LIGO and Advanced Virgo run”. In: *Phys. Rev. D* 104 (12 Dec. 2021), p. 122004.
- [19] R. Abbott et al. “Constraints on dark photon dark matter using data from LIGO’s and Virgo’s third observing run”. In: *Phys. Rev. D* 105 (6 Mar. 2022), p. 063030.

BIBLIOGRAPHY

- [20] R. Abbott et al. “Constraints on Cosmic Strings Using Data from the Third Advanced LIGO–Virgo Observing Run”. In: *Phys. Rev. Lett.* 126 (24 June 2021), p. 241102.
- [21] J. Aasi, et al. “Advanced LIGO”. In: *Classical and Quantum Gravity* 32.7 (Mar. 2015), p. 074001.
- [22] F. Acernese et al. “Advanced Virgo: A Second-Generation Interferometric Gravitational Wave Detector”. In: *Class. Quantum Grav.* 32.2 (Dec. 2014), p. 024001.
- [23] T Akutsu et al. “Overview of KAGRA: KAGRA science”. In: *Progress of Theoretical and Experimental Physics* 2021.5 (Aug. 2020), 05A103.
- [24] K L Dooley for the LIGO Scientific Collaboration. “Status of GEO 600”. In: *Journal of Physics: Conference Series* 610.1 (Apr. 2015), p. 012015.
- [25] M Saleem et al. “The science case for LIGO-India”. In: *Classical and Quantum Gravity* 39.2 (Dec. 2021), p. 025004.
- [26] J. Mizuno et al. “Resonant sideband extraction: a new configuration for interferometric gravitational wave detectors”. In: *Physics Letters A* 175.5 (Apr. 1993), pp. 273–276.
- [27] Craig Cahillane et al. “Calibration Uncertainty for Advanced LIGO’s First and Second Observing Runs”. In: *Phys. Rev. D* 96.10 (10 Nov. 2017), p. 102001.
- [28] Ling Sun et al. “Characterization of Systematic Error in Advanced LIGO Calibration”. In: *Class. Quantum Grav.* 37.22 (Oct. 2020), p. 225008.
- [29] S M Aston et al. “Update on quadruple suspension design for Advanced LIGO”. In: *Classical and Quantum Gravity* 29.23 (Oct. 2012), p. 235004.
- [30] David Reitze et al. “Cosmic Explorer: The U.S. Contribution to Gravitational-Wave Astronomy beyond LIGO”. In: *Bulletin of the AAS* 51.7 (Sept. 2019).
- [31] Matthew Evans et al. *A Horizon Study for Cosmic Explorer: Science, Observatories, and Community*. 2021.
- [32] M Punturo et al. “The Einstein Telescope: a third-generation gravitational wave observatory”. In: *Classical and Quantum Gravity* 27.19 (Sept. 2010), p. 194002.

-
- [33] Alessandra Buonanno and Yanbei Chen. “Quantum noise in second generation, signal-recycled laser interferometric gravitational-wave detectors”. In: *Physical Review D* 64.4 (4 July 2001), p. 042006.
- [34] A. A. Clerk et al. “Introduction to quantum noise, measurement, and amplification”. In: *Rev. Mod. Phys.* 82 (2 Apr. 2010), pp. 1155–1208.
- [35] Vladimir B. Braginsky, Farid Ya Khalili, and Kip S. Thorne. *Quantum Measurement*. Cambridge: Cambridge University Press, 1992.
- [36] Vladimir B. Braginsky and Yurii I. Vorontsov. “Quantum-Mechanical Limitations in Macroscopic Experiments and Modern Experimental Technique”. In: *Sov. Phys. Usp.* 17.5 (May 1975), p. 644.
- [37] Carlton M. Caves. “Quantum-Mechanical Radiation-Pressure Fluctuations in an Interferometer”. In: *Phys. Rev. Lett.* 45.2 (2 July 1980), pp. 75–79.
- [38] Vladimir B. Braginsky et al. “Noise in gravitational-wave detectors and other classical-force measurements is not influenced by test-mass quantization”. In: *Phys. Rev. D* 67 (8 Apr. 2003), p. 082001.
- [39] Alessandra Buonanno and Yanbei Chen. “Optical noise correlations and beating the standard quantum limit in advanced gravitational-wave detectors”. In: *Classical and Quantum Gravity* 18.15 (July 2001), pp. L95–L101.
- [40] Haocun Yu et al. “Quantum Correlations between Light and the Kilogram-Mass Mirrors of LIGO”. In: *Nature* 583.7814 (July 2020), pp. 43–47.
- [41] J. Abadie, et al. “A gravitational wave observatory operating beyond the quantum shot-noise limit”. In: *Nature Physics* 7.12 (12 Dec. 2011), pp. 962–965.
- [42] M. Tse et al. “Quantum-Enhanced Advanced LIGO Detectors in the Era of Gravitational-Wave Astronomy”. In: *Physical Review Letters* 123.23 (23 Dec. 2019), p. 231107.
- [43] F. Acernese et al. “Quantum Backaction on Kg-Scale Mirrors: Observation of Radiation Pressure Noise in the Advanced Virgo Detector”. In: *Phys. Rev. Lett.* 125.13 (13 Sept. 2020), p. 131101.

BIBLIOGRAPHY

- [44] Simon Chelkowski et al. “Experimental Characterization of Frequency-Dependent Squeezed Light”. In: *Phys. Rev. A* 71.1 (1 Jan. 2005), p. 013806.
- [45] Eric Oelker et al. “Audio-Band Frequency-Dependent Squeezing for Gravitational-Wave Detectors”. In: *Physical Review Letters* 116.4, 041102 (4 Jan. 2016), p. 041102.
- [46] Yuhang Zhao et al. “Frequency-Dependent Squeezed Vacuum Source for Broadband Quantum Noise Reduction in Advanced Gravitational-Wave Detectors”. In: *Phys. Rev. Lett.* 124.17 (17 Apr. 2020), p. 171101.
- [47] Lisa Barsotti, Jan Harms, and Roman Schnabel. “Squeezed vacuum states of light for gravitational wave detectors”. In: *Reports on Progress in Physics* 82.1 (Dec. 2018), p. 016905.
- [48] Carlton M. Caves. “Quantum-Mechanical Noise in an Interferometer”. In: *Phys. Rev. D* 23.8 (8 Apr. 1981), pp. 1693–1708.
- [49] H. Grote et al. “First Long-Term Application of Squeezed States of Light in a Gravitational-Wave Observatory”. In: *Phys. Rev. Lett.* 110.18 (18 May 2013), p. 181101.
- [50] James Lough et al. “First Demonstration of 6 dB Quantum Noise Reduction in a Kilometer Scale Gravitational Wave Observatory”. In: *Phys. Rev. Lett.* 126.4 (4 Jan. 2021), p. 041102.
- [51] J. Aasi, *et al.* “Enhanced sensitivity of the LIGO gravitational wave detector by using squeezed states of light”. In: *Nature Photonics* 7.8 (8 Aug. 2013), pp. 613–619.
- [52] Virgo Collaboration et al. “Increasing the Astrophysical Reach of the Advanced Virgo Detector via the Application of Squeezed Vacuum States of Light”. In: *Phys. Rev. Lett.* 123.23 (23 Dec. 2019), p. 231108.
- [53] Vivishek Sudhir. “Quantum Fluctuations in Linear Systems”. In: *Quantum Limits on Measurement and Control of a Mechanical Oscillator*. Cham: Springer International Publishing, 2018, pp. 13–33.

-
- [54] Carlton M. Caves and Bonny L. Schumaker. “New Formalism for Two-Photon Quantum Optics. I. Quadrature Phases and Squeezed States”. In: *Phys. Rev. A* 31.5 (May 1985), pp. 3068–3092.
- [55] Christopher Gerry and Peter Knight. “Nonclassical light”. In: *Introductory Quantum Optics*. Cambridge University Press, 2004, pp. 150–194.
- [56] R. E. Slusher et al. “Observation of Squeezed States Generated by Four-Wave Mixing in an Optical Cavity”. In: *Phys. Rev. Lett.* 55 (22 Nov. 1985), pp. 2409–2412.
- [57] R. M. Shelby et al. “Broad-Band Parametric Deamplification of Quantum Noise in an Optical Fiber”. In: *Phys. Rev. Lett.* 57 (6 Aug. 1986), pp. 691–694.
- [58] Amir H. Safavi-Naeini et al. “Squeezed light from a silicon micromechanical resonator”. In: *Nature* 500.7461 (2013), pp. 185–189.
- [59] V. Sudhir et al. “Appearance and Disappearance of Quantum Correlations in Measurement-Based Feedback Control of a Mechanical Oscillator”. In: *Phys. Rev. X* 7 (1 Jan. 2017), p. 011001.
- [60] Amrit Pal Singh et al. “Continuous-wave squeezed states of light via ‘up-down’ self-phase modulation”. In: *Opt. Express* 27.16 (Aug. 2019), pp. 22408–22418.
- [61] Nancy Aggarwal et al. “Room-Temperature Optomechanical Squeezing”. In: *Nat. Phys.* 16.7 (July 2020), pp. 784–788.
- [62] Henning Vahlbruch et al. “Detection of 15 dB Squeezed States of Light and Their Application for the Absolute Calibration of Photoelectric Quantum Efficiency”. In: *Phys. Rev. Lett.* 117.11 (Sept. 2016), p. 110801.
- [63] Ling-An Wu et al. “Generation of Squeezed States by Parametric Down Conversion”. In: *Phys. Rev. Lett.* 57 (20 Nov. 1986), pp. 2520–2523.
- [64] D.F. Walls and Gerard J. Milburn. “Quantum Phenomena in Simple Systems in Nonlinear Optics”. In: *Quantum Optics*. Ed. by D.F. Walls and Gerard J. Milburn. Berlin, Heidelberg: Springer Berlin Heidelberg, 2008, pp. 73–91.

BIBLIOGRAPHY

- [65] Robert W. Boyd. “Chapter 2 - Wave-Equation Description of Nonlinear Optical Interactions”. In: *Nonlinear Optics (Third Edition)*. Ed. by Robert W. Boyd. Third Edition. Burlington: Academic Press, 2008, pp. 69–133.
- [66] K. Goda et al. “Photothermal fluctuations as a fundamental limit to low-frequency squeezing in a degenerate optical parametric oscillator”. In: *Physical Review A* 72 (2005), p. 043819.
- [67] S. E. Dwyer. *Quantum noise reduction using squeezed states in LIGO*. 2013.
- [68] M. J. Collett and C. W. Gardiner. “Squeezing of Intracavity and Traveling-Wave Light Fields Produced in Parametric Amplification”. In: *Phys. Rev. A* 30.3 (Sept. 1984), pp. 1386–1391.
- [69] M S Stefszky et al. “Balanced homodyne detection of optical quantum states at audio-band frequencies and below”. In: *Classical and Quantum Gravity* 29.14 (June 2012), p. 145015.
- [70] Henning Vahlbruch et al. “Coherent Control of Vacuum Squeezing in the Gravitational-Wave Detection Band”. In: *Phys. Rev. Lett.* 97.1 (July 2006), p. 011101.
- [71] E. Oelker et al. “Ultra-Low Phase Noise Squeezed Vacuum Source for Gravitational Wave Detectors”. In: *Optica, OPTICA* 3.7 (July 2016), pp. 682–685.
- [72] Simon Chelkowski et al. “Coherent Control of Broadband Vacuum Squeezing”. In: *Phys. Rev. A* 75.4 (Apr. 2007), p. 043814.
- [73] Eric Oelker. “Squeezed states for advanced gravitational wave detectors”. PhD thesis. MIT, 2016.
- [74] S. Dwyer et al. “Squeezed Quadrature Fluctuations in a Gravitational Wave Detector Using Squeezed Light”. In: *Opt. Express, OE* 21.16 (Aug. 2013), pp. 19047–19060.
- [75] N Kijbunchoo et al. “Low phase noise squeezed vacuum for future generation gravitational wave detectors”. In: *Classical and Quantum Gravity* 37.18 (Aug. 2020), p. 185014.
- [76] L. McCuller et al. “LIGO’s Quantum Response to Squeezed States”. In: *Phys. Rev. D* 104.6 (6 Sept. 2021), p. 062006.

-
- [77] Vladimir B. Braginsky, Yuri I. Vorontsov, and Kip S. Thorne. “Quantum Non-demolition Measurements”. In: *Science* 209.4456 (Aug. 1980), pp. 547–557.
- [78] Carlton M. Caves et al. “On the Measurement of a Weak Classical Force Coupled to a Quantum-Mechanical Oscillator. I. Issues of Principle”. In: *Rev. Mod. Phys.* 52.2 (Apr. 1980), pp. 341–392.
- [79] Horace P. Yuen. “Contractive States and the Standard Quantum Limit for Monitoring Free-Mass Positions”. In: *Phys. Rev. Lett.* 51.9 (Aug. 1983), pp. 719–722.
- [80] Masanao Ozawa. “Measurement Breaking the Standard Quantum Limit for Free-Mass Position”. In: *Phys. Rev. Lett.* 60.5 (Feb. 1988), pp. 385–388.
- [81] William G. Unruh. “Quantum Noise in the Interferometer Detector”. In: *Quantum Optics, Experimental Gravity, and Measurement Theory*. Ed. by Pierre Meystre and Marlan O. Scully. NATO Advanced Science Institutes Series. Boston, MA: Springer US, 1983, pp. 647–660.
- [82] F. Acernese et al. “Frequency-Dependent Squeezed Vacuum Source for the Advanced Virgo Gravitational-Wave Detector”. In: *Phys. Rev. Lett.* 131 (4 July 2023), p. 041403.
- [83] F. Ya. Khalili. “Quantum Variational Measurement and the Optical Lever Intracavity Topology of Gravitational-Wave Detectors”. In: *Phys. Rev. D* 75.8 (Apr. 2007), p. 082003.
- [84] F. Ya. Khalili. “Increasing Future Gravitational-Wave Detectors’ Sensitivity by Means of Amplitude Filter Cavities and Quantum Entanglement”. In: *Phys. Rev. D* 77.6 (6 Mar. 2008), p. 062003.
- [85] Farid Ya. Khalili, Haixing Miao, and Yanbei Chen. “Increasing the sensitivity of future gravitational-wave detectors with double squeezed-input”. In: *Phys. Rev. D* 80 (4 Aug. 2009), p. 042006.
- [86] F. Ya. Khalili. “Optimal Configurations of Filter Cavity in Future Gravitational-Wave Detectors”. In: *Phys. Rev. D* 81.12 (12 June 2010), p. 122002.
- [87] Min Jet Yap et al. “Broadband Reduction of Quantum Radiation Pressure Noise via Squeezed Light Injection”. In: *Nat. Photonics* 14.1 (Jan. 2020), pp. 19–23.

BIBLIOGRAPHY

- [88] Jan Südbeck et al. “Demonstration of Interferometer Enhancement through Einstein–Podolsky–Rosen Entanglement”. In: *Nat. Photonics* 14.4 (Apr. 2020), pp. 240–244.
- [89] Min Jet Yap et al. “Generation and Control of Frequency-Dependent Squeezing via Einstein–Podolsky–Rosen Entanglement”. In: *Nat. Photonics* 14.4 (Apr. 2020), pp. 223–226.
- [90] Jonathan Cripe et al. “Quantum Backaction Cancellation in the Audio Band”. In: *Phys. Rev. X* 10 (3 Sept. 2020), p. 031065.
- [91] P. Kwee et al. “Decoherence and Degradation of Squeezed States in Quantum Filter Cavities”. In: *Phys. Rev. D* 90.6 (6 Sept. 2014), p. 062006.
- [92] Naoki Aritomi et al. “Demonstration of length control for a filter cavity with coherent control sidebands”. In: *Phys. Rev. D* 106 (10 Nov. 2022), p. 102003.
- [93] Lee McCuller and Lisa Barsotti. “Design Requirement Document of the A+ filter cavity and relay optics for frequency dependent squeezing”. In: *LIGO Public Document* (2019).
- [94] Lee McCuller. *Filter cavity RLF phase noise quality (LIGO Livingston logbook entry)*. URL: <https://alog.ligo-la.caltech.edu/aLOG/index.php?callRep=62358>.
- [95] Sheon S. Y. Chua et al. “Backscatter tolerant squeezed light source for advanced gravitational-wave detectors”. In: *Opt. Lett.* 36.23 (Dec. 2011), pp. 4680–4682.
- [96] Andrew R. Wade et al. “A Squeezed Light Source Operated under High Vacuum”. In: *Sci. Rep.* 5.1 (Dec. 2015), p. 18052.
- [97] F. Matichard et al. “Seismic Isolation of Advanced LIGO: Review of Strategy, Instrumentation and Performance”. In: *Class. Quantum Grav.* 32.18 (Aug. 2015), p. 185003.
- [98] T. Isogai et al. “Loss in Long-Storage-Time Optical Cavities”. In: *Opt. Express*, OE 21.24 (Dec. 2013), pp. 30114–30125.

- [99] Bram J. J. Slagmolen et al. “Tip-tilt mirror suspension: Beam steering for advanced laser interferometer gravitational wave observatory sensing and control signals”. In: *Review of Scientific Instruments* 82.12, 125108 (2011), p. 125108.
- [100] M. Evans et al. “Realistic filter cavities for advanced gravitational wave detectors”. In: *Phys. Rev. D* 88.2 (2 July 2013), p. 022002.
- [101] Eleonora Capocasa et al. “Measurement of optical losses in a high-finesse 300 m filter cavity for broadband quantum noise reduction in gravitational-wave detectors”. In: *Phys. Rev. D* 98 (2 July 2018), p. 022010.
- [102] Thomas Corbitt, Nergis Mavalvala, and Stan Whitcomb. “Optical Cavities as Amplitude Filters for Squeezed Fields”. In: *Phys. Rev. D* 70.2 (2 July 2004), p. 022002.
- [103] Michele Maggiore. *Gravitational Waves. Vol. 1: Theory and Experiments*. Oxford Master Series in Physics. Oxford University Press, 2007.
- [104] Lee Samuel Finn and David F. Chernoff. “Observing binary inspiral in gravitational radiation: One interferometer”. In: *Phys. Rev. D* 47 (6 Mar. 1993), pp. 2198–2219.
- [105] M. V. Plissi et al. “GEO 600 triple pendulum suspension system: Seismic isolation and control”. In: *Review of Scientific Instruments* 71.6 (2000), pp. 2539–2545.
- [106] Álvaro Fernández-Galiana et al. “Advanced LIGO Squeezer Platform for Backscattered Light and Optical Loss Reduction”. In: *Class. Quantum Grav.* 37.21 (Oct. 2020), p. 215015.
- [107] “Low-loss Faraday Isolators for the LIGO A+ detectors”. In: *in preparation* (2024).
- [108] Varun Srivastava et al. “Piezo-Deformable Mirrors for Active Mode Matching in Advanced LIGO”. In: *Opt. Express, OE* 30.7 (Mar. 2022), pp. 10491–10501.
- [109] Huy Tuong Cao et al. “High Dynamic Range Thermally Actuated Bimorph Mirror for Gravitational Wave Detectors”. In: *Appl. Opt., AO* 59.9 (Mar. 2020), pp. 2784–2790.

BIBLIOGRAPHY

- [110] James Alexander Clark et al. “Observing gravitational waves from the post-merger phase of binary neutron star coalescence”. In: *Classical and Quantum Gravity* 33.8 (2016), p. 085003.
- [111] Katerina Chatziioannou et al. “Inferring the post-merger gravitational wave emission from binary neutron star coalescences”. In: *Phys. Rev. D* 96 (12 Dec. 2017), p. 124035.
- [112] Hsin-Yu Chen et al. “Distance measures in gravitational-wave astrophysics and cosmology”. In: *Classical and Quantum Gravity* 38.5 (Jan. 2021), p. 055010.
- [113] B. P. Abbott et al. “GWTC-1: A Gravitational-Wave Transient Catalog of Compact Binary Mergers Observed by LIGO and Virgo during the First and Second Observing Runs”. In: *Phys. Rev. X* 9 (3 Sept. 2019), p. 031040.
- [114] A. Staley et al. “High precision optical cavity length and width measurements using double modulation”. In: *Opt. Express* 23.15 (July 2015), pp. 19417–19431.
- [115] M Rakhmanov, M Evans, and H Yamamoto. “An optical vernier technique for in situ measurement of the length of long Fabry-Pérot cavities”. In: *Measurement Science and Technology* 10.3 (Mar. 1999), p. 190.
- [116] Victoria Xu. *FC IR mode-matching (LIGO Hanford logbook entry)*. URL: <https://alog.ligo-wa.caltech.edu/aLOG/index.php?callRep=66793>.
- [117] Victoria Xu. *NLG HD sweep, HD mystery losses fully resolved, 8dB HD SQZ with new crystal spot (LIGO Hanford observatory logbook entry)*. URL: <https://alog.ligo-wa.caltech.edu/aLOG/index.php?callRep=73562>.
- [118] Craig Cahillane. *DARM offset and contrast defect (LIGO Hanford logbook entry)*. URL: <https://alog.ligo-wa.caltech.edu/aLOG/index.php?callRep=67305>.
- [119] Jeff Kissel. *DARM Sensing Function and Calibration Systematic Error vs. SRCL Offset (LIGO Hanford logbook entry)*. URL: <https://alog.ligo-wa.caltech.edu/aLOG/index.php?callRep=67613>.
- [120] Aidan F. Brooks et al. “Overview of Advanced LIGO Adaptive Optics”. In: *Appl. Opt.*, AO 55.29 (Oct. 2016), pp. 8256–8265.

-
- [121] Dhruva Ganapathy. *SQZ data GPS times (LIGO Hanford logbook entry)*. URL: <https://alog.ligo-wa.caltech.edu/aLOG/index.php?callRep=67498>.
- [122] Dhruva Ganapathy. *Interactive SQZ analysis script (LIGO Hanford logbook entry)*. URL: <https://alog.ligo-wa.caltech.edu/aLOG/index.php?callRep=67565>.
- [123] Sebastiano Bernuzzi et al. “Tidal effects in binary neutron star coalescence”. In: *Phys. Rev. D* 86 (4 Aug. 2012), p. 044030.
- [124] Tanja Hinderer et al. “Tidal deformability of neutron stars with realistic equations of state and their gravitational wave signatures in binary inspiral”. In: *Phys. Rev. D* 81 (12 June 2010), p. 123016.
- [125] A. Bauswein and H.-T. Janka. “Measuring Neutron-Star Properties via Gravitational Waves from Neutron-Star Mergers”. In: *Phys. Rev. Lett.* 108 (1 Jan. 2012), p. 011101.
- [126] Haixing Miao, Huan Yang, and Denis Martynov. “Towards the design of gravitational-wave detectors for probing neutron-star physics”. In: *Physical Review D* 98.4 (Aug. 2018).
- [127] Denis Martynov et al. “Exploring the sensitivity of gravitational wave detectors to neutron star physics”. In: *Physical Review D* 99.10 (May 2019).
- [128] K. Ackley et al. *Neutron Star Extreme Matter Observatory: A kilohertz-band gravitational-wave detector in the global network*. 2020.
- [129] John Miller et al. “Prospects for doubling the range of Advanced LIGO”. In: 91.6, 062005 (6 Mar. 2015), p. 062005.
- [130] L Barsotti et al. *The A+ design curve*. Tech. rep. T1800042. LIGO, 2018.
- [131] A. Buikema et al. “Sensitivity and performance of the Advanced LIGO detectors in the third observing run”. In: *Phys. Rev. D* 102.6 (6 Sept. 2020), p. 062003.
- [132] Jun Mizuno. “Comparison of optical configurations for laser-interferometric gravitational-wave detectors”. PhD thesis. Hannover U., 1995.

BIBLIOGRAPHY

- [133] Alessandra Buonanno and Yanbei Chen. “Signal recycled laser-interferometer gravitational-wave detectors as optical springs”. In: *Physical Review D* 65.4 (Jan. 2002), p. 042001.
- [134] Peter Fritschel, Matthew Evans, and Valery Frolov. “Balanced homodyne readout for quantum limited gravitational wave detectors”. In: *Opt. Express* 22.4 (Feb. 2014), pp. 4224–4234.
- [135] Tobin T Fricke et al. “DC readout experiment in Enhanced LIGO”. In: *Classical and Quantum Gravity* 29.6 (Feb. 2012), p. 065005.
- [136] Ka Wa Tsang, Tim Dietrich, and Chris Van Den Broeck. “Modeling the post-merger gravitational wave signal and extracting binary properties from future binary neutron star detections”. In: *Phys. Rev. D* 100 (4 Aug. 2019), p. 044047.
- [137] Sebastiano Bernuzzi, Tim Dietrich, and Alessandro Nagar. “Modeling the Complete Gravitational Wave Spectrum of Neutron Star Mergers”. In: *Phys. Rev. Lett.* 115 (9 Aug. 2015), p. 091101.
- [138] Feryal Özel et al. “On the mass distribution and birth masses of neutron stars”. English (US). In: *Astrophysical Journal* 757.1 (Sept. 2012).
- [139] Haixing Miao, Nicolas D. Smith, and Matthew Evans. “Quantum Limit for Laser Interferometric Gravitational-Wave Detectors from Optical Dissipation”. In: *Phys. Rev. X* 9 (1 Mar. 2019), p. 011053.
- [140] Osamu Miyakawa et al. “Measurement of optical response of a detuned resonant sideband extraction gravitational wave detector”. In: *Phys. Rev. D* 74 (2 July 2006), p. 022001.
- [141] S Hild et al. “Demonstration and comparison of tuned and detuned signal recycling in a large-scale gravitational wave detector”. In: *Classical and Quantum Gravity* 24.6 (Mar. 2007), pp. 1513–1523.
- [142] Wenxuan Jia et al. *LIGO operates with quantum noise below the Standard Quantum Limit*. 2024.
- [143] Aaron W. Goodwin-Jones et al. “Single and coupled cavity mode sensing schemes using a diagnostic field”. In: *Opt. Express* 31.21 (Oct. 2023), pp. 35068–35085.

-
- [144] Aaron W. Goodwin-Jones et al. “Transverse mode control in quantum enhanced interferometers: a review and recommendations for a new generation”. In: *Optica* 11.2 (Feb. 2024), pp. 273–290.
- [145] Yiqiu Ma et al. “Proposal for gravitational-wave detection beyond the standard quantum limit through EPR entanglement”. In: *Nature Physics* 13.8 (2017), pp. 776–780.
- [146] Mikhail Korobko et al. “Quantum expander for gravitational-wave observatories”. In: *Light: Science & Applications* 8.1 (2019), p. 118.
- [147] Jonas Junker et al. “Frequency-Dependent Squeezing from a Detuned Squeezer”. In: *Phys. Rev. Lett.* 129 (3 July 2022), p. 033602.
- [148] Emil Zeuthen, Eugene S. Polzik, and Farid Ya. Khalili. “Trajectories Without Quantum Uncertainties in Composite Systems with Disparate Energy Spectra”. In: *PRX Quantum* 3 (2 June 2022), p. 020362.
- [149] Teng Zhang et al. “Gravitational-Wave Detector for Postmerger Neutron Stars: Beyond the Quantum Loss Limit of the Fabry-Perot-Michelson Interferometer”. In: *Phys. Rev. X* 13 (2 May 2023), p. 021019.
- [150] David Mason et al. “Continuous force and displacement measurement below the standard quantum limit”. In: *Nature Physics* 15.8 (2019), pp. 745–749.
- [151] Daniel Carney, Kyle G. Leach, and David C. Moore. “Searches for Massive Neutrinos with Mechanical Quantum Sensors”. In: *PRX Quantum* 4 (1 Feb. 2023), p. 010315.
- [152] Alaina Attanasio et al. “Snowmass 2021 White Paper: The Windchime Project”. In: *Snowmass 2021*. Mar. 2022.
- [153] M. Malnou et al. “Squeezed Vacuum Used to Accelerate the Search for a Weak Classical Signal”. In: *Phys. Rev. X* 9 (2 May 2019), p. 021023.
- [154] M. J. Jewell et al. “New results from HAYSTAC’s phase II operation with a squeezed state receiver”. In: *Phys. Rev. D* 107 (7 Apr. 2023), p. 072007.
- [155] Charlotte Bond et al. “Interferometer techniques for gravitational-wave detection”. In: *Living Reviews in Relativity* 19.1 (2017), p. 3.

BIBLIOGRAPHY

- [156] Jason Oberling. *FC1 alignment (IAS) and balancing report (LIGO Hanford logbook entry)*. URL: <https://alog.ligo-wa.caltech.edu/aLOG/index.php?callRep=60803>.
- [157] Jason Oberling. *FC2 Initial Alignment Complete (LIGO Hanford logbook entry)*. URL: <https://alog.ligo-wa.caltech.edu/aLOG/index.php?callRep=65509>.
- [158] Dhruva Ganapathy. *Rough estimate of FC length noise related back-scatter in DARM (LIGO Hanford logbook entry)*. URL: <https://alog.ligo-wa.caltech.edu/aLOG/index.php?callRep=67586>.
- [159] Michael P. Scripsick and Gary E. Ruland. "Laser Induced Optical Damage in KTP". In: *Advanced Solid State Lasers*. Optica Publishing Group, 1998, p. VL13.
- [160] Haocun Yu. *OPO Cavity Loss Study*. URL: <https://dcc.ligo.org/LIGO-T2000150>.
- [161] Dorotea Macri. *OPO green trans/refl power trend over the past year (LIGO Hanford observatory logbook entry)*. URL: <https://alog.ligo-wa.caltech.edu/aLOG/index.php?callRep=73456>.
- [162] B. Boulanger et al. "Optical studies of laser-induced gray-tracking in KTP". In: *IEEE Journal of Quantum Electronics* 35.3 (1999), pp. 281–286.
- [163] S. Wang, V. Pasiskevicius, and F. Laurell. "Peculiarities of green light-induced infrared absorption dynamics in PPKTP". In: *Advanced Solid-State Photonics (TOPS)*. Optica Publishing Group, 2004, p. 461.
- [164] B. Boulanger et al. "Study of KTiOPO₄ gray-tracking at 1064, 532, and 355 nm". In: *Applied Physics Letters* 65.19 (Nov. 1994), pp. 2401–2403.
- [165] Chang-Long Zhang et al. "Growth and optical properties of bulk KTP crystals by hydrothermal method". In: *Journal of Crystal Growth* 310.7 (2008). the Proceedings of the 15th International Conference on Crystal Growth (ICCG-15) in conjunction with the International Conference on Vapor Growth and Epitaxy and the US Biennial Workshop on Organometallic Vapor Phase Epitaxy, pp. 2010–2014.

- [166] S. Motokoshi et al. “Control of gray-tracking formation for KTP and LBO crystals”. In: *Technical Digest. CLEO/Pacific Rim 2001. 4th Pacific Rim Conference on Lasers and Electro-Optics (Cat. No.01TH8557)*. Vol. 2. 2001, pp. II-II.
- [167] Regina Lee. *Trending OPO IR Trans to Refl Ratio Over the Past Year (LIGO Hanford observatory logbook entry)*. URL: <https://alog.ligo-wa.caltech.edu/aLOG/index.php?callRep=73454>.